Functional Heptagon-Centred Polyaromatics

ANDREW THOMAS TURLEY

Durham University
Department of Chemistry

Functional Heptagon-Centred Polyaromatics

Andrew Thomas Turley

A Thesis Submitted for the Degree of Doctor of Philosophy

January 2020

Dedicated to my loving Friends and Family

Table of Contents

Abstract ..... *vii*

Declaration ..... *viii*

Conferences Attended and Presentations Given ..... *ix*

Acknowledgments ..... *x*

Published Journals ..... *xi*

List of Abbreviations ..... *xii*

General Experimental Methods ..... *xiv*

Thesis Layout ..... *xvi*

CHAPTER 1: CYCLOHEPTATRIENE AND POLYAROMATIC HYDROCARBONS: SYNTHESIS, PROPERTIES AND APPLICATIONS. **1**

Synopsis 2

1.1 Cycloheptatriene 3

1.1.1 Norcaradiene-Cycloheptatriene Equilibrium 3

1.1.2 Advances in Cycloheptatriene Synthesis 7

1.1.3 Cycloheptatriene as a Synthetic Building Block 9

1.2 The Tropylium Cation 12

1.2.2 Synthesis of the Tropylium Cation 13

1.2.2 Substituted Tropylium 13

1.3 Molecular Graphenoids and Nanographenes 16

1.3.1 Edge Functionalization of Graphenoids 18

1.3.2 Non-conventional synthetic methods 22

1.3.3 Warped Nanographenes 24

1.4 Optical Properties of PAHs and Molecular Graphenoids 31

1.4.1 Structure-Property Relationship in Aggregation-Induced Emission 32

1.4.2 Aggregation Induced Emission: Photocyclization and Isomerization 37

1.5 Overview 40

1.6 References 41

CHAPTER 2: PROBING THE PHOTOCYCLIZATION LOSS PATHWAY IN THE DESIGN OF NEW AIE EMITTERS. **47**

Synopsis & Acknowledgements 48

2.1 Introduction 49

2.2 Results and Discussion 50

2.3 Conclusions 59

2.4 Experimental Details 60

2.4.1 Specific Experimental Methods 60

2.4.2 Synthetic Procedures 61

2.5 Appendix of Supplementary Data and Discussion 70

2.5.1 Variable-Temperature (VT) NMR Spectroscopy 70

2.5.2 X-ray Crystallographic Analysis 77

2.5.3 UV-Vis Absorption Spectra 90

2.5.4 Variable-Temperature Fluorescence 95

2.5.5 Fluorescence Solvatochromism 102

2.5.6 Phenanthrene 104

2.5.7 Photooxidation 105

2.5.8 Time-Correlated Single Photon Counting (TCSPC) 106

2.5.8 Computational Analysis 106

2.6 References 107

CHAPTER 3: TWISTED TROPYLIUMS. **109**

Synopsis & Acknowledgements 110

3.1 Introduction 111

3.2 Results and Discussion 112

3.2.1 Photophysical Properties of Tropylium Isomers 118

3.3 Conclusions 120

3.4 Future Work 121

3.5 Experimental Details 121

3.5.1 Specific Experimental Methods 121

3.5.2 Synthetic Procedures 122

3.6 Appendix of Supplementary Data and Discussion 130
3.6.1 Synthesis of 3,8-Diethylacenaphtenequinone 130
3.6.2 NMR Spectroscopy 131
3.6.3 Calculated Tropylium Isomers 133
3.6.4 X-ray Crystallographic Analysis 134
3.6.5 UV-Vis Absorption Spectra 139
3.6.6 Room-Temperature Fluorescence 141
3.6.7 Phosphorescence ICCD 142
3.6.8 Time-Correlated Single Photon Counting (TCSPC) 144
3.7 References 145

CHAPTER 4: TOWARDS A REDOX-ACTIVE C_7-SYMMETRIC WARPED NANOGRAPHENE. 147
Synopsis & Acknowledgements 148
4.1 Introduction 149
4.2 Results and Discussion 150
4.2.1 Peripheral Ring Functionalisation 153
4.2.2 Synthesis of Substituted Cyclopropenes 154
4.2.3 Synthesis of Substituted Cyclopentadieneones 155
4.2.4 Intramolecular Oxidative Cyclodehydrogenation 157
4.2.5 Synthesis *via* Tropone Derivatives 159
4.2.6 Photocyclisation 161
4.3 Conclusions 162
4.4 Future Work 163
4.5 Experimental Details 163
4.5.1 Specific Experimental Methods 163
4.5.2 Synthetic Procedures 164
4.5.3 Smaller Precursor Synthesis 178
4.5.4 Intramolecular Oxidative Cyclodehydrogenation Conditions 181
4.6 Appendix of Supplementary Data and Discussion 183
4.6.1 Variable-Temperature NMR Spectroscopy 183

4.6.2 Thermally Induced Isomerization 184
4.6.3 Tropylium Cation Synthesis *via* Epoxidation 186
4.6.4 Scholl Reactions 188
4.6.5 X-Ray Crystallographic Analysis 189
4.7 References 193

CHAPTER 5: MODULATION OF CHARGE TRANSFER BY *N*-ALKYLATION TO CONTROL FLUORESCENCE ENERGY AND QUANTUM YIELD. 195

Synopsis & Acknowledgements 196
5.1 Introduction 197
5.2 Results and Discussion 198
5.3 Conclusions 204
5.4 Experimental Details 205
5.4.1 Specific Experimental Methods 205
5.4.2 Synthetic Procedures 205
5.5 Appendix of Supplementary Data and Discussion 210
5.5.1 X-ray Crystallographic Analysis 210
5.5.2 Photoluminescence Quantum Yield Measurements 212
5.6 Theoretical Study 218
5.7 References 223

Abstract

Although normally associated with neutral carbon frameworks, aromaticity can also be found in charged systems. Carbon frameworks bearing unsaturated, odd-numbered rings are known to exhibit the same type of stabilising electron delocalisation as traditional aromatics when they hold a positive or negative charge. High impact neutral carbon materials such as graphene can be modified to possess the unique properties of charged aromatic systems through implementing unsaturated odd numbered rings (aromatic ions).[1] We are attempting to achieve this by building an extended nanographene from a central tropylium cation providing a redox-active polycyclic aromatic hydrocarbon (Figure 1a).

Synthesising a family of cycloheptatriene centred molecular rotor precursors also allows us to study the photophysical properties associated with charged, aromatic molecular rotors. The photoluminescence of phenyl-ring molecular rotors bearing seven phenyl groups are reported to originate, not from the localized excited state as one might expect, but from unanticipated through-space aromatic-dimer states.[2]

This Thesis will discuss investigations into the structure-property relationships of cycloheptatriene embedded molecular rotors. The applications of heptaphenylcycloheptatriene have been discussed through Chapters 2-4 with key findings revealing the importance of modifying both the central and peripheral rings of these molecular rotors in tuning their chemical and photophysical properties.

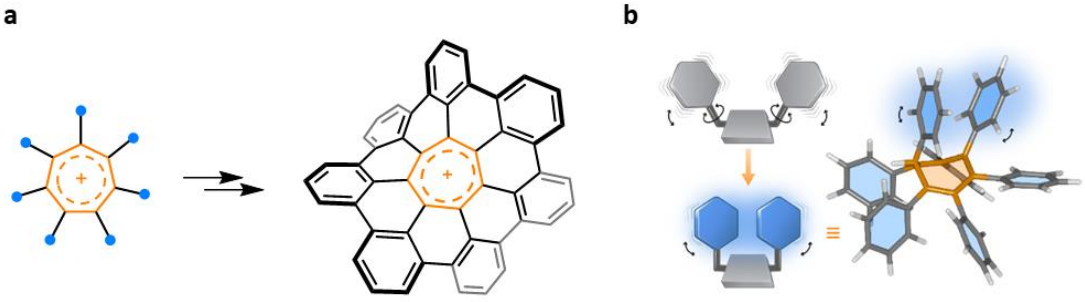

Figure 1. a) Proposed synthetic route towards a C_7-symmetric warped nanographene. b) Through-space aromatic interactions in the excited state alter the conformation and fluorescence properties of cycloheptatriene rotors.

1. K. Kawasumi, Q. Zhang, Y. Segawa, L. T. Scott and K. Itami, *Nat. Chem.*, 2013, **5**, 739–744.
2. J. Sturala, M. K. Etherington, A. N. Bismillah, H. F. Higginbotham, W. Trewby, J. A. Aguilar, E. H. C. Bromley, A.-J. Avestro, A. P. Monkman and P. R. McGonigal, *J. Am. Chem. Soc.*, 2017, **139**, 17882–17889.

Declaration

The scientific work described in this Thesis was carried out in the Chemistry Department at Durham University between October 2016 and December 2019. Unless otherwise stated, it is the work of the author and has not been submitted in whole or in support of an application for another degree or qualification at this or any other University or institute of learning.

Signed:

Date: 8th January 2020

Conferences Attended and Presentations Given

1. RSC Macrocyclic and Supramolecular Chemistry Meeting, University of Edinburgh, UK, December 2016.
Poster presentation: *Towards a Redox Active Nanographene*

2. RSC North Eastern Organic Division Regional Meeting, University of Durham, UK, March 2017.

3. 12th International Symposium on Macrocyclic & Supramolecular Chemistry, University of Cambridge, UK, July 2017.
Poster presentation: *Towards a Redox Active Nanographene*

4. 16th European Symposium on Organic Reactivity, University of Durham, UK, September 2017.
Poster presentation: *Towards a Redox Active Nanographene*

5. 8th Chemical Nanoscience Symposium, Newcastle University, UK, April 2018.
Poster presentation: *Towards a Redox Active Nanographene*

6. Durham University Chemistry Postgraduate Gala, University of Durham, UK, June 2017.
Poster presentation: *Cycloheptatriene and Tropylium Polyaromatics*

7. Supramolecular Chemistry at Work (SupraLyom), University of Lyon, France, December 2018.
Poster presentation: *Probing Through Space Interactions of Molecular Rotors*

8. Durham University Chemistry Postgraduate Gala, University of Durham, UK, June 2017.
Oral presentation: *Probing the Through Space Interactions of Molecular Rotors*

Acknowledgements

No More Zero Days – Thank You Past Me

Paul McGonigal. Thank you for your guidance and support over the years, I would not have made it this far without having such an amazing supervisor. Allowing me to develop my own ideas and be as creative as possible has made me fall in love with Chemistry more than I could have ever imagined. I will never forget your mentorship and all the success I have in my life will be built on the foundations you gave to me.

Durham University and Funding Agencies. I am grateful to Durham University for providing me endless resources and to the EPSRC and RSC for funding my research over the past three years.

Collaborators. Marc Etherington, Basile Curchod and Andrew Danos – thank you for all your support and all the hours spent in meetings with Paul and I to develop our ideas and help decipher photophysical and computational findings. None of this work would have been possible without the three of you and I am forever grateful.

Academic Staff. Certain staff members deserve a mention for their input towards my PhD and they include Matt Kitching, Alyssa Avestro and James Walton.

Technical Staff. Thank you to the following members of staff responsible for their technical support: Dr Juan A Aguilar Malavia for running 2D NMR measurments and always going the extra mile to ensure the resulting data is perfect. Dr David Parker and Peter Stokes for proving high-resolution accurate mass support. Finally Dr Dmitry Yufit for being the greatest crystallographer to ever live. (Lawrence Bragg who?)

Friends of CG233. Thank you to every member of CG233/235 past and present for being amazing colleagues and friends, you have made my time at Durham University amazing.

Specific Shout Outs: Thank you to Phil for all the amazing times, from work to our California road trip, I love you more than anything and the brother I never had. Kas, I wish I knew you more during our time at Newcastle but having you here for my PhD has been amazing! Aisha, even though you are really annoying on always on everyone's back about everything, thank you so much for being here since day one!

Published Journals

RSC Funded Summer Placement:

1. Whitfield, C.; **Turley, A**.; Tuite, E.; Connolly, B.; Pike, A. Enzymatic Method For The Synthesis Of Long DNA Sequences With Multiple Repeat Units. *Angewandte Chemie International Edition,* 2015, **54**, 8971-8974.

Master of Chemistry: Newcastle University

2. Ruiz-Sanchez, A.; Higgs, P.; Peters, D.; **Turley, A**.; Dobson, M.; North, A.; Fulton, D. Probing The Surfaces Of Biomacromolecules With Polymer-Scaffolded Dynamic Combinatorial Libraries. *ACS Macro Letters*, 2017, **6**, 903-907.

Abbreviations

^{13}C	Carbon-13 NMR Spectroscopy
^{1}H	Proton NMR Spectroscopy
AIE	Aggregation Induced Emission
ASAP	Atmospheric Solid Analysis Probe-Mass Spectrometry
CHT	Cycloheptatriene
CNT	Carbon Nanotube
CT	Charge Transfer
d	Doublet
DCE	Dichloroethene
DFT	Density Functional Theory
DMF	Dimethylformamide
DMSO	Dimethylsulfoxide
EDG	Electron Donating Group
E_{ex}	Excitation Energy
E_{max}	Energy of Emission Maxima
Equiv	Equivalence
ESI	Electron Spray Ionisation
eV	Electron Volts
EWG	Electron Withdrawing Groups
HMBC	Heteronuclear Multiple Bond Correlation
HSQC	Heteronuclear Single Quantum Coherence Spectroscopy
LE	Locally Excited
m	Multiplet
*m*CPBA	meta-Chloroperoxybenzoic acid
M.P	Melting Point
Me	Methyl
Meerwein's Salt	Triethyloxonium Tetrafluoroborate
NCD	Norcaradiene
NG	Nanographene
NMR	Nuclear Magnetic Resonance
OMe	Methoxy

Ph	Phenyl
PH	Phosphorescence
PLQY	Photoluminescence Quantum Yield
Py	Pyridyl
Qn	Quinine
RDS	Rate Determining Step
rt	Room Temperature
s	Singlet
SPhos	2-Dicyclohexylphosphino-2',6'-dimethoxybiphenyl
t	Triplet
TADF	Thermally Activated Delayed Fluorescence
^{t}Bu	Tert-butyl
TFA	Trifluoro Acetic Acid
THF	Tetrahydrofuran
TLC	Thin Layer Chromatography
TP	Tropylium
TPE	Tetraphenyl ethylene
UV	Ultraviolet
VT	Variable-Temperature
VT NMR	Variable-Temperature Nuclear Magnetic Resonance

Note: conventional abbreviations for units, physical quantities and stereochemical terms are not included here.

General Experimental Methods

Materials: All reagents were purchased from commercial suppliers (Sigma-Aldrich, Acros Organics, Fluorochem or Alfa Aesar) and used without further purification.

Instrumentation and Analytical Techniques: Analytical thin-layer chromatography (TLC) was performed on neutral aluminium sheet silica gel plates (Fluka, 60778-25EA) and visualised under UV irradiation (254 nm). Nuclear magnetic resonance (NMR) spectra were recorded using a Bruker Advance (III)-400 (^{1}H 400.130 MHz and ^{13}C 100.613 MHz), Varian Inova-500 (^{1}H 500.130 MHz and ^{13}C 125.758 MHz), Varian VNMRS-600 (^{1}H 600.130 MHz and ^{13}C 150.903 MHz) or a Varian VNMRS-700 (^{1}H 700.130 MHz and ^{13}C 176.048 MHz) spectrometer, at a constant temperature of 298 K unless otherwise stated. For variable-temperature (VT) measurements, operating temperatures were calibrated using an internal calibration solution of MeOH and glycerol. Chemical shifts (δ) are reported in parts per million (ppm) relative to the signals corresponding to residual non-deuterated solvents [$CDCl_3$: δ = 7.26 or 77.16, CD_2Cl_2: δ = 5.32 or 54.00, CD_3CN = δ = 1.94, 1.32 or 118.26, $(CD_3)_2CO$ = δ = 2.50 or 39.5. Coupling constants (J) are reported in Hertz (Hz). ^{13}C NMR Experiments were proton-decoupled, whereas ^{19}F NMR experiments are coupled and referenced to an internal standard, hexafluorobenzene (HFB, δ = 164.99 ppm), unless otherwise stated. Assignments of ^{1}H and ^{13}C NMR signals were accomplished by two-dimensional NMR spectroscopy (COSY, NOESY, HSQC, HMBC). NMR spectra were processed using MestReNova version 11. Data are reported as follows: chemical shift; multiplicity; coupling constants; integral and assignment. Low-resolution atmospheric solids analysis probe (ASAP)-MS were performed using a Waters Xevo QTOF equipped with an ASAP. High-resolution electrospray (HR-ESI) and ASAP (HR-ASAP) mass spectra were measured using a Waters LCT Premier XE high resolution, accurate mass UPLC ES MS (also with ASAP ion source). Melting points (M.P.) were recorded using a Gallenkamp (Sanyo) apparatus and are uncorrected. . UV-Vis-NIR absorbance spectra of solution samples were recorded using an Agilent Technologies Cary Series UV-vis-NIR spectrophotometer at room temperature. Dynamic light scattering was performed using a Zetasizer Nano. X-ray single crystal data were collected at 120 K unless otherwise stated, on an Agilent XCalibur (Sapphire-3 CCD detector, finefocus sealed

tube, graphite monochromator, λMoKα radiation, λ=0.71073 Å) diffractometer equipped with a Cryostream (Oxford Cryosystems) open-flow nitrogen cryostat. Structures were solved by direct method and refined by full-matrix least squares on F2 for all data using Olex23 and SHELXTL4 software. All non-hydrogen atoms were refined anisotropically and hydrogen atoms were placed in the calculated positions and refined in riding mode. Steady-state photoluminescence of films and solutions were measured using Jobin Yvon Fluoromax and Fluorlog with machine specific calibration curves. The low temperature and temperature-dependent photoluminescence spectra were measured using a Janis Research Co. Inc. nitrogen filled cryostat. Thus, at low temperature, films were in a nitrogen atmosphere and solutions in a sealed long-neck cuvette. Timecorrelated single photon counting experiments were conducted using a Ti:Sapphire laser (Mira 900, Coherent) with a narrow pulse width (> 2 ps), which was frequency tripled (using a beta barium borate (BBO) crystal) to 293 nm. The beam was vertically polarized, initially by rotating the horizontal beam and then passing it through two separate Glan-Thompson polarizers, to ensure it was highly polarized. The sample, either a solution in a quartz cuvette at room temperature or a longnecked cuvette in a cryostat for temperature dependent measurements, was illuminated by this beam. Emission collection optics, perpendicular to the excitation beam, allowed the emission to pass through a polarizer and a double monochromator (Acton Spectra Pro 2300i) before being collected by a micro-channel plate which covers a total time of with a detection channel width of 3.26 ps.

Thesis Layout

Chapter 1 introduces cycloheptatriene, discussing its properties, synthesis and modern-day approaches in polyaromatic hydrocarbons. Polyaromatic hydrocarbons are further discussed, with popular synthetic methods and structures and how they have forged a field of nanographene research. The chapter ends with the introduction of the role of polyaromatic hydrocarbons in aggregation-induced emission and how this phenomenon has revolutionised the field of photoluminescence. **Chapter 2** is presented in the form of an article, which has recently been prepared for submission to a peer-review journal focusing on our investigations into non-radiative loss pathways in aggregation-induced emission utilising cycloheptatriene centred molecular rotors. **Chapter 3** discusses unconventional isomers of tropylium resulting from introducing conformation twist. **Chapter 4** overviews the undergoing research towards a C_7 symmetric redox-active warped nanographene, formed around a tropylium centre. The Chapter reports how to synthesise a range of heptaarylcycloheptatrienes and our efforts to fuse peripheral aryl groups to form a fully fused nanographene. Chapters 3 and 4 have been formulated in a style suitable for publication later, including a focussed discussion of the key data followed by a more comprehensive account of the data in Experimental Sections and Appendices. **Chapter 5** focuses on a research project in collaboration with Dr Marc Etherington of the Department of Physics and Durham University. The work is written for publication and details a new photoluminescence quantum yield standard by improving on the current acidified quinine sulphate standard.

CHAPTER 1

CYCLOHEPTATRIENE AND POLYAROMATIC HYDROCARBONS: SYNTHESIS, PROPERTIES AND APPLICATIONS.

Synopsis

This introductory chapter focuses first on the structure and synthesis of cycloheptatriene (CHT), describing how the investigation into the norcaradiene-cycloheptatriene equilibrium through ^{13}C NMR and UV-Vis unravelled how functionality influences the conformation of CHT. This explanation is followed by discourse on polyaromatic CHTs and investigations into its stable aromatic cation of tropylium. Early investigations into polyaromatic CHTs synthesis are explored and the uses of polyaromatic hydrocarbons in molecular graphenoids and nanographenes are covered. We observe how the introduction of CHTs into these supramolecular architectures gives rise to a range of new properties and conformations, opening up a new field of single molecule materials. Finally, the field of aggregation-induced emission and the importance of polyaromatic compounds in the field are evaluated.

1.1 Cycloheptatriene

Cycloheptatriene (CHT) (**1**) is a non-planar, non-aromatic, seven membered ring system consisting of a conjugated triene and an sp^3 hybridised carbon methylene (Figure 1.1a). In the lowest energy conformation, the methylene bridge of CHT sits above the plane of the triene resulting in its characteristic non-planar structure (Figure 1.1b). CHT adopts a boat conformation that in the ground state can interconvert through a planar structure to an inverted boat structure with an energy barrier of ~24 kJ mol^{-1}.[1] Ab initio calculations reported by Donovan show the out-of-plane geometry of CHT, with angles of 30° and 50° out of plane at either end of the boat conformation.[2] (Figure 1.1c)

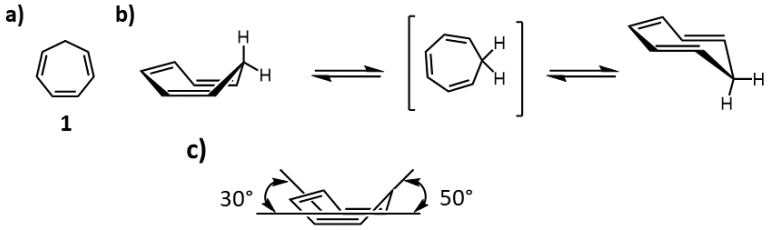

Figure 1.1. a) CHT b) Conformational interconversion of CHT **c**) round state geometry of CHT as reported by Donovan.

In 1881 Albert Ladenburg first reported the isolation of CHT through the decomposition of tropine.[3] However, as late as 1901 the structure remained unproven until Richard Willstätter reported the synthesis and characterisation of CHT, from cycloheptanone.[4] Over the next century, CHT has played an integral part in the chemical synthesis of taxanes and rotaxanes[5] and a η^6-cycloheptatriene ligand;[6,7] it has even been exploited as a reference in electrospray mass spectrometry.[8] Although less common compared to its aromatic homologue benzene, CHT has also found its place in nature, acting as the carbon framework that forms the basis of a range of natural products, including colchicine, a medication used to treat gout and Bechet's disease.[9]

1.1.1 Norcaradiene-Cycloheptatriene Equilibrium

Following the first report of a diazocarbonyl compound[10] by Curtis in 1883, Buchner began focussing on the addition of carbenes (derived from α-diazocarbonyl compounds) to benzenes, in pursuit of novel CHTs. Buchner reported the product of the thermal decomposition of ethyl diazoacetate in benzene as ethyl 7-

norcaradienecarboxylate (**3**).[11] A mixture of three isomeric CHT ethyl esters (**4**) were also observed.[12] The synthetic route, that has now been coined the Buchner ring expansion, was developed in 1885 by E. Buchner and has since provided a very powerful tool to access CHTs from stable aromatic rings (Scheme 1.1). Ring expansion of benzene with carbene intermediate (**2**) synthesises CHTs such as **4** *via* the reversible 6π electrocyclic ring opening rearrangement of a norcaradiene (NCD) derivative (**3**) to the more stable CHT tautomer. The ring opening mechanisms to produce CHT exist in an equilibrium between the bicyclic NCD and the monocyclic CHT tautomer through a thermally allowed disrotatory electrocyclic ring opening.[13] Since its first discovery, metal catalysts have been used to refine the Buchner reaction by mediating formation of a stabilised carbene (**2**) through an entropically favourable release of $N_{2(g)}$. Catalysts such as the rhodium (II) trifluoroacetate dimer have been shown to increase the reaction yields up to more than 90%.[14,15]

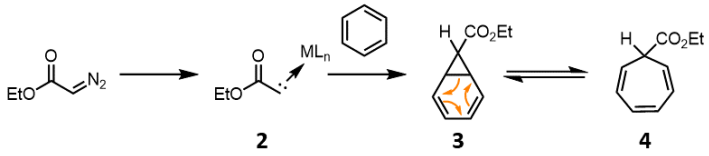

Scheme 1.1. Buchner ring expansion of benzene by ethyl diazoacetate.

Subsequently, Buchner investigated the NCD–CHT equilibrium, with the existence of the NCD tautomer much disputed. In 1951, Schenck proposed that under photochemical conditions, the decomposition of ethyl diazoacetate in benzene resulted in solely NCD[16,17] (**3**). Doering repeated Buchner's reaction conditions in 1956 and confirmed that CHT **4** exists as three isomeric trienes that result from a series of 1,3 sigmatropic shifts in a dynamic equilibrium with the kinetic NCD product.[18] It was not until 1957, when Meerwein described the product as a mixture of the two valence isomers that the debate was resolved.[19] Further studies have investigated the nature of this equilibrium and the presence and stability of the NCD tautomer. The presence of the tautomer has been further concluded through advances in cycloaddition reactions which trap the tautomer in a larger polyaromatic system.[20,21] The advancement of NMR spectroscopy also provided a method (^{13}C NMR spectroscopy) to study the dynamic equilibrium between the tautomers. Low temperature NMR spectroscopy at -150 °C failed to show the bicyclic tautomer. However, it gave a detailed insight into the fundamental structure of CHT and helped to identify a non-planar geometry which

undergoes interconversion between two boat conformations.[1,22,23] Gunther utilised the use of low temperature ^{13}C NMR spectroscopy as a tool to observe the NCD tautomer, reporting only 3% of the tautomer as a component of the dynamic equilibrium.[24] Following Gunthers findings, variable temperature NMR was employed by Balci to directly observe the dynamic equilibrium in cycloheptatrienecarbaldehyde (**5**) (Scheme 1.2.). It was found that the norcaradiene tautomer was present in 7%, exceeding the 3% observed by Gunther through the incorporation of an electron withdrawing aldehyde functionality.[25]

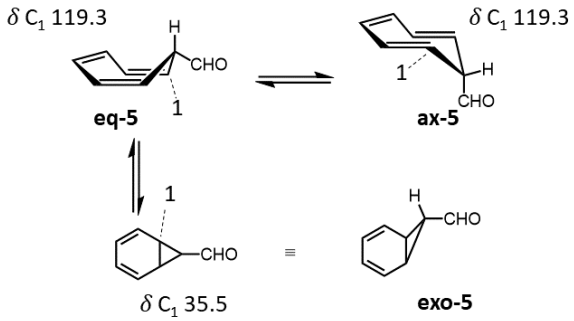

Scheme 1.2. Observed chemical shifts of CHT-carbaldehyde in dynamic equilibrium.

Subsequent investigation into the NCD-CHT equilibrium led to multiple studies focusing on the effect of different substitutions on the dynamic equilibrium. In simple systems, the CHT tautomer is favoured over the NCD tautomer due to relief of ring strain caused by the cyclopropane moiety in bicyclic NCD. However, the equilibrium between the two tautomers can be shifted to favour either side through alterations of steric, electronic or conformational effects.[26] In 1977, Stalet and Cairncross reported that π-electron donors stabilise NCDs,[27] conflicting previous reports by Hoffman who reported that electron donating groups donate from the unoccupied 2p orbital into the LUMO of the cyclopropane ring, destabilising NCDs.[28] Kollman contradicted the report from Stalet and Cairncross by using *ab initio* self-consistent field-molecular orbital (SCF MO) methods, to show that the cyclopropane ring is a weak π-electron acceptor, but a strong π-electron donor.[29] A computational study of the stabilising effects on cyclopropane rings by Schlayer in 1984 provided a detailed understanding of substituent effects on the NCD-CHT equilibrium.[30] The results supported Hoffman's original theory, however rather than only considering π-interactions, von Rague

Schleyer indicated the impact of σ-effects. This observation is a result of the ability of the cyclopropane C_1 to act as a σ- or π- acceptor which means that donation into this σ-antibonding orbital causes a lengthening in the C_1-C_2 bond and shortening of the C_2-C_3 bond, thus stabilising the cyclopropane ring. Conversely, substitution with a strong σ- acceptor shortens the C_1-C_2 bond and lengthens the C_2-C_3 bond, thereby destabilising the cyclopropane.

In 1981 Rubin reported the first direct synthesis of NCD through photolysis at 77 K using UV irradiation,[31] providing an insight into the kinetics of its interconversion to CHT. Following his initial report, Rubin reported the observation of substituted NCDs, 2,4-di-*tert*-butyl norcaradiene and 2,3,4,5-tetracholoronorcaradiene.[32] The difference in the absorption spectra between the NCD and CHT isomers allowed the rate of isomerisation (*k*) to be calculated using the Arrhenius equation (Equation 1) at the measured temperatures (90–150 K). The results show that the differences in rate of isomerisation arises from the two orders of magnitude difference in the preexponential factor (A) rather than changes in the activation energy (E_A = ~40 kJ mol^{-1} and ~28 kJ mol^{-1} respectfully).

$$k = Ae^{-\frac{E_A}{RT}}$$

Equation 1. Arrhenius equation. (*k* = Rate constant, A = Preexponential factor, E_A = Activation energy, R = Gas constant and T = Temperature)

Whilst Ruben reported the stabilising effects of substituting at the C_4-C_7 positions, Kohmotos' studies[33–35] have shown that the stability of the NCD tautomer (**6**) is largely controlled by the nature of the C_1 substituent. It was reported that electron withdrawing groups tend to shift the equilibrium towards the NCD tautomer (Table 1, entry 2) and electron donating groups stabilise the CHT tautomer (Table 1, entry 3). However, whilst true in some examples, this statement is a gross oversimplification. Trifluoromethyl groups (Table 1, entry 4) are strong electron acceptors through strong inductive effects, however, can also donate into the non-bonding C_1 orbital. This, in-turn destabilises the cyclopropane and therefore results in the equilibrium lying towards the CHT tautomer (**7**).[36] If one of the trifluoromethyl groups is replaced with an electron withdrawing group with increased resonance withdrawing effects such as a

nitrile group (Table 1, entry 5), then a dynamic equilibrium exists between the two rapidly exchanging tautomers that can be studied using variable temperature NMR spectroscopy.[37]

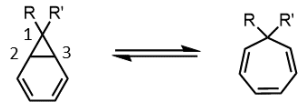

6 **7**

Entry	R	R′	Major tautomer
1	H	H	CHT
2	CN	CN	NCD
3	OCH_3	OCH_3	CHT
4	CF_3	CF_3	CHT
5	CF_3	CN	NCD/CHT
6	CO_2Me	CO_2Me	NCD

Table 1. C_1 substituent effects on the NCD-CHT tautomeric equilibrium.[38]

1.1.2 Advances in Cycloheptatriene Synthesis

The previously discussed ring expansion catalysed by rhodium complexes provide a convenient synthetic route towards CHTs. Inefficiencies arise when larger scales are sought after due to rhodium complexes being very expensive, toxic and non-reusable. As a result, there has been a large focus in recent years on alternative routes to optimise CHT synthesis.

Cycloadditions are a type of pericyclic reaction that forms a cyclic product from two or more unsaturated species in either an intramolecular or intermolecular reaction. The formation of the cyclic product occurs with no net reduction of bond multiplicity, making cycloadditions a perfect method for producing large cyclic molecules. Correlation diagram analysis can be used in conjugation with Woodward–Hoffman rules to determine if the cycloaddition is either thermally allowed or photochemically allowed. The allowed route of the cycloaddition is determined by the symmetry of the frontier molecular orbitals and as a result, the energy level of the electrons. The interactions of orbitals can be described as either suprafacial where the interaction occurs on the same face or antarafacially, where opposite faces interact.

Table 2. Woodward–Hoffman rules demonstrating thermally allowed and photochemically allowed cycloadditions.

Number of Electron Pairs	Photochemical	Thermal
Even (4n)	Suprafacial–suprafacial	Suprafacial–antarafacial
Odd (4n + 2)	Suprafacial–antarafacial	Suprafacial–suprafacial

A Diels–Alder [4+2] is a type of cycloaddition reaction that forms a six-membered carbocycle through the concerted reaction of a conjugated diene (4π electrons) and a dienophile (2π electrons) (Figure 1.2b). The method was popularised to produce cyclohexene in 1928, by Otto Diels[39] and Kurt Alder, who won the Nobel Prize in Chemistry in 1950. The reaction is concerted, occurring *via* a single cyclic transition state with no intermediates. The reaction mechanism can be described as [4πs+2πs], (Figure 1.2a) meaning it is a 4n+2 suprafacial–suprafacial orientation, making it a thermally allowed cycloaddition.

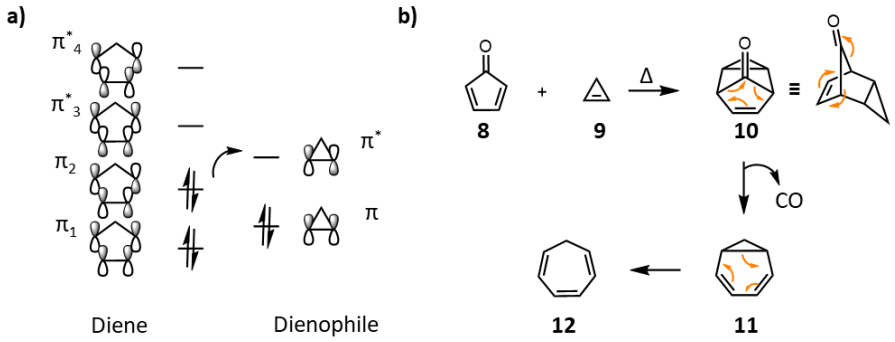

Figure 1.2. a) Orbital overlap diagram of thermally allowed Diels-Alder cycloaddition b) Mechanism of CHT formation.

The Diels–Alder reaction can be applied to the synthesis of CHTs through the reaction of dienophile cyclopropene (**9**) and diene cyclopentadieneone (**8**) derivatives *via* a tricyclic intermediate (**10**). The reaction is entropically driven by the subsequent loss of $CO_{(g)}$ through a cheletropic cycloreversion to form the NCD (**11**) which rearranges into a CHT (**12**). Battiste[40] and Breslow[41] first demonstrated that heptaphenylcycloheptatriene (**15**) can be formed through this method with further optimisation by McGonigal *et al.* in 2017[42] (Scheme 1.3a). The Diels–Alder reaction provides a highly versatile and operationally simple method to produce CHTs, however difficulties can be encountered when synthesising the highly substituted precursors.

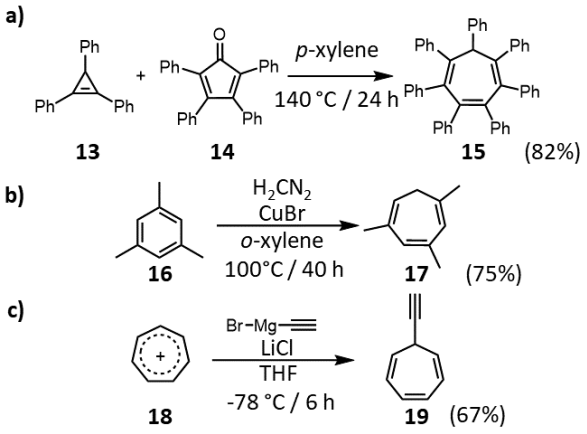

Scheme 1.3. a) Synthesis of **15** *via* [4+2] cycloaddition. b) Synthesis of **17** *via* Buchner ring-expansion. c) Synthesis of **19** from tropylium tetrafluoroborate **18**.

For the formation of non-aryl CHTs, the Buchner ring-expansion still provides a popular method to multi-substituted CHTs such as **17**. An alternative method to the Buchner ring-expansion to synthesise 7-substitued CHTs utilises commercially available tropylium tetrafluoroborate (**18**). Nucleophilic addition of the desired functionality through its corresponding Grignard allows easy access to mono substituted CHTs at the 7- position such as **19**,[43] providing a very popular initial step towards other cyclic and polycyclic compounds.

1.1.3 Cycloheptatrienes as a Synthetic Building Block

Cyclic and polycyclic moieties are vital structural components which play an important role in the activity of numerous pharmaceutical and natural products. As such, there has been a significant driving force in recent years towards the development of an efficient and robust method that facilitates the synthesis of medium rings in organic chemistry.

Annulation

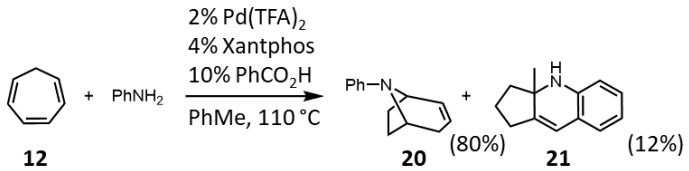

Scheme 1.4. Annulation of CHT **12** to access alkaloid **20**.

CHTs have found uses as a convenient, commercially available starting material for otherwise long multistep synthetic routes.[44–46] Hartwig and Co-workers reported a metal-catalysed dual hydroamination of **12**, through an intermolecular hydroamination

of the triene[47] (Scheme. 1.4). This method provides easy access to bridged polycyclic centres common in alkaloids such as cocaine and derivatives.

[6+2] Cycloadditions

Thermal and photochemical metal catalysed [6+2] cycloadditions of **12** with allenes,[48] alkynes[7,49,50] and even through intramolecular tethers[51], can provide easy access to higher cyclic hydrocarbon frameworks. Utilising chiral 2π partners can also offer synthetic methods to enantioenriched bicyclo[4.2.1]nonanes.[52] In 2013, D'yakonov *et al*. furthered the investigation into increasing the efficiency and scope of metal catalysed [6+2] cycloadditions from **12.**[53] Utilising their novel Ti-Al catalyst, $Ti(acac)_2Cl_2$-Et_2AlCl_3, they demonstrated the transformation of **12**, to give the corresponding bi- and polycyclic hydrocarbons in high yields (Scheme 1.5). Successful homodimerization of **12** with $Ti(acac)_2Cl_2$-Et_2AlCl_3, gave two isomers of diamantane, **22** and **23** in a 2:1 ratio respectively. The ratio of isomers can be tuned to a 1:2 ratio by changing the catalyst from $Ti(acac)_2Cl_2$ to $Ti(tBuO)_2Cl_2$. Conventional synthesis of diamantane ranges from thermal cracking of long chain hydrocarbons to Lewis acid catalysed rearrangements of various pentacyclic tetradecanes however yields vary from 1% to ~70% yield.[54] Research interests in diamantane result from its high densities, low surface energies and resistance to oxidation.[55]

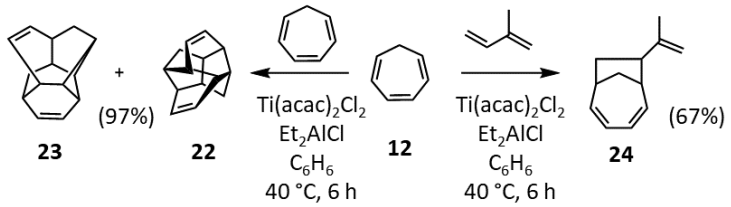

Scheme 1.4. Ti catalysed modifications of **12** to diamantane **22+23** and amantane **24**

A series of pharmaceutically important amantane compounds, including **24** (Scheme 1.4), can also be synthesised from **12** through a [6+2] cycloaddition with 1,3-dienes. They provide access to important intermediates for a variety of antiparkinsonian drugs such as memantine and amantadine.[56]

Retro-Buchner

CHT is not only useful as a method to access higher cyclic and polycyclic compounds but also can be used to reach smaller, more strained systems that would otherwise be difficult to synthesise. While the Buchner reaction concerns the expansion of a six-

membered ring to its seven-membered ring counterpart, a retro-Buchner can be used to synthesise substituted cyclopropanes from substituted CHTs. In contrast to traditional copper and rhodium catalysed processes,[57,58] 7-substituted CHT **29** can coordinate with Au(I) complexes under catalytic conditions to generate Au(I) carbenes[59] through NCD **30**. Further advancements in the field have been made by utilising a range of catalysts as well as modifying previous Rh catalysts[60] to perform under very mild conditions, thus providing a convenient synthetic route towards substituted cyclopropanes. (Scheme 1.5)

Studies show that the rate determine step for the reaction is the cleavage of the first C-C of NCD **31** to give a Wheland cationic intermediate **32** (Scheme 1.5b). The cationic intermediate can be further stabilised by the presence of an electron donating group on **32**. The final step cleaves the second C-C bond, eliminating benzene in an entropically favoured reaction, resulting in the formation of a new C=M bond **33**. The new C=M bond can now react as a metal carbene, undergoing a [2+1] cycloaddition with a desired alkene.

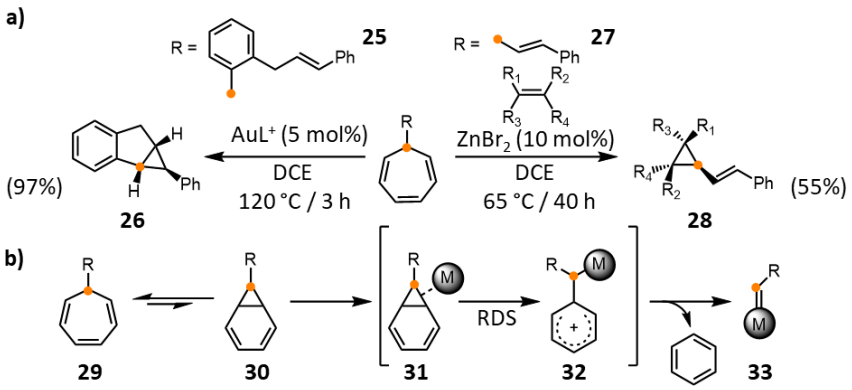

Scheme 1.5. a) Au(I) and Zn(II) catalysed retro-Buchner reaction of 7-CHT **29** b) Hypothesises mechanism of retro-Buchner to form metal carbenes.

While most reports demonstrate the use of this catalytic reaction through intermolecular interaction of Au(I) with alkenes, in 2013 Echavareen *et al.* demonstrated an intramolecular retro-Buchner to produce highly strained polycycles, featuring substituted cyclopropanes.[61] Functionalising a 7-sustitued CHT with an alkene tether (**25**), an intramolecular cyclisation can occur, forming a new polycyclic complex through the formation of a cyclopropane **26**, via a retro-Buchner reaction. (Scheme 1.5a)

In 2018, Echavaren *et al*. made further synthetic advancements, demonstrating the use of Au(I) catalyst; [(JohnPhos)Au(MeCN)]SbF_6 as a method of producing highly substituted cyclopropanes in high yields at room temperature compared to the previously reported high temperature coniditons.[62] Furthermore, Echavaren was the first to report the use of Zn(II) catalysts in the retro-Buchner formation of highly substituted cyclopropanes **28** from unactivated alkenes **27**. Echavaren also demonstrated applications of this catalytic pathway, towards a novel, diastereoselective 3-step total synthesis of (±)-lactobacillic acid[63] using 7-subsituted CHT and tolyl styrene to form the cyclopropane core.

1.2 The Tropylium Cation

The tropylium cation [$C_7H_7^+$] (TP), predicted by Huckel[64] in 1931, was first synthesised and characterised in 1954 by Doering and Knox[65] through the decomposition of dibromotroilidene, with the structure confirmed by infrared and ultra violet spectroscopy. The TP cation contains 6 π-electrons in a single conjugated system forming a closed electron shell, fulfilling Hückel's rule of aromaticity, with a calculated delocalisation energy of 1.98β.[66] Many years later, X-ray crystallography was used to confirm the planar structure of TP, showing equal bond lengths of 1.39 Å. The high symmetry (D_{7h}) is reflected by the small number of infrared and Raman absorption bands.[67] The aromaticity can also be demonstrated by the ease of formation of TP from CHT with an oxidising agent.

The physical properties of TP have been extensively studied to give information on the nature of the elusive cation and how it can be manipulated for various applications. The equilibrium between the TP cation and its halide counter ions in tropylium salts can be influenced to exploit the charge-transfer (CT) band in the absorption spectra. Rettig *et al*. reported that higher anion concentrations caused a blue shift in the CT-band due to the formation of higher associates like [CHT^+] [$2Br^-$].[68] It was also found by the same group that the ionic strength of the solution did not influence the short wavelength transition of the aryl TP cation; however, the concentrations of the aryl TP salt and the ionic strength of the solution did have an effect on the fluorescence quantum yield. Investigations into a variety of aryl substituted TP ions have shown fluorescence is

absent for those with electron donating groups.[69] This occurs due to the donor groups producing twisted excited state structures with an energy minimum in the S_1-state and possessing a very small S_1-T_1 energy gap causing fast non-radiative decay.

1.2.1 Synthesis of the Tropylium Cation

TP has been synthesised since the mid-20th century and several methods utilising different conditions have been exploited to perform the oxidation of CHT, with varying success. One common procedure involves producing tropylium salts by treating a CHT methoxide with acid to give the TP salt of the conjugate base. This method has become well established and is now a simple route to form tropylium tetrafluoroborate (**18**). Other salts of tropylium can be produced by salt exchange, with halide salts being commonly reported.[70] Whilst the oxidation of CHT is a simple process, increasing the degree of substitution on the CHT makes these oxidations more challenging.

Direct oxidation of CHT to TP can be achieved without the need to go via a CHT methoxide. The first reported synthesis, by W. Doering *et al*. in 1954, used bromine to oxidise CHT to TP bromide (Scheme 1.6). The greater leaving group character of bromide compare to CHTs hydride means upon heating, TP bromide (**34**) can be formed in high yields. An alternative route to chemical oxidation is via electrochemical oxidation, as demonstrated by David Geske in 1959 whereby electrooxidation of CHT to TP was achieved applying a voltage of +1.06 V (vs. Ag / $AgNO_3$) in MeCN using a platinum electrode.[71]

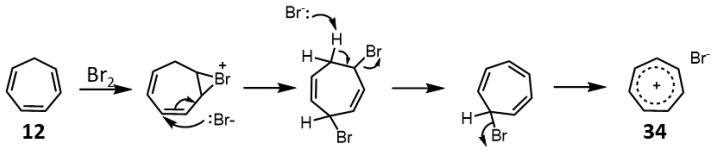

Scheme 1.6. Oxidation of **12** with bromine to produce Tropylium bromide (**34**).

1.2.2 Substituted Tropylium

Dewar and Pettit first attempted to synthesise a norcaradineneol with the aim of rearrangement into an alcohol-substituted TP upon reaction with a strong acid. However, the unsubstituted tropylium salt was obtained instead.[72] A year later, in 1956, Dewar and Pettit attempted to produce TP through the decarboxylation of cycloheptatrienecarboxylic acids, structures that had been previously assigned. It was determined; however, that previous assignment was in error as this method to yield TP

salts was found to be unsuccessful at the time. Johnson *et al*. showed a TP-substituted with an electron withdrawing carboxy group lowers the pK_a from +4.75 to +3.3, quantifying the decrease in stability of the TP cation.[70] Jutz *et al*. were able to produce methyl TP, which retained TP aromaticity in the product by utilising an ionic salt to stabilise the cation.[73] From the methyl TP, further reactions to increase the bond order and complexity were performed, forming an iminium salt utilising $POCl_3$ as a Lewis acid and a phenyl substituted TP ion.

Conrow[74] found that a 7-methyl TP (**36**) can be formed through direct reaction of TP (**18**) and a 7-methyl CHT (**35**). The methyl group stabilises the TP (**36**) by an additional 3.7 ± 0.4 kcal/mol relative to the unsubstituted TP (**18**). It was found that during the reaction, the amount of **12** begins to plateau, while the amount of 7-methyl TP (**36**) continues to decrease. After the initial oxidation of **35** by **18**, a further equilibrium forms where **36** oxidises remaining **35** to form a mixture of isomeric methyl-CHTs (**37**). These results allowed Conrow to propose the following pathway. (Scheme 1.7)

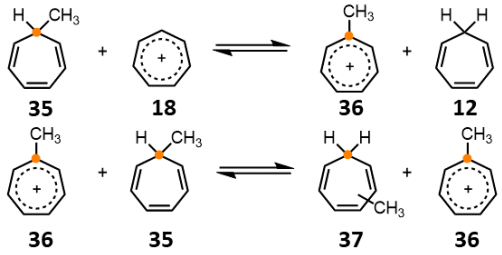

Scheme 1.7. Oxidation of 7-methyl TP (**36**) with unsubstituted TP (**18**).

Further substitution of methyl groups onto tropylidenes should give thermodynamically more effective hydride donors, while the tropylium ion should be a more effective hydride acceptor than its alkylated homologues. Phenyl substituents behave as a weak electron-acceptor substituent in relation to the tropylium cation.[75] Jutz calculated the acidity constants (pK_a) for 7-phenyl-TP as +3.87, compared to TP +4.01. This was explained by the fact that the phenyl and tropylium rings are inclined at an angle to 45-50°, disrupting the conjugation between the phenyl ring and the TP centre, resulting in a negative inductive effect.[67]

The geometry of 7-phenyl TPs is influenced by the strength of the electron donor character on the phenyl ring, which is ultimately dictated by modifying the inductive effect. Kharlanov[76] calculated the extent of the change in torsion angle upon modifying the donor strength of the TP substituent, studying phenyl TP (**38**), *p*-methoxyphenyl TP (**39**) and *p*-aminophenyl TP (**40**) (Figure 1.3). It was concluded that stronger electron donors result in a more planar geometry in the ground state, lowering the activation barrier (ΔE) from the ground state geometry to a planar geometry (α = 0°). (**38** = 18.8 kJ mol^{-1}, **39** = 12.2 kJ mol^{-1} and **40** = 8.83 kJ mol^{-1}).

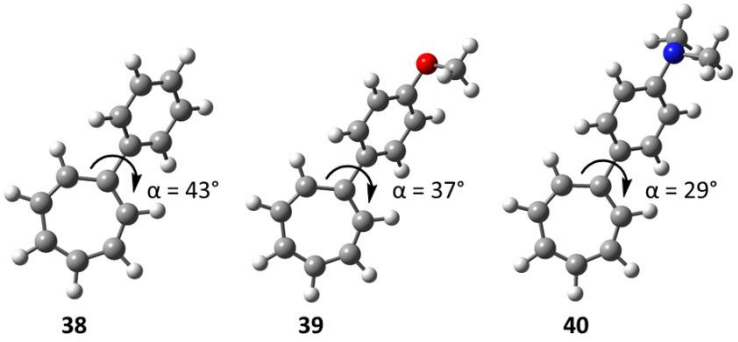

Figure 1.3. Ground state geometries of TPs **38**, **39** and **40** calculated by HF/6-31G*.

Kharlanov further investigated the relationships between the geometries of TPs and their photophysical properties. It was observed that across the same compound series the emission strength decreased, and the absorption strength increased from **38** to **40**. The following conclusion could then be made; increasing planarity of the aryl TPs results from an increase in the electron donor property, which in-turn increases the CT character of the excitation from the aryl to the tropylium ring.

Heptaphenyl substitution

The general synthesis of **15** utilising a [4+2] Diels–Alder reaction[40], as previously seen in (Figure 1.3a), has remained the same since its first published synthesis in 1961, with conditions being optimised over the years to increase efficiency. Breslow reported[77] that treating **15** with bromine gives rise to the bromide salt of $C_7Ph_7^+$, as seen previously (Scheme 1.6). Phenyl substitution around the CHT and TP centre exerts a destabilizing effect as the peripheral phenyl rings are held away from coplanarity (and, hence, out of conjugation) by steric overcrowding. This destabilizing effect was quantified by Battiste in 1968,[78] reporting a decrease in pK_a of $C_7Ph_n^+$ compounds upon increasing

the number of phenyl substituents. Interestingly $Ph_7C_7^+$ showed a higher pK_a than $Ph_6C_7^+$, indicating an apparent stabilising effect by a severely twisted phenyl.

Despite the efforts of numerous crystallography groups, the structure of $C_7Ph_7^+$ was not successfully characterised until 1995 by McGlinchey *et al*.[79] Just 3 years later in 1998, the same research groups showed that the trend of $C_nPh_n^+$ compounds adopting a non-linear, propeller type conformations continued through to $C_7Ph_7^+$. The angle subtended at the centre of the TP ring was found to be 51.4 °,[80] the lowest of all $C_nPh_n^+$ compounds due to the increased number of phenyl groups. The angle represents a compromise between the ideal coplanar arrangement between the central ring and the external phenyls for maximising π-overlap (θ = 0°) and the dihedral angle at which the steric interactions between adjacent phenyls is minimised (θ = 90°).

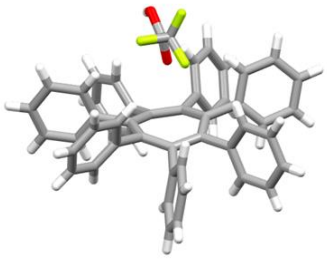

Figure 1.4. Crystal structure of heptaphenyltropylium, $Ph_7C_7 \cdot O_2CCF_3$

1.3 Molecular Graphenoids and Nanographenes

Polycyclic aromatic hydrocarbons (PAHs) are organic compounds with two or more connected aromatic rings, either by $\sigma_{C\text{-}C}$ single bonds or by virtue of being fused together, allowing electrons to be delocalised over a large area. The electron delocalization of the polycyclic aromatic structures give rise to interesting optical and electronic properties.[81] The structure and properties of the PAHs are dictated by the number and size of the rings, with "large" PAH's consisting of 6 or more aromatic rings. Most research on PAHs has been conducted with "small" structures, such as anthracene, due to their commercial availability and ease of functionalisation.

The most notable advancement in PAHs occurred in 2004, by Geim and Novoselov, when the first single atom layer from graphite was isolated, giving the two-dimensional material graphene.[82] Over the past 15 years graphene has been a hot topic for research due to its exceptional properties, particularly its exceptionally high charge-carrier

mobilities, with previously reported results of 15,000 $cm^2V^{-1}s^{-1}$. The theoretical potential limit of charge-carrier mobility has been calculated at 200,000 $cm^2V^{-1}s^{-1}$ being limited by the scattering of graphenes acoustic photons.[83] This limit can be surpassed, as demonstrated by Bolotin *et al.*[84] in 2008, where they reported that a suspension of graphene above a Si/SiO_2 gate electrode at 5 K can reach 230,000 $cm^2V^{-1}s^{-1}$. The limited applications of this high mobility is a result of graphenes lack of band gap, resulting from indistinguishable π and π* bands at the fermi energy level, producing zero-gap semiconductor properties. To reliably introduce a band gap in graphene it is essential to cut it into narrow strips of less than 10 nm in width.[85]

Consequently, structurally well-defined molecules derived from sections of graphene, known as nanographenes, have attracted renewed synthetic interest, focusing on a large range of applications such as nanoelectronics. In contrast to conventional infinite graphene, nanographenes, provides access to a non-zero band gap, governed by their size and configurations. Unlike graphene, nanographenes are synthesised from a bottom-up approach allowing access to monodisperse nanographenes with perfectly defined structures and properties. As the field grows, more complex and extended structures are being synthesised, with the introduction of heteroatoms[86], edge groups[87] and even deviating from a planar structure to synthesise 'warped' nanographenes.

The synthesis of PAHs was established during the 20th century by Scholl and Clar through a multitude of synthetic strategies. One efficient strategy involves forming new C-C bonds between neighbouring aryl rings and known as intramolecular oxidative cyclodehydrogenation (IOCD). This strategy allows allowing access to a wide variety of π-extended PAHs containing sp^2 frameworks.

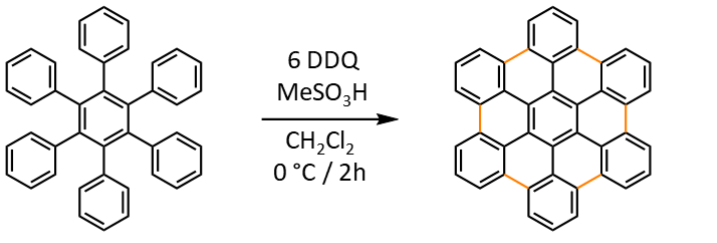

41 **42** (99%)

Scheme 1.8. A 6-fold DDQ catalysed intramolecular oxidative cyclodehydrogenation of **41** to **42**.

Hexaphenyl benzene (HPB) (**41**) was first reported in 1933 by Trosken *et al*. as the Diels-Alder product of **14** and diphenylacetylene.[88] Since then, a vast number of hexaaryl benzenes (HABs) have been synthesised that exhibit a range of structural, electronic and photophysical properties. HABs such as **40** exhibit a nonplanar structure as a result of easily rotatable peripheral aryl rings, oriented almost orthogonally, at 65° with the plane of the central ring as confirmed by X-ray crystalography.[89] As a result, HABs exhibit poor intramolecular π-conjugation, leading to a large a HOMO–LUMO gap, poor self-aggregation, poor crystalline character[90] and higher solubility allowing for potential applications including OLEDs[91], liquid crystalline materials[92], redox materials[93] and molecular receptors.[94]

Synthesised through IOCD of HPB (**40**), hexa-peri-hexabenzocoronene (*p*-HBC) (**42**) can be regarded as the smallest possible nanographene and was first synthesised by Mullen *et al*.[95] in 1995. Since then, Scholl's original conditions utilising $FeCl_3$ as a one electron oxidant for IOCD, have been further developed. Rathore *et al*[96] reported DDQ in the presence of a protic acid as an alternative oxidant, providing a cleaner and more efficient alternative to form *p*-HBC with a yield and purity >99% (Scheme 1.8). *p*-HBC exhibits a complete planar topology and is known to self-assemble into columnar phase[97] that can lead to carbon nanotubes.[98]

1.3.1 Edge Functionalisation of Graphenoids

While most physical properties of molecular graphenoids are primarily governed by their highly conjugated aromatic core, some can be 'tuned' by edge functionalisation of the peripheral aromatic rings. Introducing chemically reactive groups such as halogens allows access to further structural functionalisation, however development can be limited due to challenging bottom-up synthesis. Furthermore, the introduction of a large amount of steric hindrance or vast changes in the electronic energy, may prevent IOCD during late stage synthesis, resulting in a functionalised PAH rather than a functionalised nanographene. Late stage edge halogenation followed by IOCD can overcome this problem and allow access to various metal-catalysed coupling reactions, such as Buchwald coupling with primary and secondary amines, Suzuki coupling with boronic acids/esters and Sonogashira coupling with alkynes.

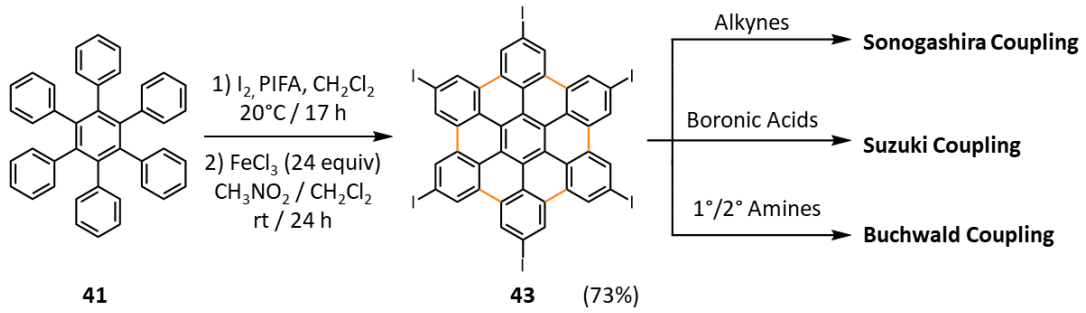

Scheme 1.9. Iodination of HPB to access more complex functionalised graphenoids.

The first synthesis of a highly functionalised hexaiodo-HBC (**43**) was reported in 2004 by Wu *et al*. as a precursor to accessing multivalent arylamine-HBCs for the development of organic semiconductors.[99] **41** was subjected to a six-fold iodination with I_2 and hypervalent iodine source (Bis(trifluoroacetoxy)iodo)benzene (PIFA) to give hexaiodo-HPB followed by IOCD with $FeCl_3$ to give **43** in a 73% yield over two steps.

One common functionalisation is the introduction of alkyl chains to modify solubility and self-assembly behaviour, giving rise to very useful compounds in liquid crystals and opto-electronic devices. *p*-HBC planar topology and high charge-carrier mobility provides an ideal core in the synthesis of distotic liquid crystals that rely on the formation of columnar phase packing. Spiess *et al.*[100] first reported the synthesis of alkylated HBC core in 1996. The synthesis utilised early aryl alkylation followed by a Sonogashira coupling to synthesises alkylated diphenylacetylene that can undergo a [2+2+2] cycloaddition to form its HAB derivate in >92% yields. Utilising this synthesis, Choi *et al.*[101] investigated the phase behaviour of HBC-C_{12} (**44**) in *p*-xylene with differential scanning calorimetry (DSC), polarized optical microscopy (POM), small angle neutron scattering (SANS) and wide-angle x-ray scattering (WAXS). They observed the formation of stacked cylindrical particles measuring between 11–13 HBC units in the isotropic phase, reinforcing the original hypothesis by Spiess of a columnar nature of alkylated hexa-peri-hexabenzocoronene.

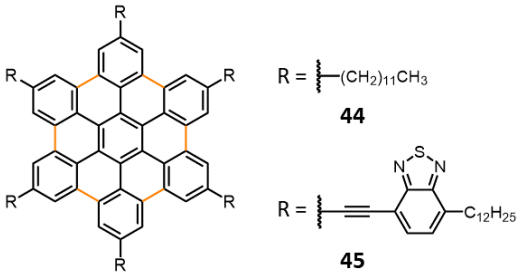

Figure 1.5. Edge-functionalisation of *p*-HBC to synthesise liquid crystal **44** and D-A complex **45**.

More recently the synthesis of Donor–Acceptor (D–A) compounds with a functionalised *p*-HBC core have been reported.[102] Mullen *et al*. reported the synthesis of D-A complex **45** through a six fold Sonogashira–Hagihara cross-coupling reaction of **43**, isolating the complex in a 64% yield. The Benzo[c][1,2,5]thiadiazole (BTZ) moiety of **45** is widely used as an electron acceptor unit in the construction of organic semiconductors. Previously, Mullen *et al*. reported the synthesis of a HBC-BTZ D-A system, where two BTZ units were directly bound to peripheral carbons. Synthesis of HBC with >2 BTZ units were unsuccessful due to steric hindrance, resulting in out of plane BTZ groups, that disrupted the π-system. This was overcame by introducing a conjugated ethylene spacer, which minimised interaction of neighbouring BTZ units, resulting in the successful formation of a HBC-BTZ6 adduct (**45**). This adduct showed a more promising D-A complex as a result of introducing more BTZ groups around the electron rich HBC core. The same group also reported an increased stability of the liquid crystalline state of **45** compared to other HBC D–A complexes, with no phase change observed over a wide range of temperatures, encouraging further applications in organic electron devices.

Edge functionalisation of HABs and HBCs also provide a highly effective, scalable bottom-up synthetic route towards extended graphenoids. One dimensional extension of *p*-HBC leads to ribbon shaped nanographenes with high aspect rations, which are called graphene nanoribbons (GNRs). While many methods to produce graphene sheets have been reported, most rely on top-down synthetic strategies such as exfoliation[103] or chemical oxidation,[104] producing graphene of varying quality in a non-scalable or reproducible manner. Yang *et al*. were first to report a bottom-up method to produce GNRs such as **50**, with lengths up to 12 nm, through edge-functionalised HPB.[105] (Scheme 1.10)

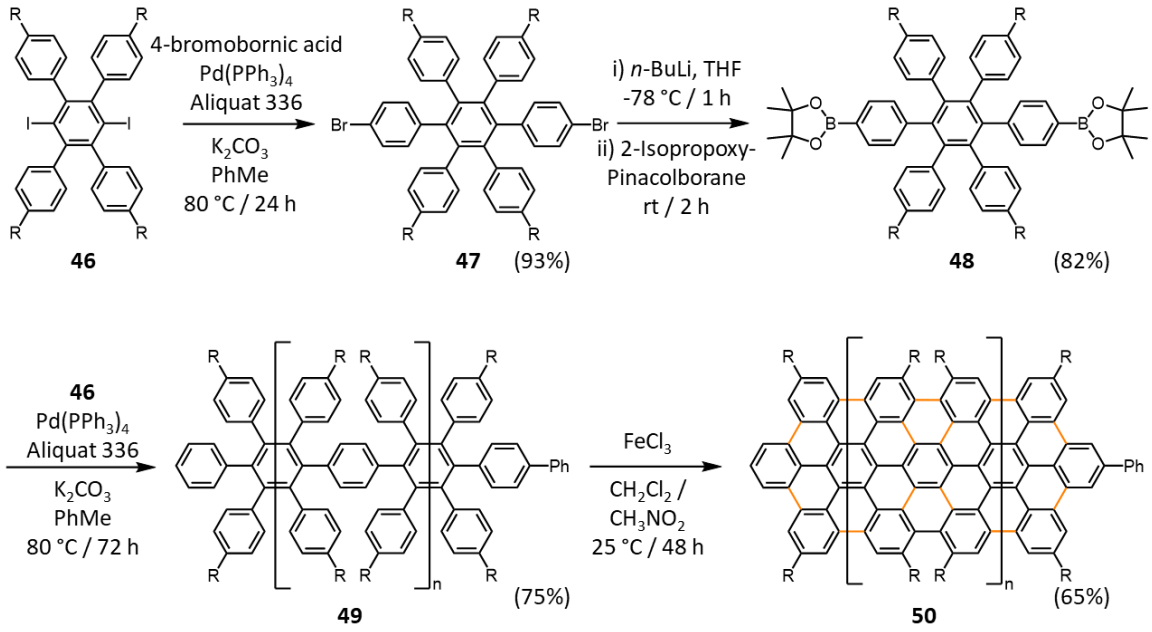

Scheme 1.10. Synthesis of graphene nanoribbon (GNR) **50**.

In the interest of synthesising a highly soluble GNR, Mullen functionalised **50** with various alkyl chains to reduce aggregation in solution. As a result, each synthesis begins with the formation of an alkylated 1,4-diiodo-2,3,5,6-tetraphenylbenzene derivative (**46**) through the Grignard addition of the desired alkyl-benzene to 1,4-dichloro-2,3,5,6-tetrabromobenzene and subsequent halogen exchange. Suzuki-Miyaura coupling of (**46**) with 4-bromoboronic acid with phase transfer catalyst Aliquat 336 produced HAB **47** in a 93% yield. A two-fold lithiation of the peripheral aryl halides gives boronic ester (**48**) that, through a further Suzuki-Miyaura coupling with **46**, produces polymeric edge-functionalised HPB in moderate yield. Finally, IOCD Scholl reactions at ambient temperatures provides organic soluble GNR **50** in a 65% yield. Since this first report, the field of GNRs has expanded into a research theme over a multitude of research fields and applications, in which utilising edge-functionalised HPBs remains a popular method to produced highly tuned GNRs at nanometre scale length.[106]

GNRs can be categorized by their edge structure, and display either ‘armchair’ or zigzag’ configurations. The nature of the configurations and the width of the GNR dictates the electronic properties. Armchair GNRs such as **50** have non-magnetic semiconducting properties with relatively large bandgaps that are inversely proportional to their width.[107] They also possess high charge-carrier mobilities, giving

rise to potential uses in logic applications.[108] Zig-zag conformations on the otherhand possess edge-to-edge configuration between neighbouring phenyl rings rather than through a C-C bond as seen in **50**. They have been reported to show localized edge states that can be spin polarized, giving rise to applications to spintronic devices.[109]

1.3.2 Non-Conventional Methods

Synthetic routes towards nanographenes *via* HBC can be limited due to steric hindrance and electronic effects that can prevent a successful Diels-Alder reaction. Moreover, rearrangements upon IOCD to produce nanographenes are widely reported in the literature, hindering the scope of research into NGs. Dichtel *et al*.[110] reported the synthesis of a HBC derivative through a non-conventional method, using oligophenylene precursors such as **51**, to synthesise previously inaccessible NGs. Regioselective benzannulation of **51** with a $Cu(OTf)_2$ and trifluoroacetic acid, allows access to **52**, a compound with similar IOCD ability to HPB (**41**). This method avoids synthetic difficulties involved with the Diels-Alder reaction and IOCD of hindered substrates, allowing introduction of large R groups such as ^{t}Bu in near quantitative yields (Scheme 1.11). Interestingly the following IOCD using $FeCl_3$ proceeds via a two-step rate limited process, allowing **53** to be isolated and characterised. The first, four-fold Scholl reaction occurs extremely fast, most likely due to the lack of functionalisation in close proximity to the new C-C bonds formed whereas an extended reaction time is needed to complete the fusion of the more hindered positions to synthesise NG **54**.

Synthesis *via* this method showed no signs of unwanted rearrangement that had been observed by King *et al*. in 2008.[111] As a result, this provides a very effective method to synthesise structurally precise NGs where conventional methods have failed. Furthermore, it provides a method to isolate partially fused variations, such as **53**, in a regioselective manner which could not be achieved through conventional IOCD of *p*-HBCs. Such partially fused products offer unique properties as a result of their non-planar structure, most notably **53** exhibits enhanced visible absorption and a smaller optical gap (-0.21 eV) compared to fully fused **54**.

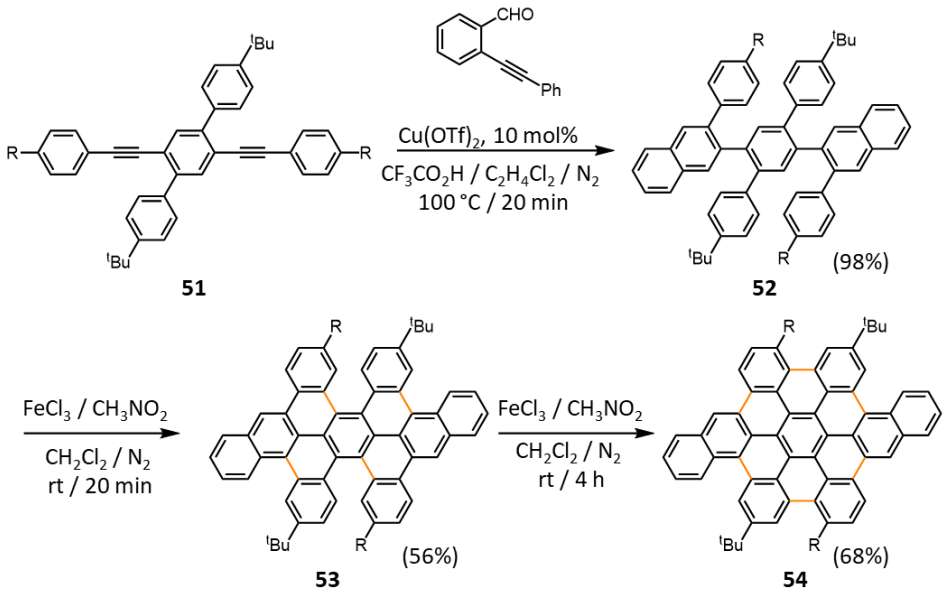

Scheme 1.11. Synthesis of nanographene **54**.

A facile two-step synthetic route towards a C_3 symmetric hexa-cata-hexabenzocoronenes (*c*-HBCs) (**57**) and larger nanographene (**58**) was later reported by Wei *et al*. in 2014[112] (Scheme 1.12). Despite the first synthesis of *c*-HBC being reported as long ago as 1965 by Clar and Stephen[113], the field has been widely unexplored, which can be attributed to the difficult syntheses. Through a three-fold Suzuki coupling of 1,3,5-tri(bromomethylbenzene) (**55**) and a 3,4-substituted phenylboronic acid precursor, intermediate **56** can be synthesised. An efficient one-pot $FeCl_3$ mediated Friedel-Crafts hydroarylation and intramolecular alkylation with a 3,4-substituted benzaldehyde, followed by dehydrogenative aromatization and intramolecular Scholl reaction gives *c*-HBC **57**. They describe the one-pot reaction as a 'covalent self-sorting assembly' (CSA) strategy and it results in the construction of twelve new C-C bonds and six new rings in a single 6-fold, self-sorting annulation (Scheme 1.12).

The efficiency of this reaction made the synthesis of enhanced structures possible by prefunctionalising the aromatic rings of the starting boronic acid and/or aldehydes. Wei *et al*. report a large scope of R groups, all of which are successful in the synthesis of derivatives of **57**. Electron-rich aromatic aldehydes (e.g, bearing OMe groups) are favourable to give c-HBCs by promoting Friedel-Crafts alkylation and stabilising

Scholl reactions, giving yields of up to 97%, while electron-poor aromatics (e.g. bearing CF_3 groups) hinder the reaction and give yields closer to 40%.

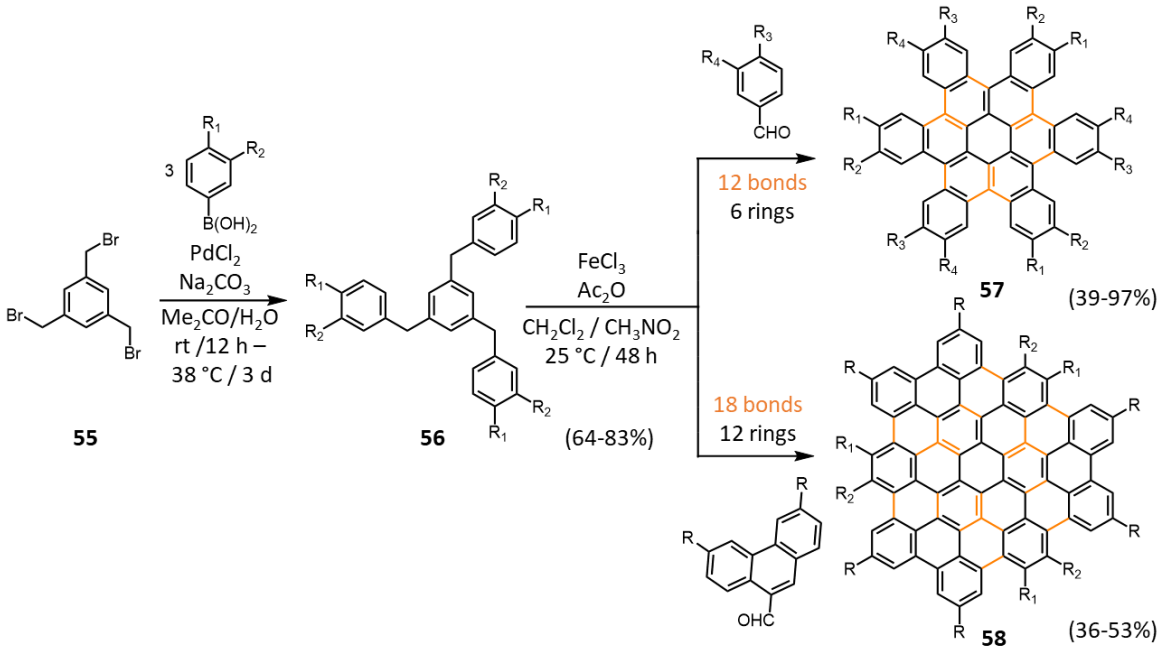

Scheme 1.12. Synthesis of extended nanographenes **57** and **58**.

The success of *c*-HCB synthesis turned focus to the assembly of larger π-systems using the same CSA strategy. The use of a range of substituted 9,10-phenanthro- moieties in the one-pot CSA strategy leads to the formation of a 3-fold symmetric hexa-peri-hexabenzocircumcoronene (HBCC) **58** in moderate yields. The resulting structure is comprised of 72 aromatic carbon atoms, 12 new rings and 18 new C-C bonds to give a fully-fused system with an 'armchair' configuration that satisfies Clar's π-sextet rule as a full-benzenoid PAH with 12 full π-sextets.[114] This method has provided a platform for the construction of larger and more complex graphenoids and supramolecular architectures[115–117] without requiring the preparation of corresponding oligophenylene precursors as seen in Scheme 1.11.

1.3.3 Warped Nanographenes

Not all polycyclic aromatic compounds possess the perfectly planar π-surface that is normally associated with hexagonal ring structures. Microscopy studies have shown that graphene does contain rings of other sizes, including five, seven and eight membered defects that are formed at the boundaries of graphene sheets which have been grown by chemical vapour deposition (CVD).[118] NGs can be used to model

perfect hexagonal graphene's by representing a small section of the extended material. The problem is that few graphene materials are defect free, but at the same time there are very few models of defect graphene available. Stone–Wales defect describes a rearrangement where hexagonal units of graphene can reorganise their structure by rotating one of the C-C bonds by 90° to produce two adjacent heptagons and two pentagons. The position at which this rearrangement occurs becomes more nucleophilic because of a decrease in resonance stabilisation which make it more susceptible to chemical reactions for various applications.[119] Non-hexagonal rings in PAHs produce a curved π-surface by forcing the structure out of plane to minimise C–C bond length strain. They have been a field of high interest in recent years due to their strained structures and resulting unusual properties. These curved π-surfaces can also be formed from steric strain due to atom crowding that forces the structure out of plane. Non-planar PAHs have poorer stacking capability due to increased difficulty in forming favourable intermolecular π-interactions, and hence higher solubility compared to planar compounds.

The smallest curved PAHs are [n]-circulenes shown in Figure 1.6. Scholl and Meyer first pioneered the interest of circulenes, reporting the first synthesis for the planar molecule, [6]-circulene (**60**) (more commonly known as coronene) in 1932.[120] This work was further expanded on throughout the 20th century, not just for synthetic purposes but for the physical and chemical properties that these compounds possess. In 1966 J. B. Siddall, first reported the synthesis of [5]-circulene (**59**) (more commonly known as corranulene), a cyclopentane central motif, formed from five fused benzene rings, and the first example of a curved PAH that can be extended to a fully curved sphere to form C_{60}-Fullerene. [7]-circulene (**61**)[121] and [8]-circulene have more recently been reported in 1983 and 1991 respectively, by Yamamoto *et al*., and can be regarded as graphene-type fragments with central seven- and eight-membered rings. [7.7] circulene was also synthesised by the same group in 1991, containing two seven membered rings. Despite these early examples, however, seven membered rings in PAHs still remain elusive[122].

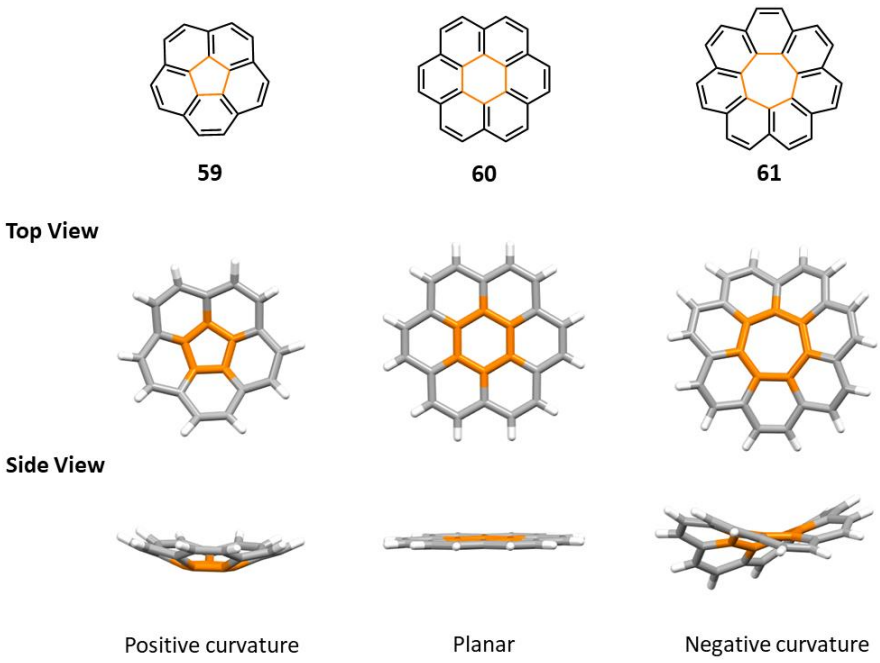

Figure 1.6. Structure and X-ray crystal structures of [n]-circulenes **59, 60** and **61**.

Warped nanographenes are structures that contain these non-hexagonal ring 'defects' and can be intentionally implemented into PAHs to manipulate their surface conformation. Whilst reports of compounds utilising 7- or 8-membered ring defects are still sparse, Scott, Itami and colleagues have pioneered the development of structures containing a five-membered ring centre in an otherwise hexagonal lattice.[123]

In 2007 Scott *et al*. reported the synthesis of extended corannulene structures pentaindenocorannulene (**63**)[124] (Scheme 1.13a). Direct chlorination of corannulene **59** provides a synthetically useful functionalised building block 1,3,5,7,9-pentachloroannulene (**62**) which is an important pre-cursor towards many nanographenes synthesised by Scott. Scott performed a five-fold Suzuki-Miyaura coupling with 2-chlorophenyl-boronic acid to give **63**, which undergoes a Pd-catalysed five-fold intramolecular arylation to give **64** in moderate yields. In agreement with p-orbital axis vector (POAV) calculations, the crystal structure of **64** shows that the trigonal carbon atoms at the core suffer greater pyramidalization than that exhibited by carbon atoms of C_{60} (12.1˚ for **64**, compared to 11.6˚ for C_{60}).

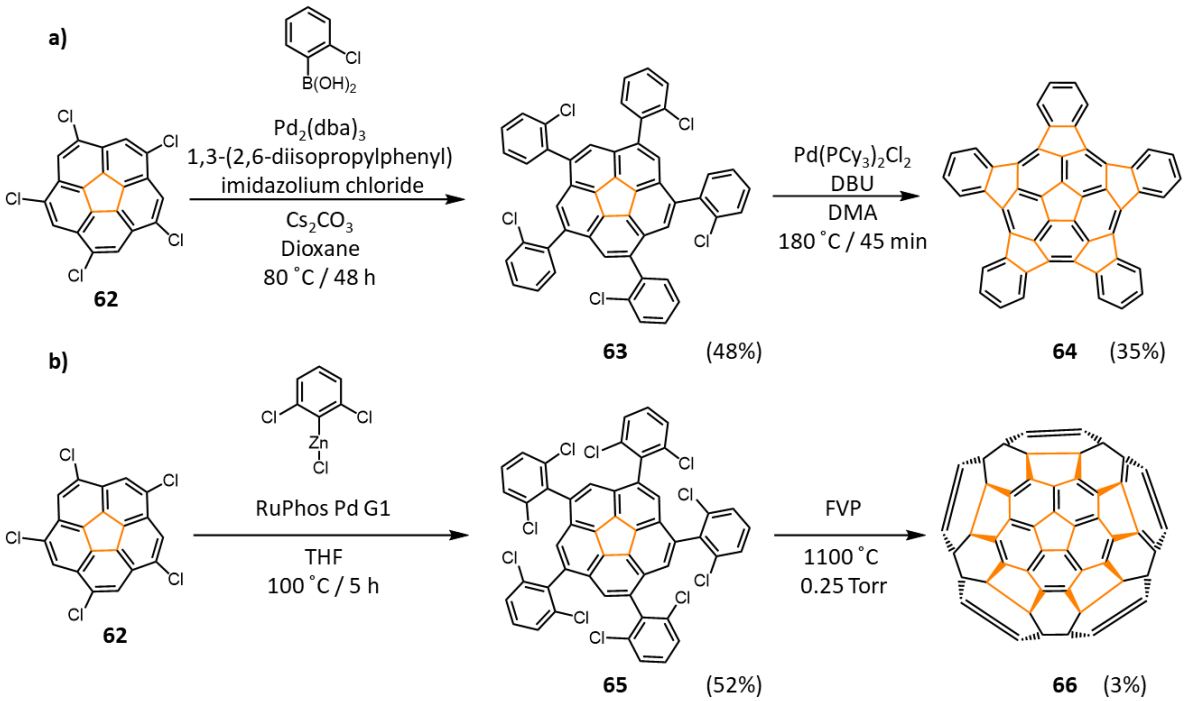

Scheme 1.13. a) Synthesis of pentaindenocorannulene (**63**) b) Synthesis of a hemispherical $C_{50}H_{10}$ template (**65**) towards a [5.5] carbon nanotube. (RuPhos Pd G1 = Chloro-(2-Dicyclohexylphosphino-2′,6′-diisopropoxy-1,1′-biphenyl)[2-(2-aminoethyl)phenyl]palladium(II)).

Building on this work, in 2012 Scott published the synthesis of a short [5,5] carbon nanotube (CNT) end cap upon the 2D extension of bowl-shaped nanographene **66**. Unlike conventional CNT synthesis, elongation from **66** would result in CNTs where the diameter and chirality of all CNT would be identical (1 nm diameter in a [5.5] CNT). Furthermore, the diameter and chirality of future CNTs could simply be tuned by modifying the template structure. The synthesis of **66** passes through an unfused intermediate **65** synthesised by a five-fold Negishi coupling with 2,6-dichlorophenylzinc chloride. Unlike in the synthesis of **64**, fusion of the peripheral rings of **65** requires flash-vacuum-pyrolysis (FVP), a high temperature technique that can form new C-C bonds. The pyrolysis cleaves the C-Cl bonds to generate aryl radicals than can join to form a series of five-membered rings between the coranulene core and the peripheral phenyls. X-ray analysis of crystals of **66** confirm the structure and measures a bowl depth of 5.16 Å.

In 2013, Scott, Itami and co-workers made a further breakthrough in warped-nanographene synthesis, reporting an efficient two-step synthesis (Scheme 1.14) of a ‘grossly warped nanographene’ (**69**) whereby a corannulene centre is surrounded by

five embedded seven-membered rings. C-H borylation of **59** followed by a ten-fold Suzuki–Miyaura coupling of the resulting 1,3,5,7,9-pentakis(pinacolatoboranyl)corannulene gives unfused derivatives **67** and **68** in moderate yields. A ten-fold IOCD catalysed by either $FeCl_3$ or DDQ results in the synthesis of **69a** and **69b** respectively.

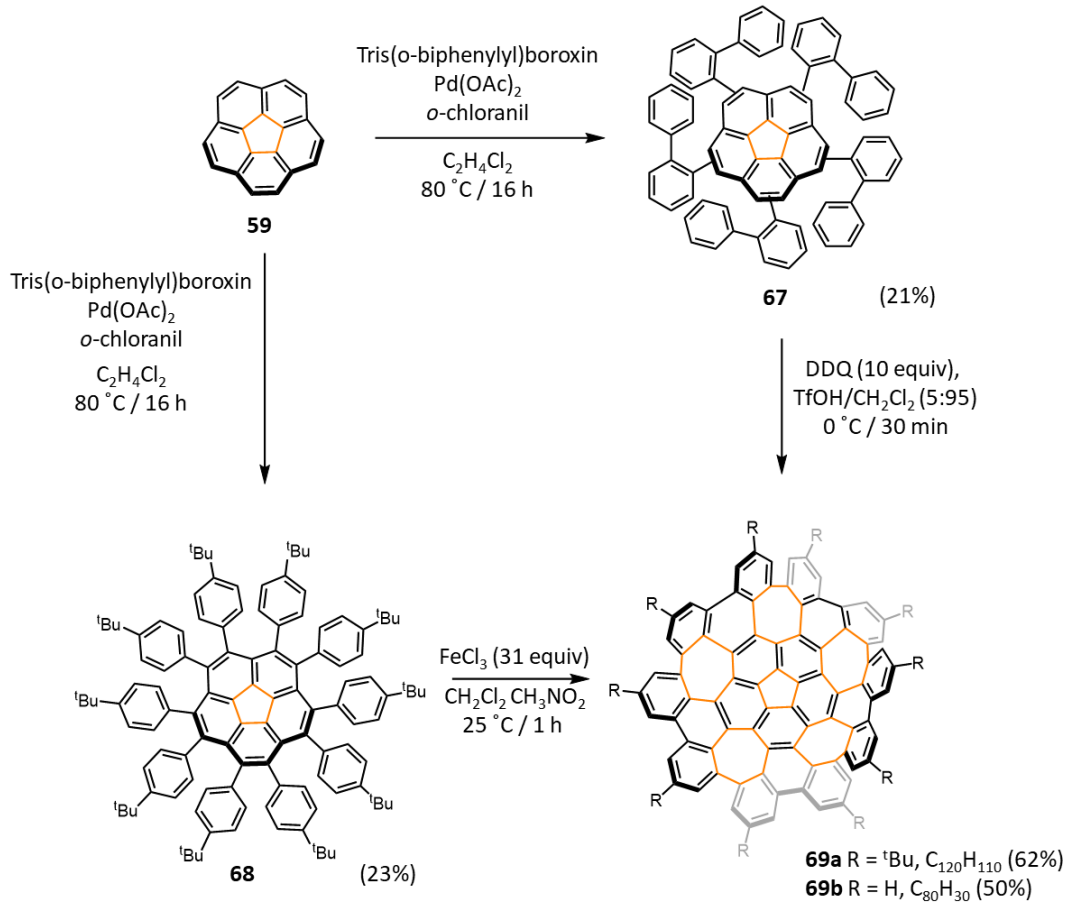

Scheme 1.14. a) Synthetic route towards $C_{80}H_{30}$ (**69b**) and its deca-t-butyl derivative $C_{120}H_{110}$ (**69a**).

The presence of the seven-membered rings gives rise to 'negative curvature', on top of corannulenes already curved structure, resulting in a unique double-concave structure.[123] It was noticed that the heptagonal rings are puckered and each rapidly interconvert in conformation between left and right twist at room temperature, making the compound chiral[125]. The presences of the heptagonal rings were also seen to slightly flatten out the curved [5]-circulene bowl structure, however the structure remains warped. The warped structure of these nanographenes makes aggregation and formation of strong Van der Waals interactions less energetically favourable enhancing their solubility's in organic solvents. The distorted structure was also shown to exhibit

a wider bang gap, higher fluorescence and reversible oxidation/reduction behaviour through stable charged intermediates.

More recently, in 2019, Scott *et al*. examined the self-assembly of **69** on Au(111), Ag(111), and Cu(111) surfaces. This study allowed investigations the nature of the intermolecular interactions (namely, π–π and CH···π) between $C_{80}H_{30}$ (**69b**) units.[126] High resolution STM shows that the highly nonplanar $C_{80}H_{30}$ gives rise to self-assembled enantiomorphic porous network during high molecular coverage. The porous network consists of 12 $C_{80}H_{30}$ dimers, forming a single hexagonal pore with an area of 6.5 nm^2 that is extended through CH···π interactions to produce the enantiomorphic network (Figure 1.7). This study indicates the potential for negatively curved nanographenes to form regular homochiral networks, a useful tool when designing chiral nanostructures.

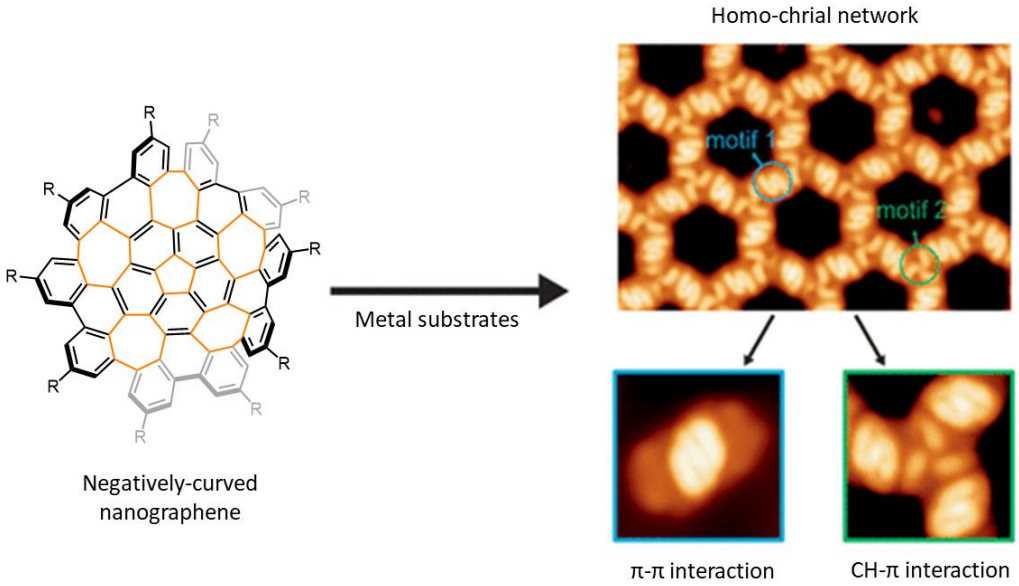

Figure 1.7. Self-assembled homochiral network of nanographene $C_{80}H_{30}$ on a Cu(111) surface.

The synthesis of warped nanographenes is not limited to a corannulene centre, with few literature examples showing HPB derivatives with seven-membered rings formed through edge-functionalisation. In 2015 Miao *et al*.[127] reported the synthesis of a *p*-HBC centred warped nanographene bearing two tropone subunits to give the saddle like conformation (Scheme 1.15b). Aromatic saddles **71** and **72** are obtained through π-extension of the diketone units on **70**, and subsequent IOCD (Scheme 1.15a). X-ray

crystallography reveals a saddle shaped conformation, as a result of a planar central six-membered ring, compared to a 'wave' structure observed in **69.**

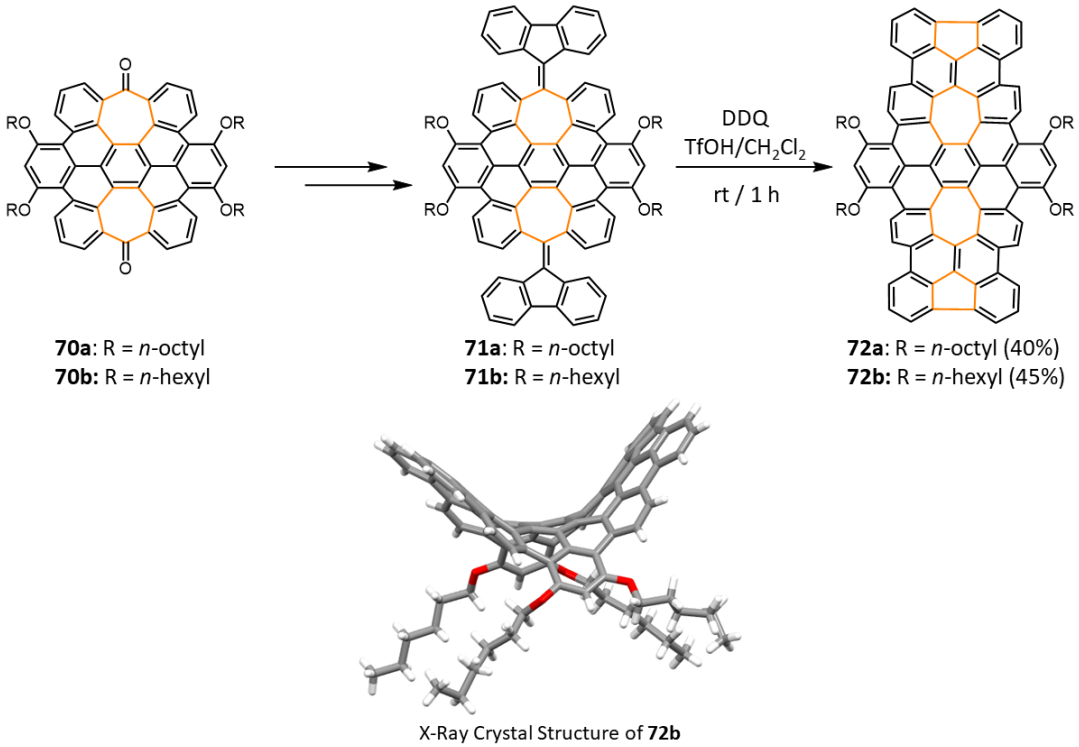

Scheme 1.15. a) Synthesis of a saddle shaped warped nanographenes **71** and **72** with a *p*-HBC centre. b) X-ray crystal structure of aromatic saddle **72b**.

The literature examples that contain odd membered rings are embedded with nonaromatic odd-membered rings, i.e. not 'true' cyclopentadienyl anions and cycloheptatrienyl cations. The seven membered rings embedded in nanographenes **69-72** are formed with seven radial π-electrons as a result of edge-to-edge arrangement of the surrounding conjugated six-membered rings. As a result, the molecular orbitals show non-degeneracy and a resulting SOMO, giving rise to their unique properties. Fundamental research from groups like Scott's[128] and Campaña's[129] have widened interest to develop a synthetic route to formally produce heptagon containing nanographenes so further studies into their promising physical and optical properties can be undertaken.

The electronic properties and versatility of PAHs make them promising materials for organic devices, such as light-emitting diodes (LEDs), field effect transistors (FETs), liquid crystal displays (LCDs) and solar cells.[130] The optical absorption and emission

behaviour is of particular interest for those working with PAHs. The absorption spectra produced by PAHs are characteristic of their structure, like molecular fingerprints.[118] Whilst all PAHs consist of a sp^2 carbon framework, even slight differences in the geometry and size can dramatically alter the optical and chemical properties of the compound. Computational studies suggest that heptagon-embedded nanographenes with a negative Gaussian curvature possess a magnetic moment[131] and UV studies show increased fluorescence[123] to the planar counterparts. It is important to note that the alterations in electronic and optical properties of nanographenes are not only from non-planarity but also from simple changes in connectivity and introduction of functional groups.

1.4 Optical Properties of PAHs and Molecular Graphenoids

The optical properties of PAHs span all areas of photophysics giving rise to a very wide range of applications. This section will specifically review the fundamentals of aggregation induced emission (AIE) and its role in PAHs, reviewing recent advances and highlighting structural characteristics that lead to their AIE effects. To understand the structure-property relationship in the design of AIE compounds, a fundamental understanding of absorption and emission must be had.

The Jablonski diagram (Figure 1.8), shows the absorption and emission pathways for organic compounds. Upon absorbing a photon (Purple arrow), electrons are excited from the single ground state (S_0) to higher energy excited states ($\geq S_1$). Kasha's rule states that subsequent emission derives from the lowest energy excited state (S_1). The decay from $S_1 \rightarrow S_0$ can occur *via* either a non-radiative pathway through internal conversion (IC) (purple dashed arrow) where the energy is released as thermal energy or through a radiative pathway to produce fluorescence (red arrow). If there is sufficient spin-orbit coupling between S_1 and the lowest energy triplet state (T_1), intersystem crossing can occur by which decay can occur again by either non-radiative pathway or radiative producing phosphorescence.

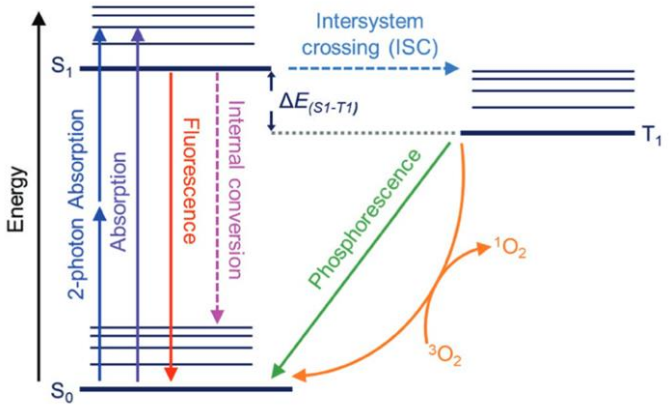

Figure 1.8. Jablonski diagram illustrating the different photophysical relaxation processes.

1.4.1 Structure-property Relationship in Aggregation-Induced Emission

Conventional luminogens are usually planar, disc-like molecules that can emit efficiently when dispersed in solution. The planar structure however gives rise to a high tendency to undergo strong intermolecular π–π interactions resulting in the formation of aggregates that can quench the luminescent properties. This is known as the aggregation caused quench (ACQ) effect. On the otherhand in the Aggregation-Induced Emission (AIE) process, a phenomena that was first reported in 2001 by Tang *et al.*[132], non-emissive luminogens emit upon the formation of aggregates. Tang *et al.*[133] concluded two factors which determine the AIE property of a compound: 1) The moieties that can undergo active intramolecular motions sufficiently dissipating excited-state energy in their isolated molecular forms. 2) The twisted 3D structures in the aggregated states effectively prevent detrimental π–π stacking interactions.

Considering these two factors for AIE activity, molecular rotor type PAHs are the perfect structures in the construction of functional AIE compounds due to their rotatable moieties (i.e peripheral phenyl rings) and non-planarity preventing efficient π-stacking. Propeller-like or rotor structures specifically make up most AIE compounds by preventing strong π–π interactions and as a result blocking internal conversions and non-radiative pathways.

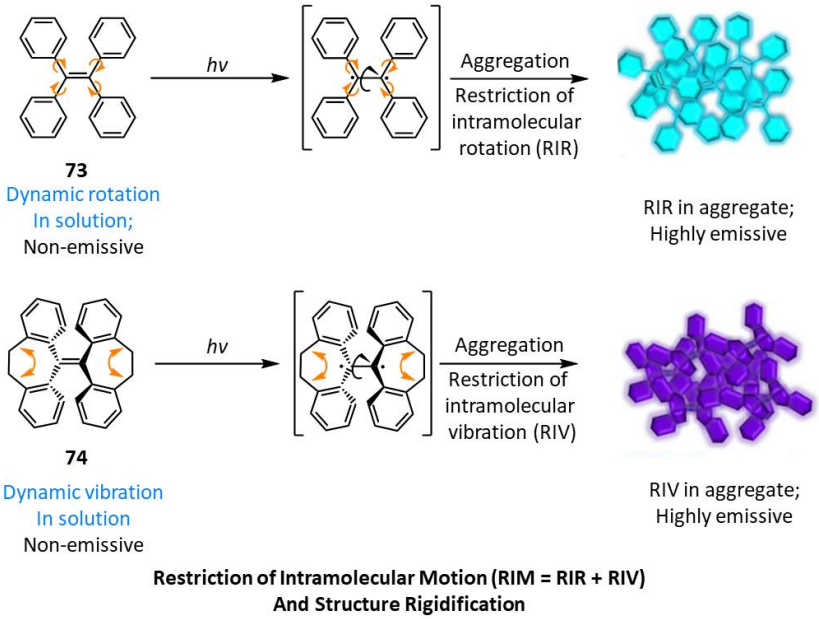

Figure 1.9. The photoexcitation of non-emissive TPE (**73**) and THBA (**74**) to form emissive aggregates through restriction of intramolecular motion.

Tetraphenylethylene (**73**) (TPE) is the best-known hydrocarbon AIE luminogen (AIEgen) and has been the focus of extensive studies which aim to establish the mechanism by which AIE occurs (Figure 1.9). TPE is comprised of a central ethylene bridge with four peripheral phenyl moieties that can freely rotate around the single C-C bond (yellow arrows). This rotation of the peripheral phenyl rings non-radiatively dissipates the exciton energy resulting in a near zero emission in dilute solutions.[134] Upon excitation, the central ethylene bond can be opened into two dipheylmethylene (DPM) units and therefore rotation around the ethylene C-C bond can occur resulting in a decrease in unfavourable intramolecular π-stacking by re-orientating out of plane. Upon aggregation, the emission of TPE is synergistically induced by the non-planar conformation preventing ACQ π–π interactions and the restricted intramolecular rotation, preventing the non-radiative dissipation of energy. The resulting aggregates display a highly emissive nature, including an increase in quantum yield from 0.2% in a 1 μM solution of THF to 13.8% in a 95% H_2O/THF mixture (A solvent mixture commonly used to induce aggregation).[135]

Luminogens with no freely rotating single bonds but significant vibrational modes such as 10,10′,11,11′-tetrahydro-5,5′-bidibenzo[a,d][7]-annulenylidene (THBA) (**74**), also shows AIE activity, due to the restriction to the intramolecular vibration (RIV) of their

conformational changes (orange double headed arrow). RIV non-radiatively dissipates the exciton energy similar to RIR causing near-zero emission in dilute solutions. The mechanism of RIR and RIV have been investigated and have been shown to be complementary effects to the existing emission enhancement pathways and can be referred to as 'Restriction of Intramolecular Motion'[136] (RIM). Experimental data and theoretical simulations identify that the RIM mechanism is highly influenced by nonradiative decay rate (k_{nr}), that can be suppressed by four orders of magnitude in the aggregated state, whereas the radiative decay rate (k_r) shows little change between solution and aggregate state.[137]

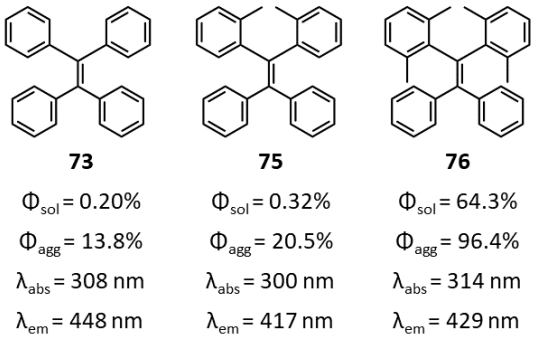

Figure 1.10. Derivatives of TPE **73** with varying degrees of steric hindrance and degree of AIE.

Introducing steric hindrance to **73** alters k_{nr} and therefore modifies RIM. **75** and **76** both show enhanced emissive properties in solution and aggregated state as a result of increasing the steric hindrance between neighbouring aromatic groups, slowing k_{nr} in the solution state. This can be seen by the vast increase in the quantum yield (Φ) in solution of **76** compared to **73** and **75**, (Figure 1.10) where the freedom of rotation of the peripheral rings is greatly reduced, lowing k_{nr} and therefore k_r can now compete, leading to an enhanced quantum yield. Zhu *et al*.[138] show that in the crystal state, the increase in steric hindrance also increases AIE favourable CH···π interactions. In the case of **73**, CH···π interactions with a distance of 2.95 Å are observed. For **75** the distance is decreased to 2.73 Å resulting in dimer formation, while **76** shows no apparent CH···π interactions, but rather weak Van der Waals interactions as a result of the bulky methyl groups. The loose packing in the crystalline state along with the vast reduction in k_{nr} gives rise to high solid-state luminescence (96.4%). Since **76** possess

high fluorescent quantum yield independent of the solvent, it has promising applications in biological imaging as a fluorescent probe.

Triphenylene (**77**) is a highly planar and well conjugated PAH where three aromatic rings are joined by three C-C bonds, resulting in a new central six-membered ring (Figure 1.11a). In solution, the photoluminscent properties of **77** are concentration dependant, with a bathochromic shift in emission upon increasing concentration. This red shift is a common phenomenon during the formation of aggregates resulting from intermolecular π-π interactions between highly planar units. The photoluminscent quantum yield of **77** in a THF solution (Φ_{sol}) is 6.0% and increases slightly in a film (Φ_{agg}) 12.0%, meaning **77** is neither AIE-active nor ACQ-active.[139]

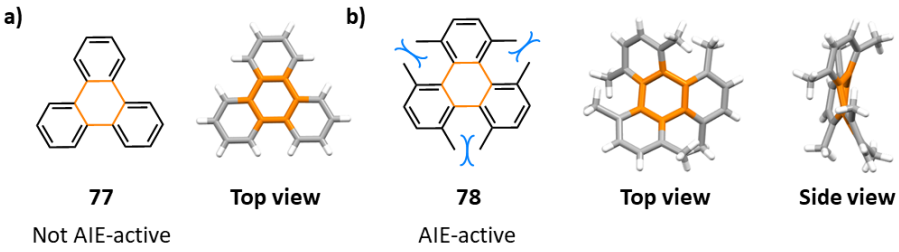

Figure 1.11. a) Structure and crystal of planar triphenylene (**77**) b) Structure and crystal of non-planar hexamethyl-triphenylene (**78**). Crystal structures retrieved from CCDC: a) (1004393) b) (668891).

Introducing six-methyl groups to the bay positions of planar **77** gives hexa(ortho-methyl)-triphenylene (**78)**, a non-planar PAH (Figure 1.11b). To overcome unfavourable intramolecular steric interactions, the conformation of **78** distorts away from planarity with a 53˚ end-to-end twist.[140] As a result, the conjugation between phenylene rings is disrupted, permitting the molecule to vibrate and nonradiatively decay from excited states, increasing k_{nr} in solution (Φ_{sol} = 5.0%). In the solid state, the non-planar structure means π-π interactions are less favourable compared to **77**, reducing ACQ-activity while simultaneously allowing RIM enhancement by the RIV pathway resulting in an increased emission (Φ_{agg} of 31.0%). Therefore **78** can be considered as an AIE active compound.

Hexaphenyl benzene, HPB (**41**) was previously discussed as a popular building block towards molecular graphenoids. HPBs photophysical properties are also very interesting and result from its non-planar, propeller like structure. In THF the emission is weakly detectable, however, the relative intensity increases twelve-fold in an 80%

H_2O-THF mixture. The peripheral phenyl rings in **41** cannot rotate as freely as **73** due to the steric repulsion of adjacent phenyl groups, hindering intramolecular rotation and hence imposing partial RIR effects and reducing k_{nr}. Therefore, even in solution, the emission of **41** can be observed. In solid state, RIR is promoted through a large number of intermolecular CH···π interactions (Figure 1.12c), rigidifying the molecules, preventing intramolecular rotation, decreasing k_{nr} and hence enhancing emission. Additionally, ACQ cannot be achieved through intermolecular π-π interactions as the propeller structure prevents close interactions, resulting in intermolecular centroid-centroid distance of **41** (~4.5 Å) being larger than the normal distance for π-π interactions.[141]

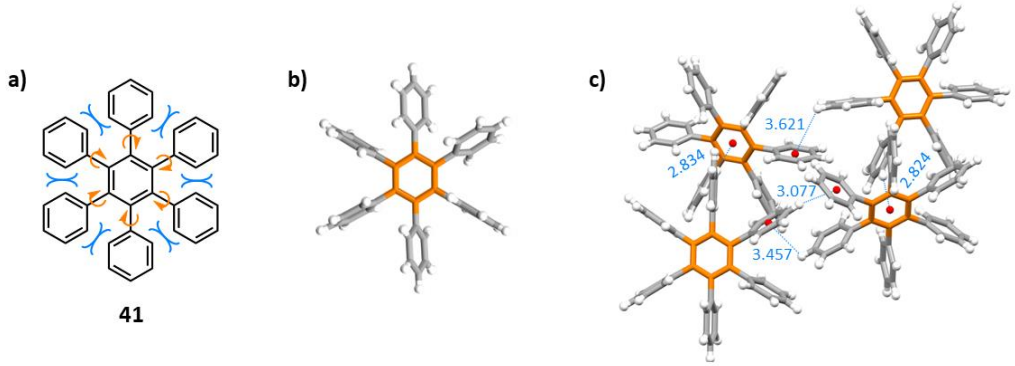

Figure 1.12. a) Structure of AIE emissive HPB (**41**) b) Top view of HPB (**41**) crystal c) Packing mode and multiple CH···π interactions in a single crystal cell of HPB (**41**). Crystal structure retrieved from CCDC (177146).

AIE luminogens are not confined to small highly symmetric phenyl rotors as discussed so far. AIE active compound, 1,2-bis[2-(9-anthracenyl)vinyl]benzene (1,2-BAVB) (**79)** is a central phenyl ring with two 9-vinylanthracene arms attached in the 1,2-positions.[142] The intense steric repulsion between neighbouring vinyl anthracenes force the large anthracene moieties to adopt highly twisted conformations, with torsion angles ranging from 53.20˚ to 73.55˚ with respect to the vinyl linker groups. The twisted structure disrupts the overall conjugation allowing free rotation of the anthracene units, thus increasing $k_{nr,}$ resulting in a near-zero emission (Φ_{sol} <1.0% in ethanol). To decipher pathways of the AIE mechanism, Yang *et al*. studied the 1,3-BAVB (**80**) and 1,4-BAVB (**81**) isomers of AIE active **79** (Figure 1.13). It was found that the small steric interactions and high conjugation of the vinyl-anthracene moieties in **80** and **81** account for the increase in planarity and rigidity in solution. This results in less freedom of rotation of the phenanthrene units, preventing any disruption to the

conjugation. The now planar structure is more susceptible to intermolecular π-π interactions between the anthracyl units in the aggregate state. This increases ACQ activity, turning off the emission in solution.

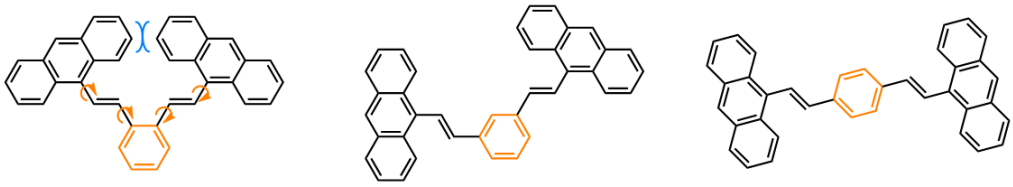

79 AIE-active | **80** Not AIE-active | **81** Not AIE-active

Figure 1.13. Isomers of 9-vinylanthrecene; 1,2- (**79**) 1,3- (**80**) and 1,4- (**81**).

1.4.2 Aggregation Induced Emission: Photocyclization and Isomerisation

Deactivation pathways such as phenyl ring rotation and the twisting of central rings have been discussed and investigated numerous times in literature and have resulted in large advancements in the field of AIE. However, to date, there are very few reports on photochemical E/Z isomerisation and cyclization deactivation pathways that have previously been suggested to be decisive factors in a compounds fluorescent properties. Thiel *et al.*[143] investigated the excited-state decay pathways in tetraphenylethene derivatives using a variety of computational methods. They reported two distinctive excited-state decay pathways, photoisomerization around the central ethylene bridge of TPE (**73**) and photocyclization of two adjacent phenyl rings, forming a new C-C bond. It was suggested that substituting TPE in the meta- position with a methyl group leads to a barrierless cyclization, resulting in an ultralow fluorescent quantum yield (Φ_{sol} = 0.1%). Methylating TPE in the 2,6-ortho positions of the peripheral rings has been seen to block both the photocyclization and photoisomerization paths by non-negligible barriers and thus fluorescence is feasible, (Φ_{sol} = 64.3%). Thiel reported a reversible photochemical oxidation, however due to the ultrafast reversible process, a lack of experimental evidence towards this pathway had been recorded. This lead to investigations (Scheme 1.16b) by Tang *et al.*[144] into deciphering the mechanism of AIE in TPE derivatives by ultrafast time-resolved spectroscopy.

Tang *et al.*[145] had first reported a photocyclization pathway of AIE in 2016 (Scheme 1.16a) whereby they identified that restriction of intramolecular cyclization (RIC) is another elementary step (in addition to RIM) in the AIE process of olefin-based AIE

systems. It was reported that close proximity of the tolyl in **82** led to facile cyclization followed by a subsequent irreversible [1,5]-hydrogen shift, affording photocyclized product **84** with enhanced blue emission relative to **82**. This first report did not result in the observation of a photocyclization induced quenching of AIE in aryl systems, most likely due to the irreversible nature of the formation of **84**. In order to investigate the mechanism of action of photocyclization quenching AIE, derivatives of TPE were required for study.

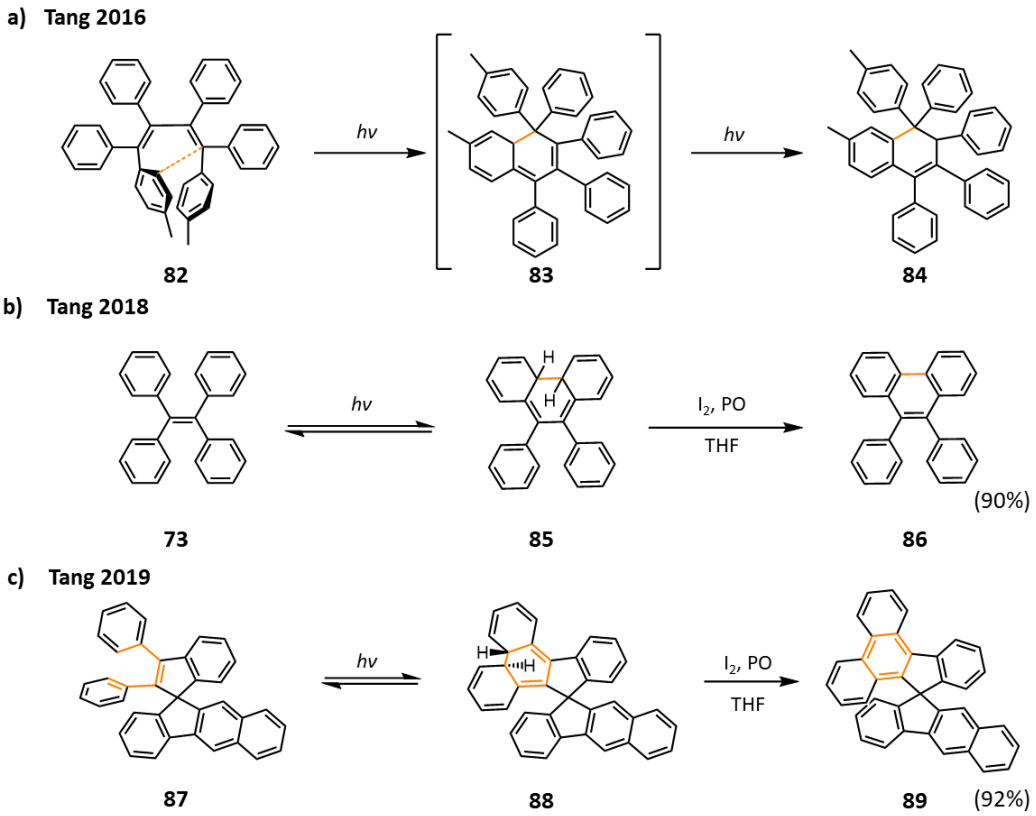

Scheme 1.16. Tang *et al*. investigations into photocyclization effects in AIE.

The electron density difference (EDD), calculated at M062X/6-311G(d), revealed that upon irradiation of **73**, the electron density moves from the central C=C bond to the adjacent C-C phenyl bonds, resulting in elongation of the C=C bond (~0.07 Å) and shortening of the peripheral phenyl bonds. This induces C=C bond twisting and phenyl torsion. Femtosecond transient absorption spectroscopy was then employed to observe the transitions occurring and relate their occurrence with changes in the absorption spectra. The presence of photocyclized intermediate **85**, was confirmed by

monoexponential fitting of a new absorption band appearing at 465 nm to yield a lifetime of 159 s, and Raman spectroscopy to reinforce computational experiments. The Photo-oxidation of **73** with I_2 as an oxidant yields fused derivative **86**, removing the reversibility of the photocyclization and further confirming the presence of intermediate **85**.

Through a comprehensive study of **73** and derivatives Tang *et al*. concluded that C=C bond elongation, quasi C=C bond twisting, phenyl torsion and photocyclization are the sequentially dominant processes in TPE derivatives upon photoexcitation in solution. Furthermore, they categorise luminescent properties based on compound rigidity, whereby in rigid derivatives, the torsion angle of peripheral phenyl rings dominates relaxation and if possible, leads to the formation of singlet ground state photocyclized intermediate. Conversely, in less rigid structures, the rotation and elongation of C=C is the dominant non-radiative process.

In 2019 Tang *et al*.[146] reported the effect of photocyclization on AIE properties and the quenching effect it has on highly emissive compounds. Spirocentre compound **87**, shows high blue AIE properties Φ_{solid} = 99.8%, however in solution is susceptible to reversible photocyclization, lowering the quantum yield (Φ_{sol} = 8.5%). The spirocentre results in two peripheral rings of **87** being pushed out of plane, increasing the torsion angle and hence decreasing ability of quenching through pi-pi interactions. The close proximity of these phenyl rings makes them susceptible to photocyclization in solution, but this is blocked in aggregation as a result of intermolecular CH···π interactions between adjacent molecules in the solid state. This observation has proven to be a very important step towards the understanding of the RIM process in AIE, where suppression of photocyclization leads to enhanced fluorescence in solution and loss of AIE properties. The full story of photocyclization in AIE has yet to be uncovered and further investigation to understand the extent of its role in RIM is needed.

1.5 Overview

Cycloheptatriene and its aromatic cation form tropylium have been only sparsely studied since their first reported in 1901 and 1954 respectively. Over the past ten years they have re-emerged as important compounds for a range of synthetic precursors. This thesis describes the use of CHT and TP as centres of large polyaromatic hydrocarbons.

Polyaromatic hydrocarbons are a unique class of supramolecular molecules that possess a range of physical and chemical properties. The large diversity in the structure of polyaromatics means they are found in all scientific and medical fields. As shown in this introduction, initial research into molecular rotors and nanographenes first focused on the synthesis of polyaromatic hydrocarbons, functionalised to enable intramolecular oxidative cyclodehydrogenation. The field of nanographene is developed from the fusion of aryl rings in polyaromatics to provide new materials with properties not found in conventional graphene. These nanographenes have provided bottom up synthetic precursors towards carbon nanotubes of controllable lengths and graphene nanoribbons for materials with semiconductor properties with relatively large band gaps. Based on recent synthetic developments, we explore nanographenes with non-hexagonal units to introduce an overall non-planar conformation, giving rise to new and exciting physical properties. Furthermore, these warped nanographenes have been shown to form more complex supramolecular architectures in the crystalline state.

Molecular rotors have become important compounds for the study and development of AIE materials. Essential knowledge into aggregation-induced emission of polyaromatic hydrocarbons and their non-radiative loss pathways will pave the way for new highly efficient emissive materials, which have the potential of transforming the field of photoluminescence.

1.6 References

1. F. A. L. Anet, *J. Am. Chem. Soc.*, 1964, **86**, 458–460.
2. W. H. Donovan and W. E. White, *J. Org. Chem.*, 1996, **61**, 969–977.
3. A. Ladenburg, *Berichte der Dtsch. Chem. Gesellschaft*, 1881, **14**, 2126–2131.
4. R. Willstätter, *Justus Liebig's Ann. der Chemie*, 1901, **317**, 204–265.
5. W. Abraham, L. Grubert, U. W. Grummt and K. Buck, *Chem. Eur. J.*, 2004, **10**, 3562–3568.
6. A. Pidcock and B. W. Taylor, *J. Chem. Soc. A*, 1967, **0**, 877-879.
7. M. Achard, and A. Tenaglia and G. Buono, *Org. Lett.*, 2005, **7**, 2353-2356.
8. G. Hvistendahl, K. Undheim and P. Gyöösi, *Org. Mass Spectrom.*, 1973, **7**, 903–905.
9. E. E. Van Tamelen, T. A. Spencer, D. S. Allen and R. L. Orvis, *J. Am. Chem. Soc.*, 1959, **81**, 6341–6342.
10. T. Curtius, *Berichte der Dtsch. Chem. Gesellschaft*, 1883, **16**, 2230–2231.
11. E. Buchner and T. Curtius, *Berichte der Dtsch. Chem. Gesellschaft*, 1885, **18**, 2371–2377.
12. E. Buchner and T. Curtius, *Berichte der Dtsch. Chem. Gesellschaft*, 1885, **18**, 2377–2379.
13. J. F. Liebman and A. Greenberg, *Chem. Rev.*, 1989, **89**, 1225–1246.
14. A. J. Anciaux, A. Demonceau, A. F. Noels, A. J. Hubert, R. Warin and P. Teyssie, *J. Org. Chem.*, 1981, **46**, 873–876.
15. L. Kurti and B. Czako, *Strategic Applications of Named Reactions in Organic Synthesis : Background and Detailed Mechanisms.*, Elsevier Science, 2005.
16. G. O. Schenck and H. Ziegler, *Naturwissenschaften*, 1951, **38**, 356–356.
17. G. O. Schenck, H. Eggert and W. Denk, *Justus Liebigs Ann. Chem.*, 1953, **584**, 177–198.
18. W. von E. Doering, G. Laber, R. Vonderwahl, N. F. Chamberlain and R. B. Williams, *J. Am. Chem. Soc.*, 1956, **78**, 5448–5448.
19. H. Meerwein, H. Disselnkötter, F. Rappen, H. V. Rintelen and H. Van De Vloed, *Justus Liebigs Ann. Chem.*, 1957, **604**, 151–167.
20. K. Tamao, K. Sumitani and M. Kumada, *J. Am. Chem. Soc.*, 1972, **94**, 4388.
21. T. C. Celius, *J. Chem. Educ.*, 2010, **87**, 1236–1237.
22. F. A. L. Anet, *J. Am. Chem. Soc.*, 1964, **86**, 458–460.
23. J. B. Lambert, L. J. Durham, P. Lepoutere and J. D. Roberts, *J. Am. Chem. Soc.*, 1965, **87**, 3896–3899.
24. R. Wehner and H. Guenther, *J. Am. Chem. Soc.*, 1975, **97**, 923–924.
25. W. Adam, M. Balci and B. Pietrzak, *J. Am. Chem. Soc.*, 1979, **101**, 6285–6291.
26. O. A. McNamara and A. R. Maguire, *Tetrahedron*, 2011, **67**, 9–40.
27. S. W. Staley, M. A. Fox and A. Cairncross, *J. Am. Chem. Soc.*, 1977, **99**, 4524–4526.
28. R. Hoffmann, *Tetrahedron Lett.*, 1970, **11**, 2907–2909.
29. S. Durmaz and H. Kollmar, *J. Am. Chem. Soc.*, 1980, **102**, 6942–6945.

30. T. Clark, G. W. Spitznagel, R. Klose and P. Schleyer, *J. Am. Chem. Soc.*, 1984, **106**, 4412–4419.

31. M. B. Rubin, *J. Am. Chem. Soc.*, 1981, **103**, 7791–7792.

32. M. B. Rubin, *Tetrahedron Lett.*, 1984, **25**, 4697–4700.

33. S. Kohmoto, T. Kawatsuji, K. Ogata, M. Yamamoto and K. Yamada, *J. Am. Chem. Soc.*, 1991, **113**, 5476–5478.

34. S. Kohmoto, T. Funabashi, N. Nakayama, T. Nishio, I. Iida, K. Kishikawa, M. Yamamoto and K. Yamada, *J. Org. Chem.*, 1993, **58**, 4764–4766.

35. S. Kohmoto, I. Koyano, T. Funabashi, K. Kishikawa, M. Yamamoto and K. Yamada, *Tetrahedron Lett.*, 1995, **36**, 553–554.

36. D. M. Gale, W. J. Middleton and C. G. Krespan, *J. Am. Chem. Soc.*, 1966, **88**, 3617–3623.

37. E. Ciganek, *J. Am. Chem. Soc.*, 1965, **87**, 652–653.

38. L. Bateman, O. McNamara, N. Buckley, P. O'Leary, F. Harrington, N. Kelly, S. O'Keeffe, A. Stack, S. O'Neill, D. McCarthya and A. Maguire, *Org. Biomol. Chem.*, 2015, **13**, 11026.

39. O. Diels and K. Alder, *Justus Liebig's Ann. der Chemie*, 1928, **460**, 98–122.

40. B. M. A, *Chem Ind*, 1961, **1961**, 550–551.

41. R. Breslow and H. W. Chang,. *J . Am. Chem. Soc*, 1965, **87**, 2200.

42. J. Sturala, M. K. Etherington, A. N. Bismillah, H. F. Higginbotham, W. Trewby, J. A. Aguilar, E. H. C. Bromley, A.-J. Avestro, A. P. Monkman and P. R. McGonigal, *J. Am. Chem. Soc.*, 2017, **139**, 17882–17889.

43. S. Ferrer and A. M. Echavarren, *Angew. Chemie Int. Ed.*, 2016, **55**, 11178–11182.

44. Y. Hayakawa, Y. Baba, S. Makino and R. Noyori, *J. Am. Chem. Soc.*, 1978, **100**, 1786–1791.

45. V. C. Pham and J. L. Charlton, *J. Org. Chem.*, 1995, **60**, 8051–8055.

46. J.-L. Paparin, C. Crévisy, L. Toupet and R. Grée, *European J. Org. Chem.*, 2000, **2000**, 3909–3918.

47. N. Sakai, A. Ridder and J. F. Hartwig, *J. Am. Chem. Soc*., 2006, **128**, 8134-8135.

48. H. Clavier, K. Le Jeune, I. de Riggi, A. Tenaglia and G. Buono, *Org. Lett.*, 2011, **13**, 308–311.

49. I. Fischler, F.-W. Grevels, J. Leitich and S. Özkar, *Chem. Ber.*, 1991, **124**, 2857–2861.

50. N. Toselli, D. Martin, M. Achard, A. Tenaglia, T. Bürgi and G. Buono, *Adv. Synth. Catal.*, 2008, **350**, 280–286.

51. A. Tenaglia and S. Gaillard, *Angew. Chemie Int. Ed.*, 2008, **47**, 2454–2457.

52. J. H. Rigby, S. B. Laurent, Z. Kamal and M. J. Heeg, *Org. Lett.*, 2008, **10**, 5609–5612.

53. U. M. Dzhemilev, G. N. Kadikova, D. I. Kolokol'tsev and V. A. D'yakonov, *Tetrahedron*, 2013, **69**, 4609–4611.

54. T. M. Gund, E. Osawa, V. Z. Williams and P. V. R. Schleyer, *J. Org. Chem.*, 1974, **39**, 2979–2987.

55. N. Fokina, B. Tkachenko, J. Dahl, R. Carlson, A. Fokin and P. Schreiner, *Synthesis.*, 2012, **44**, 259–264.

56. J. Liu, D. Obando, V. Liao, T. Lifa and R. Codd, *Eur. J. Med. Chem.*, 2011, **46**, 1949–1963.

57. S. Levin, R. R. Nani and S. E. Reisman, *J. Am. Chem. Soc.*, 2011, **133**, 774–776.

58. P. A. McDowell, D. A. Foley, P. O'Leary, A. Ford and A. R. Maguire, *J. Org. Chem.*, 2012, **77**, 2035–2040.

59. C. R. S.Alvarado, Y. Wang and A. M. Echavarren, *J. Am. Chem. Soc.*, 2011, **133**, 11952–11955.

60. M. Mato and A. M. Echavarren, *Angew. Chemie Int. Ed.*, 2019, **58**, 2088–2092.

61. Y. Wang, P. R. McGonigal, B. Herlé, M. Besora and A. M. Echavarren, *J. Am. Chem. Soc.*, 2014, **136**, 801–809.

62. M. Mato, B. Herlé and A. M. Echavarren, *Org. Lett.*, 2018, **20**, 4341–4345.

63. B. Craven and G. A. Jeffrey, *J. Am. Chem. Soc.*, 1960, **82**, 3858–3860.

64. E. Huckel, *Zeitschrift fur Phys.*, 1931, **70**, 204–286.

65. W. Von E.Doering and L. H. Knox, *J. Am. Chem. Soc.*, 1954, **76**, 3203–3206.

66. W.-C. Lin, *J. Chinese Chem. Soc.*, 1955, **2**, 37–44.

67. G. D. Kolomnikova and Z. N. Parnes, *Russ Chem. Rev.*, 1967, **36**, 735-750

68. W. Abraham, B. Dreher, D. Kreysig, N. A. Sadovskij and M. G. Kuzmin, *J. fur Prakt. Chemie*, 1987, **329**, 569–578.

69. V. A. Kharlanov, W. Abraham and W. Rettig, *J. Photochem. Photobiol. A Chem.*, 2001, **143**, 109–117.

70. A. W. Johnson, A. Langemann and M. Tisler, *J. Chem. Soc.*, 1955, **0**, 1622.

71. D. H. Geske, *J. Am. Chem. Soc.*, 1959, **81**, 4145–4147.

72. M. J. S. Dewar and R. Pettit, *J. Chem. Soc*., 1958, **0**, 3073-3076.

73. C. Jutz, *Chem. Ber.*, 1964, **97**, 2050–2065.

74. K. Conrow, *J. Am. Chem. Soc.*, 1961, **83**, 2343–2350.

75. J. F. J. Dippy, *Chem. Rev.*, 1939, **25**, 151–211.

76. V. Kharlanov, W. Abraham and W. Rettig, *J. Photochem. Photobiol. A Chem.*, 2001, **143**, 109–117.

77. R. Breslow and H. W. Chang, *J. Am. Chem. Soc.*, 1961, **33**, 3727.

78. M. A. Battiste and T. J. Barton, Tetrahedron Lett., 1968, **9**, 2951–2954.

79. L. C. F. Chao, H. K. Gupta, D. W. Hughes, J. F. Britten, S. S. Rigby, A. D. Bain and M. J. Mcglinchey, *Organometallics*, 1995, **14**, 1139–1151.

80. S. Brydges, J. F. Britten, L. C. F. Chao, H. K. Gupta, M. J. McGlinchey and D. L. Pole, *Chem. - A Eur. J.*, 1998, **4**, 1201–1205.

81. A. G. MacDiarmid, *Angew. Chemie Int. Ed.*, 2001, **40**, 2581–2590.

82. K. S. Novoselov, A. K. Geim, S. V Morozov, D. Jiang, Y. Zhang, S. V Dubonos, I. V Grigorieva and A. A. Firsov, *Science*, 2004, **306**, 666–9.

83. J. H. Chen, C. Jang, S. Xiao, M. Ishigami and M. S. Fuhrer, *Nat. Nanotechnol.*, 2008, **3**, 206–209.

84. K. I. Bolotin, K. J. Sikes, Z. Jiang, M. Klima, G. Fudenberg, J. Hone, P. Kim and H. L. Stormer, *Solid State Commun.*, 2008, **146**, 351–355.

85. L. Chen, Y. Hernandez, X. Feng and K. Müllen, *Angew. Chemie - Int. Ed.*, 2012, **51**, 7640–7654.

86. X. Wang, G. Sun, P. Routh, D. H. Kim, W. Huang and P. Chen, *Chem. Soc. Rev.*, 2014, **43**, 7067–7098.

87. Z. Xiang, Q. Dai, J.-F. Chen and L. Dai, *Adv. Mater.*, 2016, **28**, 6253–6261.

88. W. Dilthey, W. Schommer and O. Trösken, *Berichte der Dtsch. Chem. Gesellschaft (A B Ser.*, 1933, **66**, 1627–1628.

89. D. Gust, *J. Am. Chem. Soc.*, 1977, **99**, 6980–6982.

90. E. Gagnon, S. D. Halperin, V. Métivaud, K. E. Maly and J. D. Wuest, *J. Org. Chem.*, 2010, **75**, 399–406.

91. K. R. J. Thomas, M. Velusamy, J. T. Lin, S. S. Sun, Y.-T. Tao and C.-H. Chuen, *Chem. Commun.*, 2004, **20**, 2328.

92. Y. Geng, A. Fechtenkötter and K. Müllen, *J. Mater. Chem.*, 2001, **11**, 1634–1641.

93. R. Rathore, C. L. Burns and M. I. Deselnicu, *Org. Lett*., 2001, **3**, 2887-2890.

94. S. R. Waldvogel, A. R. Wartini, P. H. Rasmussen and J. Rebek, *Tetrahedron Lett.*, 1999, **40**, 3515–3518.

95. A. Stabel, P. Herwig, K. Müllen and J. P. Rabe, *Angew. Chemie Int. Ed. English*, 1995, **34**, 1609–1611.

96. L. Zhai, R. Shukla and R. Rathore, *Org. Lett.*, 2009, **11**, 3474–3477.

97. R. Bin Zhang, G. Ungar, X. Zeng and Z. Shen, *Soft Matter*, 2017, **13**, 4122–4131.

98. Y. Yamamoto, G. Zhang, W. Jin, T. Fukushima, N. Ishii, A. Saeki, S. Seki, S. Tagawa, T. Minari, K. Tsukagoshi and T. Aida, *Proc. Natl. Acad. Sci. U. S. A.*, 2009, **106**, 21051–21056.

99. J. Wu, M. Baumgarten, M. G. Debije, J. M. Warman and K. Müllen, *Angew. Chemie Int. Ed.*, 2004, **43**, 5331–5335.

100. P. Herwig, C. W. Kayser, K. Müllen and H. W. Spiess, *Adv. Mater.*, 1996, **8**, 510–513.

101. H.-S. Kim, J.-H. Lee, T.-H. Kim, S. Okabe, M. Shibayama and S.-M. Choi, *J. Phys. Chem. B*, 2011, **115**, 7314–7320.

102. Y. Hu, L. F. Dössel, X.-Y. Wang, S. Mahesh, W. Pisula, S. De Feyter, X. Feng, K. Müllen and A. Narita, *Chempluschem*, 2017, **82**, 1030–1033.

103. J. Lu, J. X. Yang, J. Wang, A. Lim, S. Wang and K. P. Loh, *ACS Nano*, 2009, **3**, 2367–2375.

104. M. Rosillo-Lopez and C. G. Salzmann, *Carbon N. Y.*, 2016, **106**, 56–63.

105. X. Yang, X. Dou, A. Rouhanipour, L. Zhi, and H. J. Räder and K. Müllen, *J. Am. Chem. Soc*., 2008, **130**, 4216-4217.

106. G. Pacchioni, *Nat. Rev. Mater.*, 2017, **2**, 17062.

107. V. Barone, O. Hod and G. E. Scuseria, *Nano Lett.*, 2006, **6**, 2748-2754.

108. X.-R. Wang, Y. Shi and R. Zhang, *Chinese Phys. B*, 2013, **22**, 098505.

109. Y.-W. Son, M. L. Cohen and S. G. Louie, *Nature*, 2006, **444**, 347–349.

110. H. Arslan, F. J. Uribe-Romo, B. J. Smith and W. R. Dichtel, *Chem. Sci.*, 2013, **4**, 3973.

111. J. L. Ormsby, T. D. Black, C. L. Hilton, and B. T. King, *Tetrahedron*, 2008, **64**, 11370–11378.

112. Q. Zhang, H. Peng, G. Zhang, Q. Lu, J. Chang, Y. Dong, X. Shi and J. Wei, *J. Am. Chem. Soc.*, 2014, **136**, 5057–5064.

113. E. Clar and J. F. Stephen, *Tetrahedron*, 1965, **21**, 467–470.

114. M. Solà, *Front. Chem.*, 2013, **1**, 4–11.

115. N. C. Davy, G. Man, R. A. Kerner, M. A. Fusella, G. E. Purdum, M. Sezen, B. P. Rand, A. Kahn and Y. L. Loo, *Chem. Mater.*, 2016, **28**, 673–681.

116. J. Yu, Y. Chen, Y. H. Zhang, X. Xu and Y. Liu, *Org. Lett.*, 2016, **18**, 4542–4545.

117. B. Liu, D. Shi, Y. Yang, D. Liu, M. Li, E. Liu, X. Wang, Q. Zhang, M. Yang, J. Li, X. Shi, W. Wang and J. Wei, *European J. Org. Chem.*, 2018, **2018**, 869–873.

118. R. Rieger and K. Mullen, *J. Phys. Org. Chem.*, 2010, **23**, 315–325.

119. S. Letardi, M. Celino, F. Cleri and V. Rosato, *Surf. Sci.*, 2002, **496**, 33–38.

120. R. Scholl and K. Meyer, *Eur. J. Org. Chem*., 1932, **1**, 201-224.

121. K. Yamamoto, T. Harada, M. Nakazaki, T. Naka, Y. Kai, S. Harada and N. Kasai, *J. Am. Chem. Soc.*, 1983, **105**, 7171–7172.

122. A. Narita, X.-Y. Wang, X. Feng and K. Müllen, *Chem. Soc. Rev.*, 2015, **44**, 6616–6643.

123. K. Kawasumi, Q. Zhang, Y. Segawa, L. T. Scott and K. Itami, *Nat. Chem.*, 2013, **5**, 739–744.

124. E. A. Jackson, B. D. Steinberg, M. Bancu, A. Wakamiya and L. T. Scott, *J. Am. Chem. Soc*, 2007, **129**, 33.

125. B. T. King, *Nat. Chem.*, 2013, **5**, 730-731.

126. J. J. Urgel, M. Di Giovannantonio, Y. Segawa, P. Ruffieux, L. T. Scott, C. A. Pignedoli, K. Itami and R. Fasel, *J. Am. Chem. Soc*., 2019, **141**, 13158-13164.

127. K. Y. Cheung, X. Xu and Q. Miao, *J. Am. Chem. Soc.*, 2015, **137**, 3910–3914.

128. H.-A. Lin, Y. Sato, Y. Segawa, T. Nishihara, N. Sugimoto, L. T. Scott, T. Higashiyama and K. Itami, *Angew. Chemie Int. Ed.*, 2018, **57**, 2874–2878.

129. C. M. Cruz, I. R. Márquez, S. Castro-Fernández, J. M. Cuerva, E. Maçôas and A. G. Campaña, *Angew. Chemie Int. Ed.*, 2019, **58**, 8068–8072.

130. Y. Gao, X. Chang, X. Liu, Q. Li, G. Cui and W. Thiel, *J. Phys. Chem. A*., 2017, **121**, 2572-2579.

131. N. Park, M. Yoon, S. Berber, J. Ihm, E. Osawa and D. Tománek, *Phys. Rev. Lett.*, 2003, **91**, 237204.

132. J. Luo, Z. Xie, Z. Xie, J. W. Y. Lam, L. Cheng, H. Chen, C. Qiu, H. S. Kwok, X. Zhan, Y. Liu, D. Zhu, B. Z. Tang, B. Z. Tang and B. Z. Tang, *Chem. Commun.*, 2001, **18**, 1740–1741.

133. J. Mei, N. L. C. Leung, R. T. K. Kwok, J. W. Y. Lam and B. Z. Tang, *Chem. Rev.*, 2015, **115**, 11718–11940.

134. J. Mei, Y. Hong, A. Qin, Y. Tang and B. Z. Tang, *Adv. Mater.*, 2014, **26**, 5429–5479.

135. G. F. Zhang, Z. Q. Chen, M. P. Aldred, Z. Hu, T. Chen, Z. Huang, X. Meng and M. Q. Zhu, *Chem. Commun.*, 2014, **50**, 12058–12060.

136. N. L. C. Leung, N. Xie, W. Yuan, Y. Liu, Q. Wu, Q. Peng, Q. Miao, J. W. Y. Lam and B. Z. Tang, *Chem. - A Eur. J.*, 2014, **20**, 15349–15353.

137. Q. Peng, Y. Yi, Z. Shuai and J. Shao, *J. Am. Chem. Soc.*, 2007, **129**, 9333–9339.

138. G.-F. Zhang, Z.-Q. Chen, M. P. Aldred, Z. Hu, T. Chen, Z. Huang, X. Meng and M.-Q. Zhu, *Chem. Commun*, 1205, **50**, 12058.

139. E. Di Donato, D. Vanzo, M. Semeraro, A. Credi and F. Negri, *J. Phys. Chem. A*, 2009, **113**, 6504–10.

140. Y. Wang, A. D. Stretton, M. C. McConnell, P. A. Wood, S. Parsons, J. B. Henry, A. R. Mount and T. H. Galow, *Recent Res. DeV. Appl. Phys*, 1981, **8**, 7.

141. R. Kruszynski and T. S. Sierański, *Cryst. Growth Des*., 2016, **16**, 587-595.

142. Y. X. Li, Z. Chen, Y. Cui, G. M. Xia and X. F. Yang, *J. Phys. Chem. C*, 2012, **116**, 6401-6408.

143. Y. J. Gao, X. P. Chang, X. Liu, Q. S. Li, G. Cui and W. Thiel, *J. Phys. Chem. A*, 2017, **121**, 58.

144. Y. Cai, L. Du, K. Samedov, X. Gu, F. Qi, H. H. Y. Sung, B. O. Patrick, Z. Yan, X. Jiang, H. Zhang, J. W. Y. Lam, I. D. Williams, D. L. Phillips, A. Qin and B. Zhong, *Chem. Sci*., 2018, **9**, 4662-4670.

145. Y. Liu, J. W. Y. Lam, X. Zheng, Q. Peng, R. T. K. Kwok, H. H. Y. Sung, I. D. Williams and B. Z. Tang, *Macromolecules*, 2016, **49**, 5817–5830.

146. Z. Zhou, S. Xie, X. Chen, Y. Tu, J. Xiang, J. Wang, Z. He, Z. Zeng and B. Zhong Tang, *J. Am. Chem. Soc*., 2019, **141**, 9803-9807

CHAPTER 2 |

PROBING THE PHOTOCYCLIZATION LOSS PATHWAY IN THE DESIGN OF NEW AIE EMITTERS.

Synopsis

This chapter discusses the structural modification of previously reported *sym*-heptaphenylcycloheptatriene (**Ph_7C_7H**) through two distinct single-step methods to create a series of six-compounds with varying rigidity and photoluminescence properties. Unexpectedly, disrupting the central ring conjugation of **Ph_7C_7H** reveals dramatic increase in the susceptibility towards photocyclisation-induced quenching (PCIQ) in the excited state. Through dynamic NMR, crystallography, photoluminescence and DFT analysis, we probe the PCIQ loss pathway for molecular rotors in the design of new AIE materials.

Acknowledgements

The following people are gratefully acknowledged for their contribution to this chapter: Dr Marc Etherington for assisting with data collection and analysis of all photophysical measurements. Dr Andrew Danos for measuring the solid state PLQYs and aiding in the study of prolonged excitation effects. Dr Basile Curchod for DFT modeling. Dr Dimitry S. Yufit solved all the X-ray crystal structures. Dr Aisha Bismillah performed the variable-temperature NMR measurements.

2.1 Introduction

In conventional luminogens, aggregation-caused quenching (ACQ) is well known as the most significant factor in the suppression of emission in otherwise highly emissive compounds through intermolecular face-to-face interactions.[1–5] Such ACQ effects greatly hinder the application of organic luminogens in optical electronics[6] and chemical sensors[7], leading to the need to develop non-planar emitters that boast enhanced emission upon aggregation, opening up the field of aggregation-induced emission (AIE).[8–11] In AIE luminogens, ACQ is prevented and intramolecular non-radiative decay processes are well agreed upon as the most prominent factor in dictating photoluminescence efficiencies. Non-radiative decay refers to an energy loss pathway that is not accompanied by luminescence and therefore suppressing this has been a hot topic for scientist as a method of improving efficiency. Typical AIE systems show quenched emission in solution state where dynamic intramolecular motion provides a non-radiative decay pathway for the excited state.[12] Less common loss pathways have been reported through the formation of through-space aromatic dimers[13], E/Z isomerisation[14] and photocyclisation that all account for non-radiative decay of the excited state. Photocyclisation has previously been studied through ultra-fast spectroscopy[15] and has been suggested to be dominant non-radiative loss pathway, that if suppressed can lead to a large increase in luminescent efficiency[16], however there is still a need for further investigation into the true role of photocyclization loss pathways in AIE materials and how they can be manipulated. Tetraphenylethylene (TPE) is regarded as the simplest archetypal AIE active structure, possessing a molecular rotor type structure with rotatable phenyl rings.[17–19] Herein, we modify previously reported **Ph_7C_7H** molecular rotor[13] to study the effects of minimal structural change on non-radiative loss pathways. The boat-like conformation of the C_7-molecular rotors provide ideal compounds for the study non-radiative decay pathways as they boast multiple phenyl rings where multiple different non-radiative pathways can occur. Specifically, in this chapter we utilise C_7-molecular rotors with relatively poor photo-luminescence quantum yields to investigate the mechanism behind photocyclization induced quenching (PCIQ) and the structural motifs that favour this loss pathway in AIE materials.

2.2 Results and Discussion

We synthesised modified molecular rotors of **Ph_7C_7H** to further investigate the unique AIE properties we have previously reported in 2017.[13] Minimal structural modifications have been achieved through two methods: 1) Fusion of two peripheral phenyl rings and 2) Epoxidation of the central seven-membered ring. *sym*-Heptaphenylcycloheptatriene (**Ph_7C_7H**), *sym*-phenpentaphenylcycloheptatriene (***sym*-phenPh$_5$C$_7$H)** and *asym*-phenpentaphenylcycloheptatriene (***asym*-phenPh$_5$C$_7$H)** (Figure 2.1) make up a series of three molecular rotors with a seven-membered carbocycle centre that differ only by the introduction of a single C-C bond between two peripheral rings and its isomer form. Subsequent epoxidation of each compound expands the series to six compounds (Figure 2.1), giving **Ph_7C_7H-O**, ***sym*-phenPh$_5$C$_7$H-O** and ***asym*-phenPh$_5$C$_7$H-O** respectively.

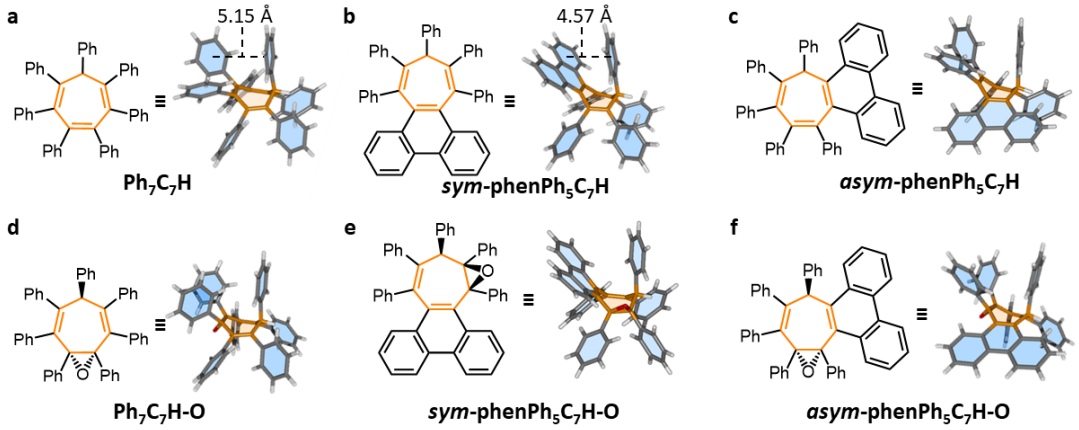

Figure 2.1. Structural formulas and X-ray crystal structures of (a) **C_7Ph_7H**, (b) ***sym*-phenPh$_5$C$_7$H** (c) ***asym*-phenPh$_5$C$_7$H** (d) **C_7Ph_7H-O** (e) ***sym*-phenPh$_5$C$_7$H-O** (f) ***asym*-phenPh$_5$C$_7$H-O**, showing modifications to the radial orientation of peripheral rings around the central cycloheptatriene centre (orange).

Analysis of X-ray crystal structures (Figure 2.1) shows the close proximity of the phenyl rings prevents co-planar conformations, giving rise to propeller-like conformations. The flexible cycloheptatriene core adopts a shallow boat-like conformation whereby phenyl groups at either end of the structure are orientated above the central ring. We have previously reported the observation of AIE properties through the formation of local intramolecular phenyl dimer states as a result of this orientation.[13] Epoxidation of the central ring (Figure 2.1 d–f) occurs stereoselectivly and has minimal influence of the boat-

like conformation of cycloheptatriene or the orientation of the peripheral phenyl groups. However, the epoxidation modifies electronic properties significantly through disruption of the central triene carbocycle. Variable-temperature (VT) NMR spectroscopy measurements (Figures 2.5-2.12 of appendix) revealed ground state energy barriers at 298K ($\Delta G^{\ddagger}_{298K}$) of 44.5 kJ mol^{-1} and 40.5 kJ mol^{-1} for ***sym*-phenPh$_5$C$_7$H** and **Ph$_7$C$_7$H-O,** respectively (Tables 3-4 of appendix) for the 180˚ rotation of their most hindered phenyl rings. For **Ph$_7$C$_7$H** a $\Delta G^{\ddagger}_{298K}$ of 48.2 kJ mol^{-1} is observed, showing both epoxidation and ring fusion result in only small differences in $\Delta G^{\ddagger}$. This observation is consistent with the geometries found (Figure 2.1) in the solid state – the structural modifications causes only minor changes in the orientations and steric environments of the rotatable phenyl groups.

2.2.1 Temperature-Dependent Steady-State Emission

Steady-state emission spectra were acquired of dilute 2-methyl-tetrahydrofuran (2-MeTHF) solutions of each rotor at various temperatures (290K–80K) (Figure 2.2). At room temperature solutions of ***sym*-phenPh$_5$C$_7$H** (Figure 2.1b) showed moderate blue emission. This compound emits noticeably more intensely compared to the rest of the rotor series; whose emission is extremely weak. Upon cooling the samples, emission increases in each case as the rate of non-radiative decay (k_{nr}) is slowed and can be attributed to the slowing of peripheral ring rotation and vibration at colder temperatures. The compound-specific relationships between the energy of the emission maximum (E_{max}) and temperature are plotted in Figure 2.31. This observation can be quantified (Equation 1) by comparing the change in relative emission intensity of the E_{max} at two temperatures. To allow comparisons between compounds, the Jacobian correction (Equation 2) is applied to each VT emission spectra to ensure changes in the energy of E_{max} can be accounted for. The results indicate the increase in ring fusion, and hence increase in rigidity, leads to a smaller $\Delta I_{290\text{-}90K,}$ attributed to lessening non-radiative decay through phenyl ring rotation. (Table 1).

$$\Delta I_{290-90\mathrm{K}} = \frac{I_{E_{\max}(90K)}}{I_{E_{\max}(290K)}} \quad \textbf{(Equation 1)}$$

$$f(E) = -f(\lambda)\frac{hc}{E^2} \quad \textbf{(Equation 2)}$$

***sym*-phenPh$_5$C$_7$H**, similarly to **Ph$_7$C$_7$H**, shows (Figure 2.2) a gradual hypsochromic shift in E_{max} from 2.84 eV to 3.15 eV as the temperature decreases indicating a two-state emission that occurs from accessing a relaxed dimer state, whereby a face-to-face interaction between the phenanthrene moiety and single phenyl at the sp^3-C of the seven-membered ring interact through space.[13] X-ray crystal structure analysis shows (Figure 2.1) the phenanthrene–Ph distance for ***sym*-phenPh$_5$C$_7$H** is 4.57 Å, significantly shorter than the Ph-Ph distance of than **Ph$_7$C$_7$H** and the rest of the C_7 rotor series (Table 5, appendix), indicating Ph-Ph distance is not the sole reason for the observed two-state emission. Interestingly, ***asym*-phenPh$_5$C$_7$H** shows (Figure 2.2c) monomer emission at 3.3 eV independent of temperature, however a concentration-dependant bathochromic shift is observed from 3.33 eV to 2.70 eV at 130 K when the concentration is increased to 20 μM (Figure 2.30), indicating the formation of intermolecular ground-state dimers, a property not observed in the rest of the rotor series. Similarly to molecular phenanthrene,[20,21] we can assume the extended π-surface of the phenanthrene of ***asym*-phenPh$_5$C$_7$H** is sufficiently exposed and unhindered that it is available to undergo intermolecular dimerization driven by solvophobic forces.

Epoxidation of the central C_7 ring has minimal effect on the crystal packing (Figures 2.13–2.25 of appendix) or to ring rotation, $\Delta G^{\ddagger}$ (Table 3, appendix). However, the smooth fluorescence peaks observed for the trienes are replaced with highly structured vibronic emission at high energy (3.09 eV to 3.55 eV) that are independent of concentration (Figure 2.30, appendix) or temperature (Figure 2.1 d–f). The resulting vibronic emission and the E_{max} for the epoxide rotors appears reminiscent of the emission spectrum of molecular phenanthrene. Even in **Ph$_7$C$_7$H-O** where no phenanthrene moiety is present, the vibronic, phenanthrene like vibronic emission is observed. To form new phenanthrene units in **Ph$_7$C$_7$H-O**, two peripheral rings would be required to fuse a form a compound similar to ***sym*-phenPh$_5$C$_7$H-O** or ***asym*-phenPh$_5$C$_7$H-O**. This may be possible through photooxidation, similar to Tangs reports[22] of photocyclisation of diphenyl ethylene units in TPE. The structure of **Ph$_7$C$_7$H-O** can be seen to have two isolated diphenylethylene-like units as a result of the disruption of central ring conjugation that may result in the

epoxide series being more susceptible to photooxidation as a result. To rule out other effects, solvatochromism studies, X-ray crystal analysis, lifetime measurements and solid state photoluminscent measurements were undertaken.

For all rotors, no solvatochromism was observed in a series of absorption and emission spectra acquired using solvents of different polarities, so any observed properties do not arise as a result of solvent relaxation. (Figure 2.26 and 2.34). Furthermore, the crystal packing was studied for each compound to ensure the absence of significant intramolecular face-to-face aromatic interactions that could result in unwanted aggregation-caused quenching (**ACQ**) and explain vibronic emission of the epoxides (Figure 2.13–2.25). The fluorescence lifetimes, τ, of ***sym*-phenPh$_5$C$_7$H** and **Ph$_7$C$_7$H-O** increase compared to **Ph$_7$C$_7$H**, (Table 1) suggesting that the presence of the epoxide decreases non-radiative decay. This may also suggest a second radiative process is occurring in the epoxide systems as they adopt a broad, triple exponential slope, which is sharpened when the epoxide is not present. (Figure 2.38, appendix)

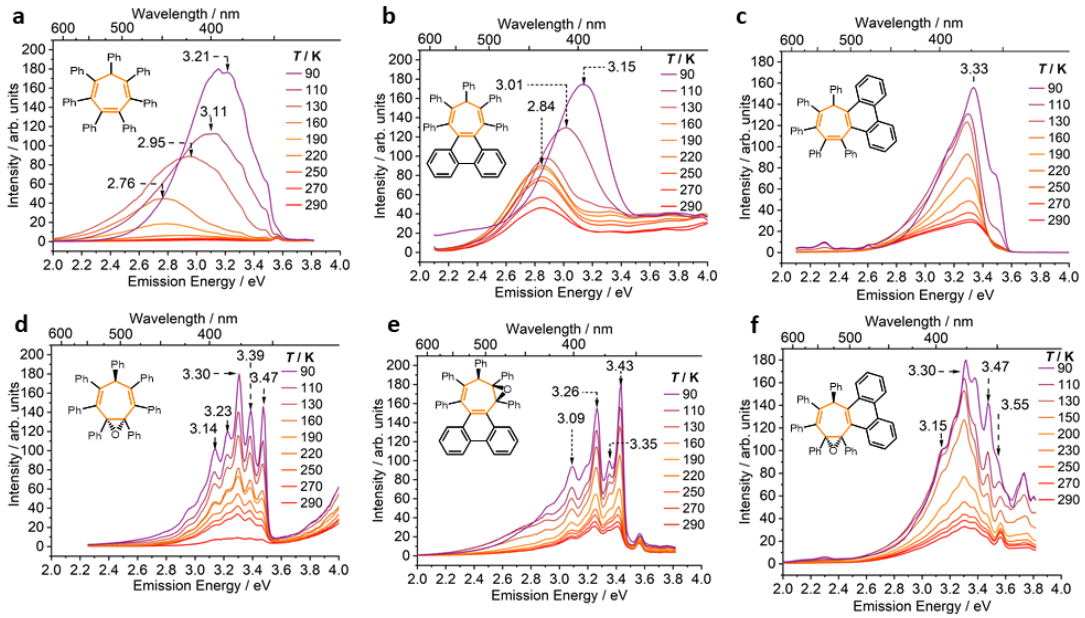

Figure 2.2. VT fluorescence spectra of 2-MeTHF solutions (l = 10 mm, T = 90–290 K, c = 2 μM) of (a) **Ph$_7$C$_7$H** λ_{ex} = 315 nm, c = 2 μM; (b) ***sym*-phenPh$_5$C$_7$H** λ_{ex} = 300 nm; (c) ***asym*-phenPh$_5$C$_7$H** λ_{ex} = 315 nm; (d) **Ph$_7$C$_7$H-O** λ_{ex} = 280 nm; (e) ***sym*-phenPh$_5$C$_7$H-O** λ_{ex} = 315 nm; (f) ***asym*-phenPh$_5$C$_7$H-O** λ_{ex} = 315 nm. Inset in panel (a): Legend for temperatures in all panels.

We also measured the VT fluorescence spectra (Figure 2.33, appendix) of all compounds as 1% dispersions in an optically clear olefin polymer (ZEONEX) matrix. This film were

prepared by drop-casting. The rigid environments whereby intermolecular interactions can be excluded due to the low concentration dispersion. The restriction of motion in films and resulting decrease in k_{nr} can be observed by the decrease in $\Delta I_{290\text{-}90K}$ (Table 1). Despite the restricted motion and possibility of intermolecular interactions, we observed essentially the same E_{max} and peak structure as the solution measurements, allowing us to conclude the observed luminescent properties derive from monomeric species and intramolecular phenomena. The photoluminescence quantum yields (PLQYs) of 1% Zeonex films (Φ_{film}) were measured using a calibrated Horiba Quanta-Phi integrating sphere coupled to a Fluorolog spectrometer and calculated using the included FluoEssence software and are outlined in Table 1. Excitation wavelengths for all measurements were chosen from regions of high absorbance of the individual materials. **Ph_7C_7H-O** and ***sym*-phenPh_5C_7H-O** show negligible Φ_{film} values whereas their non-epoxide counterparts, while low, have measurable PLQY values. This observation suggests that epoxidations introduces or accelerates a non-radiative loss pathway.

Table 1. Physical Properties of Molecular Rotors.

Rotor	E_{ex}[a] (eV)	E_{max} (eV)				τ (ns)[b]	$\Delta I_{290\text{-}90K}$[c]		Φ_{film}[d]
		160 K[b]	90 K[b]	160 K[c]	Film[d]	290 K	Sol[b]	Film	
C_7Ph_7H-O	4.35	3.30	3.30	3.31	3.47	16.0	4.82	1.19	0.00
sym-phenPh_5C_7H-O	3.94	3.43	3.43	3.43	3.34	11.5	5.76	0.69	0.00
asym-phenPh_5C_7H-O	3.94	3.30	3.30	3.31	3.47	19.9	5.47	2.62	3.30
C_7Ph_7H	3.95	2.76	3.21	2.84	3.02	0.003	52.1	9.91	6.75
sym-phenPh_5C_7H	4.13	2.84	3.15	2.84	3.01	0.004	3.75	2.13	1.75
asym-phenPh_5C_7H	4.13	3.33	3.33	3.07	3.07	0.024	6.24	2.63	4.03
Phenanthrene	4.13	3.56	3.56	-	3.06	15.0	5.13	0.56	-

[a]Excitation wavelengths were chosen to match peaks in absorption spectra (Figure 2.26). [b]2 uM solution in 2-MeTHF, all lifetime values can be found in Table 6 of the appendix. [c]20 uM in 2-MeTHF. [d]1% w/w film in Zeonex.

2.2.2 Photocyclization of Diphenylethylene Units

The observed vibronic emission profile, E_{max} and fluorescence lifetimes (τ) (Table 1) of the epoxide series are, in all cases, strikingly similar to molecular phenanthrene (Figure 2.36). 'Removal' of the epoxide, forming a central triene, decreases τ by orders of

magnitude and the vibronic emission is replaced with a bathochromic shift 3.30 eV to 2.76 eV between **Ph$_7$C$_7$H-O** to **Ph$_7$C$_7$H** at 160K, respectively. Even in ***sym*/*asym*-phenPh$_5$C$_7$H-O**, the vibronic nature can be suppressed when no epoxide is present even though peripheral ring fusion remains unchanged. With these observations, coupled with literature sources[16,22] we hypothesised that the spectroscopic feature, may be caused by photocyclisation (PC) of isolated (nonconjugated) diphenylethylene (DPE) moieties that are prone to photocyclisation.

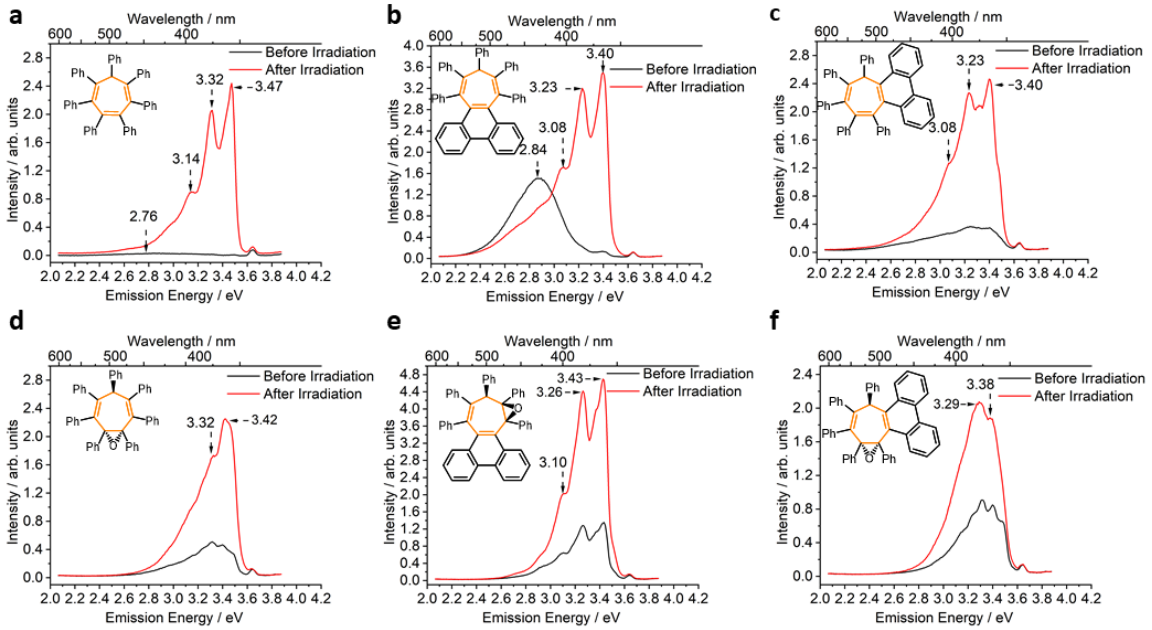

Figure 2.3. Room temperature emission spectra of 2 μM in 2-MeTHF solutions of a) **Ph$_7$C$_7$H**, b) ***sym*-phenPh$_5$C$_7$H** c) ***asym*-phenPh$_5$C$_7$H** d) **Ph$_7$C$_7$H-O** e) ***sym*-phenPh$_5$C$_7$H-O** f) ***asym*-phenPh$_5$C$_7$H-O,** showing changes in the emission profile before (black) and after (red) prolonged exposure to 4.0 eV light. **a–c** show the result of >1 h irradiation whereas **d–f** show the result of <5 min irradiation.

During solution-state PL investigations, we observed an increase in the intensity of the well-defined vibronic peaks associated with the epoxide rotors upon repeated measurements. Unlike in similar reports using tetraphenylethylene (TPE)[19], lowering the excitation energy to a lower energy absorption band does not curb the photo-oxidation. Furthermore, an enhancement in the absorption band at 257 nm is observed in the irradiated sample (Figure 2.28, appendix). The formation of near identical absorption bands at 257nm attributed to the photocyclized species are also observed for ***sym*-phenPh$_5$C$_7$H-O** and ***asym*-phenPh$_5$C$_7$H-O**. This would suggest that the epoxide rotors are extremely prone to

PC, even to the point where immediately upon excitation for a single measurement results in the formation of highly vibronic emission, as observed in Figure 2.2.

PC was further investigated by exciting a 2 μM sample of each rotor at 4.0 eV for 1 hour (Figure 2.3) and measuring the increase of intensity of E_{max} band (3.4 eV) over time. The E_{max} stays the same in all three epoxides upon excitation and showed a non-linear increase in intensity over time. (Figure 2.4b). The change in intensity was observed to be reversible with emission intensity decreasing over time when the stimulus is removed, indicating the possible presence (Scheme 2.1) of a photocyclized intermediate **IM** that is the cause of the emission quenching. Surprisingly, prolonged exposure of the non-epoxide series to 4.1 eV light also showed the reversible formation of a new highly emissive band, also at 3.4 eV with vibronic character along with a new absorption band at 257 nm (Figure 2.28), however the relative rate of formation was much slower than for the epoxide series, with each compound requiring 1 hour of constant excitation to observe significant ΔI.

The reversible photocyclization is also observed in the solid state, whereby prolonged exposure of **sym-phenPh$_5$C$_7$H-O** in a 1% ZEONEX dispersion to 4.1 eV light shows reversible photochromic yellowing of the clear film, a phenomenon that has been reported for photocyclisation of diarylethylene (DAE) derivatives previously.[23] This can be accredited with the formation of the photocyclized product, and we confirmed this with the formation of a new absorption band at 270 nm.

2.2.3 Oxidative Photocyclization

To validate the formation of a photocyclized intermediate (**IM**), an oxidant was added to an irradiated sample of **Ph$_7$C$_7$H-O** in THF to trap **IM** through the formation of a new irreversible C-C bond. (**Scheme 1**). Through two-dimensional NMR spectroscopy and X-ray crystallography we could confirm a quantitative formation of a doubly photocyclized product ***sym*-phen$_2$Ph$_3$C$_7$H-O** from **Ph$_7$C$_7$H-O** to give two new phenanthrene moieties. The addition of more equivalents of I_2 and extended irradiation do not promote any further photocyclization. The position of the new C-C bonds forms only in diphenylethylene-like positions where a new isolated phenanthrene moiety can form. Conversely, photooxidation

of non-epoxides under a range of conditions did not lead to isolation of their cyclised product experimentally, even though vibronic emission is observed after an hour of prolonged irradiation. This idea supports the idea of the epoxides being more susceptible to photocyclized quenching where vibronic emission is observed instantaneously and the photooxidised product can be isolated in quantitative yields.

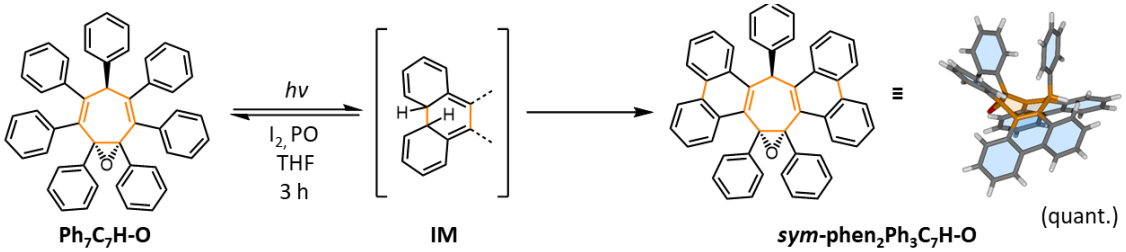

Scheme 2.1. Synthesis of ***sym*-phen$_2$Ph$_3$C$_7$H-O** through photocyclization of **Ph$_7$C$_7$H-O** and its X-ray crystal structure to show two new phenanthrene moieties.

We suggest that upon excitation of **Ph$_7$C$_7$H-O**, a steady state immediately forms with **IM** causing photocyclized induced quenching (PCIQ) of **Ph$_7$C$_7$H-O**. The resulting vibronic emission profile is attributed from **IM** being further photoexcited again after photocyclisation and then emitting giving highly structured emission similar to phenanthrene. Formation of the steady state mixture if **Ph$_7$C$_7$H-O** and **IM** can be directly observed by the increased PCIQ over time of prolonged excitation, as the population of **IM** increases, causing drastic increase in intensity of E_{max} and a reduction of ΔI as the stimulus is removed. Due to the rapid photocyclization of the epoxide series, the resulting emission spectra's would not truly represent the emission profile of the structure shown but of their corresponding **IM** state. To ensure O_2 was not acting as an oxidant and resulting in the vibronic emission, a sample of **Ph$_7$C$_7$H-O** was degassed through freeze-pump-thaw and purged with N_2 however, it resulted in no change in the emission profile, further supporting the hypothesis that PCIQ must be occurring through a long–lived **IM** species. Furthermore, we monitored the rate of change in ΔI of E_{max} at 4.0 eV for **Ph$_7$C$_7$H-O** with the addition of I_2 (Figure 2.4b) to show noticeable difference compared to when the oxidant is absent. In the presence of an oxidant, the photocyclized product ***sym*-phen$_2$Ph$_3$C$_7$H-O** begins to form irreversibly, decreasing the concentration of **IM** present over time as E_{max} shifts from that of **IM** to ***sym*-phen$_2$Ph$_3$C$_7$H-O**. An intensity maximum is reached and the

intensity of the 3.40 eV emission band beings to slowly decrease as the formation of ***sym*-phen$_2$Ph$_3$C$_7$H-O** dominates, resulting in a bathochromic shift of E_{max} from 3.42 to 3.29 eV (Figure 2.4a).

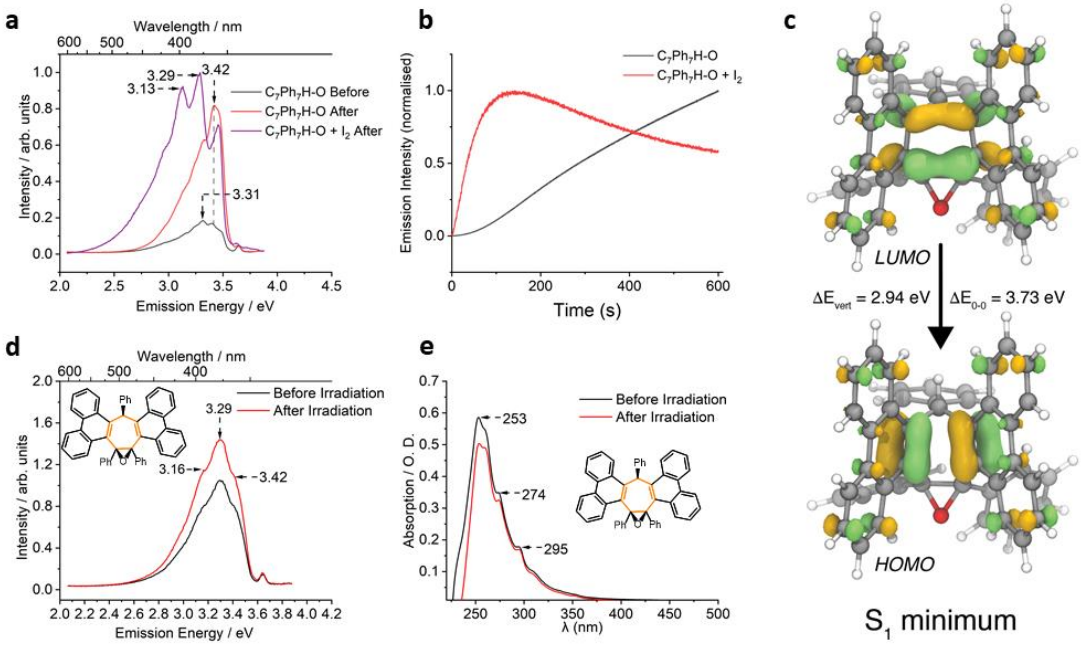

Figure 2.4. Spectroscopic data for the photocyclisation of **Ph$_7$C$_7$H-O;** a) Emission spectra showing the change in E_{max} before and after prolonged irradiation. b) Change in the emission intensity at 3.30 eV over prolonged irradiation c) NTOs of ***sym*-phen$_2$Ph$_3$C$_7$H-O** d) Room temperature emission spectra of ***sym*-phen$_2$Ph$_3$C$_7$H-O** before and after prolonged irradiation e) ***sym*-phen$_2$Ph$_3$C$_7$H-O** absorption spectra before and after prolonged irradiation.

We have proven experimentally that photooxidation of the epoxide series results in the formation of two new compounds, ***sym*-phen$_2$Ph$_3$C$_7$H-O** and **a*sym*-phen$_2$Ph$_3$C$_7$H-O**, and that further equivalents of an oxidant does not result in further oxidation as all possible phenanthrene-like moieties have formed. Therefore we would expect PCIQ to be suppressed in both of the new compounds, and hence the vibronic nature to be suppressed, as the formation of a new quenching **IM** species is prevented. The steady state-emission and absorption spectra were recorded before and after prolonged excitation of ***sym*-phen$_2$Ph$_3$C$_7$H-O** with 4.0 eV light (Figure 2.4e) and showed negligible ΔI and no change in lineshape or formation of new bands in either case. VT steady-state emission indicates the absence of intra-molecular dimers, shows no hypsochromic shift at low temperatures and only small $\Delta I_{290\text{-}90K}$ in both solution and film of 1.67 and 1.50, respectively (Figure 2.37, appendix). The X-ray crystal packing for ***sym*-phen$_2$Ph$_3$C$_7$H-O** (Figure 2.25) shows

no intermolecular π -π interactions and hence **ACQ** can be disregarded at rt. Possible intermolecular dimerization can be identified upon cooling a 2 μM sample of ***sym*-phen$_2$Ph$_3$C$_7$H-O** (Figure 2.37a, appendix) where a slight bathochromic shift and broadening is observed between 220–110 K. Remnants of vibronic structure remains for ***sym*-phen$_2$Ph$_3$C$_7$H-O** however significantly suppressed compared to **Ph$_7$C$_7$H-O**, meaning the vibronic emission is not solely from **IM** but also represents the formation of the new photocyclized product. This is further supported by the VT steady state emission of ***asym*-phen$_2$Ph$_3$C$_7$H-O** showing vibronic emission in both solution and film. Upon formation of the new permanent C-C bonds in ***sym*-phen$_2$Ph$_3$C$_7$H-O** and ***asym*-phen$_2$Ph$_3$C$_7$H-O,** the PLQY increases to 6.42 and 9.82 from 0.00 in **Ph$_7$C$_7$H-O** and ***sym*-phenPh$_5$C$_7$H-O** respectively (Table 2). This further indicates PCIQ has been prevented by the phenanthrene groups from the isolated DPE moieties.

Table 2. Physical Properties of photocyclized molecular rotors.

Rotor	E_{ex}[a] (eV)	E_{max} (eV)			$\Delta I_{290\text{-}90K}$[b]		Φ_{film}
		160 K[b]	90 K[b]	Film[d]	Sol[b]	Film	
***sym*-phen$_2$Ph$_3$C$_7$H-O**	4.0	3.72	3.76	3.28-3.43	1.67	1.50	6.42
***asym*-phen$_2$Ph$_3$C$_7$H-O**	4.0	3.10-3.43	3.10-3.43	3.10-3.43	4.19	2.77	9.82

The experimental absorption values closely match the calculated values (Figure 2.4c) confirming the fact that the ground state and excited state structure remains similar and no drastic photocyclisation is occurring now all isolated DPE moieties are removed. The natural transition orbitals (NTOs) shows emission occurring from the central ring rather from the fused phenanthrene explaining why phenanthrene-like vibronic is not occurs like what is observed in the photocyclized product of TPE.[22] This demonstrates the dominance of PCIQ in non-radiative decay by moving emission from the central ring to the **IM** state.

2.3 Conclusion

In summary, by investigating the effect of small structural changes on the photo-luminescent properties of **Ph$_7$C$_7$H** we have been able to further study photocyclization induced quenching (PCIQ) as a dominant loss pathway in AIE systems. Furthermore, it

shows the ease of access to a photocyclized **IM** state in systems with poorly conjugated diphenylethylene units, resulting in emission from **IM** that prevents the observation of the true photo-luminescent properties of the material. PCIQ has been shown to be suppressed through increasing the conjugation of isolated DPE units across a larger molecular rotor. Finally, PCIQ should be carefully considered when designing AIE systems and to understand structural characteristics that make materials susceptible for its occurrence and how to design new materials that can avoid PCIQ.

2.4 Experimental Details

2.4.1 Specific Experimental Methods

Materials: All reagents were purchased from commercial suppliers (Sigma-Aldrich, Acros Organics, or Alfa Aesar) and used without further purification. *meta*-Chloroperbenzoic acid (*m*CPBA) was purchased and used as a mixture of 77% purity, where the remainder is *m*-chlorobenzoic acid and water.

Measurements: Steady-state photoluminescence of films and solutions were measured using Jobin Yvon Fluoromax and Fluorlog with machine specific calibration curves. The low temperature and temperature-dependent photoluminescence spectra were measured using a Janis Research Co. Inc. nitrogen filled cryostat. Thus, at low temperature, films were in a nitrogen atmosphere and solutions in a sealed long-neck cuvette. Timecorrelated single photon counting experiments were conducted using a Ti:Sapphire laser (Mira 900, Coherent) with a narrow pulse width (> 2 ps), which was frequency tripled (using a beta barium borate (BBO) crystal) to 293 nm. The beam was vertically polarized, initially by rotating the horizontal beam and then passing it through two separate Glan-Thompson polarizers, to ensure it was highly polarized. The sample, either a solution in a quartz cuvette at room temperature or a longnecked cuvette in a cryostat for temperature dependent measurements, was illuminated by this beam. Emission collection optics, perpendicular to the excitation beam, allowed the emission to pass through a polarizer and a double monochromator (Acton Spectra Pro 2300i) before being collected by a micro-channel plate which covers a total time of with a detection channel width of 3.26 ps.

2.4.2 Synthetic Procedures

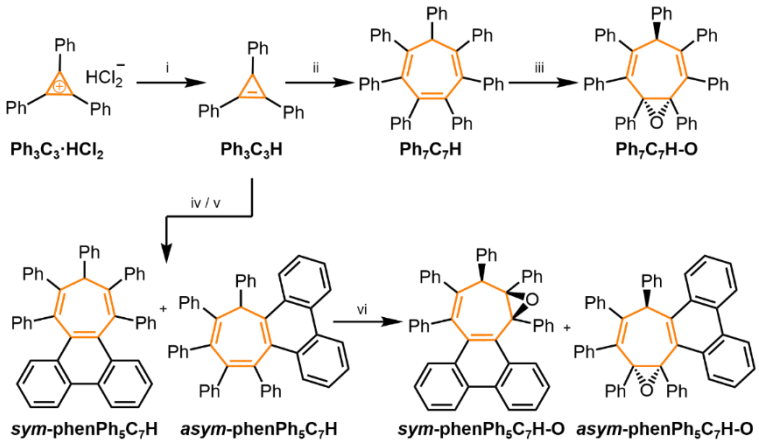

Scheme 2.2. Synthesis route used to prepare the functionalized cycloheptatrienes. Reagents and conditions: i) $NaBH_4$ / EtOH / rt / 16 h / 97%; ii) tetraphenylcyclopentadieneone / *p*-xylene / 140 °C / 36 h / 82%; iii) *m*CPBA / $CHCl_3$ / 0 °C to 55 °C / 24 h / 70%; iv) phencyclone / *p*-xylene / reflux / 66 h / 26%; ***sym*-phenPh$_5$C$_7$H**; v) phencyclone / *p*-xylene / 200 °C / 12 h / 24% ***sym*-phenPh$_5$C$_7$H**, 48% ***asym*-phenPh$_5$C$_7$H**; vi) *m*CPBA / $CHCl_3$ / 0 °C to 55 °C / 22 h / 5% ***sym*-phenPh$_5$C$_7$H-O**, 55% ***asym*-phenPh$_5$C$_7$H-O**.

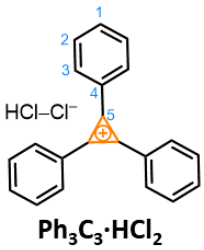

Triphenylcyclopropenylium hydrogen dichloride (Ph$_3$C$_3$·HCl$_2$): Diphenylacetylene (18.5 g, 104 mmol) and potassium *tert*-butoxide (35.0 g, 312 mmol) were placed in a two-necked oven-dried 500 mL round-bottomed flask fitted with a septum, under a N_2 atmosphere. Dry benzene (200 mL) was added and the mixture was stirred. α,α-Dichlorotoluene (25.0 g, 155 mmol) was added to the reaction mixture uniformly over a period of 30 min using a syringe pump. The reaction mixture was then heated to reflux for 3 h at 80 °C. After cooling, H_2O (200 mL) was added to dissolve the inorganic salts. The layers were separated and the aqueous layer was extracted with Et_2O (2 × 200 mL). The ether extracts were combined with the benzene layer and dried over $MgSO_4$, before the solvent was removed under reduced pressure to give a solid, orange residue. This crude mixture was dissolved in a mixture of 2:1 Et_2O–CH_2Cl_2 (200 mL) and then sparged with gaseous HCl, leading to the formation of a colorless precipitate. Sparging was continued until no more precipitation was observed, then the mixture was filtered through a sintered glass funnel and the solid washed with Et_2O. The solid was dried under vacuum to yield **Ph$_3$C$_3$·HCl$_2$** as cream powder (18.6 g, 61.4 mmol, 43%). **M.P.** 186 – 188 °C. **^{1}H NMR** (600 MHz, CD_3CN) δ 8.83 – 8.39 (m, 6H, H_3), 8.20 – 8.00 (m, 3H, H_1), 7.97 – 7.86 (m,

6H, H_2). **^{13}C NMR** (151 MHz, CD_3CN) δ 154.1 (C_5), 139.1 (C_1), 136.6 (C_2), 131.4 (C_3), 121.6 (C_4). **HRESI-MS** *m/z* = 267.1169 $[M\text{-}HCl_2]^+$ (calculated for $C_{21}H_{15}^+$ = 267.1168).

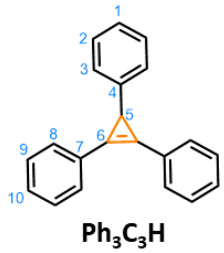

Ph_3C_3H

***sym*-Triphenylcyclopropene (Ph_3C_3H)**: Sodium borohydride (9.30 g, 246 mmol) was added to a solution of **$Ph_3C_3{\cdot}HCl_2$** (18.6 g, 61.4 mmol) in EtOH (460 mL). The mixture was allowed to stir overnight at rt. The reaction was quenched with H_2O (500 mL) then extracted with Et_2O (3 × 200 mL). The organic layers were combined and washed with H_2O (500 mL) and brine (500 mL). The combined organic extracts were then dried over $MgSO_4$ and the solvent was removed under reduced pressure to give **Ph_3C_3H** as a colorless solid (14.2 g, 53.1 mmol, 97%). **M.P.** 113 – 115 °C. **^{1}H NMR** (400 MHz, $CDCl_3$) δ 7.71 – 7.66 (m, 4H, H_8), 7.47 – 7.40 (m, 4H, H_9), 7.38 – 7.32 (m, 2H, H_{10}), 7.24 (br s, 2H, H_2), 7.23 – 7.22 (m, 2H, H_3), 7.17 – 7.10 (m, 1H, H_1), 3.27 (s, 1H, H_5). **^{13}C NMR** (101 MHz, $CDCl_3$) δ 144.6 (C_4), 130.0 (C_8), 128.9 (C_9), 128.8 (C_{10}), 128.7 (C_7), 128.3 (C_3), 126.0 (C_2), 125.6 (C_1), 112.7 (C_6), 24.5 (C_5). **HR-ESI MS** *m/z* = 267.1172 $[M-H]^+$ (calculated for $C_{21}H_{15}^+$ = 267.1168).

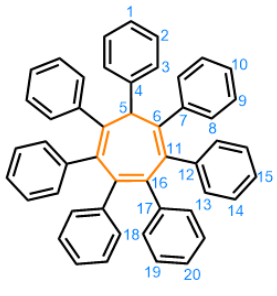

Ph_7C_7H

***sym*-Heptaphenylcycloheptatriene** (**Ph_7C_7H**): To a 20 mL microwave vial was added **Ph_3C_3H** (1.2 g, 4.47 mmol), tetraphenylcyclopentadienone (1.79 g, 4.47 mmol) and anhydrous *p*-xylene (13.5 mL). The reaction vessel was sealed and the mixture deoxygenated (3 × freeze–pump–thaw cycles under N_2) then stirred for 36 h at 140 °C in a microwave reactor. Upon cooling to rt, a crystalline solid formed, which was isolated by filtration through a sintered glass funnel, washing with Et_2O (3 × 10 mL). The solid was dried under vacuum to yield **Ph_7C_7H** as a pale pink solid (2.30 g, 3.68 mmol, 82%) in high purity (no observable impurities by ^{1}H NMR spectroscopy). Samples for UV-vis and fluorescence measurements were further purified by recrystallization. A saturated solution of **Ph_7C_7H** in 1:1 $CHCl_3$–EtOH was allowed to slowly evaporate, yielding colorless crystals. **M.P.** 291 – 292 °C. **^{1}H NMR** (700 MHz, $(CD_3)_2CO$) δ 8.17 – 7.99 (m, 2H, H_3),

7.62 – 7.48 (m, 2H, H_2), 7.44 – 7.34 (m, 1H, H_1), 7.26 – 7.18 (m, 4H, H_8), 7.15 (br s, 4H, H_{13}), 7.05 – 7.02 (m, 4H, H_{14}), 7.02 – 6.98 (m, 4H, H_9), 6.98 – 6.96 (m, 2H, H_{15}), 6.96 – 6.93 (m, 2H, H_{10}), 6.63 – 6.59 (m, 2H, H_{20}), 6.60 – 6.55 (m, 4H, H_{19}), 6.36 – 6.32 (m, 4H, H_{18}), 5.35 (s, 1H, H_5). **^{13}C NMR** (176 MHz, $(CD_3)_2CO$) δ 144.8 (C_{16}), 144.4 (C_7), 144.1 (C_4), 141.9 (C_{12}), 141.6 (C_{17}), 140.2 (C_6), 138.0 (C_{11}), 132.7 (C_{13}), 132.3 (C_{18}), 130.7 (C_8), 129.4 (C_2), 128.5 (C_9), 128.1 (C_{14}), 127.9 (C_3), 127.7 (C_1), 127.3 (C_{10}), 126.93 (C_{15}), 126.87 (C_{19}), 126.0 (C_{20}), 59.0 (C_5). **HR-ESI MS** *m/z* = 625.2892 $[M+H]^+$ (calculated for $C_{47}H_{37}$ = 625.2890).

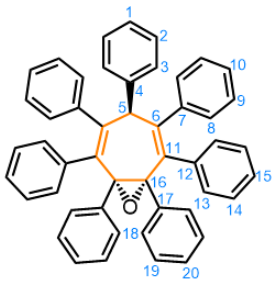

Ph_7C_7H-O

Ph_7C_7H-O: *sym*-Heptaphenylcycloheptatriene (1.0 g, 1.6 mmol) was dissolved in $CHCl_3$ (50 mL) and cooled to 0 °C. The mixture was stirred for 5 min. A cooled solution of *m*CPBA (1.6 g, 6.5 mmol) in $CHCl_3$ (20 mL) was added and stirred for a further 5 min before being allowed to warm to rt. The mixture was slowly heated to 55 °C and left to stir for 16 h. The mixture was allowed to cool to rt and a further equivalent of *m*CPBA (0.28 g, 1.6 mmol) was added. The mixture was heated to 55 °C for 3 h before allowing to cool to rt. A saturated aqueous solution of $NaHCO_3$ (20 mL) was added and the resulting biphasic mixture was stirred for 15 min. The organic layer was separated and then washed with a saturated aqueous solution of $NaHCO_3$ (2 × 20 mL) and brine (30 mL), before being dried over $MgSO_4$, filtered and evaporated to dryness to give a crude orange solid. The crude mixture was recrystallized by slow evaporation of a saturated EtOAc solution to yield the title compound as a crystalline colorless solid (0.72 g, 1.12 mmol, 70%). **M.P.** > 350 °C. **^{1}H NMR** (700 MHz, $CDCl_3$) δ 8.11 – 8.05 (m, 2H, H_3), 7.60 (t, *J* = 7.7 Hz, 2H, H_2), 7.49 – 7.43 (m, 1H, H_1), 7.14 – 7.12 (m, 4H, H_8), 7.11 – 7.08 (m, 4H, H_{13}), 7.06 – 6.98 (m, 12H, H_9, H_{10}, H_{14} and H_{15}), 6.81 – 6.75 (m, 2H, H_{20}), 6.72 – 6.66 (m, 4H, H_{19}), 6.63 – 6.52 (m, 4H, H_{18}), 5.14 (s, 1H, H_5). **^{13}C NMR** (176 MHz, $CDCl_3$) δ 146.7 (C_6), 144.6 (C_4), 144.5 (C_7), 140.4 (C_{12}), 138.8 (C_{11}), 137.4 (C_{17}), 131.0 (C_{13}), 129.0 (C_8), 128.9 (C_2 or C_3), 128.8 (C_2 or C_3), 128.8 (C_{18}), 128.0 (C_9 or C_{14}), 127.4 (C_9 or C_{14}), 127.2 (C_1), 126.6 (C_{10} or C_{15} or C_{20}), 126.5 (2C, C_{10} and/or C_{15} and/or C_{20}), 126.4 (C_{19}), 74.7 (C_{16}), 58.4 (C_5). **HRMS-ASAP** *m/z* = 641.2834 $[M+H]^+$, calculated for $C_{49}H_{37}O^+$: 641.2839.

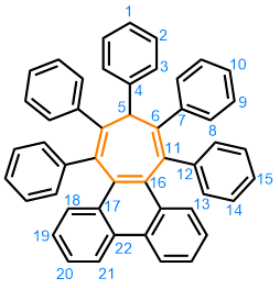

***sym*-phenPh$_5$C$_7$H**

***sym*-phenPh$_5$C$_7$H**: Phencyclone (0.71 g, 1.86 mmol), *sym*-triphenylcyclopropene (0.50 g, 1.86 mmol) and anhydrous *p*-xylene (30 mL) were added to a 100 mL round bottom flask. The mixture was deoxygenated (3 × freeze-pump-thaw cycles under argon) before being heated to reflux for 66 h. The mixture was allowed to cool to rt where a white precipitate was produced. Me_2CO (20 mL) was added to induce further precipitation. The solid was isolated by filtration, washing on the filter with cold *p*-xylene (3 mL), then dried under vacuum to give **sym-phenPh$_5$C$_7$H** as a white solid (0.30 g, 0.48 mmol, 26%). Where possible, ^{1}H and ^{13}C NMR resonances have been assigned using bidimensional NMR techniques. However, some resonances could not be assigned on account of overlap between peaks and the similarity of some nuclear environments. **M.P.** 318 – 321 °C. **^{1}H NMR** (700 MHz, 1:7 CD_2Cl_2–CS_2) δ 8.31 (d, *J* = 8.3 Hz, 2H, H_{21}), 7.82 (d, *J* = 8.4 Hz, 2H, H_{18}), 7.46 (d, *J* = 8.1, 2H, H_3), 7.35 – 7.29 (m, 2H, H_{20}), 7.15 – 7.11 (m, 4H, $H_{8\text{-}10}$ or $H_{13\text{-}15}$), 7.11 – 7.08 (m, 2H, H_{19}), 7.08 – 7.04 (m, 11H, $H_{8\text{-}10}$ or $H_{13\text{-}15}$), 7.04 – 7.02 (m, 5H, $H_{8\text{-}10}$ or $H_{13\text{-}15}$), 6.63 – 6.58 (m, 2H, H_2), 6.56 – 6.53 (m, 1H, H_1), 5.21 (s, 1H, H_5). **^{13}C NMR** (176 MHz, 1:7 CD_2Cl_2–CS_2) δ 146.4 (C_6), 143.1 (C_{11}), 143.1 (C_7), 140.0 (C_4), 137.3 (C_{16}), 133.8 (C_{12}), 131.2 ($C_{8\text{-}10}$ or $H_{13\text{-}15}$), 130.3 (C_{17}), 130.3 (C_{18}), 129.9 ($C_{8\text{-}10}$ or $H_{13\text{-}15}$), 129.4 (C_{22}), 128.0 ($C_{8\text{-}10}$ or $H_{13\text{-}15}$), 127.8 (C_2), 127.3 ($C_{8\text{-}10}$ or $H_{13\text{-}15}$), 126.7 ($C_{8\text{-}10}$ or $H_{13\text{-}15}$), 126.0 ($C_{8\text{-}10}$ or $H_{13\text{-}15}$), 125.8 (C_{20}), 125.5 (C_1), 125.4 (C_{19}), 124.8 (C_3), 122.0 (C_{21}), 60.5 (C_5). **HRMS-ASAP** *m/z* = 622.2685 $[M]^+$, calculated for $C_{49}H_{34}^+$: 622.2655.

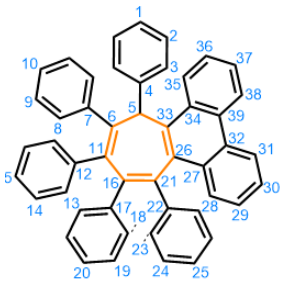

***asym*-phenPh$_5$C$_7$H**

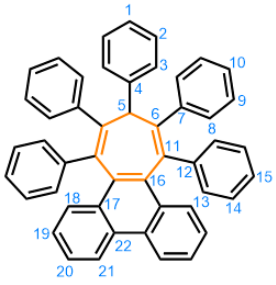

***sym*-phenPh$_5$C$_7$H**

Mixture of ***asym*-phenPh$_5$C$_7$H** and ***sym*-phenPh$_5$C$_7$H**: *sym*-triphenylcyclopropene (297 mg, 1.10 mmol), phencyclone (424 mg, 1.10 mmol) and *p*-xylene (2.20 mL) were added to a microwave vial. The vial was sealed with a septum and the mixture degassed (3 × freeze-pump-thaw cycles) then stirred for 12 h at 200 °C in a microwave reactor. Upon cooling, a precipitate formed,

which was isolated by filtration, washing with *p*-xylene. This solid was dried under vacuum to yield a light yellow solid, which was recrystallized by slow evaporation of a 2:1 CH_2Cl_2—EtOH solution to give the first batch of a mixture of ***asym*-phenPh$_5$C$_7$H** and ***sym*-phenPh$_5$C$_7$H** as a colorless solid (262 mg, 0.42 mmol, 38%). Separately, the filtrate was concentrated under reduced pressure and the resulting residue was purified by column chromatography (Teledyne Isco CombiFlash Rf+ system, 40 g SiO_2, petroleum ether−EtOAc, gradient elution). A fraction containing a mixture of ***asym*-phenPh$_5$C$_7$H** and ***sym*-phenPh$_5$C$_7$H** was isolated, which was concentrated under reduced pressure yielding 84 mg, 0.14 mmol, 12% as a colorless solid. Another fraction was also isolated containing the desired products along with impurities. This fraction was further purified by recrystallisation by slow evaporation of a 5:3 CH_2Cl_2—EtOH solution, yielding a third batch of ***asym*-phenPh$_5$C$_7$H** and ***sym*-phenPh$_5$C$_7$H** as a colorless solid (181 mg, 0.29 mmol, 26%). The three batches were combined, giving ***asym*-phenPh$_5$C$_7$H** and ***sym*-phenPh$_5$C$_7$H** (527 mg, 0.76 mmol, 72% overall yield). **^{1}H NMR** spectroscopic analysis showed the two isomers were present in a ***asym*-phenPh$_5$C$_7$H**-to-***sym*-phenPh$_5$C$_7$H** ratio of 2:1. The ***asym*-phenPh$_5$C$_7$H** was present as a racemic mixture of *R*- and *S*-stereoisomers. **M.P.**: 288 – 290 °C. **HRMS-ASAP** *m/z* = 622.2668 $[M]^+$, calculated for $C_{49}H_{34}^+$: 622.2655.

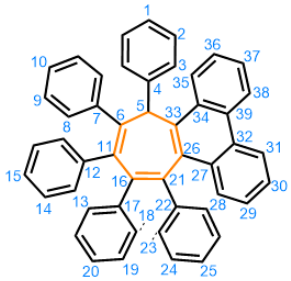

***asym*-phenPh$_5$C$_7$H**

***asym*-phenPh$_5$C$_7$H:** A pure sample of ***sym*-phenPh$_5$C$_7$H** (300 mg, 0.48 mmol) was placed in a 5 mL microwave vial. The solid was heated using a heat gun until a melt formed (~320 °C), before being allowed to cool to rt and solidify. This heat/cool cycle was repeated 5 times. The resulting black solid was sonicated in $(CH_3)_2CO$ (4 mL) and the supernatant was collected and evaporated to dryness to give a crude yellow solid of a 6:1 mixture of *asym*:*sym* isomers. The crude solid was purified by column chromatography (Teledyne Isco CombiFlash Rf+ system**,** high performance 24 g SiO_2, Hexane). Pure factions were identified by TLC and combined. The title compound was isolated as a white crystalline solid of the single ***asym*-phenPh$_5$C$_7$H** isomer (5 mg, 8.0 μM, 1.7%). The remaining solid was isolated as a mixture of the *asym:sym* isomers. **M.P.** 302 – 304 °C.

^{1}H NMR (700 MHz, $CDCl_3$) δ 8.76 (dd, *J* = 8.4, 1.2 Hz, 1H, H_{28}), 8.64 (dd, *J* = 8.4, 1.2 Hz, 1H, H_{38}), 8.16 (d, *J* = 8.4 Hz, 1H, H_{31}), 7.96 – 7.92 (m, 1H, H_{35}), 7.66 (ddd, *J* = 8.2, 6.9, 1.2 Hz, 1H, H_{29}), 7.58 (d, *J* = 7.6 Hz, 2H, H_{18}), 7.55 (m, 1H, H_{30}), 7.46 (m, 1H, H_{37}), 7.28 (m, 2H, H_{19}), 7.25 (m, 1H, H_{36}), 7.23 (m, 1H, H_{20}), 7.11 (m, 3H, H_{13+15}), 7.02 – 6.95 (m, 5H, H_{8-10}), 6.86 (m, 1H, H_1), 6.78 (m, 1H, H_{25}), 6.73 (m, 2H, H_{25}), 6.71 (m, 2H, H_{23}), 6.68 (m, 2H, H_2), 6.36 (s, 1H, H_5), 5.70 (d, *J* = 7.7 Hz, 2H, H_3). **^{13}C NMR** (176 MHz, $CDCl_3$) δ 143.8 (C_6), 143.5 (C_{26}), 143.4 (C_{16}), 143.1 (C_{11}), 142.7 (C_{21}), 142.5 (C_{33}), 142.1 (C_4), 140.7 (C_{22}), 140.2 (C_{17}), 139.5 (C_{12}), 138.4 (C_7), 138.0 (C_{39}), 132.2 (C_{32}), 131.7 (C_{23}), 131.5 (C_{34}), 131.5 (C_{27}), 131.2 (C_3), 129.5 (C_{35}), 129.43 (C_{14}), 129.0 ($C_{8 \text{ or } 9 \text{ or } 10}$), 128.7 ($C_{36}$), 127.7 ($C_{8 \text{ or } 9 \text{ or } 10}$), 127.67 ($C_{15}$), 127.6 ($C_{30}$), 127.1 ($C_{18}$), 126.9 ($C_{29}$), 126.79 ($C_{24}$), 126.7 ($C_{13}$), 126.5 ($C_{20}$), 126.5 ($C_2$), 126.3 ($C_{8 \text{ or } 9 \text{ or } 10}$), 125.9 ($C_{19}$), 125.8 ($C_{37}$), 125.7 ($C_{25}$), 125.7 ($C_1$), 124.4 ($C_{31}$), 123.2 ($C_{28}$), 122.7 ($C_{38}$), 50.3 ($C_5$). **HR-ASAP MS** *m/z* = 622.2662 $[M]^+$, calculated for $C_{49}H_{34}^+$: 622.2655.

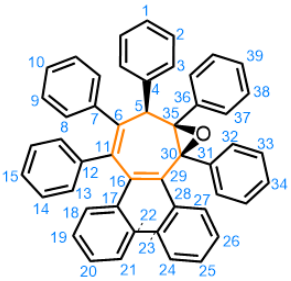

***sym*-phenPh$_5$C$_7$H-O**

***sym*-phenPh$_5$C$_7$H-O:** An isomerically pure sample of ***sym*-phenPh$_5$C$_7$H** (20 mg, 0.03 μmol) was dissolved in $CHCl_3$ (0.5 mL) and cooled to 0 °C before adding a saturated aqueous solution of $NaHCO_3$ (0.1 mL). Solid *m*CPBA (40 g, 0.23 mmol) was added. The biphasic mixture was heated to 70 °C and left to stir for 22 h before allowing to cool to rt. A saturated aqueous solution of $NaHCO_3$ (2 mL) was added and the resulting biphasic mixture was stirred for 15 min. The reaction mixture was diluted with $CHCl_3$ (5 mL) and the organic layer was separated and then washed with a saturated aqueous solution of $NaHCO_3$ (2 × 5 mL) and brine (5 mL), before being dried over $MgSO_4$, filtered and evaporated to dryness to give a crude yellow solid. This reaction was repeated **10** times before the crude solids were combined and purified. The crude solid was purified by column chromatography (Teledyne Isco CombiFlash Rf+ system, 24 g SiO_2, Hexanes: CH_2Cl_2, 0 – 25%). The title compound was isolated as a colourless crystalline solid (10 mg, 0.016 mmol, 5%) **M.P.** > 350 °C. **^{1}H NMR** (700 MHz, $CDCl_3$) δ ^{1}H NMR (700 MHz, $CDCl_3$) δ 8.45 (m, 2H, H_{18+27}), 8.05 (d, *J* = 8.4 Hz, 1H, H_{24}), 8.00 (d, *J* = 8.4 Hz, 1H, H_{25}), 7.49 – 7.45 (m, 2H, H_{37}), 7.45

– 7.39 (m, 2H, H_{19+26}), 7.31 – 7.25 (m, 6H, $H_{3+20+25+32}$), 7.23 (m, 2H, H_{14}), 7.14 (m, 2H, H_8), 7.10 (m, 3H, H_{1+2}), 7.08 – 7.03 (m, 6H, $H_{9+10+13+15}$), 7.00 (m, 3H, H_{33+34}), 6.72 (m, 2H, H_{38}), 6.66 (m, 1H, H_{39}), 4.90 (s, 1H, H_5). **^{13}C NMR** (176 MHz, $CDCl_3$) δ 143.8 (C_{11}), 143.6 (C_{16}), 142.5 (C_6), 140.9 (C_{12}), 140.1 (C_{31}), 138.8 (C_{36}), 136.4 (C_7), 135.9 (C_4), 131.5 (C_{28}), 131.5 (C_{23}), 131.1 (C_{17}), 130.7(C_{22}), 129.9 (C_{29}), 129.6 (C_8), 129.5 (C_{21}), 129.4 (C_{20}), 128.6 (C_{37}), 128.2 (C_{24}), 127.9 (C_2), 127.9 ($C_{9\text{ or }10}$), 127.8 ($C_{9\text{ or }10}$), 127.6 (C_3), 127.6 (C_{15}), 127.2 (C_{14}), 127.1 (C_{13}), 126.9 (C_{38}), 126.9 (C_{33}), 126.9 (C_{34}), 126.7 (C_1), 126.5 (C_{25}), 126.4 (C_{19}), 126.3 (C_{26}), 125.6 (C_{32}), 125.4 (C_{39}), 122.5 (C_{18}), 122.2 (C_{27}), 78.9 (C_{35}), 66.3 (C_{30}), 58.0 (C_5). **HR-ESI MS** *m/z* = 639.2664 $[M+H]^+$, calculated for $C_{49}H_{35}O^+$: 639.2688.

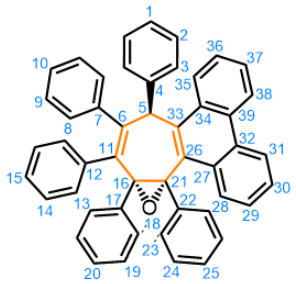

***asym*-phenPh$_5$C$_7$H-O**

***asym*-phenPh$_5$C$_7$H-O:** The previously obtained 2:1 mixture of ***asym*-phenPh$_5$C$_7$H** and ***sym*-phenPh$_5$C$_7$H** (20 mg, 30 μmol) was dissolved in $CHCl_3$ (0.5 mL). Solid *m*CPBA (0.04 g, 0.23 mmol) was added. The mixture was heated to 70 °C and left to stir for 22 h before allowing to cool to rt. A saturated aqueous solution of $NaHCO_3$ (2 mL) was added and the resulting biphasic mixture was stirred for 15 min. The reaction mixture was diluted with $CHCl_3$ (5 mL) and the organic layer was separated and then washed with a saturated aqueous solution of $NaHCO_3$ (2 × 5 mL) and brine (5 mL), before being dried over $MgSO_4$, filtered and evaporated to dryness to give a crude off white solid. The crude mixture was purified by column chromatography (Teledyne Isco CombiFlash Rf+ system, 24 g SiO_2, Hexanes: CH_2Cl_2, 0–30%). The title compound was isolated as a colorless crystalline solid (5 mg, 8.0 μM, 25%). **M.P.** > 350 °C. **^{1}H NMR** (700 MHz, $CDCl_3$) δ 8.82 (dd, *J* = 8.4, 1.2 Hz, 1H, H_{38}), 8.72 (d, *J* = 8.3 Hz, 1H, H_{31}), 8.22 (dd, *J* = 8.3, 1.2 Hz, 1H, H_{28}), 8.16 (d, *J* = 8.4 Hz, 1H, H_{35}), 7.76 – 7.67 (m, 3H, H_{3+37}), 7.61 (ddd, *J* = 8.3, 6.9, 1.3 Hz, 1H, H_{36}), 7.57 (ddd, *J* = 8.3, 6.9, 1.3 Hz, 1H, H_{29}), 7.45 (m, 3H, H_{1+2}) 7.31 (m, 1H, H_{10}), 7.10 – 6.94 (m, 12H, $H_{8+9+13+14+23+24}$), 6.91 (tt, *J* = 7.4, 1.3 Hz, 1H, H_{15}), 6.84 – 6.75 (m, 1H, H_{25}), 6.78 – 6.64 (m, 6H, $H_{18+19+20,30}$), 6.41 (s, 1H, H_5). **^{13}C NMR** (176 MHz, $CDCl_3$) δ 145.8 (C_{11}), 144.4 (C_{33}), 143.2 (C_4), 140.1 (C_{22}), 139.5(C_{17}), 139.1 (C_7), 138.9 (C_6), 137.9 (C_{27}), 135.6 (C_{32}), 132.5 (C_{39}), 132.3 (C_8), 132.3 (C_9), 131.3 (C_{14}), 130.9 (C_{26}), 130.9 (C_{34}),

130.5 (C_{12}), 128.9 (C_{24}), 128.8 (C_3), 128.7 (C_{13}), 128.2 ($C_{18 \text{ or } 20}$), 128.1 (C_2), 127.8 (C_{28}), 127.4 (C_{36}), 127.1 (C_{23}), 126.9 (C_{37}), 126.83 (C_{15}), 126.8 (C_{10}), 126.6 (C_1), 126.5 ($C_{20 \text{ or } 18}$), 126.5 (C_{25}), 126.4 (C_{29}), 126.23 (C_{19+37}), 124.7 (C_{30}), 123.3 (C_{35}), 122.6 (C_{38}), 122.5(C_{31}) 74.2 (C_{16}), 71.9 (C_{21}), 50.5 (C_5). **HR-ESI MS** *m/z* = 639.2671 $[M+H]^+$, calculated for $C_{49}H_{35}O^+$: 639.2688.

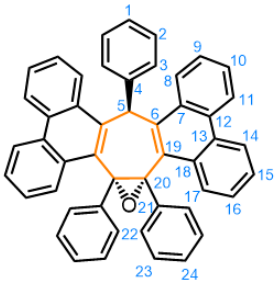

sym-phen$_2$Ph$_3$C$_7$H-O

***sym*-phen$_2$Ph$_3$C$_7$H-O: Ph$_7$C$_7$H-O** (55 mg, 90 µmol) and iodine (51 mg, 20 µmol, 2.1 equiv) were added to a 7 mL small quartz tube, which was fitted with a septum and purged with $N_{2(g)}$. THF (6 mL) was degassed through 3 × freeze-pump-thaw cycles and added. The mixture was sparged with $N_{2(g)}$ for 10 min followed by the addition of propylene oxide (0.5 mL) and sparging with $N_{2(g)}$ for a further 5 min. The reaction mixture was then irradiated by 4 × 9W 254 nm bulbs for 3 h, while being sparged through with $N_{2(g)}$. A saturated aqueous solution of $Na_2S_2O_3$ (2 mL) was added and the resulting biphasic mixture was stirred for 2 min. The reaction mixture was diluted with $CHCl_3$ (5 mL) and the organic layer was separated and then washed with a saturated aqueous solution of $Na_2S_2O_3$ (2 × 5 mL) and brine (5 mL), before being dried over $MgSO_4$, filtered and evaporated to dryness to give a dark solid. The crude solid was purified by column chromatography (Teledyne Isco CombiFlash Rf+ system, 12 g SiO_2, Hexanes: CH_2Cl_2, 0 – 30%). The title compound was isolated as a colourless crystalline solid (54 mg, 90 µmol, >99%) **M.P.** > 350 °C. **^{1}H NMR** (600 MHz, $CDCl_3$) δ 8.80 (m, 2H, H_8), 8.72 (m, 2H, H_{14}), 8.61 (m, 2H, H_{11}), 8.52 (m, 2H, H_{17}), 7.91 (s, 1H, H_5), 7.72 (m, 2H, H_{16}), 7.67 (m, 2H, H_{17}), 7.54 (m, 6H,H_{2+9+10}), 7.32 (m, 2H, H_3), 7.29 (m, 1H, H_1), 7.18 (m, 4H, H_{22}), 6.85 (m, 2H, H_{24}), 6.80 (m, 4H, H_{23}).**^{13}C NMR** (151 MHz, $CDCl_3$) δ 141.8 (C_6), 138.2 (C_4), 137.4 (C_{21}), 133.4 (C_{18}), 133.2 (C_{13}), 131.4 (C_{12}), 130.9 (C_{19}), 130.9 (C_7), 129.9 (C_9), 129.4 (C_{22}), 128.5 (C_3), 127.9 (C_{16}), 127.9 (C_8), 127.9 (C_2), 126.9 (C_{24}), 126.9 (C_{10}), 126.8 (C_{23}), 126.7 (C_{15}), 126.7 (C_1), 124.7 (C_{17}), 123.4 (C_{14}), 122.6 (C_{11}), 71.3 (C_{20}), 44.0 (C_5). **HRMS-ASAP** *m/z* = 637.2505 $[M+H]^+$, calculated for $C_{49}H_{33}O^+$: 637.2531.

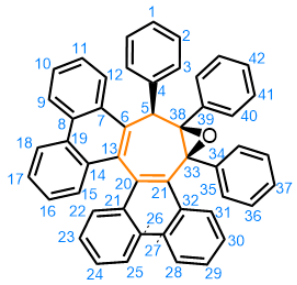

***asym*-phen$_2$Ph$_3$C$_7$H-O:** ***sym*-phenPh$_5$C$_7$H-O** (3.5 mg, 5.5 µmol) and iodine (1.5 mg, 6 µmol, 1.1 equiv) were added to a 4 mL quartz cuvette, which was fitted with a septum and sparged with $N_{2(g)}$. THF (3 mL) was degassed through 3 × freeze-pump-thaw cycles and added. The mixture was sparged with $N_{2(g)}$ for 10 min followed by the addition of propylene oxide (0.5 mL) and sparging with $N_{2(g)}$ for a further 5 min. The reaction mixture was then irradiated by 4 × 9W 254 nm bulbs for 3 h, while being sparged with $N_{2(g)}$. A saturated aqueous solution of $Na_2S_2O_3$ (2 mL) was added and the resulting biphasic mixture was stirred for 2 min. The reaction mixture was diluted with $CHCl_3$ (5 mL) and the organic layer was separated and then washed with a saturated aqueous solution of $Na_2S_2O_3$ (2 × 5 mL) and brine (5 mL), before being dried over $MgSO_4$, filtered and evaporated to dryness to give a dark solid. The crude solid was purified by preparative TLC, separated with Hexanes: CH_2Cl_2, 30%. The title compound was isolated as a colourless crystalline solid (3 mg, 4.7 µmol, 85%). The low quantity of material obtained limits the characterization data that can be obtained. However, the ^{1}H NMR, HRMS and photoluminescence data are consistent with ***asym*-phen$_2$Ph$_3$C$_7$H-O** and the structural assignment is supported by analogy of ***sym*-phen$_2$Ph$_3$C$_7$H-O**. **M.P.** > 350 °C. **^{1}H NMR** (400 MHz, $CDCl_3$) δ 8.89 (dd, *J* = 11.2, 8.4 Hz, 2H), 8.54 (d, *J* = 8.4 Hz, 2H), 8.13 (d, *J* = 8.2 Hz, 1H), 7.79 – 7.61 (m, 4H), 7.56 – 7.33 (m, 6H), 7.20 (t, *J* = 7.6 Hz, 1H), 7.10 (d, *J* = 8.0 Hz, 3H), 7.05 (dd, *J* = 7.7, 2.0 Hz, 2H), 6.92 – 6.75 (m, 6H), 6.56 – 6.43 (m, 4H), 5.88 (s, 1H, H_5). **HRMS-ASAP** *m/z* = 637.2538 $[M+H]^+$, calculated for $C_{49}H_{33}O^+$: 637.2531.

2.5 Appendix of Supplementary Data and Discussion

2.5.1 Variable-Temperature (VT) NMR Spectroscopy

We performed VT NMR measurements to determine the energy barrier to rotation of phenyl rings in ***sym*-phenPh$_5$C$_7$H**. Although we were not able to unambiguously assign all ^{13}C resonances based on 2D NMR spectra on account of overlapping signals, we have tentatively assigned (Figure 2.5) the phenyl group that experiences the highest energy barrier to rotation as ring c by analogy to our investigation of **Ph$_7$C$_7$H** reported previously.[13] VT ^{13}C NMR spectra were acquired to facilitate analysis using a two-spin system model in the WinDNMR[24] software package. In order to obtain a solution of ***sym*-phenPh$_5$C$_7$H** with a low freezing point and of sufficiently high concentration (20 mg in 0.8 mL) for ^{13}C NMR analysis, a mixture of CS_2 (0.7 mL) with CD_2Cl_2 (0.1 mL) was used as solvent. A series of spectra ranging from 24 °C to –98 °C were recorded.

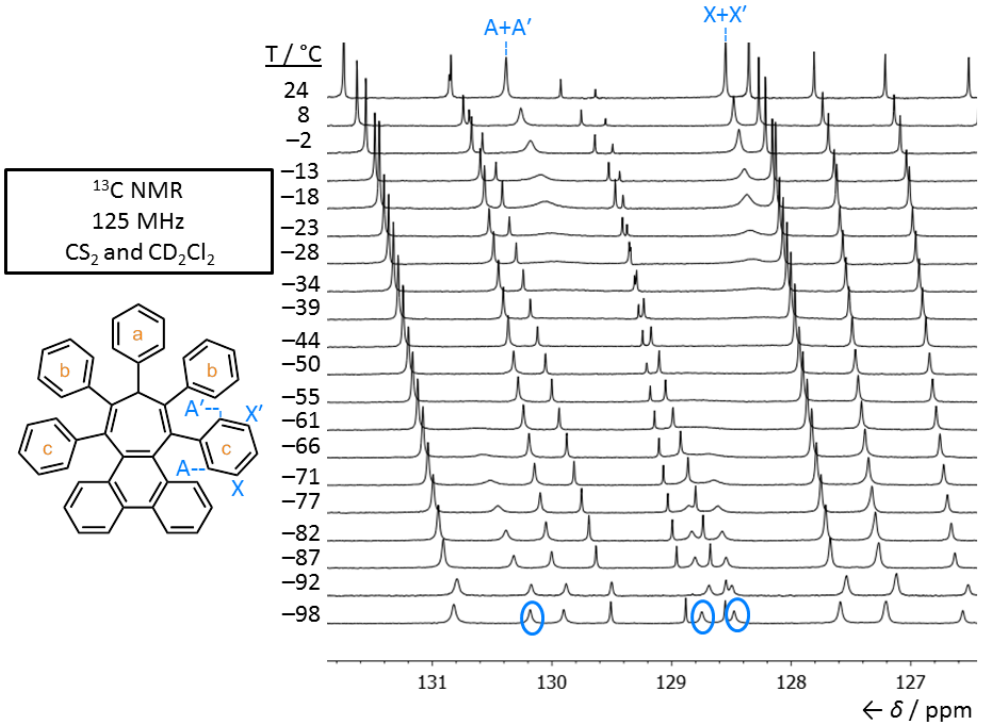

Figure 2.5. Partial ^{13}C VT NMR spectra of ***sym*-phenPh$_5$C$_7$H**. Peaks corresponding to the carbon pairs A/A′ and X/X′ are observed as individual, averaged signals in the fast exchange regime, but appear as distinct signals at low temperature in the slow exchange regime. Only three of the four signals can be distinguished at low temperature on account of overlapping signals; however, only one pair is needed to perform lineshape analysis.

Analysis of the ^{13}C spectra reveals that, within the temperature range studied, signals corresponding to ring c carbons broaden, merge into the baseline, and then re-emerge as four separate peaks as the temperature is decreased. There are two pairs of resonances in slow exchange below –60 °C. Only three resonances can be observed as distinct peaks as the fourth overlaps with other signals. In order to determine which of the three re-emerged peaks correspond to a pair of exchanging sites, a HSQC experiment was performed at –98 °C (Figure 2.6). Both ^{1}H NMR and ^{13}C NMR spectra had been recorded from 24 °C to –98 °C.

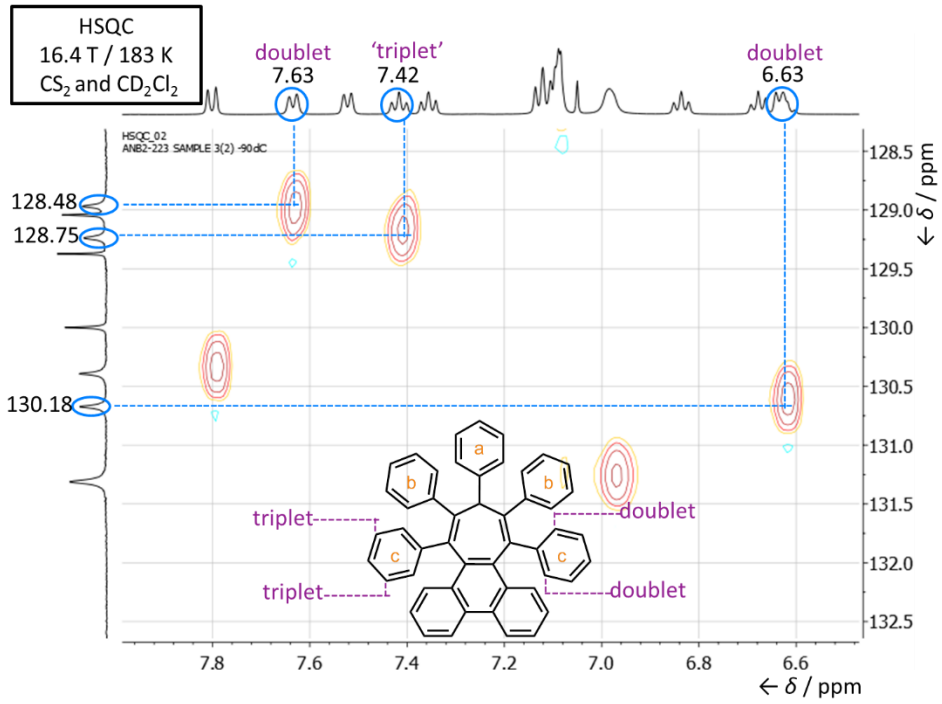

Figure 2.6. Partial HSQC NMR spectrum of ***sym*-phenPh$_5$C$_7$H** recorded at –98 °C. Correlations are highlighted between the ^{13}C signals observed to be in slow exchange by VT NMR (Figure 2.5) and the corresponding ^{1}H signals. Inset: based on the *J* coupling patterns, the different positions of ring c can be distinguished.

Analysis of the HSQC spectrum reveals that the three ^{13}C signals that have re-emerged from the baseline correlate with two doublets and a signal that appears as an apparent triplet in the ^{1}H NMR. The signals correlating to the two doublets must be the pair of exchanging nuclear environments. The doublet at 6.63 ppm looks rather broad but this is due to peaks

under the doublet and this has been confirmed by integration. Thus, we can assign (Figure 2.7) the labels A+A′ to these resonances.

We selected eight spectra for further analysis, choosing temperatures close to the transition of ring c resonances from fast to the slow exchange regimes. Lineshape analysis was performed to derive rate constants by comparison to model spectra produced using WinDNMR.

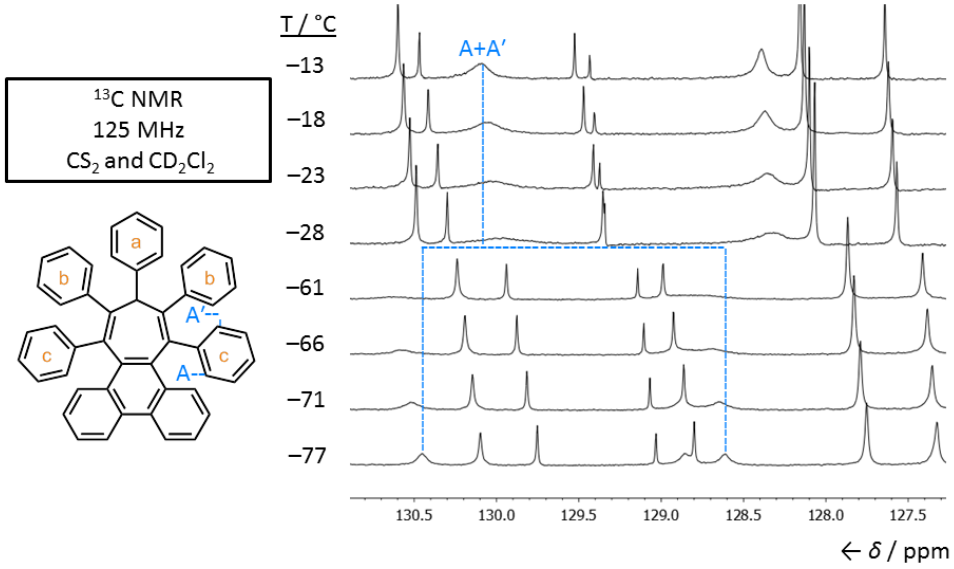

Figure 2.7. ^{13}C VT NMR spectra of ***sym*-phenPh$_5$C$_7$H** used for lineshape analysis. The dashed blue lines illustrate the resolution of a single peaks into a pair of peaks as temperature decreases.

Activation energy barriers for the rotation of ring c were calculated for each of the eight temperatures using equation **3**:

$$\Delta G^{\ddagger} = -RT \ln \frac{k_r h}{k_B T}$$

Equation 3. A variation of the Eyring equation.

Where k_r is the measured rate constant, k_B is the Boltzmann constant, T is temperature, h is Planck's constant, and R is the ideal gas constant.

Table 3. Calculated activation energies ($\Delta G^{\ddagger}$) for the rotation of ring c of ***sym*-phenPh$_5$C$_7$H**.

Entry	Temperature / K (± 0.64)	$\Delta G^{\ddagger}$ / kJ mol^{-1}
1	260.4	43.3
2	255.1	43.4
3	249.7	43.2
4	244.4	43.0
5	212.5	41.8
6	207.2	42.0
7	201.9	41.8
8	196.6	41.8

A line was fitted (Figure 2.8) to a plot of $\Delta G^{\ddagger}$ vs T. The slope of the line corresponds to $-\Delta S^{\ddagger}$ and the y-axis intercept to $\Delta H^{\ddagger}$. The entropy of activation $\Delta S^{\ddagger}$ was calculated to be –27.9 J mol^{-1} K^{-1} and enthalpy of activation $\Delta H^{\ddagger}$ was calculated to be 36.2 kJ mol^{-1}. Based on these values, we calculate a $\Delta G^{\ddagger}$ of 44.5 kJ mol^{-1} at 298K.

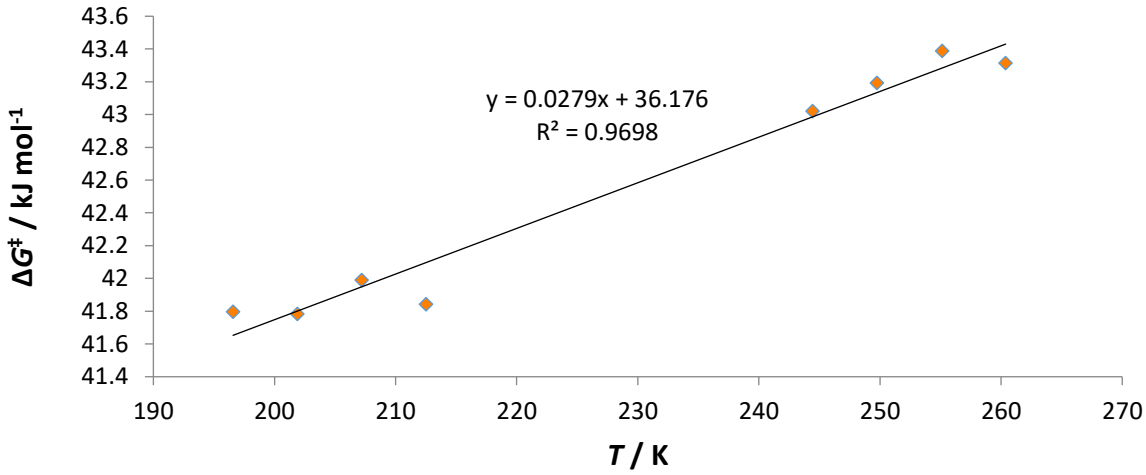

Figure 2.8. A plot of the experimentally measured free energy of activation $\Delta G^{\ddagger}$ for rotation of ring c of ***sym*-phenPh$_5$C$_7$H** as a function of temperature.

We also performed VT NMR measurements to determine the energy barrier to rotation of phenyl rings in **Ph$_7$C$_7$H-O**, using the same approach. Based on 2D NMR, we were able to assign ring d (Figure 2.9) as the phenyl group that experiences the highest energy barrier to rotation. A 20 mg sample of **Ph$_7$C$_7$H-O** was dissolved in a mixture of CS_2 (0.7 mL) with CD_2Cl_2 (0.1 mL) as the NMR solvent and a series of ^{13}C NMR spectra ranging from 24 °C to -87 °C were recorded.

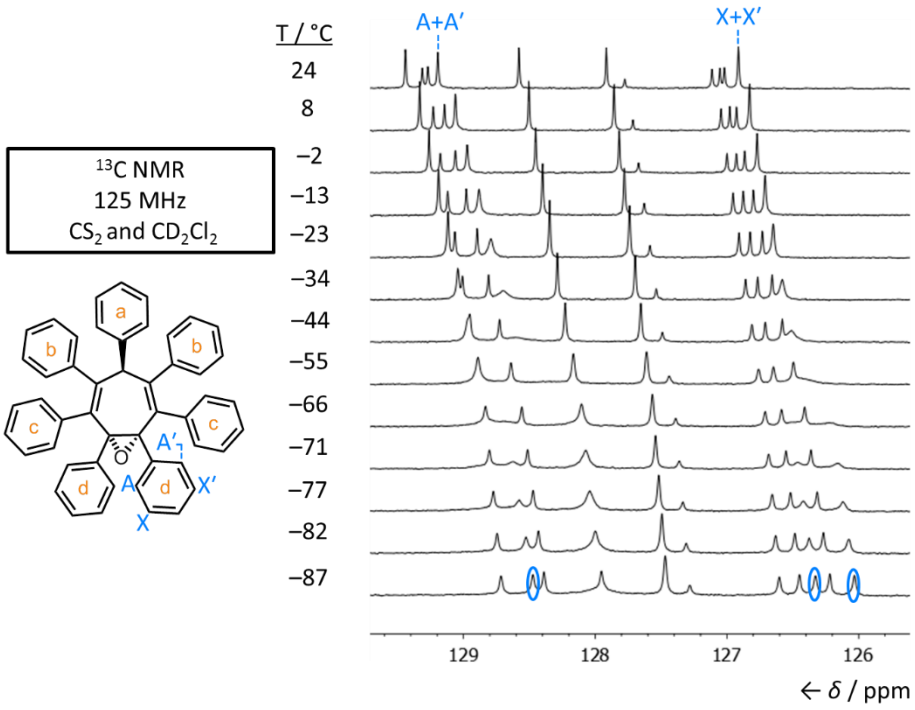

Figure 2.9. Partial ^{13}C VT NMR spectra of **Ph_7C_7H-O**. Peaks corresponding to the carbon pairs A/A′ and X/X′ are observed as individual, averaged signals in the fast exchange regime, but appear as distinct signals at low temperature in the slow exchange regime. Only three of the four signals can be distinguished at low temperature on account of overlapping signals; however, only one pair is needed to perform lineshape analysis.

Analysis of the ^{13}C spectra reveals that, within the temperature range studied, signals corresponding to ring d carbons broaden, merge into the baseline, and then re-emerge as four separate peaks as the temperature is decreased made up of two pairs of resonances in slow exchange. Only three resonances are observed as distinct peaks because the fourth overlaps with other signals. In order to determine which of the three re-emerged peaks are a pair a HSQC spectrum was acquired (Figure 2.10) at –87 °C. Both ^{1}H NMR and ^{13}C NMR spectra had been recorded from 24 °C to –87 °C.

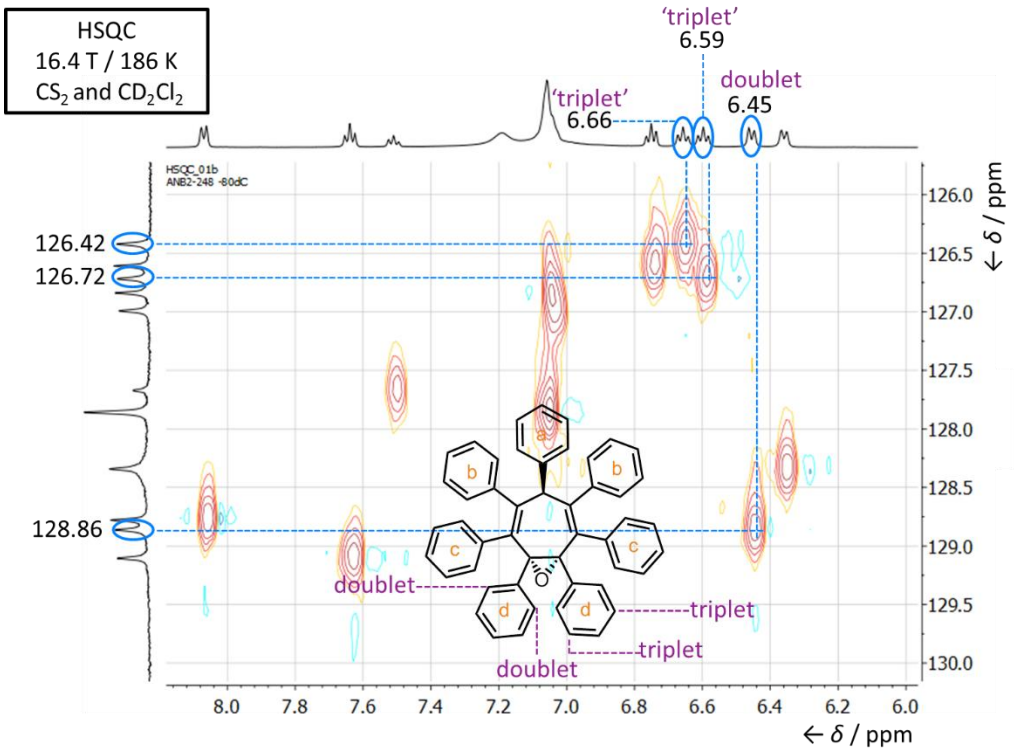

Figure 2.10. Partial HSQC NMR spectrum of **Ph_7C_7H-O** recorded at –87 °C. Correlations are highlighted between the ^{13}C signals observed to be in slow exchange by VT NMR (Figure 2.9) and the corresponding ^{1}H signals. Inset: based on the *J* coupling patterns, the different positions of ring d can be distinguished.

By matching the *J* coupling patterns of the ^{1}H signals following the approach described above for ***sym*-phenPh_5C_7H**, we can assign (Figure 2.11) the ^{13}C signals of **Ph_7C_7H-O** corresponding to X and X′. We selected five ^{13}C NMR spectra for further analysis, choosing temperatures close to the transition of ring d resonances from fast to the slow exchange regimes. As above, lineshape analysis was performed to derive rate constants by comparison to model spectra produced using WinDNMR and activation energy barriers were calculated using equation 3.

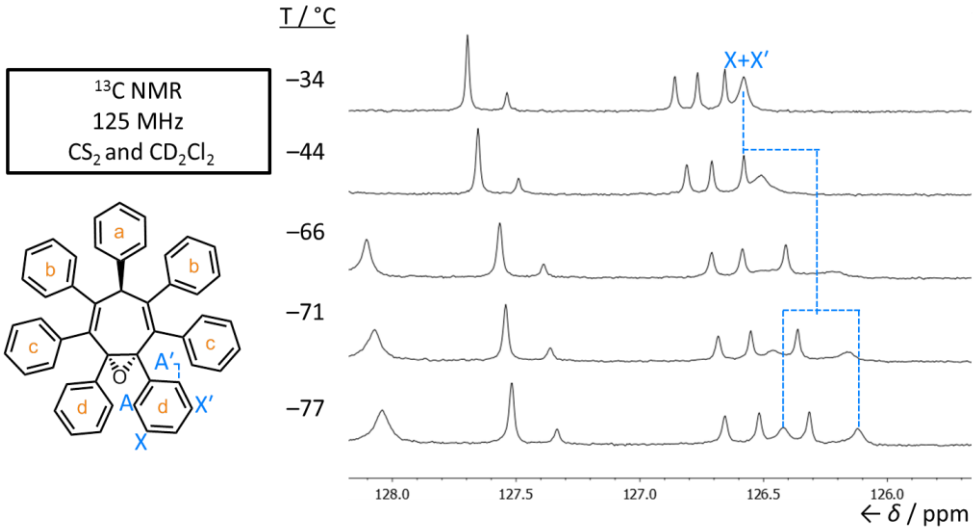

Figure 2.11. ^{13}C VT NMR spectra of **Ph_7C_7H-O** used for lineshape analysis. The dashed blue lines illustrate the resolution of a single peak into a pair of peaks as temperature decreases.

Table 4. Calculated activation energies ($\Delta G^{\ddagger}$) for the rotation of ring d of **Ph_7C_7H-O**.

Entry	Temperature / K (± 0.64)	$\Delta G^{\ddagger}$ / kJ mol^{-1}
1	239.2	42.2
2	228.5	42.3
3	207.2	42.7
4	201.9	42.9
5	196.2	43.6

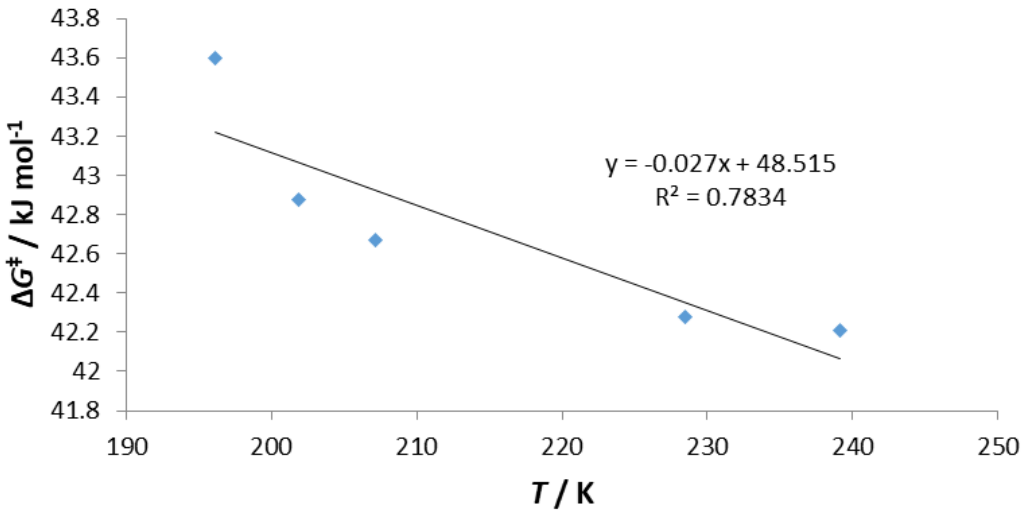

Figure 2.12. A plot of the experimentally measured free energy of activation $\Delta G^{\ddagger}$ for rotation of ring d of **Ph_7C_7H-O** as a function of temperature.

A line was fitted (Figure S23) to a plot of $\Delta G^{\ddagger}$ vs T. The entropy of activation $\Delta S^{\ddagger}$ was measured to be +27.0 J mol^{-1} K^{-1} and enthalpy of activation $\Delta H^{\ddagger}$ was measured as 48.5 kJ mol^{-1}

2.5.2 X-Ray Crystallographic Analysis

Analysis of all crystal structures and their packing are shown (Figure 2.13-2.25) with the crystal system, space group, unit cell parameters, bond lengths, bond angles and dihedral angles reported below.

Direct comparisons of important bond lengths and centroid-centroid distance between the phenyl ring bound to the tertiary sp^3-centre and the opposite phenyl ring are outlined in Table 5 below. Notably, the C_5–C_6 distance is 1.47–1.49 Å for the triene compounds but 1.50–1.51 Å for the epoxides. This increase of 2–4 pm is characteristic of the increased single–bond character in the nonconjugated epoxides.

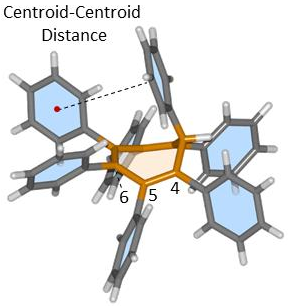

Figure 2.13. Solid-state structure of **Ph_7C_7H** viewed side-on to the seven-membered ring showing the centroid-centroid distance on the two rings associated with through-space dimers.

Table 5. Summarized bond lengths and centroid distances for the molecular rotors.

Rotor	Centroid-Centroid distance (Å)	C_4-C_5 distance (Å)	C_5-C_6 distance (Å)
C_7Ph_7H-O	5.21	1.34	1.50
***sym*-phenPh_5C_7H-O**	4.99	1.36	1.51
asym-phenPh_5C_7H-O	5.07	1.34	1.50
C_7Ph_7H	5.15	1.35	1.47
***sym*-phenPh_5C_7H**	4.57	1.35	1.49
***asym*-phenPh_5C_7H**	5.02	1.35	1.49
sym-$phen_2Ph_3C_7H$-O	5.23	1.36	1.51

Analysis of the single-crystal X-ray structure of **Ph_7C_7H** has been reported previously.[13]

Ph_7C_7H-O

Crystals of **O-Ph_7C_7H** suitable for X-ray diffraction were grown by slow cooling of a saturated MeCN solution.

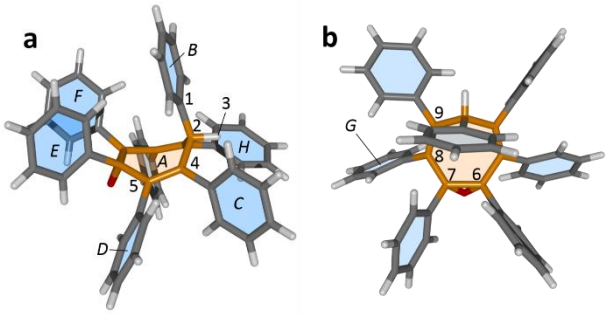

Figure 2.14. Solid-state structure of **Ph_7C_7H-O** viewed (a) side-on to the seven-membered ring and (b) from above the seven-membered ring. Selected atoms are labelled numerically, the planes of the carbocyclic rings are labelled by italicized uppercase letters. As central ring *A* is puckered, individual planes α^n are defined by a carbon vertex *n* and its two nearest neighbours within the ring, e.g., A^5 is the plane defined by atoms 4, 5, and 6.

Crystal System: Monoclinic

Space group: $P2_1/c$

Unit Cell Parameters: a = 15.9229(7) Å, b = 12.6701(5) Å, c = 17.9495(7) Å, β = 108.8982(16)°, V = 3426.02(24) $Å^3$, Z = 4

Bond lengths (Å): C2–C4, 1.53; C4–C5, 1.34; C5–C6, 1.50; C6–C7, 1.49; C7–C8, 1.50; C8–C9, 1.34; C2–C9, 1.54.

Bond angles (°): C1–C2–H3, 104.4; C1–C2–C4, 117.6; C1–C2–C9, 113.9; C4–C2–C9, 110.6; C2–C4–C5, 123.5; C4–C5–C6, 123.7; C5–C6–C7, 123.4; C6–C7–C8, 122.6; C7–C8–C9, 124.5; C2–C9–C8, 123.4; C6–O–C7, 61.6.

Dihedral angles (°): A^2–*B*, 36.1; A^4–*C*, 60.2; A^5–*D*, 55.9; A^6–*E*, 76.6; A^7–*F*, 73.0; A^8–*G*, 78.6; A^9–*H*, 52.5; *B*–*C*, 60.9; *C*–*D*, 53.9; *D*–*E*, 62.2; *E*–*F*, 58.9; *F*–*G*, 58.7; *G*–*H*, 64.8; *B*–*H*, 53.2.

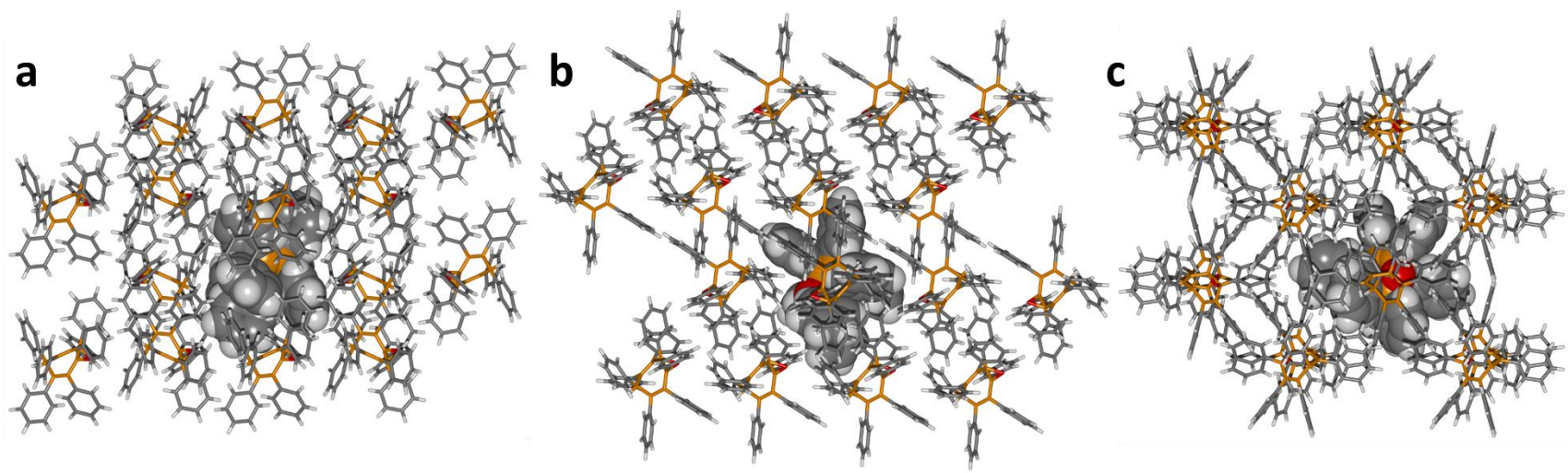

Figure 2.15. Solid-state superstructure of **Ph_7C_7H-O**. A central molecule (space filling representation) is shown embedded in a section of the lattice made up of 2×2×2 unit cells in order to illustrate the crystal packing. Projections are viewed along the crystallographic (a) *a*-, (b) *b*-, and (c) *c*-axes.

sym-phenPh$_5$C$_7$H

Crystals of ***sym*-phenPh$_5$C$_7$H** suitable for X-ray diffraction were grown by slow cooling of a saturated MeCN solution of pure ***sym*-phenPh$_5$C$_7$H**.

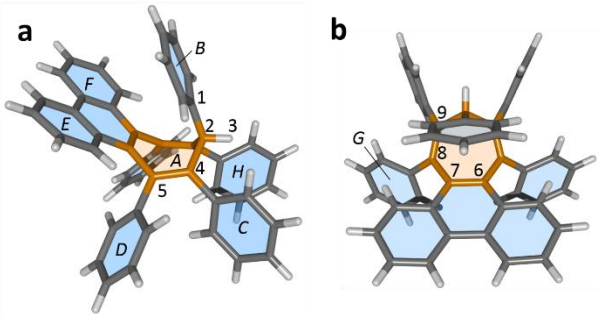

Figure 2.16. Solid-state structure of ***sym*-phenPh$_5$C$_7$H** viewed (a) side-on to the seven-membered ring and (b) from above the seven-membered ring. Selected atoms are labelled numerically, the planes of the carbocyclic rings are labelled by italicized uppercase letters. As central ring *A* is puckered, individual planes α^n are defined by a carbon vertex *n* and its two nearest neighbours within the ring, e.g., A^5 is the plane defined by atoms 4, 5, and 6.

Crystal System: Triclinic

Space group: P-1

Unit Cell Parameters: a = 9.4506(6) Å, b = 9.4870(6) Å, c = 19.2332(12) Å, α = 91.297(2)°, β = 103.684(2)°, γ = 91.779(2)°, V = 1673.85(18) Å^3, Z = 2

Bond lengths (Å): C2–C4, 1.53; C4–C5, 1.35; C5–C6, 1.49; C6–C7, 1.38; C7–C8, 1.48; C8–C9, 1.36; C2–C9, 1.53.

Bond angles (°): C1–C2–H3, 107.3; C1–C2–C4, 116.6; C1–C2–C9, 116.5; C4–C2–C9, 99.9; C2–C4–C5, 119.8; C4–C5–C6, 120.9; C5–C6–C7, 121.5; C6–C7–C8, 121.3; C7–C8–C9, 120.9; C2–C9–C8, 119.6.

Dihedral angles (°): A^2–*B*, 48.4; A^4–*C*, 59.2; A^5–*D*, 51.5; A^6–*E*, 6.6; A^7–*F*, 6.3; A^8–*G*, 46.2; A^9–*H*, 50.6; *B*–*C*, 65.0; *C*–*D*, 54.7; *D*–*E*, 83.2; *E*–*F*, 11.3; *F*–*G*, 82.6; *G*–*H*, 47.3; *B*–*H*, 73.6.

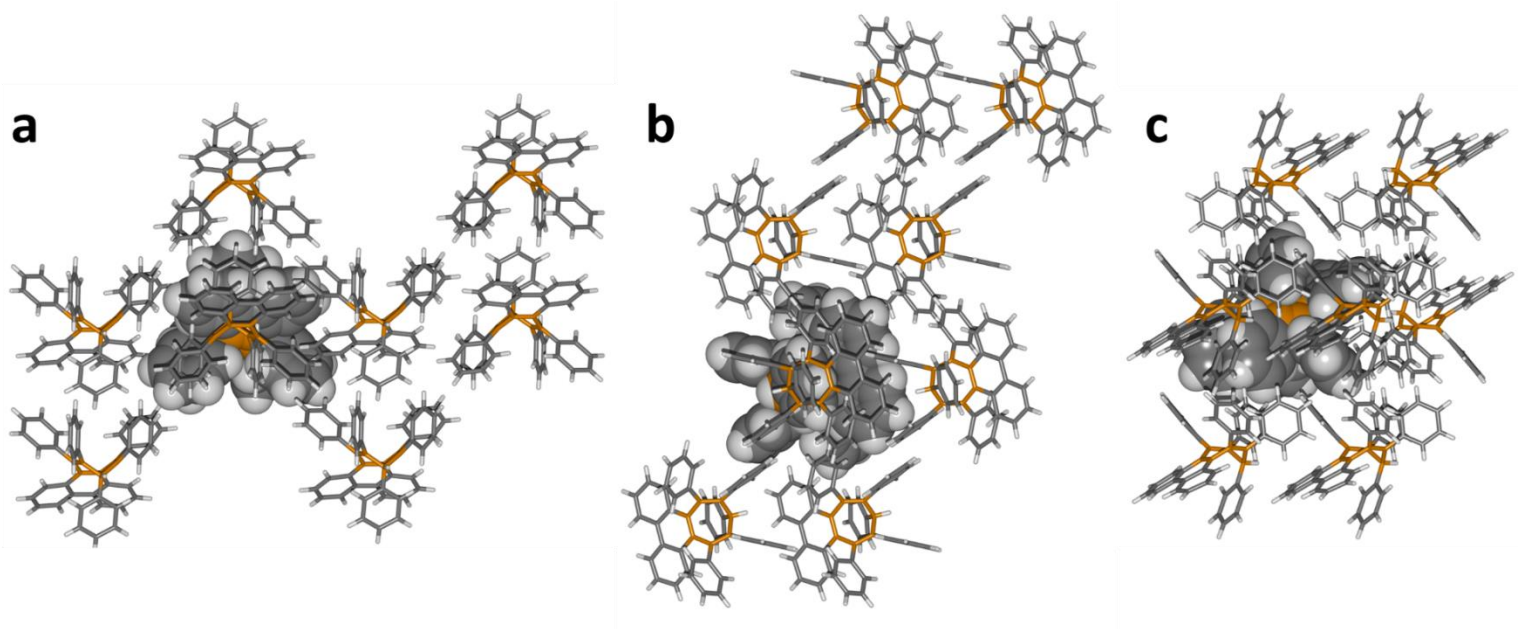

Figure 2.17. Solid-state superstructure of ***sym*-phenPh$_5$C$_7$H**. A central molecule (space filling representation) is shown embedded in a section of the lattice made up of 2×2×2 unit cells in order to illustrate the crystal packing. Projections are viewed along the crystallographic (a) *a*-, (b) *b*-, and (c) *c*-axes.

asym-phenPh$_5$C$_7$H

A single crystal of ***asym*-phenPh$_5$C$_7$H** suitable for X-ray diffraction were grown by slow cooling of a saturated MeCN solution of a 2:1 mixture of ***asym*-phenPh$_5$C$_7$H** and ***sym*-phenPh$_5$C$_7$H**.

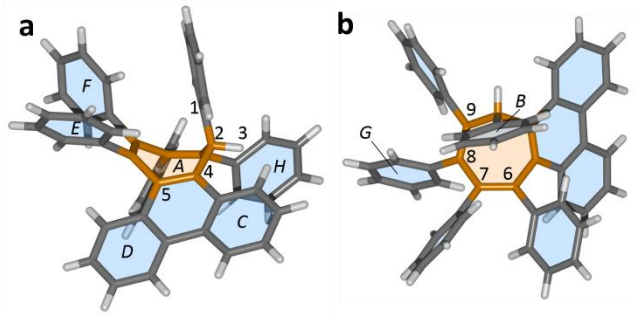

Figure 2.18. Solid-state structure of ***asym*-phenPh$_5$C$_7$H** viewed (a) side-on to the seven-membered ring and (b) from above the seven-membered ring. Selected atoms are labelled numerically, the planes of the carbocyclic rings are labelled by italicized uppercase letters. As central ring *A* is puckered, individual planes α^n are defined by a carbon vertex *n* and its two nearest neighbours within the ring, e.g., A^5 is the plane defined by atoms 4, 5, and 6.

Crystal System: Triclinic

Space group: P-1

Unit Cell Parameters: a = 9.6538(4) Å, b = 18.4913(7) Å, c = 20.4317(7) Å, α = 74.979(2)°, β = 77.015(2)°, γ = 74.871(2)°, V = 3351.98(22) Å^3, Z = 4

Bond lengths (Å): C2–C4, 1.53; C4–C5, 1.36; C5–C6, 1.49; C6–C7, 1.36; C7–C8, 1.49; C8–C9, 1.35; C2–C9, 1.53.

Bond angles (°): C1–C2–H3, 105.8; C1–C2–C4, 115.6; C1–C2–C9, 115.6; C4–C2–C9, 107.4; C2–C4–C5, 119.9; C4–C5–C6, 120.9; C5–C6–C7, 122.4; C6–C7–C8, 122.6; C7–C8–C9, 120.8; C2–C9–C8, 122.3.

Dihedral angles (°): A^2–*B*, 42.0; A^4–*C*, 11.4; A^5–*D*, 10.4; A^6–*E*, 47.5; A^7–*F*, 62.5; A^8–*G*, 69.5; A^9–*H*, 49.1; *B*–*C*, 76.6; *C*–*D*, 7.3; *D*–*E*, 87.2; *E*–*F*, 50.3; *F*–*G*, 63.4; *G*–*H*, 48.5; *B*–*H*, 74.6.

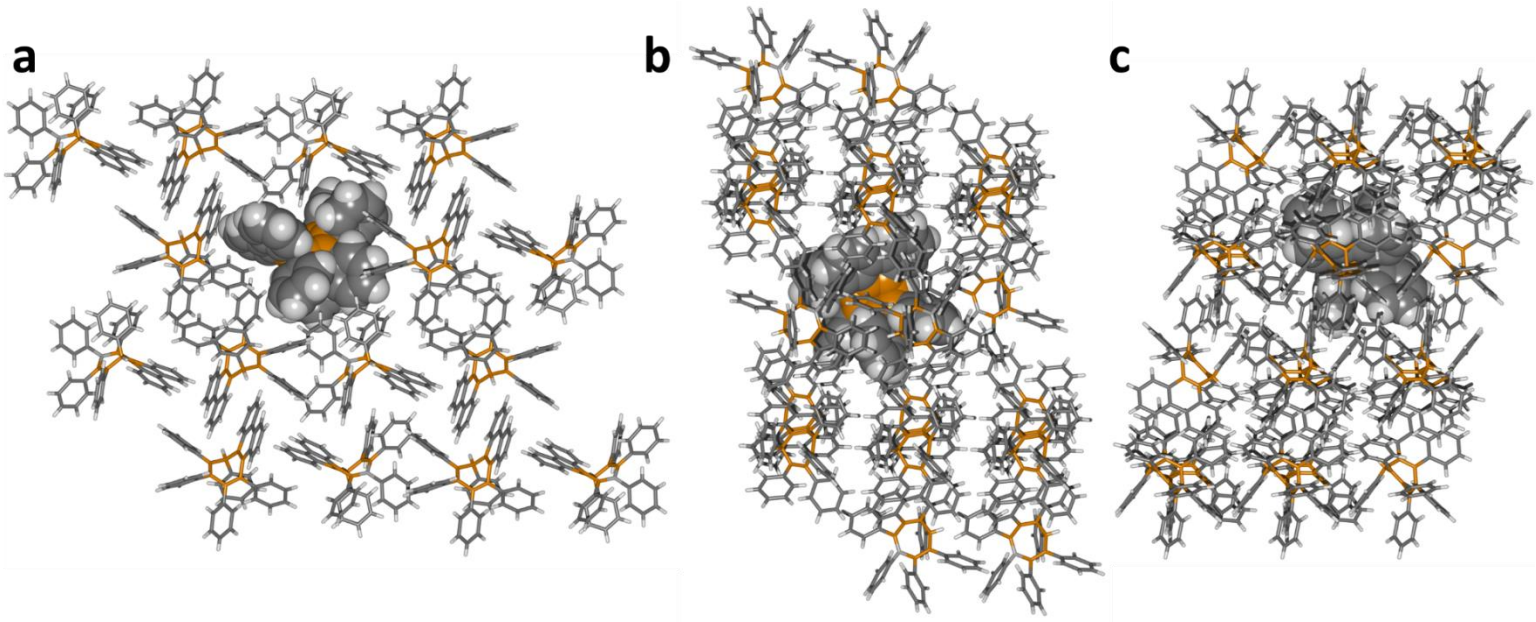

Figure 2.19. Solid-state superstructure of ***asym*-phenPh$_5$C$_7$H**. A central molecule (space filling representation) is shown embedded in a section of the lattice made up of 2×2×2 unit cells in order to illustrate the crystal packing. Projections are viewed along the crystallographic (a) *a*-, (b) *b*-, and (c) *c*-axes.

sym-phenPh$_5$C$_7$H-O

A single crystal of ***sym*-phenPh$_5$C$_7$H-O** suitable for X-ray diffraction were grown by slow cooling of a saturated MeCN solution.

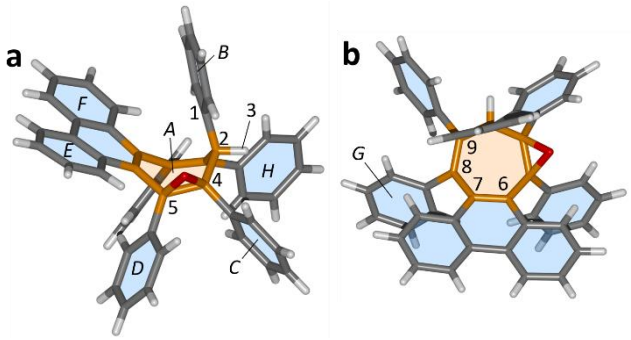

Figure 2.20. Solid-state structure of ***sym*-phenPh$_5$C$_7$H-O** viewed (a) side-on to the seven-membered ring and (b) from above the seven-membered ring. Selected atoms are labelled numerically, the planes of the carbocyclic rings are labelled by italicized uppercase letters. As central ring *A* is puckered, individual planes α^n are defined by a carbon vertex *n* and its two nearest neighbours within the ring, e.g., A^5 is the plane defined by atoms 4, 5, and 6.

Crystal System: Monoclinic

Space group: $P2_1/c$

Unit Cell Parameters: a = 9.6891(6) Å, b = 31.178(2) Å, c = 11.5786(8) Å, α = β = 109.132(3)° V = 3304.55(38) Å^3, Z = 4

Bond lengths (Å): C2–C4, 1.55; C4–C5, 1.48; C5–C6, 1.50; C6–C7, 1.37; C7–C8, 1.51; C8–C9, 1.35; C2–C9, 1.53.

Bond angles (°): C1–C2–H3, 105.3; C1–C2–C4, 118.8; C1–C2–C9, 114.5; C4–C2–C9, 106.5; C2–C4–C5, 120.1; C4–C5–C6, 119.3; C5–C6–C7, 122.6; C6–C7–C8, 123.5; C7–C8–C9, 121.7; C2–C9–C8, 120.3; C4–O–C5, 61.2.

Dihedral angles (°): A^2–*B*, 37.7; A^4–*C*, 81.6; A^5–*D*, 51.5; A^6–*E*, 5.9; A^7–*F*, 10.4; A^8–*G*, 55.2; A^9–*H*, 47.1; *B*–*C*, 30.4; *C*–*D*, 63.3; *D*–*E*, 82.4; *E*–*F*, 10.1; *F*–*G*, 83.4; *G*–*H*, 41.8; *B*–*H*, 72.0.

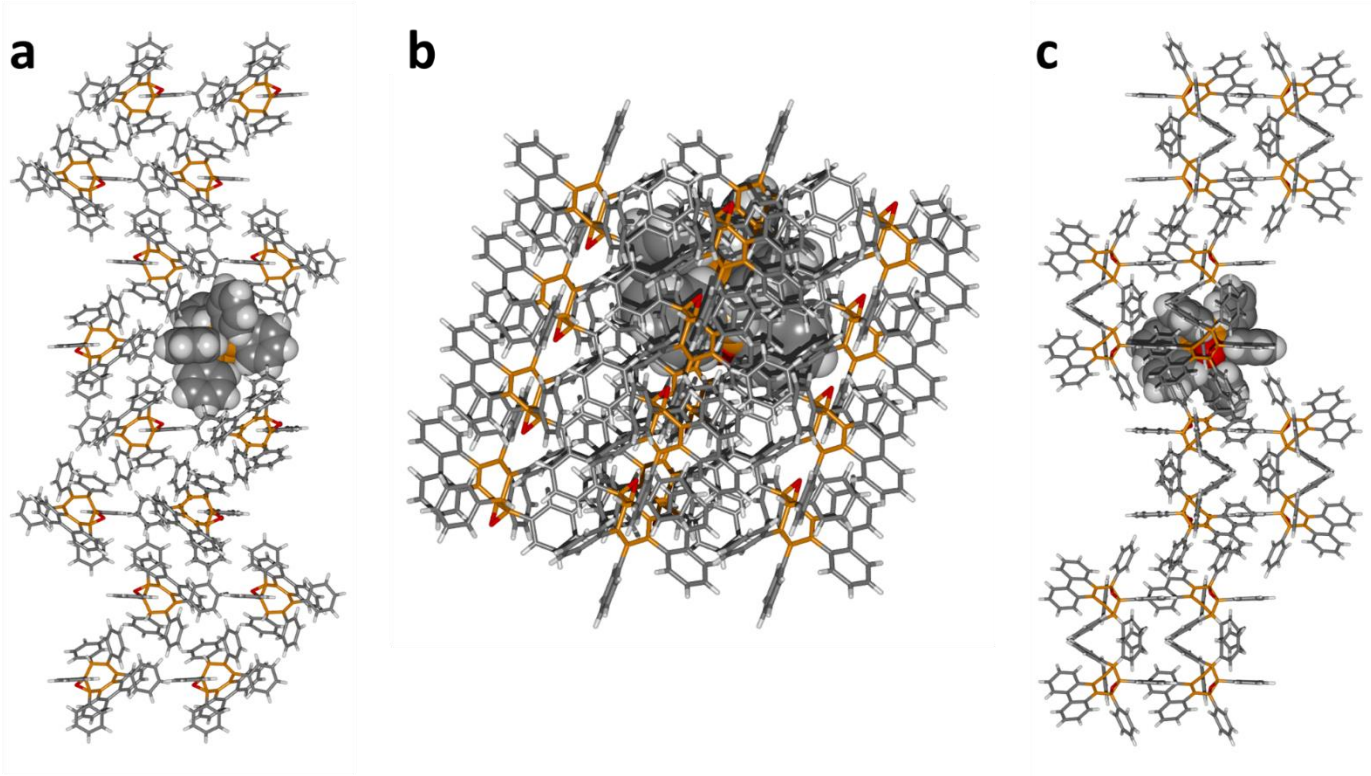

Figure 2.21. Solid-state superstructure of ***sym*-phenPh$_5$C$_7$H-O**. A central molecule (space filling representation) is shown embedded in a section of the lattice made up of 2×2×2 unit cells in order to illustrate the crystal packing. Projections are viewed along the crystallographic (a) *a*-, (b) *b*-, and (c) *c*-axes.

asym-phenPh$_5$C$_7$H-O

A single crystal of ***asym*-phenPh$_5$C$_7$H-O** suitable for X-ray diffraction were grown by slow cooling of a saturated MeCN solution.

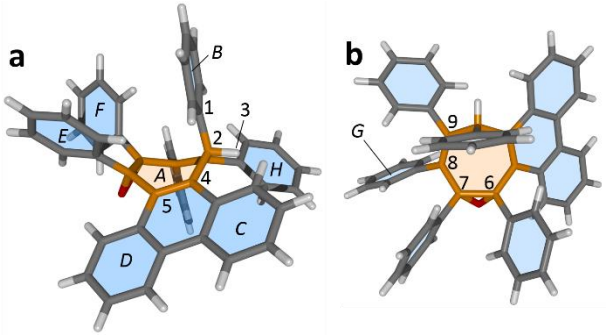

Figure 2.22. Solid-state structure of ***asym*-phenPh$_5$C$_7$H-O** viewed (a) side-on to the seven-membered ring and (b) from above the seven-membered ring. Selected atoms are labelled numerically, the planes of the carbocyclic rings are labelled by italicized uppercase letters. As central ring *A* is puckered, individual planes α^n are defined by a carbon vertex *n* and its two nearest neighbours within the ring, e.g., A^5 is the plane defined by atoms 4, 5, and 6.

Crystal System: Orthorhombic

Space group: $P2_12_12_1$

Unit Cell Parameters: a = 10.1203(6) Å, b = 16.5120(9) Å, c = 20.0664(11) Å, V = 3353.22(33) Å^3, Z = 4

Bond lengths (Å): C2–C4, 1.53; C4–C5, 1.36; C5–C6, 1.51; C6–C7, 1.49; C7–C8, 1.50; C8–C9, 1.34; C2–C9, 1.53.

Bond angles (°): C1–C2–H3, 103.8; C1–C2–C4, 114.8; C1–C2–C9, 115.8; C4–C2–C9, 113.0; C2–C4–C5, 121.8; C4–C5–C6, 123.4; C5–C6–C7, 123.4; C6–C7–C8, 122.7; C7–C8–C9, 123.2; C2–C9–C8, 125.5; C6–O–C7, 61.6.

Dihedral angles (°): A^2–*B*, 34.4; A^4–*C*, 9.4; A^5–*D*, 2.9; A^6–*E*, 47.7; A^7–*F*, 88.4; A^8–*G*, 76.3; A^9–*H*, 56.9; *B*–*C*, 76.0; *C*–*D*, 6.3; *D*–*E*, 88.3; *E*–*F*, 53.1; *F*–*G*, 40.5; *G*–*H*, 59.3; *B*–*H*, 56.2.

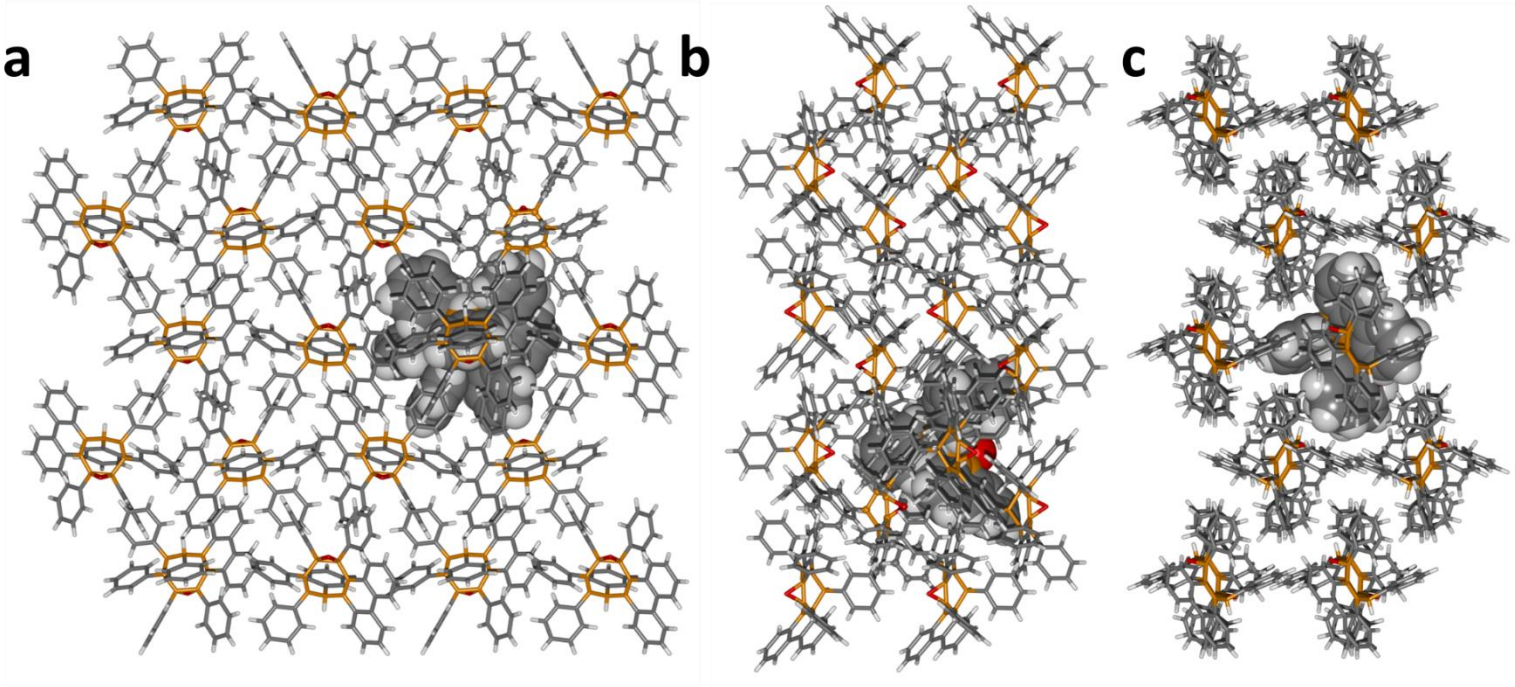

Figure 2.23. Solid-state superstructure of ***asym*-phenPh$_5$C$_7$H-O**. A central molecule (space filling representation) is shown embedded in a section of the lattice made up of 2×2×2 unit cells in order to illustrate the crystal packing. Projections are viewed along the crystallographic (a) *a*-, (b) *b*-, and (c) *c*-axes.

sym-phen$_2$Ph$_3$C$_7$H-O

A single crystal of ***sym*-phenPh$_5$C$_7$H-O** suitable for X-ray diffraction were grown by slow cooling of a saturated MeCN solution.

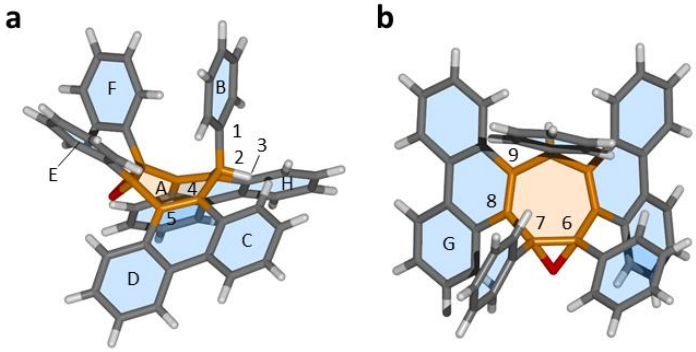

Figure 2.24. Solid-state structure of ***sym*-phen$_2$Ph$_3$C$_7$H-O** viewed (a) side-on to the seven-membered ring and (b) from above the seven-membered ring. Selected atoms are labelled numerically, the planes of the carbocyclic rings are labelled by italicized uppercase letters. As central ring *A* is puckered, individual planes α^n are defined by a carbon vertex *n* and its two nearest neighbours within the ring, e.g., A^5 is the plane defined by atoms 4, 5, and 6.

Crystal System: Monoclinic

Space group: P2$_1$/n

Unit Cell Parameters: a = 10.4829(6) Å, b = 13.2982(7) Å, c = 22.9502(13) Å, V = 3197.6(3) Å^3, Z = 4

Bond lengths (Å): C2–C4, 1.54; C4–C5, 1.36; C5–C6, 1.51; C6–C7, 1.50; C7–C8, 1.50; C8–C9, 1.37; C2–C9, 1.54.

Bond angles (°): C1–C2–H3, 102.9; C1–C2–C4, 115.4; C1–C2–C9, 117.6; C4–C2–C9, 112.4; C2–C4–C5, 122.9; C4–C5–C6, 121.4; C5–C6–C7, 120.7; C6–C7–C8, 119.41; C7–C8–C9, 121.3; C2–C9–C8, 124.0; C6–O–C7, 59.21.

Dihedral angles (°): A^2–*B*, 34.1; A^4–*C*, 12.9; A^5–*D*, 4.4; A^6–*E*, 67.6; A^7–*F*, 104.2; A^8–*G*, 10.9; A^9–*H*, 44.8; *B*–*C*, 97.4; *C*–*D*, 11.4; *D*–*E*, 76.7; *E*–*F*, 4.3; *F*–*G*, 73.9; *G*–*H*, 14.4; *B*–*H*, 77.2.

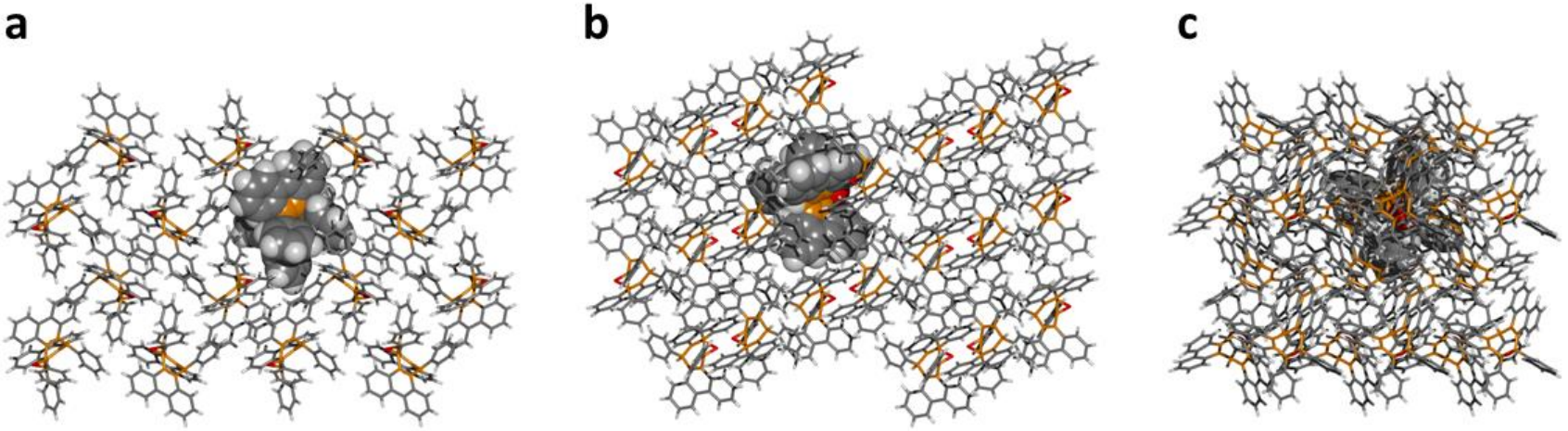

Figure 2.25. Solid-state superstructure of ***sym*-phen$_2$Ph$_3$C$_7$H-O**. A central molecule (space filling representation) is shown embedded in a section of the lattice made up of 2×2×2 unit cells in order to illustrate the crystal packing. Projections are viewed along the crystallographic (a) *a*-, (b) *b*-, and (c) *c*-axes.

2.5.3 UV-Vis Absorption Spectra

All spectra show (Figure 2.26) that the UV-vis absorption characteristics of the carbocycles are independent of the choice of solvent. UV-Vis measurements were performed using anhydrous solvents – CH_2Cl_2, methylcyclohexane (MCH), MeCN, MeOH, tetrahydrofuran (THF) or 2-methyltetrahydrofuran (2-MeTHF). Spectra were measured in 10 mm path-length cuvette at room temperature. 10 µM sample concentrations of carbocycles **Ph$_7$C$_7$H** and 20 µM sample concentrations of carbocycles (**Ph$_7$C$_7$H-O**, ***sym*-phenPh$_5$C$_7$H**, ***asym*-phenPh$_5$C$_7$H**, ***sym*-phenPh$_5$C$_7$H-O**, ***asym*-phenPh$_5$C$_7$H-O**) were used for all measurements. The intensities were plotted as molar absorptivity ε defined by the formula:

$$\varepsilon = \frac{I}{c \cdot l}$$

where I is the measured intensity, c is the concentration of sample, and l is path length of the cuvette.

Ph$_7$C$_7$H and ***sym*-phenPh$_5$C$_7$H-O** both show minimal changes in ε with solvent, however the remaining four compounds show a varying degree of ε with a slight trend on solvent polarity. Interestingly in most cases highly polar MeOH gave the lowest ε whilst non-polar 2-MeTHF, which we selected for luminescent measurements, gives high molar absorptivity for each compound.

To observe the change in absorption spectra as a result of photocyclisation and **IM** formation, Figure 2.28 compares the changes in each UV-Vis absorption spectra before and after prolonged irradiation of each compound in a degassed 20 µM MeCN solution. Each sample was irradiated in a quartz cuvette with a 310 nm lamp and the absorption spectra acquired immediately after being removed from the lamp. The samples were degassed to exclude any atmospheric oxygen that may irreversibly oxidise the **IM** to the corresponding photocyclized product. The three epoxide molecular rotors, **Ph$_7$C$_7$H-O**, ***sym*-phenPh$_5$C$_7$H-O** and ***asym*-phenPh$_5$C$_7$H-O** all showed significant changes in the UV-absorption spectra after only ten minutes of irradiation. A new absorption band at 257

nm was observed and the bands at 274 nm and 310/315 nm increased in absorbance after only 10 minutes of irradiation. Comparatively, after 10 minutes of irradiation with a 310 nm lamp, **Ph_7C_7H**, ***sym*-$phenPh_5C_7H$** and ***asym*-$phenPh_5C_7H$** shows negligible change in the UV-vis absorption spectra. To observe any change, it was essential to expose each sample for an hour to 310 nm light. After one hour the characteristic 257 nm peak is formed indicating the formation of the intermediate state.

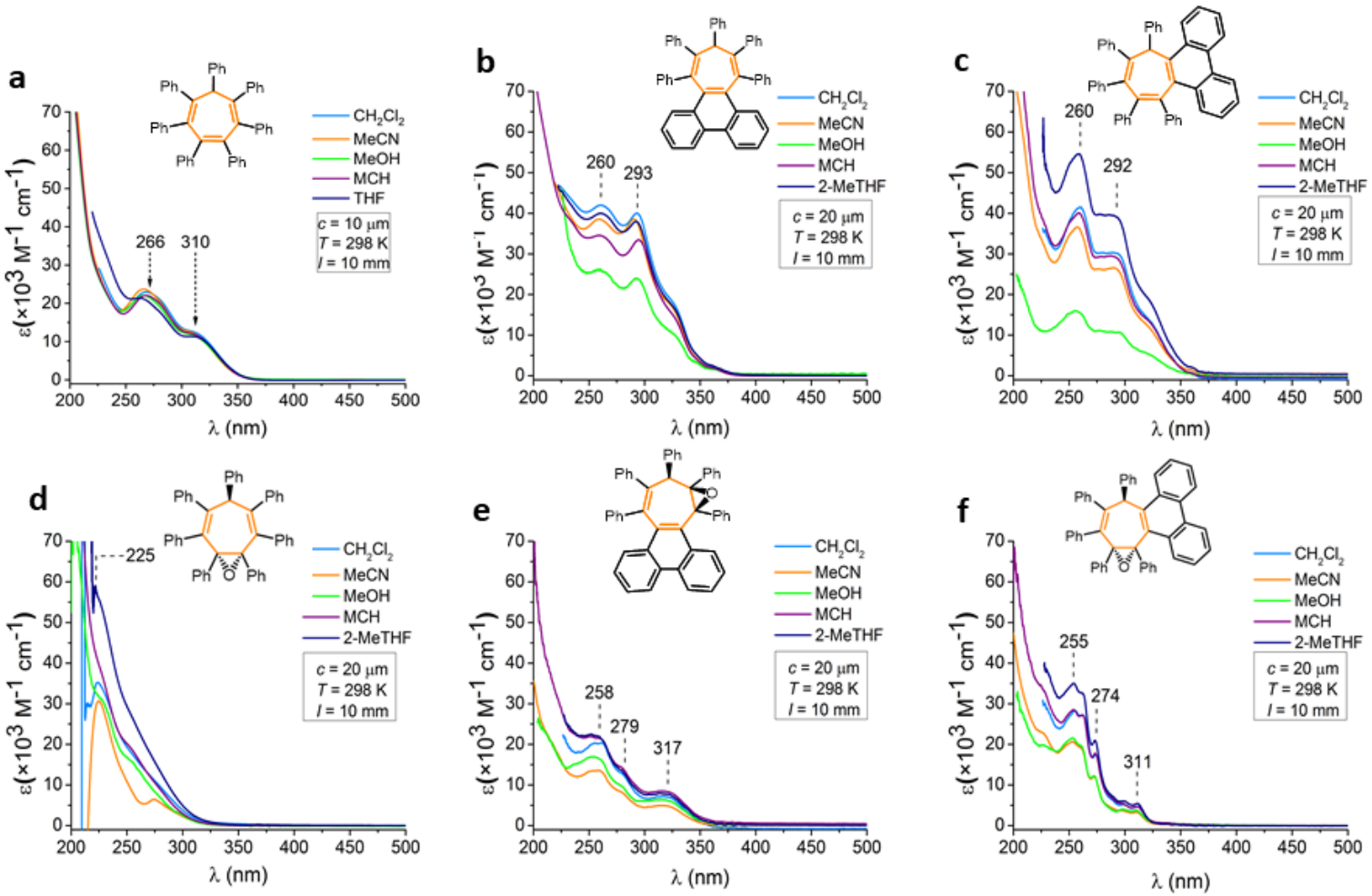

Figure 2.26. UV-Vis absorption spectra of solutions of a) **Ph_7C_7H** b) ***sym*-phenPh_5C_7H** c) ***asym*-phenPh_5C_7H**, d) **Ph_7C_7H-O** e) ***sym*-phenPh_5C_7H-O**, f) ***asym*-phenPh_5C_7H-O** in a series of apolar and polar media.

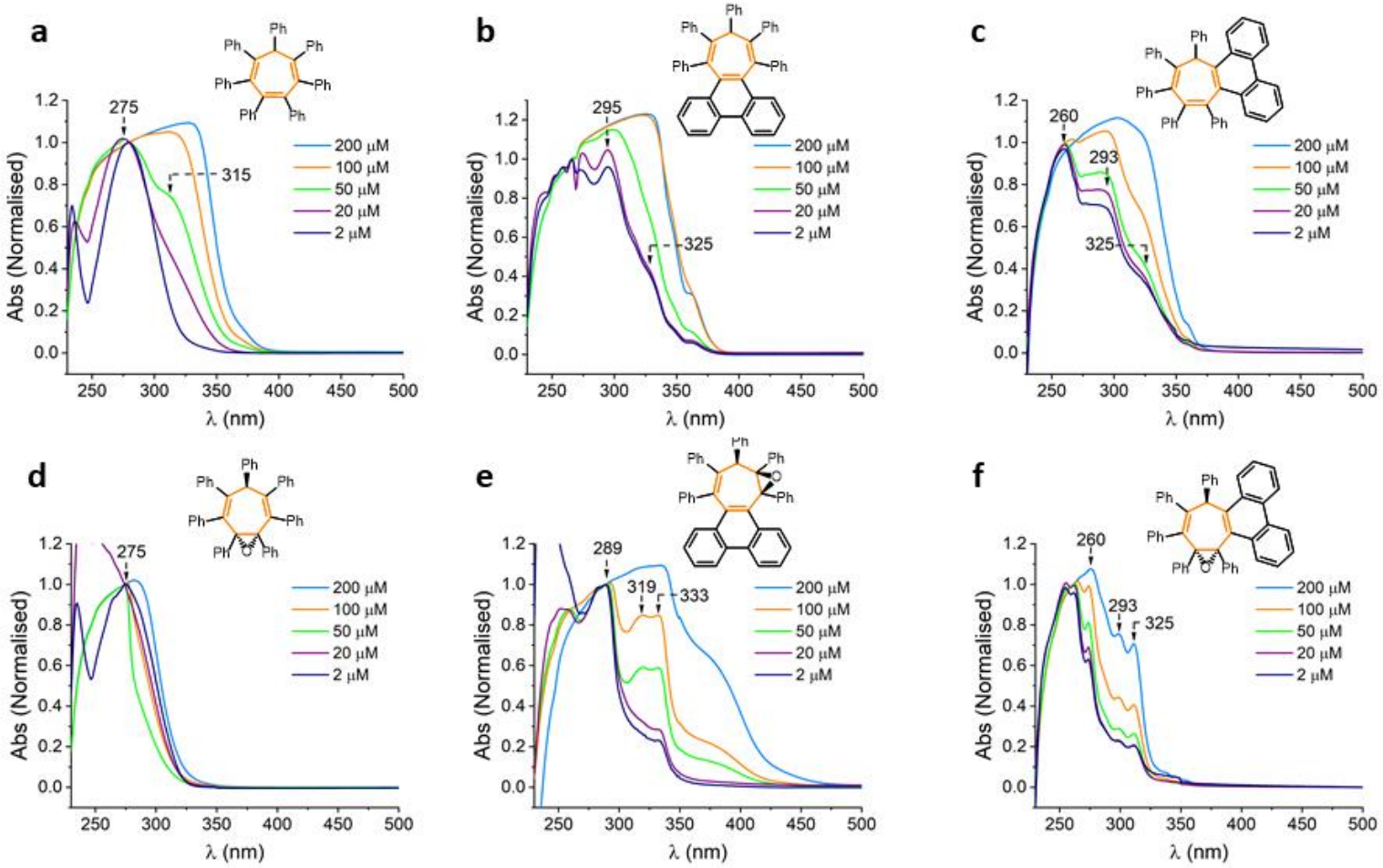

Figure 2.27. UV-Vis absorption spectra of solutions of a) **Ph_7C_7H** b) ***sym*-phenPh_5C_7H** c) ***asym*-phenPh_5C_7H**, d) **Ph_7C_7H-O** e) ***sym*-phenPh_5C_7H-O**, f) ***asym*-phenPh_5C_7H-O** at a series of concentrations in 2-MeTHF.

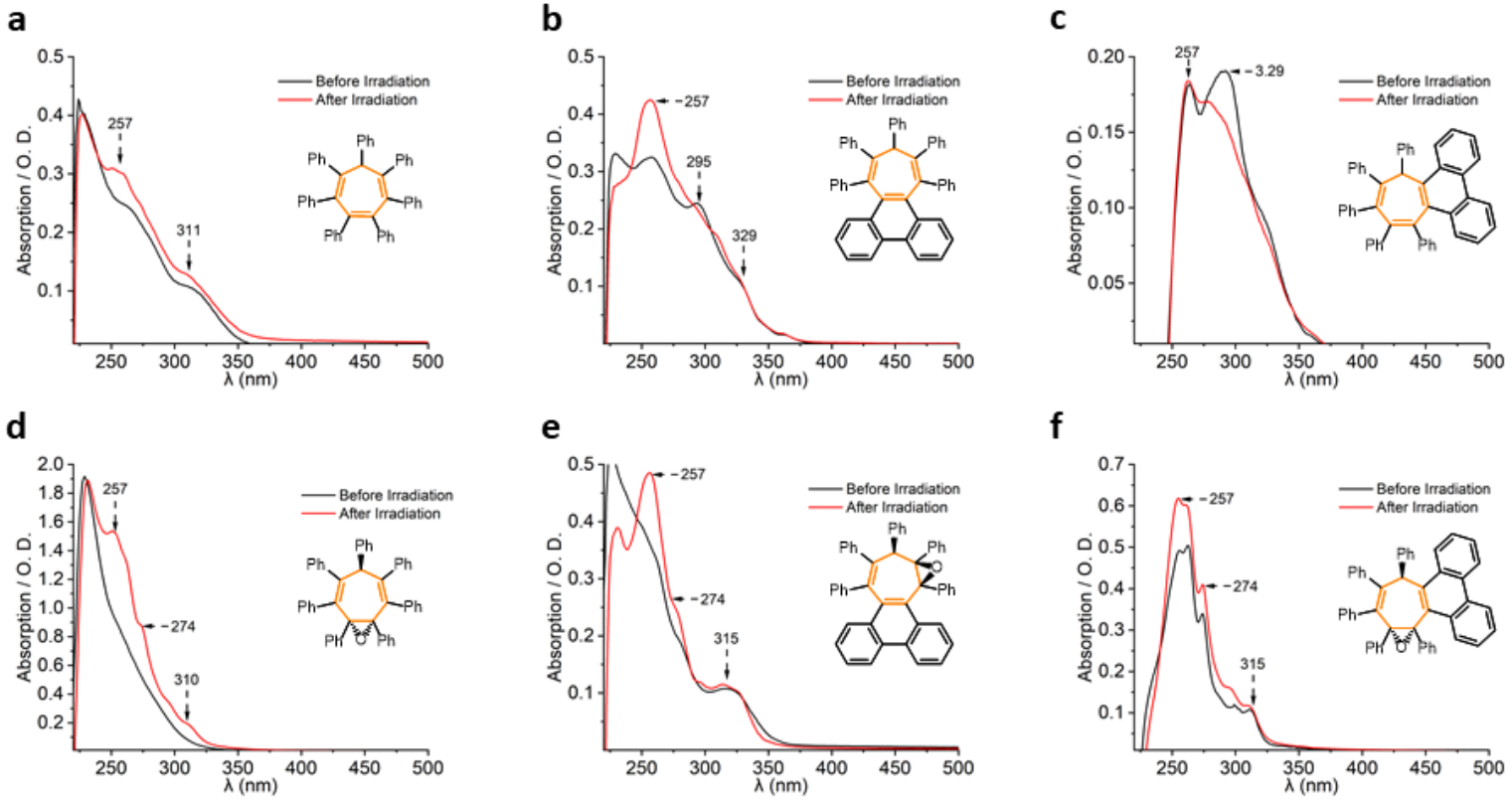

Figure 2.28. . UV-Vis absorption spectra of solutions of a) **Ph_7C_7H** b) ***sym*-phenPh_5C_7H** c) ***asym*-phenPh_5C_7H**, d) **Ph_7C_7H-O** e) ***sym*-phenPh_5C_7H-O**, f) ***asym*-phenPh_5C_7H-O** in MeCN before and after irradiation under 4.0 eV light for 10 min for d-f and 1h for a-c.

2.4.4 Variable-Temperature Fluorescence

Samples for VT fluorescence were prepared using 200 μM 2-MeTHF stock solutions. The desired quantity was measured into a vial, evaporated to dryness, then the solid residue diluted to 20 μM and 2 μM concentration in the solvent used for the measurements. Anhydrous 2-MeTHF were used as the solvent systems, because they form stable organic glasses which are UV-vis transparent at low temperatures. The samples were always kept at each temperature for at least 10 min to equilibrate prior to recording the spectra. The results of VT fluorescence are summarized in Figures 2.29 – 2.32.

Figure 2.29 shows the VT fluorescence spectra of all compounds at 20 μM, compared to the lower concentration 2 μM seen in Figure 2.2. Increasing the concentration of ***asym*-phenPh$_5$C$_7$H** to 20 μM results in a broad bathochromic shift in the emission spectra, shifting E_{max} from 3.33 eV to 2.71 eV at 130 K. This bathochromic shift is indicative of ground-state intermolecular dimer formation and interestingly is only observed in ***asym*-phenPh$_5$C$_7$H**. At 90 K, highly vibronic emission is observed for ***asym*-phenPh$_5$C$_7$H**, showing vibronic emission indicative of a phenanthrene dimer species. The X-ray crystal packing for ***asym*-phenPh$_5$C$_7$H (**Figure 2.19) suggests intermolecular CH-π interactions between the phenanthrene rings may occur. The formation of these dimers at high concentration is highly likely and would explain the bathochromic shift observed in the luminescence only at higher concentrations. Significantly increasing the concentration of each sample to 200 μM (Figure 2.32) does not show any dimerization in the other molecular rotors, 2 μM is an ideal concentration to compare the photoluminscent properties of these compounds to ensure monomeric behaviour.

The solid-state photoluminescence of carbocycles **Ph$_7$C$_7$H, Ph$_7$C$_7$H-O**, ***sym*-phenPh$_5$C$_7$H**, ***asym*-phenPh$_5$C$_7$H**, ***sym*-phenPh$_5$C$_7$H-O** and ***asym*-phenPh$_5$C$_7$H-O**) were measured at a temperature range (290-90K). The molecules were dispersed as a 1% optically clear Zeonex matrix and the results are shown in Figure 2.33. The 1% Zeonex matrix disperses the fluorophores and prevents aggregation, excluding intermolecular interactions in photoluminscent measurements. We see that ***asym*-phenPh$_5$C$_7$H** now shows monomeric behaviours similar to at 2 μM. Furthermore, the vibronic emission

associate with the epoxides remains unchanged supporting our hypothesis of photocyclisation rather than any intermolecular dimerization effects resulting in the vibronic emission.

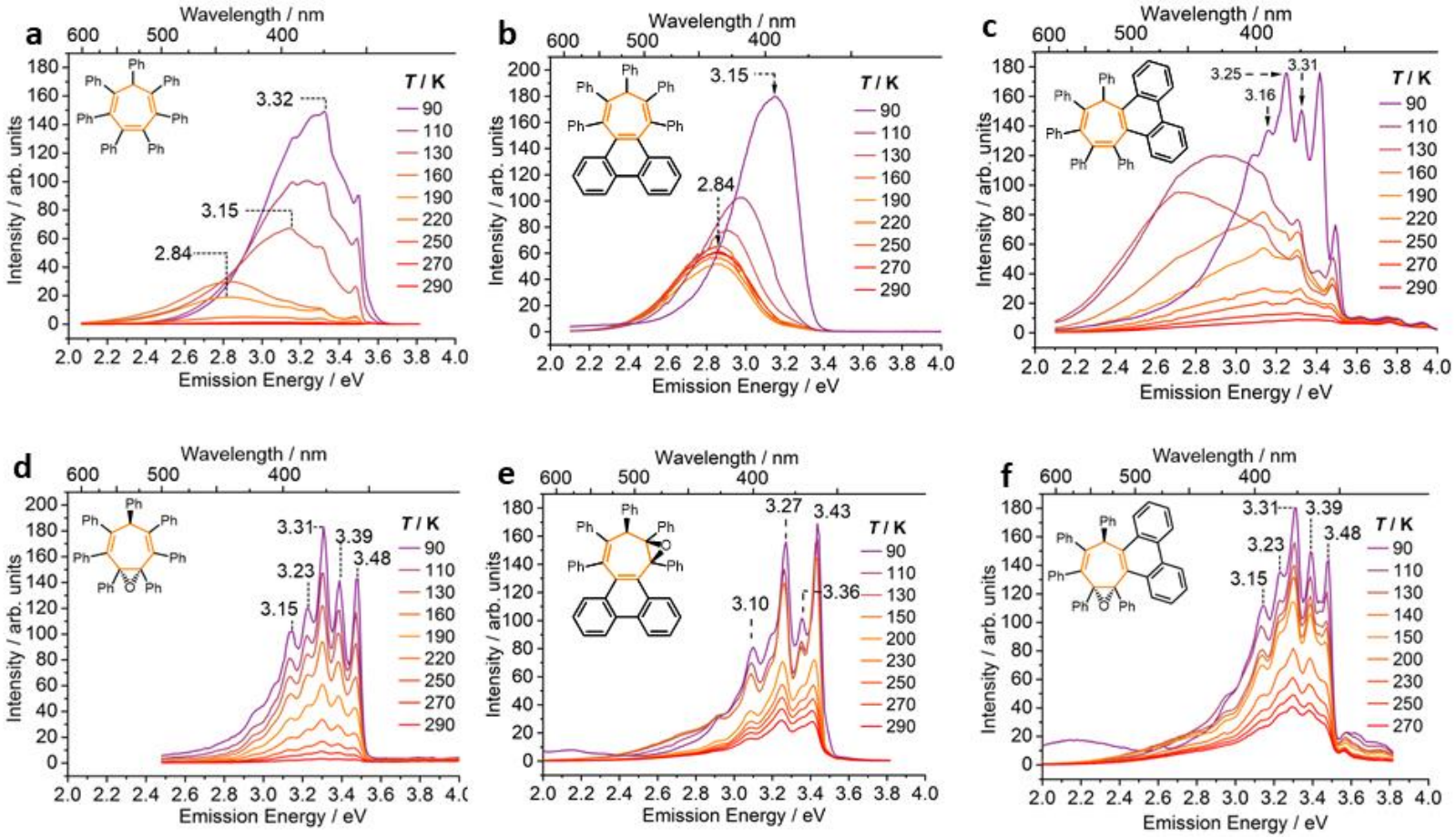

Figure 2.29. VT fluorescence spectra of 2-MeTHF solutions (l = 10 mm, T = 90–290 K) of a) **Ph_7C_7H** λ_{ex} = 315 nm, c = 10 μM; b) ***sym*-phenPh_5C_7H** λ_{ex} = 300 nm, c = 20 μM; c) ***asym*-phenPh_5C_7H** λ_{ex} = 315 nm, c = 20 μM; d) **Ph_7C_7H-O** λ_{ex} = 280 nm, c = 20 μM; e) ***sym*-phenPh_5C_7H-O** λ_{ex} = 315 nm, c = 20 μM; f) ***asym*-phenPh_5C_7H-O** λ_{ex} = 315 nm, c = 20 μM. Inset shown in all panel (a): Legend for temperatures in all panels.

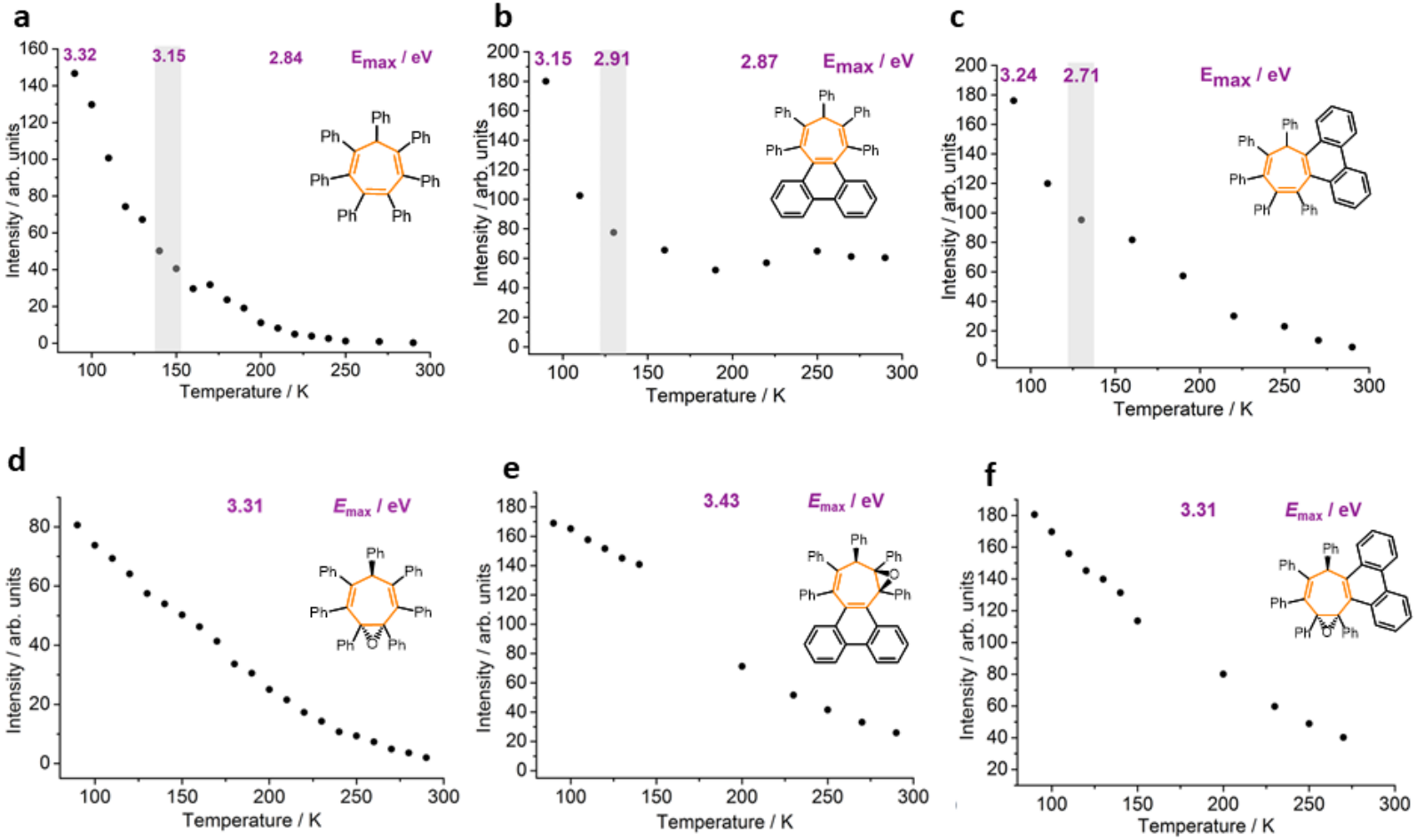

Figure 2.30. Peak emission intensities from VT fluorescence spectra of 2-MeTHF solutions (l = 10 mm, T = 90–290 K) of a) **Ph$_7$C$_7$H** λ_{ex} = 315 nm, c = 10 μM; b) ***sym*-phenPh$_5$C$_7$H** λ_{ex} = 300 nm, c = 20 μM; b) ***asym*-phenPh$_5$C$_7$H** λ_{ex} = 315 nm, c = 20 μM; d) **Ph$_7$C$_7$H-O** λ_{ex} = 280 nm, c = 20 μM; e) ***sym*-phenPh$_5$C$_7$H-O** λ_{ex} = 315 nm, c = 20 μM; f) ***asym*-phenPh$_5$C$_7$H-O** λ_{ex} = 315 nm, c = 20 μM. The emission energy of the most intense peak at each temperature was chosen. These energies are given on each panel. The most intense emission peaks of **Ph$_7$C$_7$H** and ***sym*-phenPh$_5$C$_7$H** vary with temperature, so the plots are divided into sections corresponding to different peak energies.

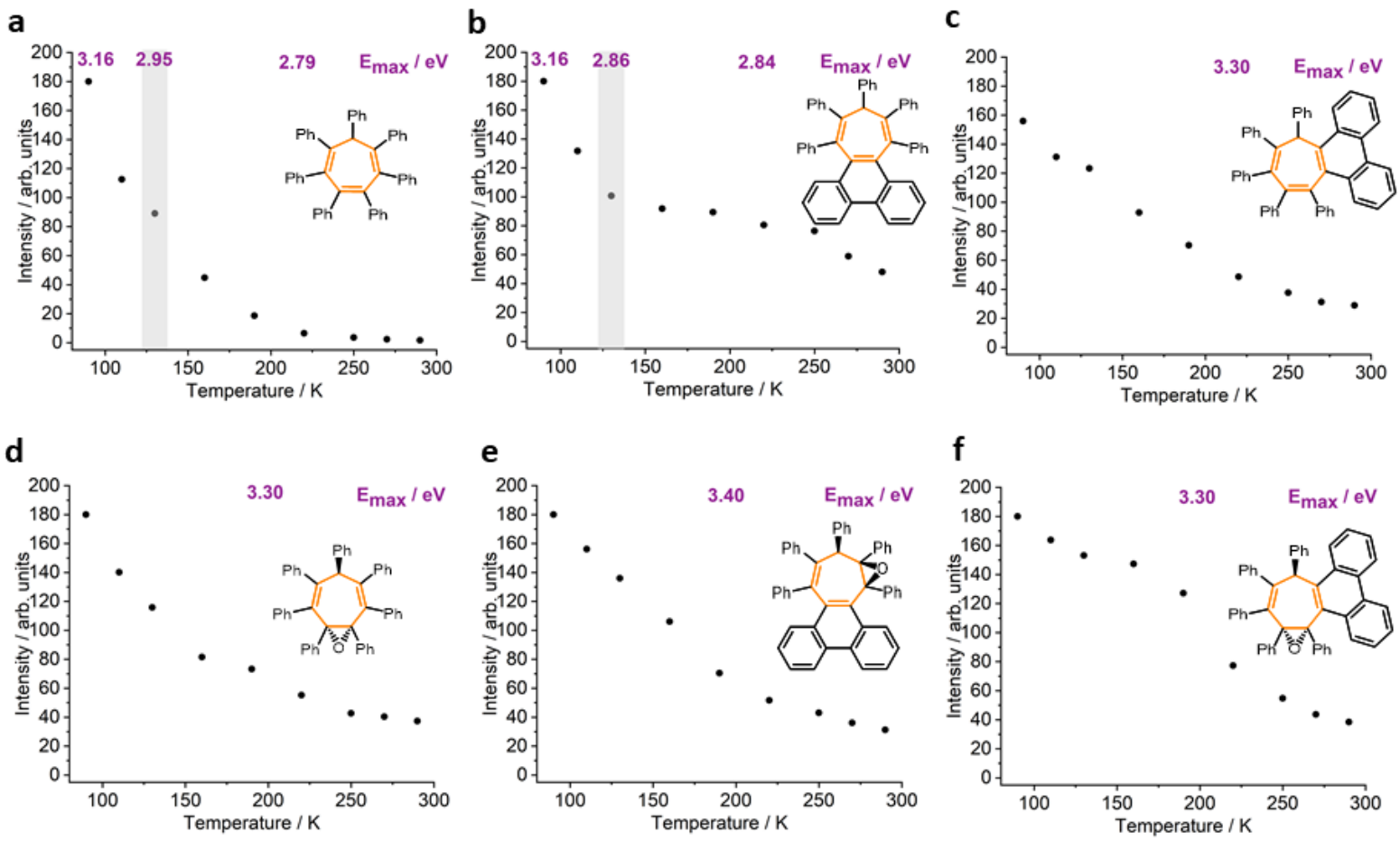

Figure 2.31. Peak emission intensities from VT fluorescence spectra of 2-MeTHF solutions (l = 10 mm, T = 90–290 K, c = 2 μM) of a) **Ph_7C_7H** λ_{ex} = 315 nm; b) ***sym*-phenPh_5C_7H** λ_{ex} = 300 nm; c) ***asym*-phenPh_5C_7H** λ_{ex} = 315 nm; d) **Ph_7C_7H-O** λ_{ex} = 280 nm; e) ***sym*-phenPh_5C_7H-O** λ_{ex} = 315 nm; e) ***asym*-phenPh_5C_7H-O** λ_{ex} = 315 nm. The emission energy of the most intense peak at each temperature was chosen. These energies are given on each panel. The most intense emission peaks of **Ph_7C_7H** and ***sym*-phenPh_5C_7H** vary with temperature, so the plots are divided into sections corresponding to different peak energies.

200 µM samples in 2-MeTHF were measured to observe any possible intermolecular dimerization and possible ACQ. ***asym*-phenPh$_5$C$_7$H** (Figure 2.32b) shows signals indicative of phenanthrene dimer species.

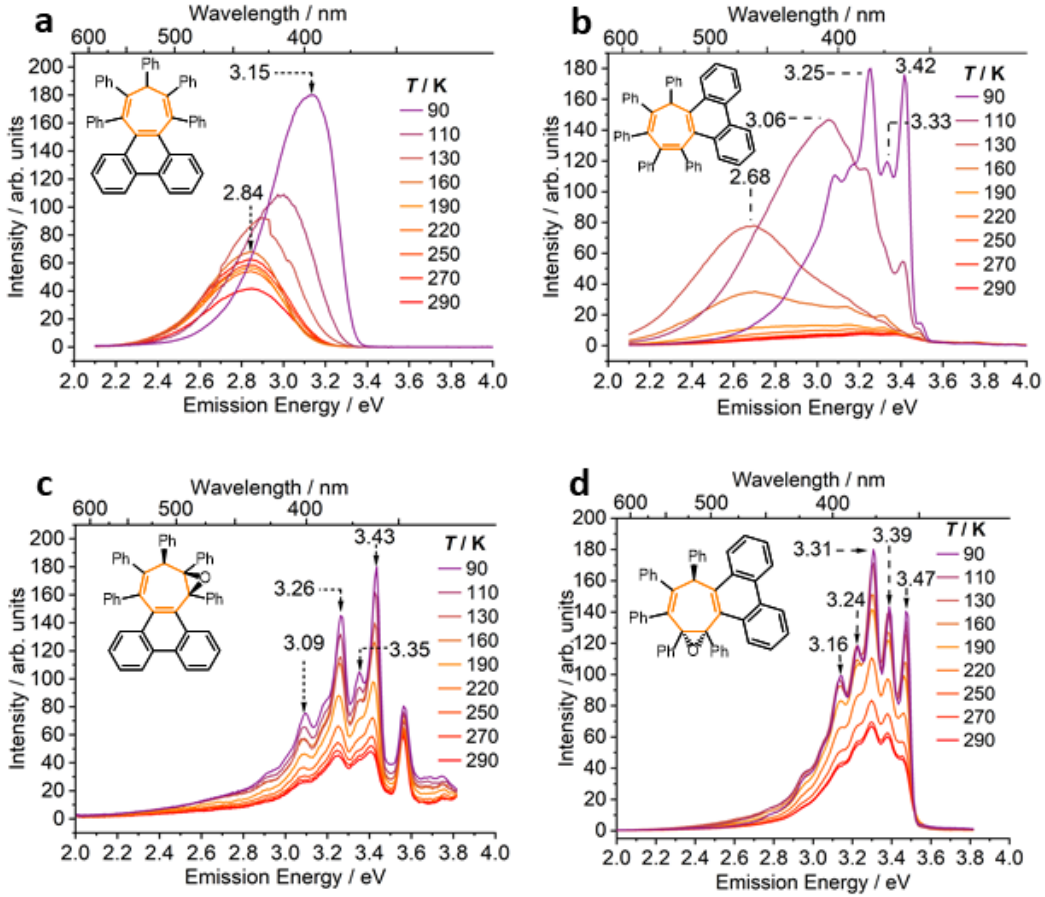

Figure 2.32. VT fluorescence spectra of 2-MeTHF solutions (l = 10 mm, T = 90–290 K) of (a) ***sym*-phenPh$_5$C$_7$H** λ_{ex} = 300 nm, c = 200 µM; (b) a***sym*-phenPh$_5$C$_7$H** λ_{ex} = 300 nm, c = 200 µM; (c) ***sym*-phenPh$_5$C$_7$H-O** λ_{ex} = 315 nm, c = 200 nM; (d) ***asym*-phenPh$_5$C$_7$H-O** λ_{ex} = 315 nm, c = 200 µM. Inset in panel (a): Legend for temperatures in all panels.

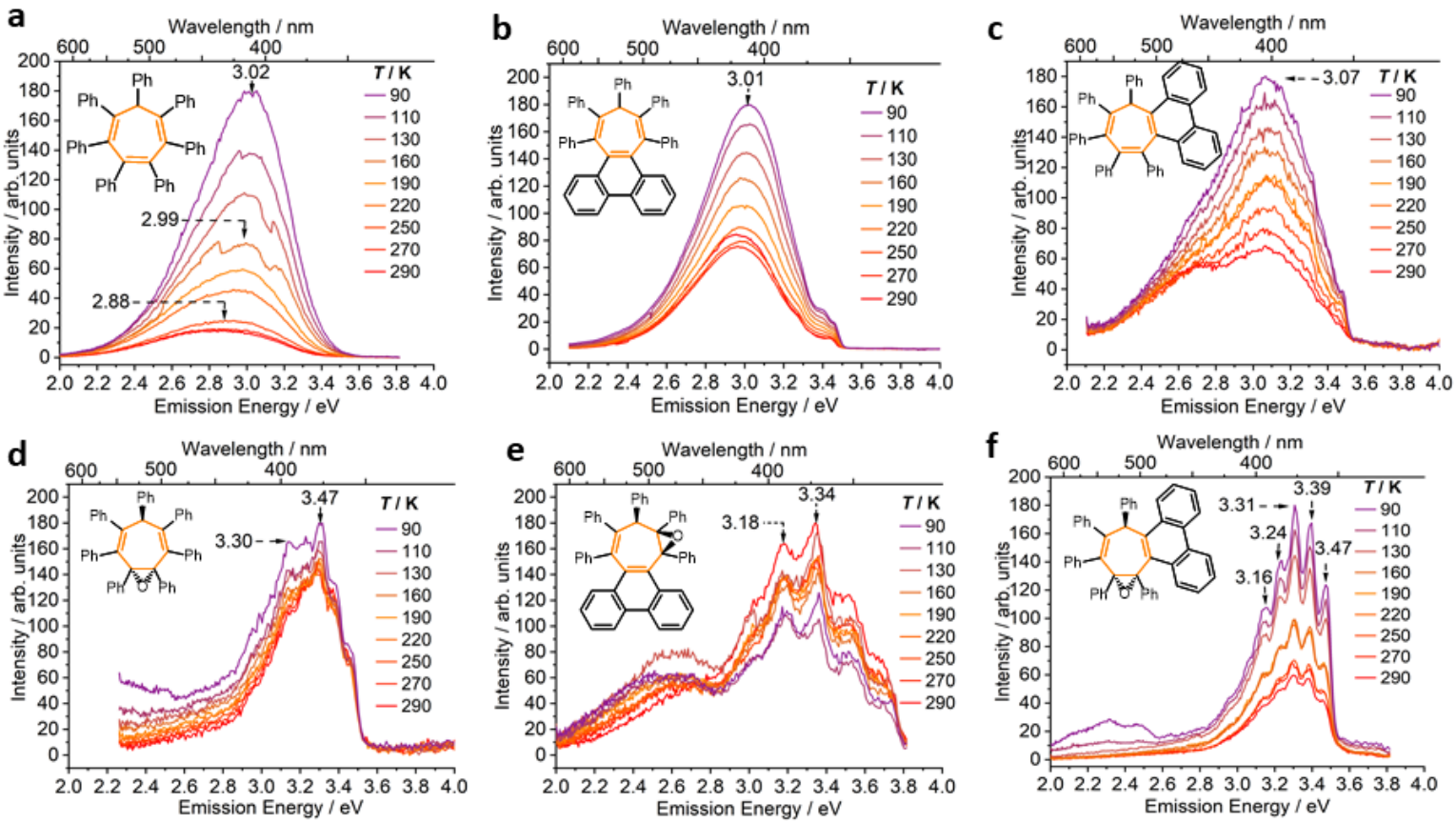

Figure 2.33. VT fluorescence spectra of 1% Zeonex matrices containing (a) **Ph_7C_7H** λ_{ex} = 315 nm; (b) ***sym*-$phenPh_5C_7H$** λ_{ex} = 300 nm; (c) ***asym*-$phenPh_5C_7H$** λ_{ex} = 315 nm; (d) **Ph_7C_7H-O** λ_{ex} = 280 nm; (e) ***sym*-$phenPh_5C_7H$-O** λ_{ex} = 315 nm; (f) ***asym*-$phenPh_5C_7H$-O** λ_{ex} = 315 nm. Inset in all panels (a): Legend for temperatures in all panels.

2.5.6 Fluorescence Solvatochromism

Fluorescence spectra were acquired (Figure 2.34) for solutions of different polarities. The samples for fluorescence were prepared using 200 μM CH_2Cl_2 stock solutions. The desired quantity was measured into a vial, evaporated to dryness, then the solid residue diluted to 20 μM concentration in the solvent used for the measurements. Although the solvents used cover a large range of polarities, the change in emission wavelength is below 0.1 eV, with the exception of ***asym*-phenPh$_5$C$_7$H** in methylcyclohexane (MCH) where the fluorescence is slightly more red-shifted. The small magnitude of these differences indicates that the observed emission does not arise from charge transfer states. Such states would be much more influenced by solvent polarity and emission wavelength would vary by a larger amount.

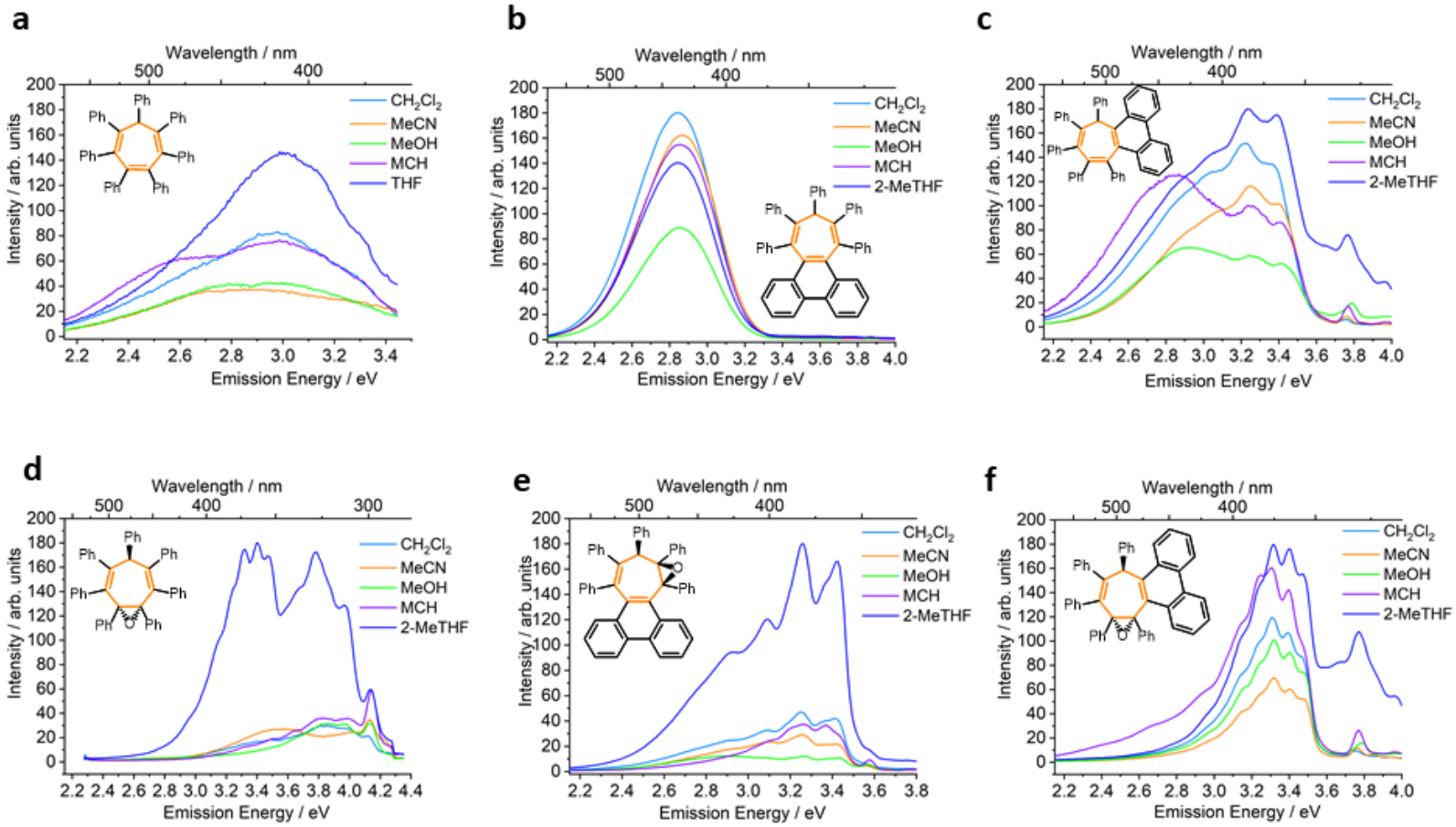

Figure 2.34. Fluorescence Solvatochromism of a) **Ph_7C_7H** b) ***sym*-phenPh_5C_7H** c) ***asym*-phenPh_5C_7H** d) **Ph_7C_7H-O** e) ***sym*-phenPh_5C_7H-O** f) ***asym*-phenPh_5C_7H-O** in MCH, CH_2Cl_2, MeOH, MeCN and 2-MeTHF or THF.

2.5.6 Phenanthrene

Fluorescence spectra were acquired for molecular phenanthrene. A concentration study (Figure 2.36a) demonstrated the formation of phenanthrene dimers at concentrations >20 μM showing vibronic emission similar to high concentration samples of ***asym*-phenPh$_5$C$_7$H**. Variable temperature fluorescent spectroscopy of a 1% ZEONEX film (Figure 2.36b) shows similar vibronic structure and E_{max} to both 2 μM and 20 μM 2-MeTHF samples (Figure 2.36c/d) with no observed bathochromic shift as the temperature decreases. This suggests that forming phenanthrene like units in our molecular rotors *via* photocyclisation, may give rise to vibronic emission from exciting the reversible intermediate form **IM**. Also, this indicates that the formation of vibronic emission in epoxides is a result of the more favourable formation of phenanthrene moieties.

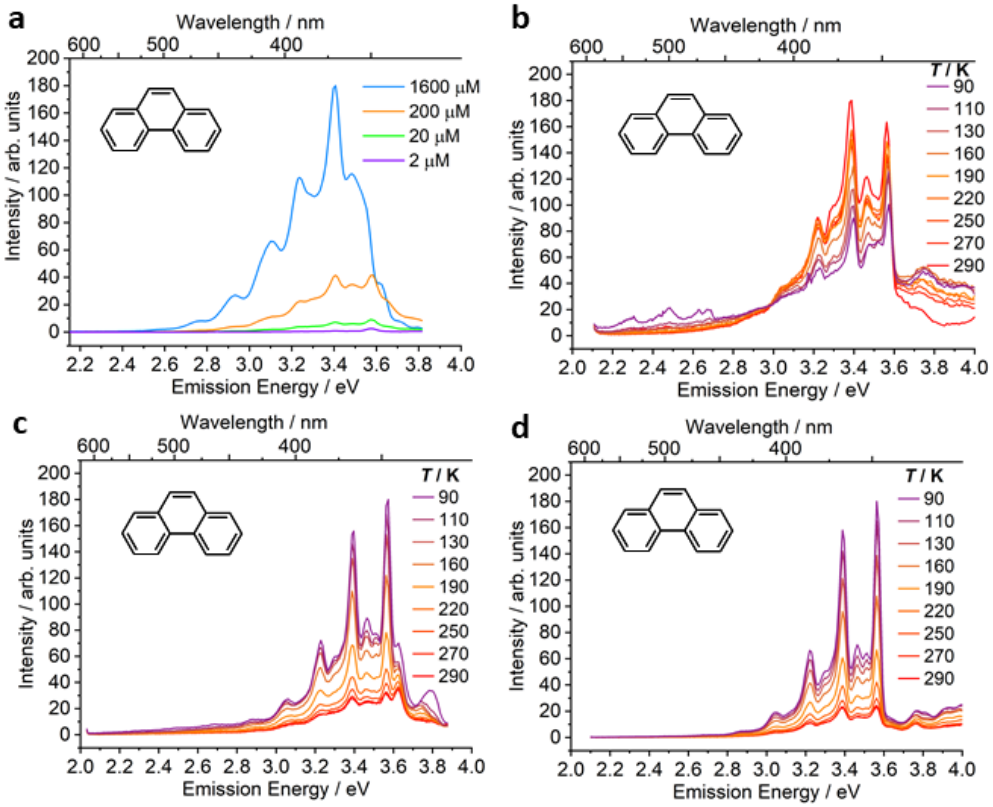

Figure 2.36. (a) Fluorescence spectra of **phenanthrene** (*l* = 10 mm, *T* = 290 K); Insert in panel (a): Legend for concentration. VT fluorescence spectra of phenanthrene in a zeonex film b) **phenanthrene** λ_{ex} = 300 nm. VT fluorescence spectra of phenanthrene in a 2-MeTHF solutions (*l* = 10 mm, *T* = 90–290 K) of c) **phenanthrene** λ_{ex} = 310 nm, *c* = 20 μM; d) **phenanthrene** λ_{ex} = 300 nm, *c* = 20 μM; Inset in panel (b-d): Legend for temperatures.

2.5.7 Photooxidation

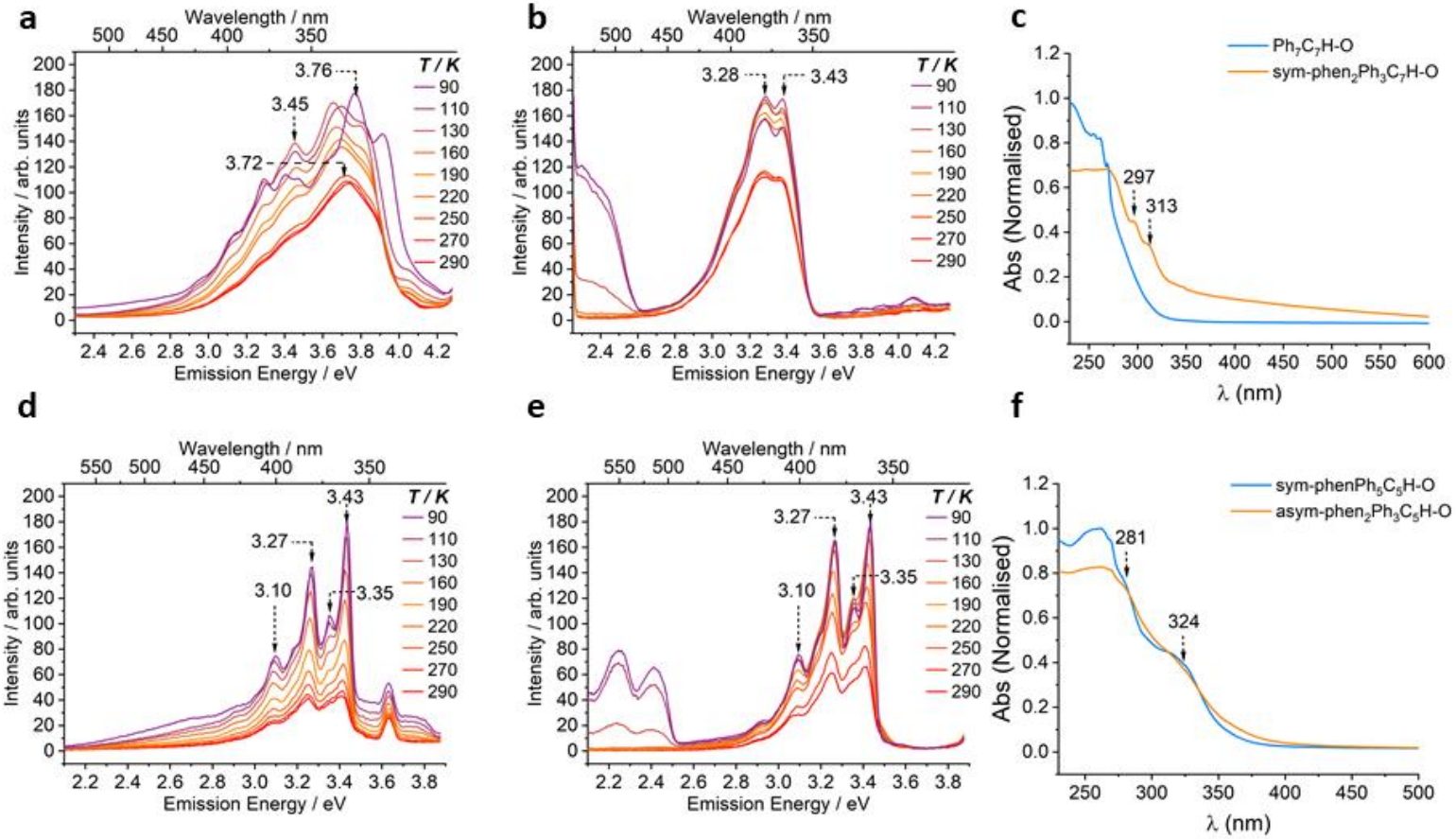

Figure 2.37. VT fluorescence spectra of photooxidised molecular rotors in a 2-MeTHF solutions (l = 10 mm, T = 90–290 K) of (a) ***sym*-phen$_2$Ph$_3$C$_7$H-O** λ_{ex} = 310 nm, c = 20 μM; (d) a***sym*-phen$_2$Ph$_3$C$_7$H-O** λ_{ex} = 310 nm, c = 20 μM; VT fluorescence spectra of photooxidised molecular rotors 1% Zeonex film of (b) ***sym*-phen$_2$Ph$_3$C$_7$H-O** λ_{ex} = 310 nm, e) a***sym*-phen$_2$Ph$_3$C$_7$H-O** λ_{ex} = 310 nm; Inset in panel (a,b,d and e): Legend for temperatures. UV-absorption spectra in 1% Zeonex film of c) ***sym*-phen$_2$Ph$_3$C$_7$H-O** f) a***sym*-phen$_2$Ph$_3$C$_7$H-O**.

2.5.8 Time-Correlated Single Photon Counting (TCSPC)

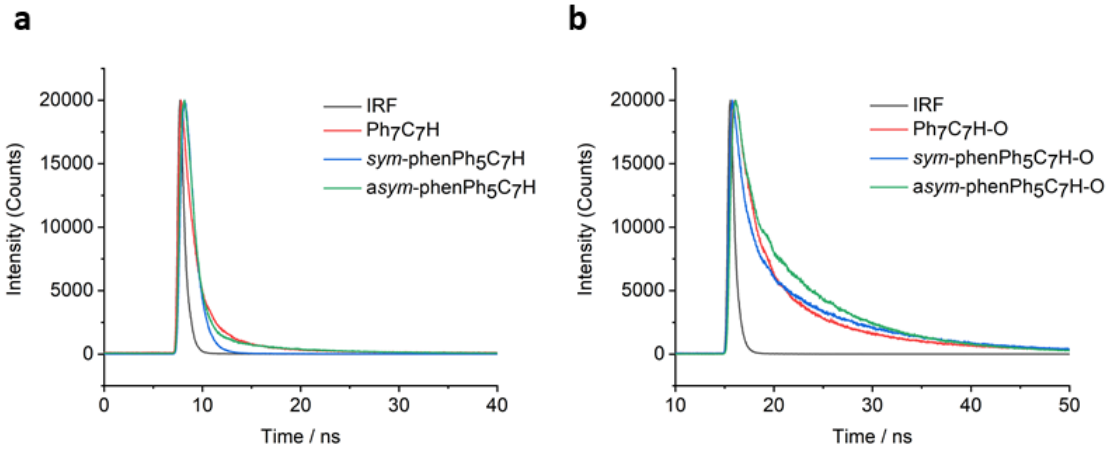

Figure 2.38. TCSPC decays of a) **Ph_7C_7H**, ***sym*-$phenPh_5C_7H$** and ***asym*-$phenPh_5C_7H$** b) **Ph_7C_7H-O**, ***sym*-$phenPh_5C_7H$-O** and ***asym*-$phenPh_5C_7H$-O**. Measured as 2 μM solutions in 2-MeTHF.

Table 6. Lifetimes from the exponential fits for the decays of molecular rotors in 2-MeTHF.

Rotor	χ^2	I(t) = a1*exp(- τ/τ1) + a2*exp(-τ/τ2)) + a3*exp(-τ/τ3)					
		a1	τ1 /ns	a2	τ2 /ns	a3	τ3 /ns
C_7Ph_7H-O	6.37	0.62325	0.89228	0.29718	5.96335	0.07957	16.02825
***sym*-$phenPh_5C_7H$-O**	4.33	0.03766	1.47670	0.93076	0.06968	0.03158	11.47156
asym-$phenPh_5C_7H$-O	2.31	0.61532	0.61737	0.37861	8.29627	0.00607	19.85027
C_7Ph_7H	6.02	0.99999	0.00336	0.00001	1.63405	0.00000	10.43118
***sym*-$phenPh_5C_7H$**	1.26	0.00000	4.04050	0.00060	0.78347	0.99940	0.00352
***asym*-$phenPh_5C_7H$**	2.65	0.81139	0.02360	0.00174	8.04750	0.18687	0.71580

2.5.9 Computational analysis

Ground state geometry optimisation of ***sym*-$phen_2Ph_3C_7H$-O** was conducted *in vacuo* employing DFT with the exchange-correlation functional ωB97X-D (long-range corrected and including an empirical dispersion correction) and a 6-31G* basis set for all atoms. Excited electronic states were computed using linear-response time-dependent density functional theory (LR-TDDFT) at the ωB97X-D/6-31G* level of theory. The nature of all stationary points located was verified by harmonic vibrational frequency calculations at the same level of theory. Results obtained with LR-TDDFT were compared with the wavefunction-based second-order algebraic diagrammatic construction method (ADC(2)), used along with the SVP basis set. ADC(2) calculations were performed with the frozen core and resolution of identity

approximations. All DFT/LR-TDDFT calculations were performed with the Gaussian09 software,[25] while we employed the Turbomole 7.3.1 program package[26] for the ADC(2) calculations. Molecular representations were produced with VMD 1.9.2 (absolute values for the orbital isosurfaces was 0.05).

The ADC(2)/SVP S_1/S_0 vertical emission energy at the LR-TDDFT/ωB97X-D/6-31G* optimised S_1 geometry of ***sym*-phen$_2$Ph$_3$C$_7$H-O** is 3.05 eV (oscillator strength: 0.0193), a value in close agreement with the 2.94 eV (oscillator strength: 0.0175) obtained at the LR-TDDFT/ωB97X-D/6-31G* level of theory. The two methods also provide a very similar electronic character for the S_1 electronic state.

2.6. References

1. G. v. Bünau, *Berichte der Bunsengesellschaft für Phys. Chemie*, 1970, **74**, 1294–1295.
2. M. Fakis, D. Anestopoulos, V. Giannetas and P. Persephonis, *J. Phys. Chem. B*, 2006, **110**, 24897–24902.
3. A. Y. Sosorev, O. D. Parashchuk, S. A. Zapunidi, G. S. Kashtanov, I. V. Golovnin, S. Kommanaboyina, I. F. Perepichka and D. Y. Paraschuk, *Phys. Chem. Chem. Phys.*, 2016, **18**, 4684–4696.
4. S. R. Amrutha and M. Jayakannan, *J. Phys. Chem. B*, 2008, **112**, 1119–1129.
5. Y. Huang, J. Xing, Q. Gong, L.-C. Chen, G. Liu, C. Yao, Z. Wang, H.-L. Zhang, Z. Chen and Q. Zhang, *Nature. Commun.*, 2019, **10**, 169
6. S. M. Borisov and O. S. Wolfbeis, *Chem. Rev.*, 2008, **108**, 423–461.
7. S. W. Thomas, G. D. Joly and T. M. Swager, *Chem. Rev.*, 2007, **107**, 1339–1386.
8. C. Zhu, R. T. K. Kwok, J. W. Y. Lam and B. Z. Tang, *ACS Appl. Bio Mater.*, 2018, **1**, 1768–1786.
9. X. Zhang, T. Liu, Q. Li, M. Li and L. Du, *Front. Chem.*, 2019, **7**, 54.
10. Y. Hong, J. W. Y. Lam and B. Z. Tang, *Chem. Soc. Rev.*, 2011, **40**, 5361–5388.
11. J. Mei, N. L. C. Leung, R. T. K. Kwok, J. W. Y. Lam and B. Z. Tang, *Chem. Rev.*, 2015, **115**, 11718–11940.
12. J. Mei, Y. Hong, J. W. Y. Lam, A. Qin, Y. Tang and B. Z. Tang, *Adv. Mater.*, 2014, **26**, 5429–5479.
13. J. Sturala, M. K. Etherington, A. N. Bismillah, H. F. Higginbotham, W. Trewby, J. A. Aguilar, E. H. C. Bromley, A.-J. Avestro, A. P. Monkman and P. R. McGonigal, *J. Am. Chem. Soc.*, 2017, **139**, 17882–17889.
14. L. Le Bras, C. Adamo and A. Perrier, *J. Phys. Chem. C*, 2017, **121**, 25603–25616.

15. Y.-J. Gao, X.-P. Chang, X.-Y. Liu, Q.-S. Li, G. Cui and W. Thiel, *J. Phys. Chem. A*, 2017, **121**, 58.

16. Z. Zhou, S. Xie, X. Chen, Y. Tu, J. Xiang, J. Wang, Z. He, Z. Zeng and B. Zhong Tang, *J. Am. Chem. Soc*., 2019, **141**, 9803-9807.

17. H. Tong, Y. Hong, Y. Dong, M. Häußler, J. W. Y. Lam, Z. Li, Z. Guo, Z. Guo and B. Z. Tang, *Chem. Commun.*, 2006, **35**, 3705–3707.

18. N. B. Shustova, T. C. Ong, A. F. Cozzolino, V. K. Michaelis, R. G. Griffin and M. Dincă, *J. Am. Chem. Soc.*, 2012, **134**, 15061–15070.

19. M. P. Aldred, C. Li and M. Q. Zhu, *Chem. - A Eur. J.*, 2012, **18**, 16037–16045.

20. E. A. Chandross and H. T. Thomas, *J. Am. Chem. Soc.*, 1972, **94**, 2421–2424.

21. D. K. K. Liu and L. R. Faulkner, *J. Am. Chem. Soc.*, 1978, **100**, 2635–2639.

22. Y. Cai, L. Du, K. Samedov, X. Gu, F. Qi, H. H. Y. Sung, B. O. Patrick, Z. Yan, X. Jiang, H. Zhang, J. W. Y. Lam, I. D. Williams, D. L. Phillips, A. Qin and B. Zhong, Chem. Sci., 2018, **9**, 4662-4670.

23. H. Tian and S. Yang, *Chem. Soc. Rev*., 2004, **33**, 85-97.

24. H. J. Reich, *J. Chem. Educ.*, 1995, **72**, 1086.

25. M. J. Frisch, G. W. Trucks, H. B. Schlegel, G. E. Scuseria, M. A. Robb, J. R. Cheeseman, G. Scalmani, V. Barone, G. A. Petersson, H. Nakatsuji, X. Li, M. Caricato, A. Marenich, J. Bloino, B. G. Janesko, R. Gomperts, B. Mennucci, H. P. Hratchian, J. V. Ortiz, A. F. Izmaylov, J. L. Sonnenberg, D. Williams-Young, F. Ding, F. Lipparini, F. Egidi, J. Goings, B. Peng, A. Petrone, T. Henderson, D. Ranasinghe, V. G. Zakrzewski, J. Gao, N. Rega, G. Zheng, W. Liang, M. Hada, M. Ehara, K. Toyota, R. Fukuda, J. Hasegawa, M. Ishida, T. Nakajima, Y. Honda, O. Kitao, H. Nakai, T. Vreven, K. Throssell, J. A. Montgomery Jr, J. E. Peralta, F. Ogliaro, M. Bearpark, J. J. Heyd, E. Brothers, K. N. Kudin, V. N. Staroverov, T. Keith, R. Kobayashi, J. Normand, K. Raghavachari, A. Rendell, J. C. Burant, S. S. Iyengar, J. Tomasi, M. Cossi, J. M. Millam, M. Klene, C. Adamo, R. Cammi, J. W. Ochterski, R. L. Martin, K. Morokuma, O. Farkas, J. B. Foresman and D. J. Fox, *Gaussian, Inc., Wallingford CT*, 2016.

26. F. Furche, R. Ahlrichs, C. Hättig, W. Klopper, M. Sierka and F. Weigend, *Wiley Interdiscip. Rev. Comput. Mol. Sci.*, 2014, **4**, 91–100.

CHAPTER 3

TWISTED TROPYLIUMS.

Synopsis

This chapter discusses the synthesis of a range of novel hepta-substituted-cycloheptatrienes and their tropylium cation derivatives. The CHTs are fitted with a range of polyaromatics moieties that induce conformational twist in an otherwise planar tropylium cation. The physical properties were measured, and the presence of a stable triplet state was studied to investigate the role as potential single fission molecules.

Acknowledgements

The following people are gratefully acknowledged for their contribution to this chapter: Dr Abhiji Malick for his synthetic contributions. Dr Dimitry S. Yufit solved all the X-ray crystal structures. Dr Marc Etherington with supporting the ICCD measurements. Dr Paul McGonigal for the modeling.

3.1 Introduction

The optical, magnetic and electronic properties of polyaromatic hydrocarbons are directly related to their electronic structure and can be tailored by modifying the shape, size and π-conjugated backbone.[1–5] Often overlooked in these systems is the twisting and curvature that PAHs can adopt which can have dramatic influence of their photophysical properties by directly modifying the HOMO-LUMO gap[6]. Molecular twisting of PAHs affects aromaticity[7], energy levels[8] and π-orbital overlap[9] as a result of orbital hybridization, leading to π-bonds having more sigma character.[10] This hybridization results in a small increase in the HOMO energy and a small decrease in the LUMO energy.

Acenes, a series of linear fused benzenes, can be classified as one-dimensional planar nanographenes, however functionalization can induce massive twisting of their conformation and have been the main sub-class of compounds used to study the photophysical effects of twisting. Charge localization[11,12] and chiroptic properties[13–15] have all been investigated with acenes derivatives and very recent reports also show that the twisting of pyrenes[16] and graphene nanoribbons[17] results in significant modification in their electronic properties. Furthermore, computational methods have shown an increase in the twist of polyaromatics results in the reduction in the S^0-T^1 energy gap, making intersystem crossing more accessible and the triplet state more populated. This property shows promise as ideal materials for singlet fission. Control of this twisting allows for access to new optical and electronic properties giving rise to a new series of 'twistacenes' which have found uses in organic field-effect transistors[18] (OFETs), solar cells[19], photodetectors[20] and organic light emitting diodes[21] (OLEDs).

Herein we deviate from the classic PAHs and acenes and investigate a class of tropylium cations that are twisted through modifications of peripheral aromatic groups. These tropylium cations are subjected to high levels of strain resulting in significant conformational twisting. We demonstrate how the increased strain of peripheral groups allows access to less common tropylium isomers and materials with stable-triplet states that may be useful as new singlet-fission materials.

3.2 Results and Discussion

The study of unconventional tropylium isomers has been extremely limited with on few reports discussing details of their properties. In 2016 Kharnaior et al[22] were the first to report a detailed computational study on the relative stabilities of tropylium isomers. It was found that in the case of $\mathbf{C_7H_7^+}$, the conventional aromatic tropylium isomer (**1**) is favoured as the lowest energy conformation. They show that at higher energy concerted isomerizations can yield isomers such as 7-norborna-1,4-dienyl (**3**) and bicyclo[3.20]heptadienyl (**4**) through bicyclic transitions state **TS1** and **TS2** (Figure 3.1). Kharnair *et al*. report the energy minimised structure (MP2) of thirty-four possible isomers of $\mathbf{C_7H_7^+}$ by ionic dissociation of $\mathbf{C_7H_7Br}$ in gas phase. Of these thirty-four theoretical conformations, fifteen isomers are outlined in Scheme 3.7 (Appendix), from most stable to least. To date, no experimental work has been undertaken to isolate and study this concerted isomerization towards unconventional tropylium isomers.

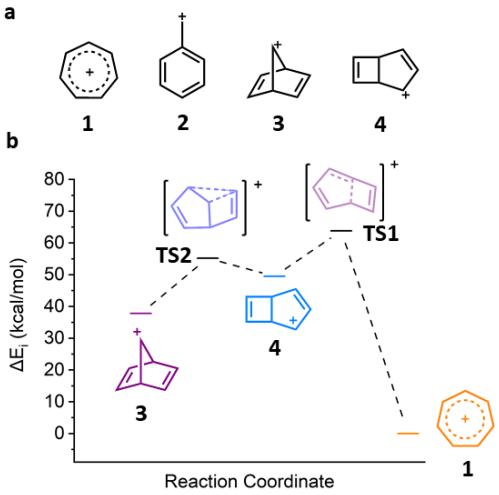

Figure 3.1. MP2/6-311++G(d,p) energy profile of $\mathbf{C_7H_7^+}$ conversion between its isomers relative to the most stable tropylium cation **1**. Figure adopted from calculated energies reported by Kharnaior *et al*.[22]

To further investigate the tropylium cation and its unconventional isomers, we synthesised a range of heptaarylsubstituted cycloheptatrienes (CHT) and heptaaryltropyliums (HATP), derived from previously reported $\mathbf{Ph_7C_7H}$.[23,24] Phenyl substituted CHTs were selected as they adopt a traditional boat-like conformation in the neutral state that is drastically modified upon oxidation as a result of their large steric bulk. In the neutral state, the peripheral phenyl rings of $\mathbf{Ph_7C_7H}$, orientated above and below the central C_7 ring. However, upon oxidation, the central C_7 ring flattens out to adopt a near planar conformation. Pole *et al*.[25] demonstrated that $\mathbf{Ph_7C_7^+}$ is not

completely planar, reporting either side of the central CHT ring sits between 8-11˚ out of plane and the dihedral angles subtended by the peripheral rings and the central C_7 ring average to 79˚, resulting in a propeller-like structure. This angle is a compromise between maximising π-orbital overlap with the central ring (θ = 0˚) and the dihedral angle at which steric interactions between adjacent phenyl rings is minimised (θ = 90˚). (Figure 3.14, appendix).

We first synthesised (Scheme 3.1) **Ph_7C_7H** through a Diels–Alder [4+2] cycloaddition of **Ph_3C_3H** and tetracyclone as we have previously reported.[23] Direct oxidation (Scheme 3.2) of **Ph_7C_7H** was possible using single electron oxidant ICl in CH_2Cl_2 to give to the corresponding TP **$Ph_7C_7{\cdot}ICl_2$**, in a 60% yield. X-ray crystallography (Figure 3.14, appendix) and NMR spectroscopy (Figure 3.3, appendix) shows that **$Ph_7C_7{\cdot}ICl_2$** is presented as the expected **TP-1** isomer that is expected to be the lowest energy isomer. Upon oxidation of **Ph_7C_7H**, the ^{1}H NMR becomes simplified, showing fewer ^{1}H environments as **$Ph_7C_7^+$** now adopts a C_7 symmetry. Similarly, to commercially available **$C_7H_7{\cdot}BF_4^-$**; **$Ph_7C_7{\cdot}Br$** and **$Ph_7C_7{\cdot}ICl_2$** are bright orange solids that exhibit weak mild blue emission upon UV excitation. The conformation of **$Ph_7C_7{\cdot}ICl_2$** observed in the solid state is consistent with literature report of **$Ph_7C_7{\cdot}Br$**,[25] adopting a non-planar propeller type conformation.

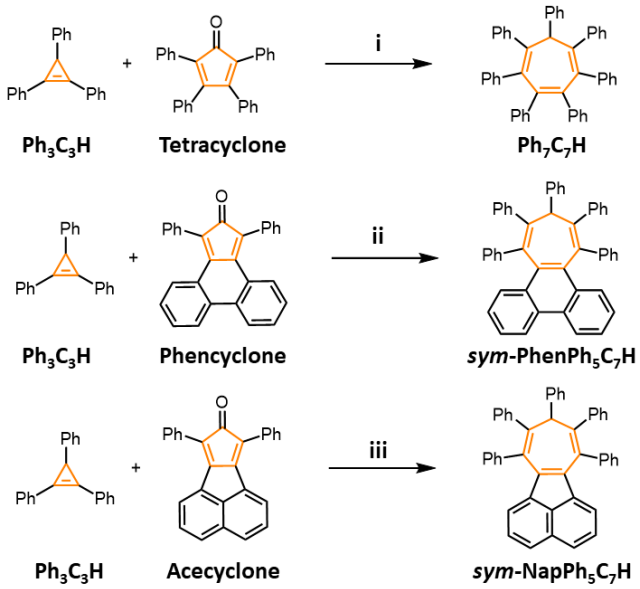

Scheme 3.1. Synthesis of **Ph_7C_7H**, ***sym*-$PhenPh_5C_7H$** and ***sym*-$NapPh_5C_7H$**. Reagents and conditions; i) *p*-xylene / μW / 160 °C / 24 h / 74%; ii) *p*-xylene / reflux / 66 h / 26%; iii) *p*-xylene / reflux / 3 d / 53%.

Under similar conditions to those used to prepare **Ph_7C_7H**, two novel CHTs **$PhenPh_5C_7H$** and **$NapPh_5C_7H$** were synthesised in moderate yields from **Ph_3C_3H** and dienes phencyclone and acecyclone, respectively (Scheme 3.1). The single electron oxidant, ICl used to synthesise **$Ph_7C_7^+$** was not successful in oxidising CHTs **$PhenPh_5C_7H$** and **$NapPh_5C_7H$** to their corresponding TP cation. Instead, even with stoichiometric amounts of ICl, only halogenation of the electron-rich phenanthrene/naphthalene moieties were observed. Attempts using Br_2, DDQ and Meerwein's salt as oxidants also failed. To overcome this problem, we modified the synthetic route to access heptaarylcycloheptatrienes (HACHTs), shown in Scheme 3.2.

The new synthetic route chosen passes through tropone intermediate **6**. This was achieved by replacing the previously used dienophile **Ph_3C_3H** with diphenylcyclopropenone, **Ph_2C_3O**. The Diels–Alder reaction of **Ph_2C_3O** with phencyclone and acecyclone, gave two new CHTs **$PhenPh_4C_7O$** and **$NapPh_4C_7O$** respectively. The conjugated ketone of **6** is then functionalised with PhMgBr to introduce the final phenyl ring to the CHT core, however this time the sp^3 proton is replaced with a tertiary alcohol (**7**), to give **$PhenPh_5C_7OH$** and **$NapPh_5C_7OH$** (Full experimental outline in Scheme 3.5, appendix). The introduction of the tertiary alcohol means the tropylium cation is much more readily accessible through oxidation with Meerwein's salt, $[(CH_3CH_2)_3O]SbCl_5$, or by using a strong acid such as methanesulfonic acid or triflic acid (TfOH).

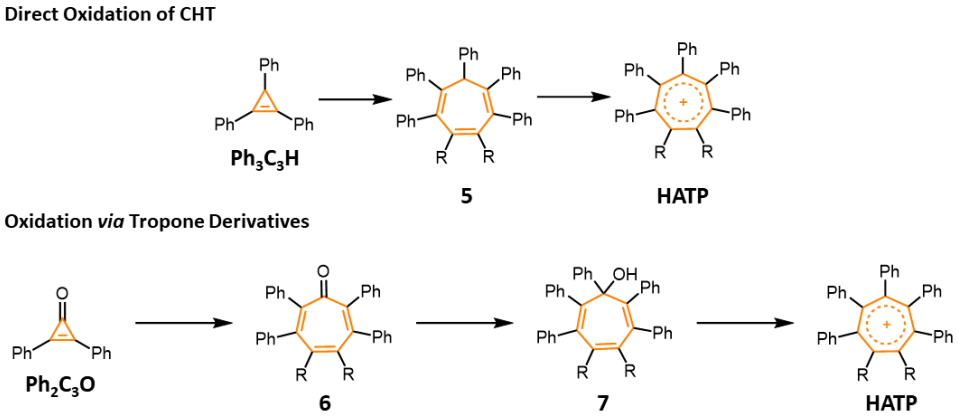

Scheme 3.2. Synthesis of heptaaryltropyliums (HATP) through i) Direct Oxidation from CHT **5** and ii) oxidation *via* tropone **6**.

Meerwein's salt was added to a solution of **$NapPh_5C_7OH$** in $CDCl_3$ under a stream of $N_{2(g)}$. The mixture turns orange upon addition of the oxidant, similarly to what was

observed upon oxidation of **Ph_7C_7H**. The ^{1}H NMR spectrum was immediately recorded (Figure 3.4, appendix) and showed an increase in symmetry indicating **$NapPh_5C_7^+$** forms the expected aromatic tropylium structure analogous to **TP-1**. The X-ray crystal structure confirms **$NapPh_5C_7{\cdot}SbCl_6$** (Figure 3.12, appendix) adopts the **TP-1** isomer and shows the peripheral phenyl rings orientated perpendicular to the central core. Unlike in its neutral state, the napthyl moiety of **$NapPh_5C_7^+$** twists 20.8˚ out of plane of the C_7 ring to minimise its steric interactions with neighbouring rings and to ensure the central tropylium ring can remain planar and maintain its stable aromatic conformation.

Unlike **$Ph_7C_7^+$** and **$NapPh_5C_7^+$**, oxidation of **$PhenPh_5C_7OH$** with Meerwein's salt yields a deep purple solid with a well resolved ^{1}H NMR spectrum containing more unique ^{1}H environments than before oxidation (Figure 3.3). This indicates the C_2 symmetry of **$PhenPh_5C_7OH$** has been disrupted and the molecule has become less symmetric upon oxidation, suggesting the **TP-1** isomer has not formed in this case. X-ray crystal analysis (Figure 3.9) reveals that **$PhenPh_5C_7{\cdot}SbCl_6$** adopts a Dewer benzene-like bicyclo[3.2.0]heptadienyl (**TP-4**) structure (Scheme 3.3). The overall strain induced by the presence of the phenanthrene moiety results in less π-character of the central ring as the bonding p-orbitals are forced out of plane, reducing overlap. As a result, the compound adopts a more di-radical nature whereby a new single C-C bond can form across the ring at the expense of breaking a C-C π-bond.

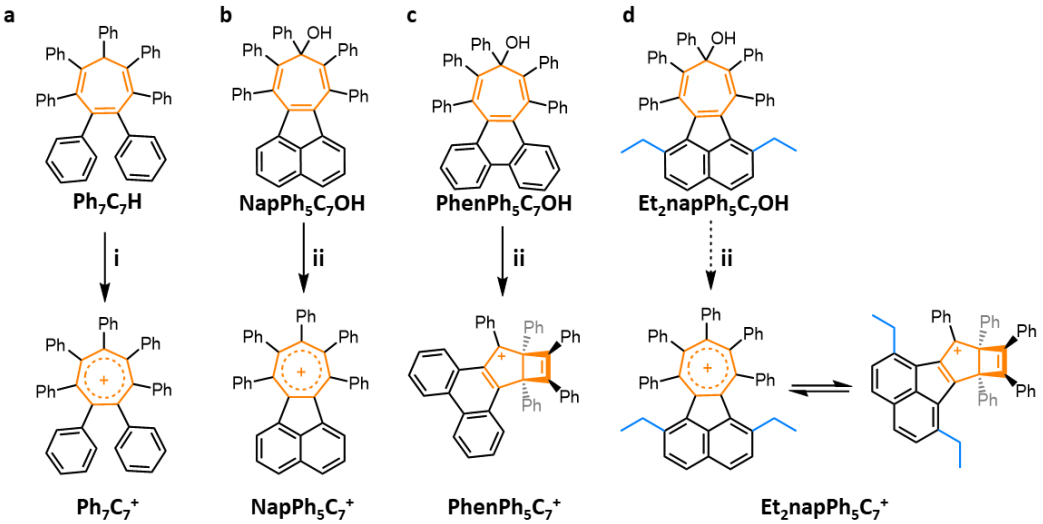

Scheme 3.3. Synthesis of four tropylium cations from their neutral cycloheptatrienes. Reagents and conditions; i) ICl / CH_2Cl_2 / rt / 16 h; ii) $[(CH_3CH_2)_3O]SbCl_5$ / $CDCl_3$ / rt. Structures of corresponding cations were confirmed through X-ray crystallography.

To understand the thermodynamic effects driving TP isomerisation, we calculated the ground-state energies of the **TP-1** and **TP-4** conformations for **NapPh$_5$C$_7^+$** and **PhenPh$_5$C$_7^+$** (Figure 3.2 a/b). The observed isomers from X-ray crystallography are consistent with the calculated lowest energy ground state structures for **NapPh$_5$C$_7^+$** and **PhenPh$_5$C$_7^+$**. Our calculations show that the formation of the non-aromatic **TP-4** bicyclic isomer lowers the ground state energy of **PhenPh$_5$C$_7^+$** by 18 kJ mol^{-1} compared to if the compound adopted the aromatic **TP-1** structure. Therefore, we can assume that the strain induced by the twisting of the phenanthrene moiety in **PhenPh$_5$C$_7^+$** is so great that it negates aromatic stabilisation energy, causing it to rearrange to **TP-4**. Interestingly, in none of the cases was **TP-3** observed even though in $C_7H_7^+$ it is expected to be a lower energy isomer than **TP-4**.

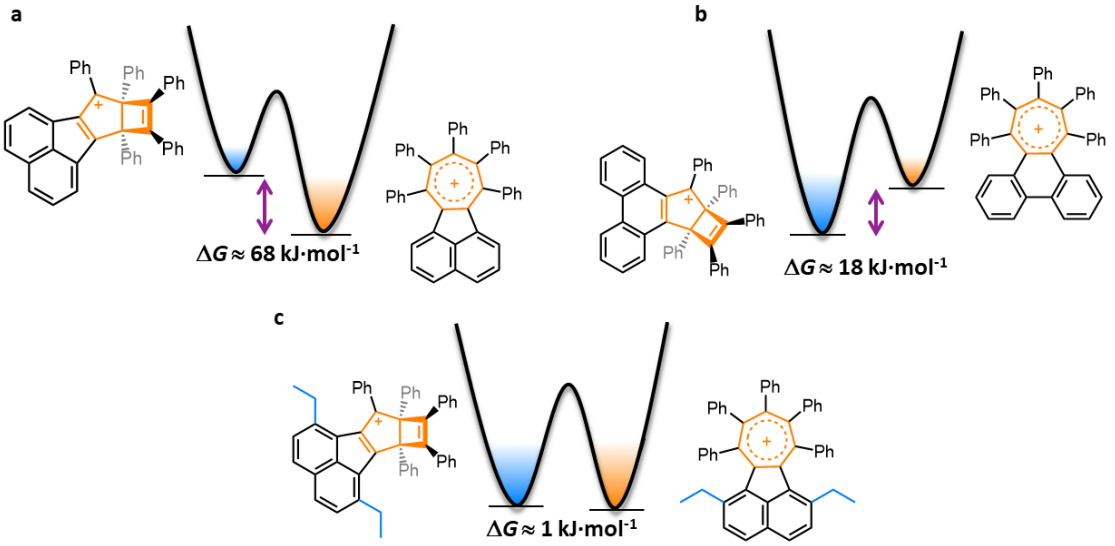

Figure 3.2. Calculated (ωB97XD/6-311G – CH_2Cl_2) ground state energies of the two isomers of a) **NapPh$_5$C$_7^+$** b) **PhenPh$_5$C$_7^+$** c) **Et$_2$napPh$_5$C$_7^+$**.

To further explore the effect of twist on the relationship between the two conformational isomers **TP-1** and **TP-4**, energy minimisation calculations were undertaken to identify an aromatic moiety that would minimise Δ*G* between the two isomers. This would allow for the study of a possible dynamic equilibrium by variable temperature (VT) NMR and allow calculation of a rate of isomerisation (k_i) to quantitatively compare the influence of strain on k_i. This computational study lead to identifying **Et$_2$napPh$_5$C$_7^+$** (Scheme 3.3d), a HACHT with a calculated Δ*G* between the aromatic TP isomer **TP-1** and the bicyclic isomer **TP-2** of ~ 1 kJ/mol^{-1} (Figure 3.4c).

The presence of the diethyl groups functionalised on the CHTs naphthalene moiety increases the steric hindrance between the napthyl group and adjacent phenyl rings. This, in turn, destabilises the conventional planar TP as the peripheral rings get closer together as the central TP becomes more planar, increasing the ground-state energy of the **TP-1** isomer.

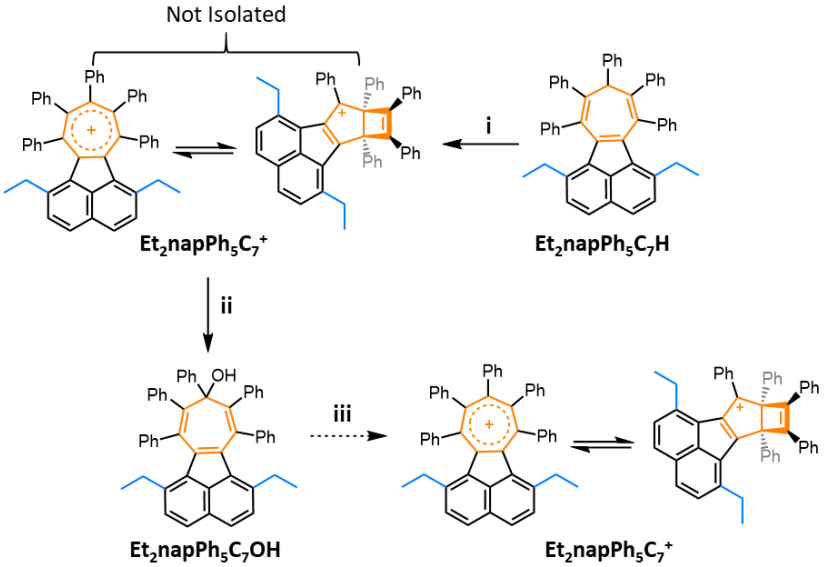

Scheme 3.4. Attempted synthesis of **Et₂napPh₅C₇⁺** *via* **Et₂napPh₅C₇OH**. Reagents and conditions; i) $[(CH_3CH_2)_3O]SbCl_6$ / $CDCl_3$ / rt / 10 min; ii) H_2O / 10 min / rt; iii) $[(CH_3CH_2)_3O]SbCl_6$ / $CDCl_3$ / rt / 10 min.

In the interest of forming the **Et₂napPh₅C₇⁺** cation, both methods of HACHT synthesis were followed and subsequent oxidation attempted. **3,8-diethylacenaphtenequinone** was first synthesised to be used as the diene in a Diels–Alder reaction with the desired dienophile. The diene was synthesised in a 35% yield over eight steps. (Synthesis outlined in Scheme 3.6, appendix). A Diels–Alder reaction of **3,8-diethylacenaphtenequinone** and **Ph₃C₃H** gave **Et₂napPh₅C₇H** in an 11% yield. X-ray crystal analysis shows **Et₂napPh₅C₇H** adopts to expected boat-like conformation, with the diethyl napthyl moiety sitting above the central CHT core. Unfortunately, treatment of **Et₂napPh₅C₇H** with $[(CH_3CH_2)_3O]SbCl_6$ does not yield the resulting TP quantitatively and isolating the product from the starting material was unsuccessful. The reaction mixture was then quenched with H_2O (Scheme 3.4) and a small amount of **Et₂napPh₅C₇OH** was isolated. Treatment of **Et₂napPh₅C₇OH** with one equivalent of $[(CH_3CH_2)_3O]SbCl_6$ causes the sharp ^1H NMR spectra of **Et₂napPh₅C₇OH** to broaden, suggesting the TP cation has formed. Unfortunately,

isolation of the **Et$_2$napPh$_5$C$_7^+$** has not yet been successful and therefore confirmation of the most stable isomer or measurements of its photophysical properties have not been carried out.

3.2.1 Photophysical Properties of Tropylium Isomers

As demonstrated in Chapter 2, molecular rotors have unique photoluminescence properties. Until now the steady-state luminescence properties of cationic molecular rotors have not been fully investigated. To understand if any significant changes occur upon oxidation of the central CHT ring, we investigated each neutral CHT and its corresponding cation by UV-Vis and fluorescence spectroscopies using 20 μM solutions in CH_2Cl_2 (Table 1). Upon oxidation of **Ph$_7$C$_7$H** to **Ph$_7$C$_7^+$**, a hypsochromic shift in the absorption band is observed (Figure 3.15a, appendix) with the absorption band shifting from 320 nm to 290 nm. Consistent with the increased absorption energy, the emission band also undergoes a bathochromic shift from 2.91 eV to 3.19 eV. No solvatochromic effects were observed for either **Ph$_7$C$_7$H** or **Ph$_7$C$_7^+$** in a series of emission spectra acquired using solvents of different polarities, so any observed properties do not arise as a result of solvent relaxation. The solubility of the other compounds prevented solvatochromism studies from being undertaken, therefore we compare all photoluminscent measurements as a 20 μM solution in anhydrous CH_2Cl_2. Cations **NapPh$_5$C$_7^+$** and **PhenPh$_5$C$_7^+$** were generated in-situ through the addition of 10 μL of TfOH to a 20 μM sample of the corresponding tertiary alcohol precursors in anhydrous CH_2Cl_2. This avoids the use to Meerwein's salt that have their own characteristic absorption bands in a similar region to our CHTs.

Interestingly, for the more twisted derivatives, the relationship between the neutral species and its cation is reversed. Oxidation of **NapC$_7$Ph$_5$OH** to the twisted aromatic TP **NapPh$_5$C$_7^+$** results in a bathochromic shift in the absorption and an increased number of absorption bands, with the lowest energy band arising at 480 nm (Figure 3.15c, appendix). The emission spectrum broadens for **NapPh$_5$C$_7^+$** and gives significantly lower emission along with a significant bathochromic shift of E_{em} from 2.65 eV to 1.91 eV. Dewer benzene homologue **PhenPh$_5$C$_7^+$** shows a similar bathochromic shift in both the absorption and emission bands. The lowest energy

absorption band (Band 1) arises at 505 nm, nearly 200 nm shift compared to the neutral species.

Table 1. Physical Properties of Twisted Tropyliums and Neutral Precursors.

Compound	E_{ex}[a] (eV)	ICCD (80K)[b] PE_{em} (eV)	Abs (nm) Band 1	E_{em}(eV)	τ(ns)[c]
Ph_7C_7H	4.0	-	320	2.91	0.003
$Ph_7C_7^+$	4.0	2.26	290	3.19	0.106
$NapPh_5C_7OH$	4.0	2.06	365	2.65	14.2
$NapPh_5C_7^+$	4.0	2.07	480	1.91-2.29	14.2
$PhenPh_5C_7OH$	4.0	2.19	325	3.00	0.834
$PhenPh_5C_7^+$	4.0	2.21	505	2.18-2.80	4.54

[a]Excitation wavelengths were chosen to match peaks in absorption spectra (Figure 3.15). Intensified Charged Couple Device (ICCD) measurements were limited to 310 nm excitation therefore was used throughout. [b]Phosphorescence was not observed at 298K for any of the compounds and only observed at 80K in any case. PE_{em} denotes energy of maximum emission. [c]20 μM solutions in anhydrous CH_2Cl_2.

The fluorescence lifetimes of **$Ph_7C_7^+$** and **$PhenPh_5C_7^+$** increases compared to their neutral species. This increase is significant between **$PhenPh_5C_7OH$** to **$PhenPh_5C_7^+$** whereby the compound rearranges into less twisted Dewer benzene-like isomer. For certain acenes, it has been reported that the fluorescence lifetime decreases with twist, accredited to increase rate of intersystem crossing which arises from increased spin-orbit coupling.[26] Interestingly **$NapPh_5C_7^+$** does not follow this trend and shows an increase in fluoresce lifetime, accompanied by an increase twist compared to **$Ph_7C_7^+$**. The increase twist of **$NapPh_5C_7^+$** does however decrease the phosphorescence emission energy (PE_{em}) and therefore a decrease in the energy of the first triplet state T_1 (PE_{em}), this becomes important when designing singlet fission materials. For singlet fission molecules, the energy of the triplet state (T_1) is required to be smaller or equal to half of the singlet (S_1) state, and thus satisfying $E_{T1\text{-}S0} = 1/2\ E_{S1\text{-}S0}$. Pentacenes and heptacenes have been reported to be highly useful singlet fission molecules as a result of their highly twisted nature, with reports showing heptacene derivates with twist of upto 180°.[27]

To investigate potential of our materials for singlet fission, we measured the phosphorescence emission (PE) spectra for each compound (Figure 3.17, appendix), capturing emission with an Intensified Charged Coupling Device camera (ICCD) and

reported the phosphorescence emission maxima (PE_{em}) in Table 1. Interestingly, **Ph_7C_7H** shows no phosphorescence emission at 80 K however upon oxidation to **$Ph_7C_7^+$** we see mild phosphorescence occurring. As the twist increases, we observed a decrease in the phosphorescence energy from 2.26 eV to 2.07 eV for **$NapPh_5C_7^+$**, similarly to the energy decrease of the S_1 state as previously discussed. The small energy gap between isomers represents the highly strained nature without too much strain to induce isomerization as seen in **$PhenPh_5C_7^+$**. In theory, further twisting could therefore provide a compound where the possibility to satisfy $E_{T1\text{-}S0} = 1/2\ E_{S1\text{-}S0}$ is most likely as observed in pentacene. So far, in these compounds we observe a decrease in $E_{T1\text{-}S0}$ with twisting however are also accompanied by a decrease in $E_{S1\text{-}S0}$ meaning $E_{T1\text{-}S0} = 1/2\ E_{S1\text{-}S0}$ is yet to be satisfied in these compounds. Furthermore, the phosphorescence strength for these compounds were relatively low therefore transient absorption measurements to quantify the triplet lifetime was not possible. As a result, further modifications are needed to perfect twisting for potential applications as singlet fission materials.

3.3 Conclusion

In summary, we have investigated the structure and photophysical properties of heptaphenyl tropylium, **$Ph_7C_7^+$**, and its derivatives with varying degrees of conformational twisting. We enforce conformational twisting by increasing the extent of steric hindrance of the peripheral rings resulting in a highly twisted aromatic tropylium conformation **$NapPh_5C_7^+$** that exhibits a 20.8˚ twist out of plane. In our compounds the degree of torsion induced towards the tropylium centre is determined by the size of the aromatic moiety and the ability for the central tropylium to retain aromaticity. This result shows that the aromatic tropylium structure is resilient to some conformational twisting. However, when the napthyl moiety is replaced with a larger phenanthrene moiety, **$PhenPh_5C_7^+$**, the increased steric hindrance with the neighbouring phenyl rings results in rearrangement to an unusual Dewer benzene like isomer. We report large changes between the photoluminscent properties of neutral and cationic C_7 molecular rotors and propose that controlling the twist angle of these molecular rotors can improve future design of tuning nanocarbons with desired properties.

3.4 Future work

Our future aims to complete this project is to first isolate **$Et_2napPh_5C_7^+$** as a pure compound and study the equilibrium between isomeric forms by variable temperature NMR spectroscopy. This will allow us to quantify the twist induced by the presence of bulky ethyl groups which is expected to distort the napthyl group further out of plane. From here we can maximise the twisting of peripheral aryl groups on the central C_7 core allowing us to study the effect of twist of physical properties and potential singlet fission molecules.

3.5 Experimental Details

3.5.1 Specific Experimental Methods

Materials: All reagents were purchased from commercial suppliers (Sigma-Aldrich, Acros Organics, or Alfa Aesar) and used without further purification. Triethyloxonium hexachloroantimonate was purchased and stored in a desiccator until used. Trifluoromethanesulfonic acid, ReagentPlus®, ≥99% was stored in a fridge under a nitrogen atmosphere. A glass Hamilton syringe was used to measure out the desired quantity of TfOH and added to the sample in one.

Measurements: Phosphorescence was measured using a system consisting excitation source, sub nanosecond pulsed YAG laser using either 3rd order harmonics (355 nm). The energy of each pulse can be tuned from nJ up to mJ, with the diameter of the beam falling on the sample normally in the range of from 0.1-1 cm. With the help of a spectrograph and other optics, luminescence is collected onto a sensitive gated ICCD (intensified CCD) camera 4 Picos (Stanford Computer Optics) with sub nanosecond resolution.

3.5.2 Synthetic Procedures

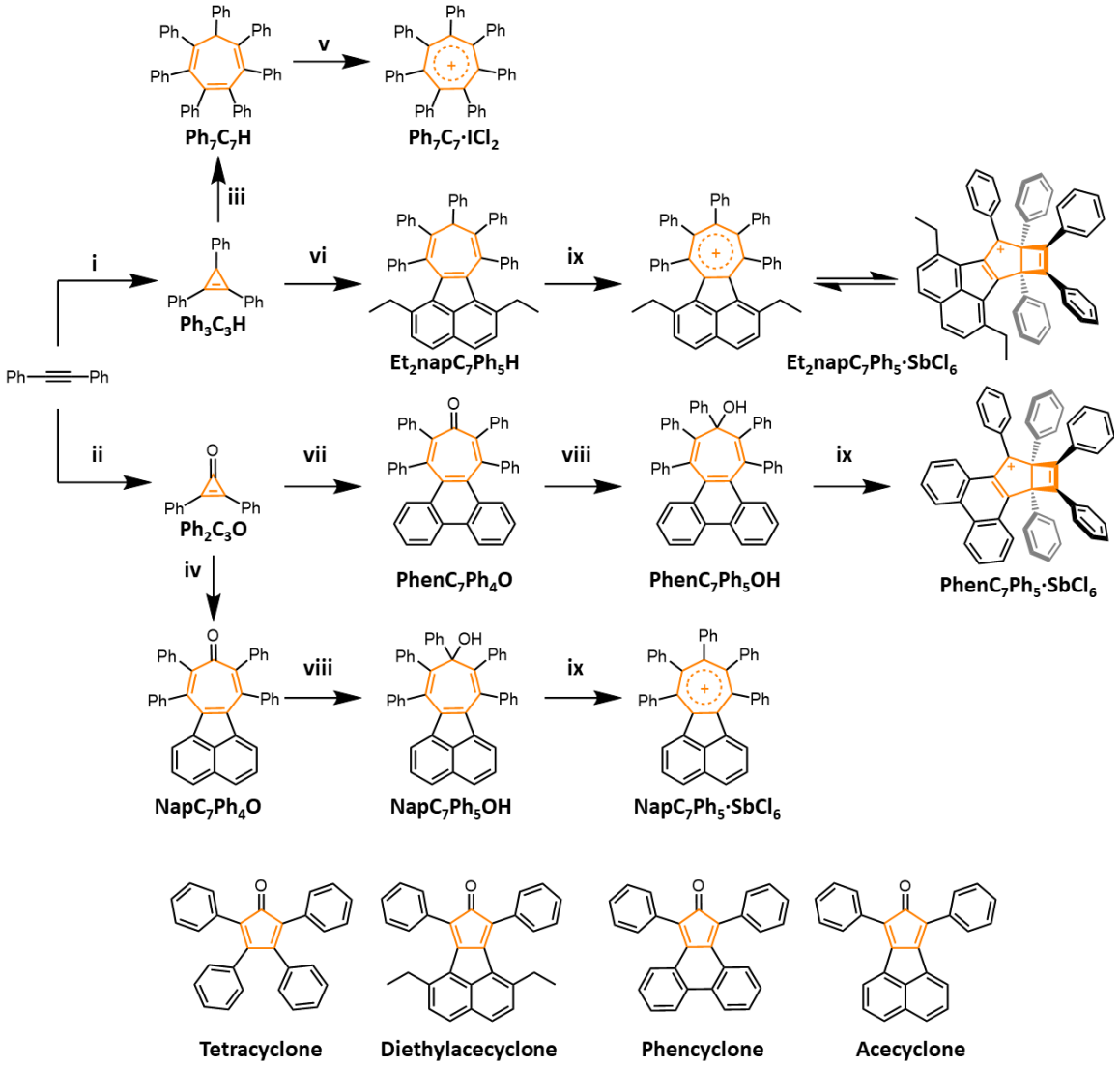

Scheme 3.5. Synthesis routes used to prepared **tropylium cations**. Reagents and conditions: i)KO^{t}Bu / *a*,*a*-dichlorotoluene / C_6H_6 / 90 °C / 3 h ; $NaBH_4$ / EtOH / rt / 16 h / 97%; ii) KO^{t}Bu / hexane / -20 °C / 18 h then HBr / Et_2O / 65%; iii) tetracyclone / *p*-xylene / 160 °C / 24 h / 74%; iv) acecyclone / PhMe / $CHCl_3$ / 130 °C / 24 h / 34%; v) ICl / CH_2Cl_2 / rt / 24 h / 60%; vi) diethylacecyclone / *p*-xylene / 190 °C / 24 h / 11%; vii) phencyclone / PhMe / 130 °C / 24 h / 40%; viii) PhMgBr / THF / 0 °C / 3.5 h / 60-68%; iv) $Et_3O^+SbCl_6^-$ / $CDCl_3$.

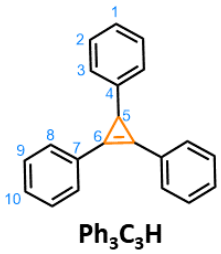

***sym*-Triphenylcyclopropene (Ph_3C_3H)**: Sodium borohydride (9.3 g, 246 mmol) was added to a solution of **$Ph_3C_3{\cdot}HCl_2$** (18.6 g, 61.4 mmol) in EtOH (460 mL). The mixture was allowed to stir overnight at rt. The reaction was quenched with H_2O (500 mL) then extracted with Et_2O (3 × 200 mL). The organic layers were combined and washed with H_2O (500 mL) and brine (500 mL). The combined organic

extracts were then dried over $MgSO_4$ and the solvent was removed under reduced pressure to give the title compound as a colorless solid (14.2 g, 53.1 mmol, 97%). **M.P.** 113 –115 °C (lit.[i] 114 – 115.5 °C). **^{1}H NMR** (400 MHz, $CDCl_3$) δ 7.71 – 7.66 (m, 4H, H_8), 7.47 – 7.40 (m, 4H, H_9), 7.38 – 7.32 (m, 2H, H_{10}), 7.24 (br s, 2H, H_2), 7.23 – 7.22 (m, 2H, H_3), 7.17 – 7.10 (m, 1H, H_1), 3.27 (s, 1H, H_5). **^{13}C NMR** (101 MHz, $CDCl_3$) δ 144.6 (C_4), 130.0 (C_8), 128.9 (C_9), 128.8 (C_{10}), 128.7 (C_7), 128.3 (C_3), 126.0 (C_2), 125.6 (C_1), 112.7 (C_6), 24.5 (C_5). **HR-ESI MS** *m/z* = 267.1172 $[M-H]^+$ (calculated for $C_{21}H_{15}^+$ = 267.1168).

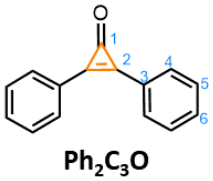

Ph_2C_3O

Diphenylcyclopropenone (Ph_2C_3O): Diphenylacetylene (6.02 g, 33.8 mmol) and KO^{t}Bu (10.6 g, 95 mmol) were dissolved in dry hexane (150 mL) and cooled to -20 °C under a N_2 atmosphere. $CHBr_3$ (2.68 mL, 30.6 mmol) was slowly added over 3 h at -20 °C and the reaction mixture was stirred and allowed to slowly warm to rt overnight. The reaction was quenched with H_2O (50 mL) and stirred for 30 min. The organic layer was then extracted with EtOAc (3 × 30 mL) and washed with a saturated aqueous solution of $Na_2S_2O_3$ (30 mL) and brine (30 mL), before being dried over $MgSO_4$, filtered and evaporated to dryness to give a dark red viscous oil. The crude solid was purified by column chromatography (Teledyne Isco CombiFlash Rf+ system, 80 g SiO_2, Hexane–EtOAc, gradient elution). The title compound was isolated as a pale yellow solid (4.54 g 21.9 mmol, 65%). **M.P.** 92 – 94 °C. **^{1}H NMR** (400 MHz, $CDCl_3$) δ 8.08 – 7.91 (m, 4H, H_4), 7.71 – 7.52 (m, 6H, $H_{5,6}$). **^{13}C NMR** (101 MHz, $CDCl_3$) δ 156.0 (C_1), 148.5 (C_3), 132.9 (C_4), 131.7 (C_5), 129.5 (C_6), 124.2 (C_2). **HR-ESI MS** *m/z* = 207.0787 $[M+H]^+$ (calculated for $C_{15}H_{11}O$ = 207.0810).

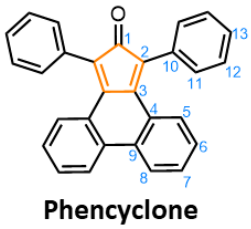

Phencyclone

Phencyclone: 9,10-phenanthrenequinone (9.06 g, 43.5 mmol) was added to a solution of 1,3-diphenylacetone (9.91 g, 46.0 mmol) in EtOH (300 mL). The reaction mixture was heated to reflux before a solution of NaOH (3.30 g, 81.9 mmol) in EtOH (90 mL) was added dropwise. The reaction was further refluxed for 15 min, then immediately placed into an ice-bath. Once cooled, the resulting precipitate was collected via vacuum filtration and washed with cold EtOH (10 mL) to give the title compound as a black solid (14.8 g, 38.7 mmol, 89%). **M.P.** 255 – 257 °C. **^{1}H NMR** (400 MHz, $CDCl_3$) δ 6.95 (t, J = 7 Hz, 2 H), 7.28–7.30 (m, 2 H), 7.36 – 7.45

(m, 10 H), 7.55 (dd, J = 8, 1 Hz, 2 H), 7.81 (d, J = 7.5 Hz, 2 H). The spectroscopic data was consistent with literature reports.[28]

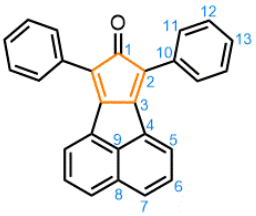

Acecyclone

Acecyclone: Acequinone (2.00 g, 11.0 mmol) was added to a solution of 1,3-diphenyl-2-propanone (2.60 g, 12.5 mmol) in EtOH (50 ml). The reaction mixture was heated to reflux before a solution of NaOH (0.79 g, 19.7 mmol) in EtOH (25 mL) was added dropwise. The reaction was further refluxed for 15 min, then immediately placed into an ice-bath. Once cooled, the resulting precipitate was collected via vacuum filtration and washed with cold EtOH (10 mL) to give the title compound as a black solid (2.95 g, 8.24 mmol, 75%). **M.P.** 280 – 282 °C. **^{1}H NMR** (700 MHz, $CDCl_3$) δ 8.07 (dd, *J* = 7.2, 0.6 Hz, 2H, H_7), 7.90 – 7.85 (m, 2H, H_5), 7.85 – 7.80 (m, 4H, H_{11}), 7.59 (dd, *J* = 8.2, 7.2 Hz, 2H, H_6), 7.54 – 7.51 (m, 4H, H_{12}), 7.41 (ddt, *J* = 7.9, 7.0, 1.3 Hz, 2H, H_{13}). **^{13}C NMR** (176 MHz, $CDCl_3$) δ 202.0 (C_1), 154.4 (C_3), 144.9 (C_4), 132.3 (C_2), 131.7 (C_{10}), 131.6 (C_8), 129.2 (C_{11}), 128.7 (C_{12}), 128.6 (C_9), 128.4 (C_6), 127.9 (C_5), 121.8 (C_{13}), 121.1 (C_7). **HR-ESI MS** *m/z* = 357.1256 $[M+H]^+$ (calculated for $C_{27}H_{17}O$ = 357.1279).

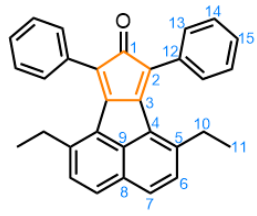

Diethylacecyclone

Diethylacecyclone: 3,8-Diethylacenaphthenequinone (0.93 g, 4.1 mmol) was added to a solution of 1,3-diphenyl-2-propanone (0.90 g, 4.5 mmol) in EtOH (20 mL). The reaction mixture was heated to reflux before a solution of NaOH (0.308 g, 7.7 mmol) in EtOH (20 mL) was added dropwise. The reaction mixture was further refluxed for 30 min, then immediately placed to ice-bath. Once cooled, the resulting precipitate was collected via vacuum filtration and washed with cold EtOH (10 mL) to give the title compound as a black solid (0.5g, 1.2 mmol, 30%). **M.P.** 140 – 142°C. **^{1}H NMR** (700 MHz, $CDCl_3$) δ 7.74 (d, *J* = 8.3 Hz, 2H, H_7), 7.45 – 7.37 (m, 10H, $H_{13,14,15}$), 7.35 (d, *J* = 8.3 Hz, 2H, H_6), 2.40 (q, *J* = 7.5 Hz, 4H, H_{10}), 0.85 (t, *J* = 7.6 Hz, 6H, H_{11}). **^{13}C NMR** (176 MHz, $CDCl_3$) δ 202.9 (C_1), 156.2 (C_3), 146.6 (C_9), 140.5 (C_5), 133.1 (C_{12}), 130.4 (C_4), 129.4 (C_{13}), 128.7 (C_{14}), 128.4 (C_{15}), 128.0 (C_7), 127.6 (C_8), 127.6 (C_6), 121.8 (C_2), 28.2 (C_{10}), 14.9 (C_{11}). **HR-ESI MS** *m/z* = 413.1894 $[M+H]^+$ (calculated for $C_{31}H_{25}O$ = 413.1900).

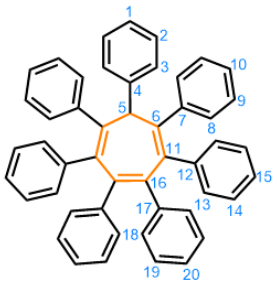

Ph_7C_7H

***sym*-Heptaphenylcycloheptatriene** (**Ph_7C_7H**): To a 20 mL microwave vial was added **Ph_3C_3H** (1.2 g, 4.47 mmol), tetraphenylcyclopentadienone (1.79 g, 4.47 mmol) and anhydrous *p*-xylene (13.5 mL). The reaction vessel was sealed, and the mixture deoxygenated (3 × freeze–pump–thaw cycles under N_2) then stirred for 36 h at 140 °C in a microwave reactor. Upon cooling to rt, a crystalline solid formed, which was isolated by filtration through a sintered glass funnel, washing with Et_2O (3 × 10 mL). The solid was dried under vacuum to yield **Ph_7C_7H** as a pale pink solid (2.3 g, 3.68 mmol, 82%) in high purity (no observable impurities by ^{1}H NMR spectroscopy). Samples for analytical measurements were further purified by recrystallization. A saturated solution of **Ph_7C_7H** in 1:1 $CHCl_3$–EtOH was allowed to slowly evaporate, yielding colorless crystals of analytically pure **Ph_7C_7H**. **M.P.** 291 – 292 °C (lit.[2] 285 – 287.5 °C). **^{1}H NMR** (700 MHz, $(CD_3)_2CO$) δ 8.17 – 7.99 (m, 2H, H_3), 7.62 – 7.48 (m, 2H, H_2), 7.44 – 7.34 (m, 1H, H_1), 7.26 – 7.18 (m, 4H, H_8), 7.15 (br s, 4H, H_{13}), 7.05 – 7.02 (m, 4H, H_{14}), 7.02 – 6.98 (m, 4H, H_9), 6.98 – 6.96 (m, 2H, H_{15}), 6.96 – 6.93 (m, 2H, H_{10}), 6.63 – 6.59 (m, 2H, H_{20}), 6.60 – 6.55 (m, 4H, H_{19}), 6.36 – 6.32 (m, 4H, H_{18}), 5.35 (s, 1H, H_5). **^{13}C NMR** (176 MHz, $(CD_3)_2CO$) δ 144.8 (C_{16}), 144.4 (C_7), 144.1 (C_4), 141.9 (C_{12}), 141.6 (C_{17}), 140.2 (C_6), 138.0 (C_{11}), 132.7 (C_{13}), 132.3 (C_{18}), 130.7 (C_8), 129.4 (C_2), 128.5 (C_9), 128.1 (C_{14}), 127.9 (C_3), 127.7 (C_1), 127.3 (C_{10}), 126.93 (C_{15}), 126.87 (C_{19}), 126.0 (C_{20}), 59.0 (C_5). **HR-ESI MS** *m/z* = 625.2892 $[M+H]^+$ (calculated for $C_{47}H_{37}$ = 625.2890).

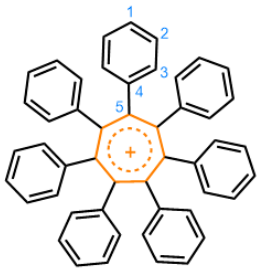

$Ph_7C_7{\cdot}ICl_2$

***sym*-Heptaphenyltropylium** (**$Ph_7C_7{\cdot}ICl_2$**): **Ph_7C_7H** (0.1 g, 0.16 mmol) was added to an over dried round bottom flask and dissolved in anhydrous CH_2Cl_2 (10 mL). A 1M solution of ICl in CH_2Cl_2 (1 mL, 1.0 mmol) was added and the mixture was stirred at rt for 24 h, before the solvent was removed under reduced pressure to give a crude dark purple solid. The crude solid was dissolved in anhydrous MeCN (15 mL) and triturated with anhydrous Et_2O (25 mL). The resulting precipitate was isolated by vacuum filtration to isolate the title compound as an orange solid. (0.097 g, 0.096 mmol, 60%) **M.P.** 280 – 282 °C. **^{1}H NMR** (400 MHz, CD_3CN) δ 6.92 – 6.88 (m, 14 H, H_3), 6.87 – 6.78 (m, 21H, H_{1+2}).

^{13}C NMR (101 MHz, CD_3CN) δ 167.3 (C_5), 141.6 (C_4), 130.5 (C_3), 127.8 (C_2), 127.6 (C_1). **HRMS-ASAP** *m/z*= 623.2712 $[M]^+$ (calculated for $C_{49}H_{35}^+$ = 623.2739).

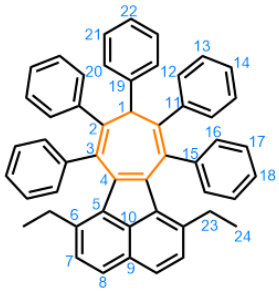

$Et_2napC_7Ph_5H$: To a 5 mL microwave vial was added **Ph_3C_3H** (0.05 g, 0.18 mmol), 2,7-diethylacecyclone (0.07 g, 0.18 mmol) and anhydrous *p*-xylene (3.5 mL) under a N_2 atmosphere. The reaction vessel was sealed, and the mixture deoxygenated (3 × freeze-pump-thaw cycles under N_2) then stirred for 24 h at 190 °C in a microwave reactor. The solvent was removed under reduced pressure and the crude mixture was purified by column chromatography (Teledyne Isco CombiFlash Rf+ system, 24 g SiO_2, Hexane−EtOAc, 0-50%). The title product was isolated as a yellow solid (0.015 g, 0.02 mmol, 11%). **M.P.** 198 – 200 °C. **^{1}H NMR** (400 MHz, $CDCl_3$) **^{1}H NMR** (400 MHz, $CDCl_3$) δ 7.52 (dd, *J* = 11.3, 7.8 Hz, 4H, $H_{8,20}$), 7.16 – 7.10 (m, 4H, $H_{18,21}$), 7.08 – 7.03 (m, 10H, $H_{12,13,14}$), 7.01 – 6.84 (m, 8H, $H_{16,17}$), 6.83 – 6.76 (m, 2H, H_7), 6.66 (t, *J* = 7.4 Hz, 1H, H_{22}), 5.48 (s, 1H, H_1), 2.27 (m, 4H, H_{23}), 0.68 (dd, *J* = 8.0, 6.9 Hz, 6H, H_{24}). **^{13}C NMR** (101 MHz, $CDCl_3$) δ 143.4 (C_{19}), 142.9 (C_{15}), 141.5 (C_{11}), 141.1 (C_6), 140.6 (C_9), 137.8 (C_3), 134.7 (C_{10}), 132.4 (C_{16}), 131.9 (C_{20}), 130.6 (C_2), 129.0 (C_5), 128.5 (C_{21}), 127.8 (C_{12}), 127.7 (C_6), 127.6 (C_{17}), 127.2 (C_{22}), 126.8 (C_{13}), 126.5 (C_{14}), 126.2 (C_{18}), 125.6 (C_7), 125.5 (C_4), 125.4 (C_8), 60.6 (C_1), 27.1 (C_{23}), 14.2 (C_{24}). **HR-ESI MS** *m/z* = 653.3223 $[M+H]^+$ (calculated for $C_{51}H_{41}$ = 653.3208).

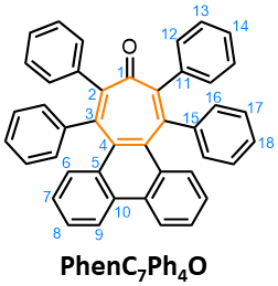

$PhenC_7Ph_4O$: To a 20 mL microwave vial was added diphenylcyclopropenone (0.40 g, 1.9 mmol), phencyclone (0.49 g, 1.2 mmol) and anhydrous PhMe (10 mL). The reaction vessel was sealed, and the mixture deoxygenated (3 × freeze-pump-thaw cycles under N_2) then stirred for 24 h at 130 °C in a microwave reactor. Upon cooling to rt, the solvent was removed under reduced pressure and the crude solid was purified by column chromatography (Teledyne Isco CombiFlash Rf+ system, 12 g SiO_2, Hexanes−CH_2Cl_2, 0-30%). The title compound was isolated as a white solid (0.31 g, 0.48 mmol, 40%). **M.P.** 248 – 250 °C. **^{1}H NMR** (700 MHz, $CDCl_3$) δ 8.59 (dd, *J* = 8.4, 1.3 Hz, 2H, H_9),

7.94 (dd, *J* = 8.5, 1.3 Hz, 2H, H_6), 7.47 (ddd, *J* = 8.3, 6.9, 1.2 Hz, 2H, H_8), 7.20 (ddd, *J* = 8.3, 6.9, 1.2 Hz, 2H, H_7), 7.17 – 7.09 (m, 14H, $H_{17,12,13,14}$), 7.07 – 6.97 (m, 6H, $_{18,16}$). **^{13}C NMR** (176 MHz, $CDCl_3$) *δ* 199.9 (C_1), 146.2 (C_3), 140.6 (C_{15}), 135.8 (C_{11}), 134.9 (C_{10}), 133.6 (C_2), 131.1 (C_4), 130.7 (C_6), 130.4 (C_{13}), 129.8 (C_5), 129.7 (C_{12}), 128.3 (C_{17}), 128.0 (C_{16}), 127.8 (C_{18}), 127.2 (C_{14}), 126.9 (C_8), 125.9 (C_7), 122.4 (C_9). **HR-ESI MS** *m/z* = 561.2222 $[M+H]^+$ (calculated for $C_{43}H_{29}O$ = 561.2218).

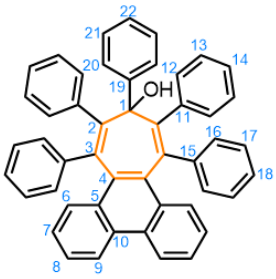

PhenC$_7$Ph$_5$OH

PhenC$_7$Ph$_5$OH: To an oven-dried two neck 50 mL flask was added **PhenC$_7$Ph$_4$O** (0.1 g, 0.18 mmol) and anhydrous THF (5 mL) under N_2 atmosphere. The reaction mixture was placed to ice bath and allowed to stir for 10 min. A 1M solution of PhMgBr in THF (0.19 mL, 0.19 mmol) was added slowly into the reaction mixture at 0 °C and stirred for 30 min. The resulting yellow solution was stirred at rt for 3 h and quenched with saturated aqueous solution of NH_4Cl (5 mL). The mixture was extracted with Et_2O (2 × 10 mL) and the organic layers were combined and dried over anhydrous $MgSO_4$, filtered and the solvent was removed under reduced pressure. The crude solid was purified by column chromatography (Teledyne Isco CombiFlash Rf+ system, 12 g SiO_2, Hexane–EtOAc, 0-5%). The title product was isolated as a white solid (0.07 g, 0.11 mmol, 60%). **M.P.** 340 – 342 °C. **^{1}H NMR** (700 MHz, $CDCl_3$) δ 8.25 (d, *J* = 8.2 Hz, 2H, H_9), 7.79 (dd, *J* = 8.4, 1.3 Hz, 2H, H_6), 7.71 (dt, *J* = 7.8, 1.5 Hz, 2H, H_{16}), 7.57 – 7.53 (m, 2H, H_{20}), 7.34 (td, *J* = 7.6, 1.3 Hz, 2H, H_{17}), 7.27 – 7.23 (m, 2H, H_8), 7.09 (tt, *J* = 7.5, 1.3 Hz, 2H, $H_{17'}$), 7.06 (ddd, *J* = 8.3, 6.9, 1.2 Hz, 2H, H_7), 6.98 – 6.90 (m, 10H, $H_{12,13,14}$), 6.85 (td, *J* = 7.6, 1.4 Hz, 2H, H_{18}), 6.76 (dt, *J* = 7.8, 1.5 Hz, 2H, $H_{16'}$), 6.48 (dd, *J* = 8.2, 6.4 Hz, 2H, H_{21}), 6.46 – 6.42 (m, 1H, H_{22}). **^{13}C NMR** (176 MHz, $CDCl_3$) δ 151.4 (C_{15}), 143.0 (C_3), 142.3 (C_{19}), 137.6 (C_2), 136.7 (C_{11}), 133.9 (C_{10}), 132.6 (C_{16}), 132.2 ($C_{16'}$), 130.9 (C_{12}), 130.1 (C_4), 129.9 (C_6), 128.9 (C_5), 127.6 (C_{18}), 127.3 (C_{13}), 127.2 (C_{17}), 127.2 ($C_{17'}$), 126.7 (C_{21}), 126.4 (C_{22}), 125.8 (C_8), 125.6 (C_{14}), 125.3 (C_{20}), 125.1 (C_7), 121.7 (C_9), 81.1 (C_1). **HR-ESI MS** *m/z* = 621.2560 $[M-OH]^+$ (calculated for $C_{49}H_{33}$ = 621.2582).

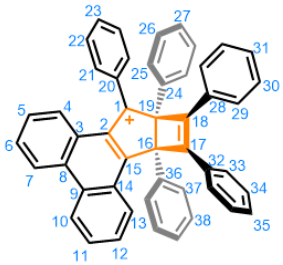

$PhenC_7Ph_5{\cdot}SbCl_6$

$PhenC_7Ph_5{\cdot}SbCl_6^-$: A pure sample of **$PhenC_7Ph_5OH$** (3.5 mg, 0.005 mmol) was dissolved in CD_2Cl_2 (0.6 mL) and added to an NMR tube. $Et_3O^+SbCl_6^-$ (5 mg, 0.01 mmol) was added to the NMR tube under a N_2 atmosphere at rt. The colourless solution immediately turned purple and measure with variable temperature NMR whereby a quantitative conversion was observed. **^{1}H NMR** (500 MHz, CD_2Cl_2, 179 K) δ 8.84 (d, *J* = 8.6 Hz, 1H, H_7), 8.79 (d, *J* = 8.5 Hz, 1H, H_{10}), 8.33 (d, *J* = 8.2 Hz, 1H, H_{13}), 8.25 – 8.18 (m, 1H, H_6), 7.95 – 7.87 (m, 1H, H_{11}), 7.83 – 7.78 (m, 1H, H_5), 7.77 (d, *J* = 8.0 Hz, 1H, H_{39}), 7.63 (dt, *J* = 11.7, 5.9 Hz, 2H, H_{37}), 7.57 (t, *J* = 7.5 Hz, 1H, H_{12}), 7.49 – 7.42 (m, 1H, H_4), 7.39 (m, 2H, H_{25}), 7.35 (t, *J* = 7.6 Hz, 1H, H_{27}), 7.30 – 7.22 (m, 6H, $H_{26,30,38}$), 7.20 (t, *J* = 8.1 Hz, 2H, H_{29}), 7.16 – 7.09 (m, 1H, H_{31}), 7.05 (t, *J* = 7.4 Hz, 1H, H_{23}), 7.00 (t, *J* = 7.6 Hz, 1H, H_{35}), 6.89 (t, *J* = 7.7 Hz, 2H, H_{22}), 6.84 – 6.79 (m, 2H, H_{21}), 6.76 (t, *J* = 7.7 Hz, 2H, H_{34}), 6.20 (m, 2H, H_{33}). **^{13}C NMR (**126 MHz, CD_2Cl_2**)** δ 185.2 (C_1), 152.6 (C_{15}), 142.7 (C_2), 141.5 (C_6), 141.1 (C_{36}), 139.7 (C_{32}), 139.7 (C_{20}), 139.0 (C_{28}), 138.9 (C_{24}), 138.8 (C_{12}), 136.4 (C_9), 135.7 (C_5), 134.2 (C_8), 134.2 (C_3), 133.6 (C_{39}), 132.9 (C_{14}), 131.7 (C_{21}), 131.0 (C_{11}), 129.9 (C_{37}), 129.7 (C_{25}), 129.6 (C_{26}), 129.2 (C_{31}), 129.1 (C_{23}), 128.9 (C_{27}), 128.9 (C_4), 128.8 (C_{30}), 128.8 (C_{38}), 128.6 (C_{19}), 128.4 (C_{22}), 128.4 (C_{33}), 128.0 (C_{35}), 128.0 (C_{34}), 127.6 (C_{16}), 127.5 (C_{29}), 127.35 (C_{18}), 127.0 (C_{13}), 126.75 (C_{17}), 125.0 (C_7), 124.8 (C_{10}). **HR-ESI MS** *m/z* = 621.2560 $[M]^+$ (calculated for $C_{49}H_{33}$ = 621.2582).

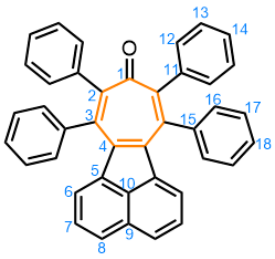

$NapC_7Ph_4O$

$NapC_7Ph_4O$: To a 5 mL microwave vial was added diphenylcyclopropenone (0.20 g, 0.97 mmol), acecyclone (0.23 g, 0.65 mmol), anhydrous PhMe (2.5 mL) and $CHCl_3$ (1.5 mL). The reaction vessel was sealed, and the mixture deoxygenated (3 × freeze-pump-thaw cycles under N_2) then stirred for 24 h at 130 °C in a microwave reactor. Upon cooling to rt, the solvent was removed under reduced pressure and the crude solid was purified by column chromatography (Teledyne Isco CombiFlash Rf+ system, 12 g SiO_2, Hexane–EtOAc, 0-10%). The title compound was isolated as a pale yellow solid (0.12 g, 0.18 mmol, 34%). **M.P.** 245 – 247 °C. **^{1}H NMR** (400 MHz, $CDCl_3$) δ 7.65 (d, *J* =

8.1 Hz, 2H, H_8), 7.43 – 7.32 (m, 8H, $H_{13,17}$), 7.34 – 7.30 (m, 2H, H_{18}), 7.30 – 7.26 (m, 4H, H_{16}), 7.17 (dd, *J* = 8.2, 7.2 Hz, 2H, H_7), 7.04 (dd, *J* = 5.1, 1.8 Hz, 6H, $H_{12,14}$), 6.36 (d, *J* = 7.1 Hz, 2H, H_6). **^{13}C NMR** (101 MHz, $CDCl_3$) δ 197.5 (C_1), 140.2 (C_3), 140.0 (C_{15}), 139.0 (C_2), 138.7 (C_{11}), 136.5 (C_4), 134.1 (C_6), 131.9 (C_{13}), 130.6 (C_{12}), 128.6 (C_5), 128.5 (C_{10}), 128.3 (C_{17}), 127.9 (C_{18}), 127.7 (C_9), 127.6 (C_{16}), 127.5 (C_{14}), 127.4 (C_7), 126.1 (C8). **HR-ESI MS** *m/z* = 535.1953 $[M+H]^+$ (calculated for $C_{41}H_{27}O$ = 535.1948).

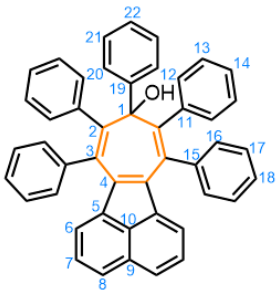

$NapC_7Ph_5OH$

$NapC_7Ph_5OH$: To a flame-dried two neck 50 mL flask was added **$NapC_7Ph_4O$** (0.1 g, 0.19 mmol) and anhydrous THF (3 mL) under N_2 atmosphere. The reaction mixture was placed to ice bath and allowed to stir for 10 min. A solution of PhMgBr (0.2 mL of 1 M solution in THF) was added slowly into the reaction mixture at 0 °C and stirred for 30 min. The resulting yellow solution was stirred at rt for 3 h and quenched with a saturated aqueous solution of NH_4Cl (5 mL). The solution was extracted with Et_2O (2 ×10 mL) and the organic layers were combined and dried over anhydrous $MgSO_4$, filtered and the solvent was removed under reduced pressure. The crude product was purified by column chromatography (Teledyne Isco CombiFlash Rf+ system, 12 g SiO_2, Hexane–EtOAc, 0-10%). The product was isolated as a yellow solid (0.08 g, 0.13 mmol, 68%). **M.P.** 205 – 207 °C. **^{1}H NMR** (700 MHz, $CDCl_3$) δ 7.78 – 7.75 (m, 2H, H_{20}), 7.43 (dd, *J* = 8.2, 0.6 Hz, 4H, H_8), 7.28 (dd, *J* = 6.7, 2.9 Hz, 4H, $H_{16,17}$), 7.16 – 7.12 (m, 6H, $H_{12,13,14}$), 7.07 (dd, *J* = 8.0, 6.6 Hz, 4H, H_{18}), 7.03 (dd, *J* = 8.1, 7.1 Hz, 2H, H_7), 6.91 – 6.87 (m, 2H, H_{21}), 6.83 – 6.81 (m, 1H, H_{14}), 6.78 – 6.74 (m, 2H, H_{22}), 6.33 (dd, *J* = 7.2, 0.6 Hz, 2H, H_6). **^{13}C NMR** (176 MHz, $CDCl_3$) δ 144.1 (C_3), 142.4 (C_{15}), 141.9 (C_2), 140.5 (C_{11}), 138.8 (C_{21}), 137.1 (C_{22}), 133.5 (C_{17}), 131.9 (C_{16}), 129.7 (C_4), 128.5 (C_5), 128.1 (C_9), 127.9 (C_{12}), 127.8 (C_{14}), 127.4 (C_{18}), 127.3 (C_{13}), 127.2 (C_{19}), 126.9 (C_7), 126.5 (C_{20}), 126.4 (C_8), 124.5 (C_6), 115.4 (C_{10}), 80.4(C_1). **HR-ESI MS** *m/z* = 595.2440 $[M-OH]^+$ (calculated for $C_{47}H_{31}$ = 595.2426).

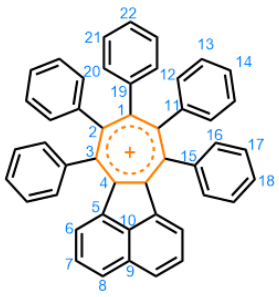

NapC$_7$Ph$_5$·SbCl$_6$: A pure sample of **NapC$_7$Ph$_5$OH** (3.6 mg, 6 µmol) was dissolved in $CDCl_3$ (0.6 mL) and taken in a NMR tube. $Et_3O^+SbCl_6^-$ (5 mg, 0.01 mmol) was added to the NMR tube under N_2 atmosphere at RT. The yellow solution immediately turned to orange colour indicating the formation of the corresponding tropylium cation. **^{1}H NMR** (700 MHz, $CDCl_3$) δ 8.22 (d, *J* = 8.0 Hz, 2H, H_8), 7.49 – 7.47 (m, 2H, H_{21}), 7.46 – 7.40 (m, 4H, H_{12}), 7.38 – 7.29 (m, 6H, $H_{16,20}$), 6.94 – 6.83 (m, 8H, $H_{7,13,14}$), 6.81– 6.71 (m, 7H, $H_{17,18,22}$), 6.38 (d, *J* = 7.8 Hz, 2H, H_6). **^{13}C NMR** (176 MHz, $CDCl_3$) δ 162.2 (C_2), 162.1 ($C_{3\text{ or }4}$), 159.6 (C_1), 157.2 ($C_{3\text{ or }4}$), 141.1 (C_9), 140.4 (C_{10}), 135.4 (C_8), 135.3 (C_{15}), 135.2 (C_5), 134.5 (C_6), 131.4 (C_{11}), 129.9 (C_{13}), 129.8 (C_{17}), 129.8 (C_{16}), 129.6 (C_7), 129.4 (C_{12}), 129.0 (C_{21}), 128.7 (C_{20}), 127.1 (C_{14}), 126.9 (C_{19}), 126.9 (C_{22}), 126.8 (C_{18}). **HR-ESI MS** *m/z* = 595.2440 $[M]^+$ (calculated for $C_{47}H_{31}$= 595.2426).

3.6 Appendix of Supplementary Data and Discussion

3.6.1 Synthesis of 3,8-Diethylacenaphthenequinone

The synthesis of 3,8-diethylacenaphtenequinone was adapted from two literature reports to give an 34% overall yield over 7 steps.[29,30]

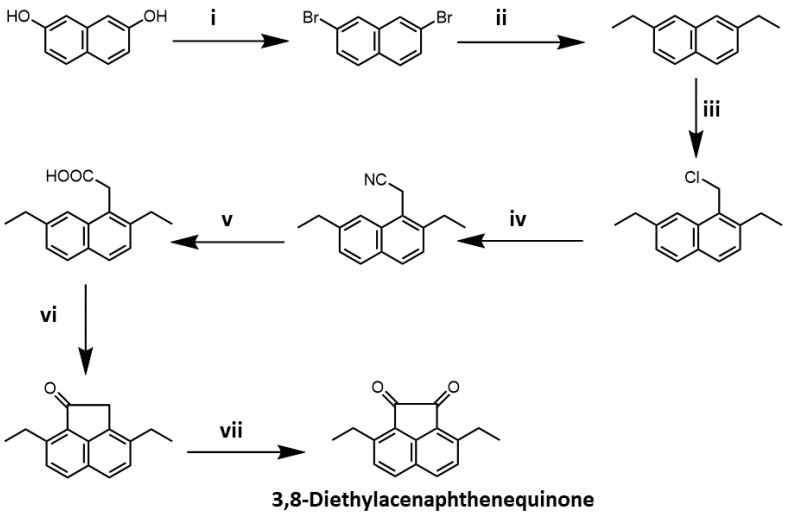

Scheme 3.6. Synthesis route used to prepare **3,8-diethylacenaphtenequinone**. Reagents and conditions: i) PPh_3 / MeCN / Br_2 / 0–250 °C / 50 min / 62%; ii) EtMgCl / $Ni(dppp)_2Cl_2$ / THF / 0 °C to reflux / 30 min / quant.; iii) Paraformaldehyde / $HCl_{(g)}$ / acetic acid / 50 °C / 20 h / 95%; iv) KCN / $(CH_3)_2CO$ / 70 °C / 18 h / 96%; v) H_2SO_4/ AcOH / Reflux / 24 h / 75%; vi) $SOCl_2$ / $AlCl_3$ / Reflux / 30 min / 90%; vii) SeO_2 / dioxane / H_2O / 70 °C / 5 h / 90%.

3.6.2 NMR Spectroscopy

Oxidation of **Ph_7C_7H** increases the symmetry from C_2 to C_7 as each peripheral phenyl ring of **$Ph_7C_7^+$** is now equivalent. This results in significant simplification of the ^1H NMR spectrum (Figure 3.2). **$NapPh_5C_7^+$** retains (Figure 3.3) its C_2 symmetry as a result of the napthyl moiety preventing the remaining five phenyl rings becoming equivalent, however some broadening can be observed along with a downfield shift for the napthyl protons. Unlike the other two cations, **$PhenPh_5C_7^+$** decreases in symmetry (Figure 3.4) as the C_2 element of cycloheptatriene is disrupted by the structural rearrangement. The Dewer benzene-like isomer means each peripheral phenyl group is inequivalent, increasing the number of unique proton environments, which is consistent with the reported X-ray crystal structure. The increase in symmetry is only possible when forming the aromatic tropylium isomer, reinforcing that all **$Ph_7C_7^+$** and **$NapPh_5C_7^+$** molecules adopt the conformation observed in the X-ray crystal structure and we do not observe selective crystallisation of one isomer.

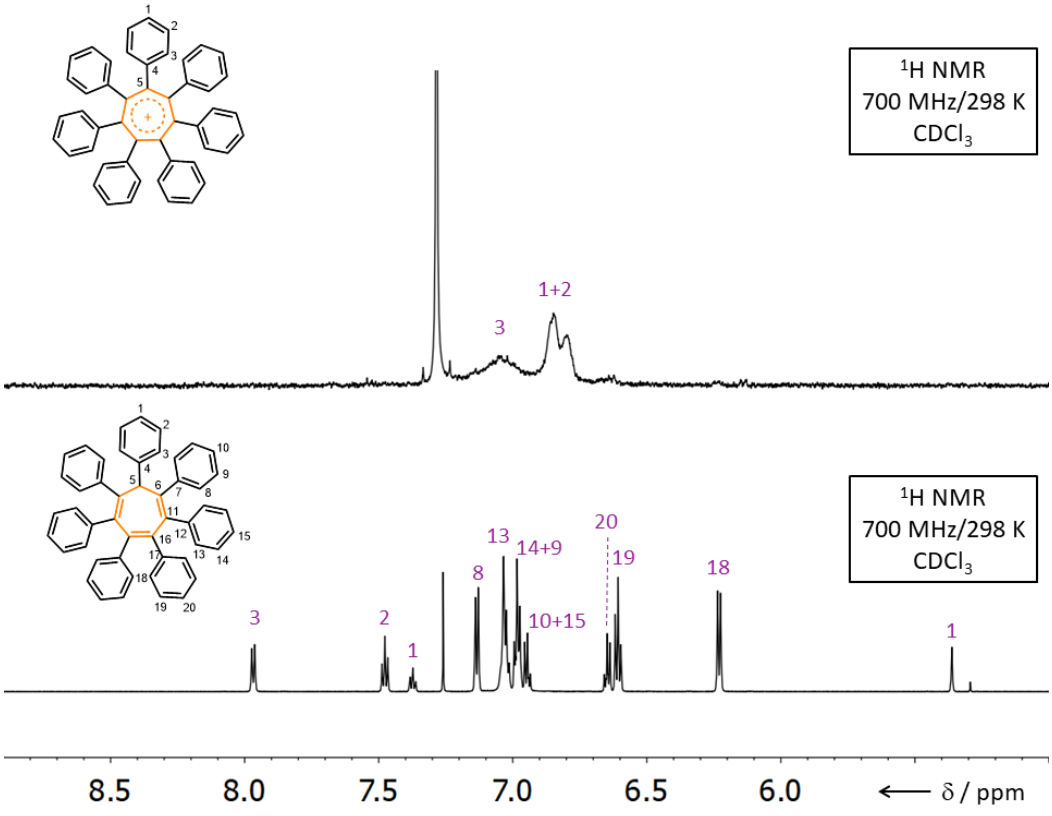

Figure 3.3. ^1H NMR spectra of **Ph_7C_7H** and **$Ph_7C_7^+$**.

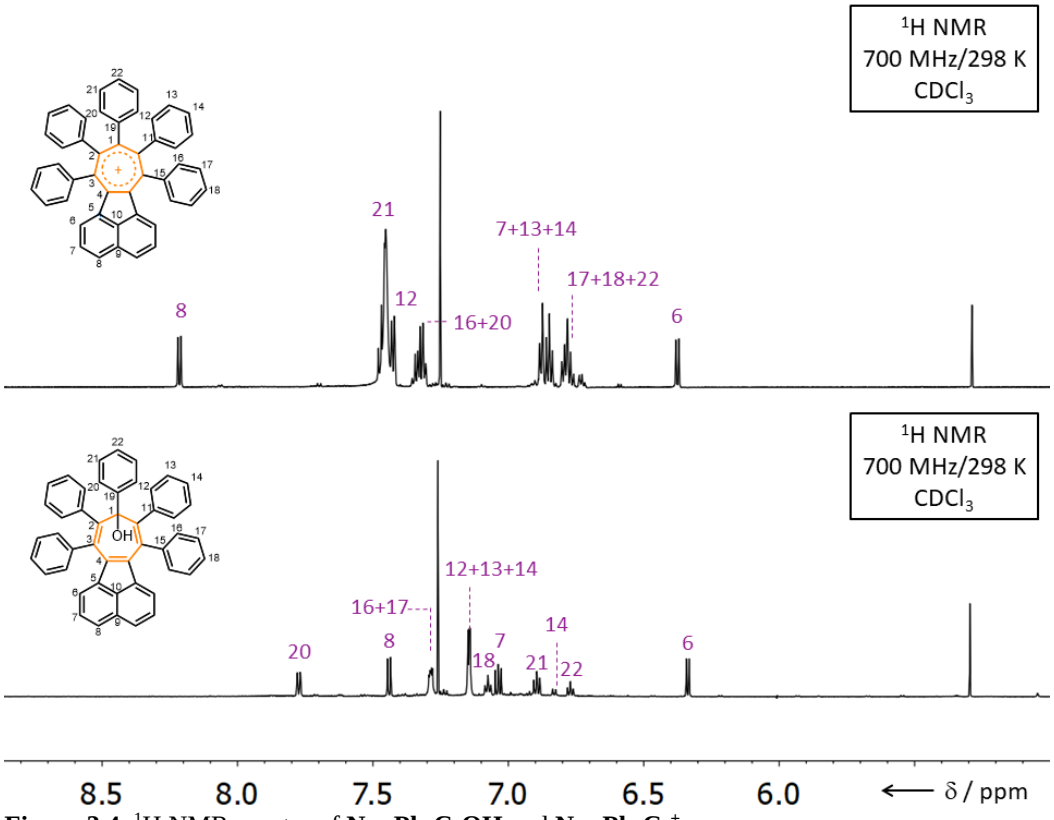

Figure 3.4. ^{1}H NMR spectra of **NapPh$_5$C$_7$OH** and **NapPh$_5$C$_7^+$**.

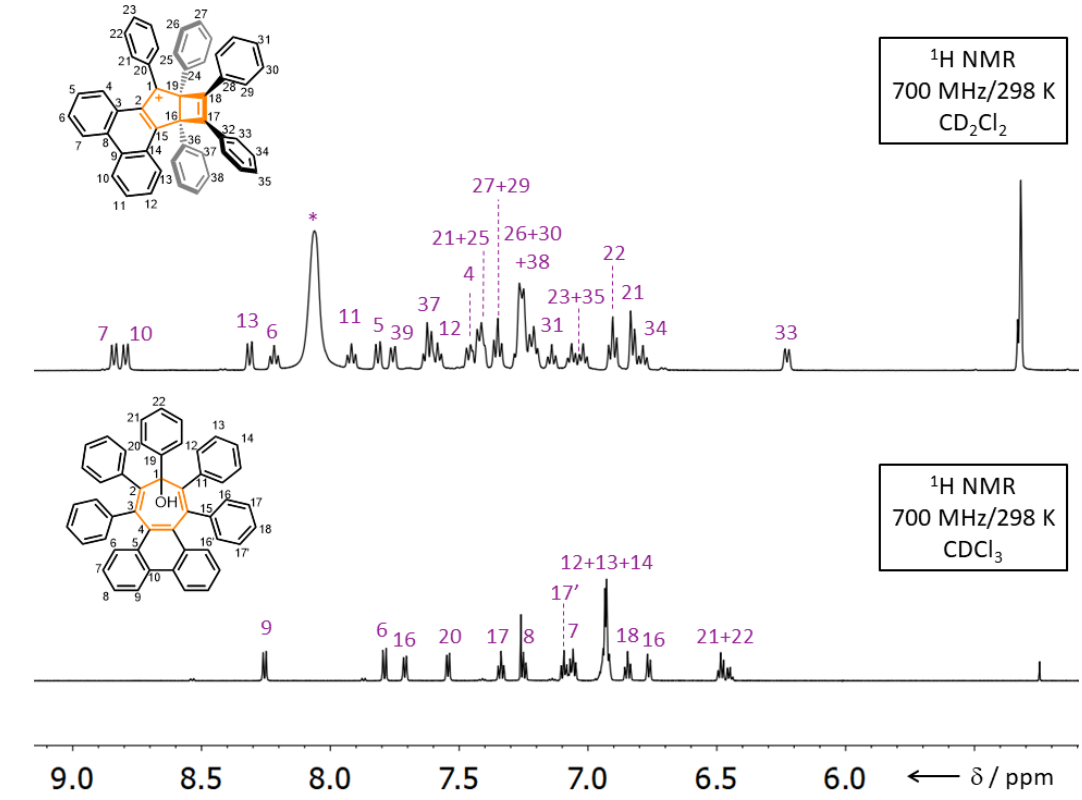

Figure 3.5. ^{1}H NMR spectra of **PhenPh$_5$C$_7$OH** and **PhenPh$_5$C$_7^+$**.

3.6.3 Calculated Tropylium Isomers

In 2016 Lyngdoh et al.[22] reported a computational study utilising B3LYP and MP2 methods to study isomerisation reactions of fifteen $C_7H_7^+$ cations in the gas phases (Scheme 3.8). In their ground state, all fifteen $C_7H_7^+$ are expected to be singlet closed shell systems. The aromatic tropyl cation **1** is the lowest energy isomer due to its aromatic stabilisation energy and lack of strain. Lyngdoh et al. also outlined the mechanisms by which these rearrangements occur (Scheme 3.7).

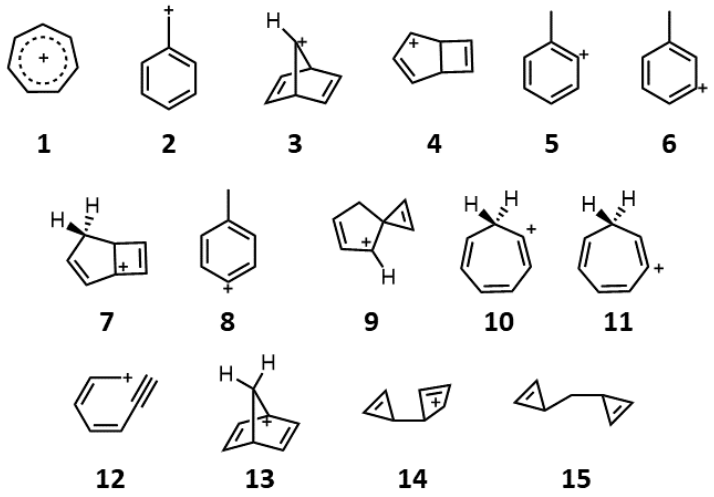

Scheme 3.7. Calculated (MP2) ground state structures of $C_7H_7^+$ in order of increasing energy as predicted by MP2 calculations.

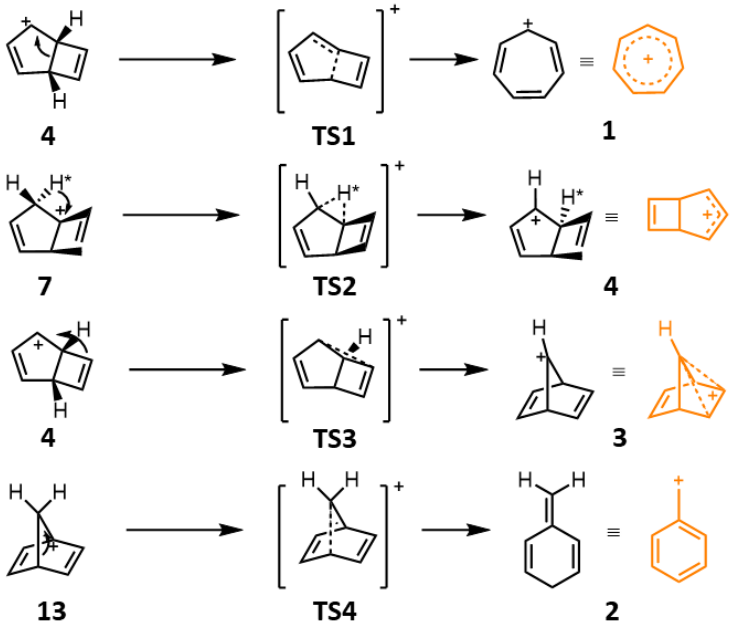

Scheme 3.8. Calculated (MP2) ground state structures of $C_7H_7^+$ in order of increasing energy as predicted by MP2 calculations.

3.6.4 X-ray Crystallographic Analysis

Analysis of all crystal structures are shown (Figure 3.6 – 3.14) with the crystal system, space group, unit cell parameters reported below.

Diethylacecyclone

Crystals of **Diethylacecylone** suitable for X-ray diffraction were grown by slow evaporation of a mixture of CH_2Cl_2-Hexane.

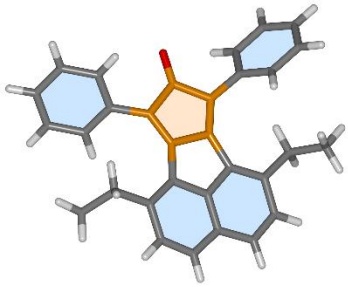

Figure 3.6. Solid-state structure of **diethylacecyclone**.

Crystal System: Monoclinic

Space group: C 1 2/c 1

Unit Cell Parameters: a = 17.2135(9) Å, b = 10.7061(4) Å, c = 24.661(1) Å, α= 90 °, β = 101.394(5) °, 98.2832(14) °, γ = 90.0000 °, V = 4455.2(4) $Å^3$, Z = 8.

PhenC$_7$Ph$_4$O

Crystals of **PhenC$_7$Ph$_4$O** suitable for X-ray diffraction were grown by slow evaporation of a PhMe.

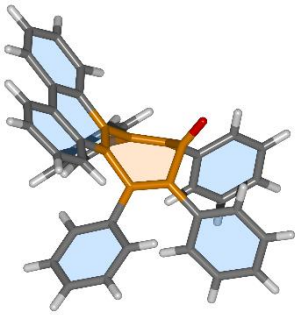

Figure 3.7. Solid-state structure of **PhenC$_7$Ph$_4$O**.

Crystal System: Triclinic

Space group: P-1

Unit Cell Parameters: a = 9.3113(6) Å, b = 10.5095(7) Å, c = 16.2093(10) Å, α 84.875(3), β = 80.864(3) °, 98.2832(14) °, γ = 75.921(3) °, V = 1516.90(17) Å^3, Z = 1.

PhenC$_7$Ph$_5$OH

Crystals of **PhenC$_7$Ph$_5$OH** suitable for X-ray diffraction were grown by slow evaporation of a mixture of CH_2Cl_2-Et_2O.

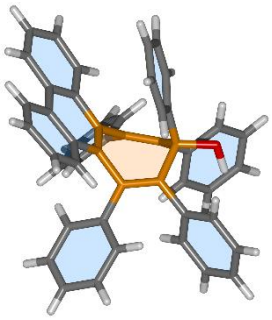

Figure 3.8. Solid-state structure of **PhenC$_7$Ph$_5$OH**.

Crystal System: Monoclinic

Space group: P-1 21/c 1

Unit Cell Parameters: a = 20.8941(13) Å, b = 9.4305(4) Å, c = 18.9622(10) Å, α = 90°, β = 115.035(7) ° γ = 90 °, V = 3385.3(4) Å^3, Z = 4.

PhenC$_7$Ph$_5$·SbCl$_6$

Crystals of **PhenC$_7$Ph$_5$·SbCl$_6$** suitable for X-ray diffraction were grown by slow evaporation of a mixture of CH_2Cl_2-Hexane.

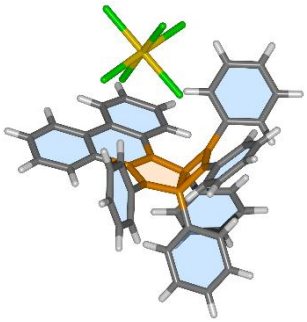

Figure 3.9. Solid-state structure of **PhenC$_7$Ph$_5$·SbCl$_6$** .

Crystal System: Monoclinic

Space group: P-1 21/n 1

Unit Cell Parameters: a = 11.0794(6) Å, b = 19.5994(11) Å, c = 59.837(3) Å, α = 90 °, β = 93.9088(15) °, γ = 90 °, V = 12963.4(12) Å^3, Z = 3.

NapC$_7$Ph$_4$O

Crystals of **NapC$_7$Ph$_4$O** suitable for X-ray diffraction were grown by slow evaporation of a mixture of CH_2Cl_2-Hexane.

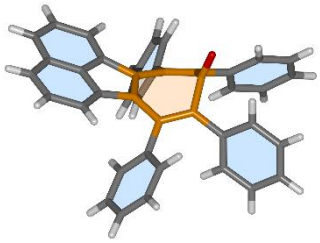

Figure 3.10. Solid-state structure of **NapC$_7$Ph$_4$O**.

Crystal System: Triclinic

Space group: P-1

Unit Cell Parameters: a = 10.3889(6) Å, b = 11.1459(7) Å, c = 14.2952(9) Å, α = 103.530(2) °, β = 103.151(2) °, γ = 112.377(2) °, V = 1392.85(15) Å^3, Z = 1.

NapC$_7$Ph$_5$OH

Crystals of **NapC$_7$Ph$_5$OH** suitable for X-ray diffraction were grown by slow evaporation of a mixture of Hexane-Et_2O.

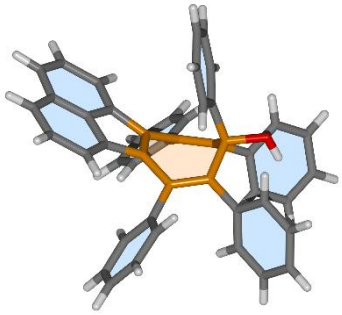

Figure 3.11. Solid-state structure of **NapC$_7$Ph$_5$OH**.

Crystal System: Monoclinic

Space group: P-1 21/c 1

Unit Cell Parameters: a = 19.5114(12) Å, b = 9.7395(6) Å, c = 19.9893(12) Å, α = 90 °, β = 107.714(4) °, γ = 90 °, V = 3618.5(4) Å^3, Z = 1.

$NapC_7Ph_5 \cdot SbCl_6$

Crystals of **$NapC_7Ph_5 \cdot SbCl_6$** suitable for X-ray diffraction were grown by slow evaporation of a mixture of CH_2Cl_2-Hexane.

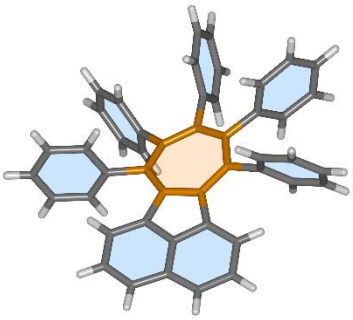

Figure 3.12. Solid-state structure of **$NapC_7Ph_5 \cdot SbCl_6$.**

Crystal System: Triclinic

Space group: P-1

Unit Cell Parameters a = 11.853(2) Å, b = 17.680(3) Å, c = 23.961(4) Å, α = 76.709(5) °, β = 76.366(5) °, γ = 89.443(6) °, V = 4743.8(14) $Å^3$, Z = 2.

$Et_2NapC_7Ph_5H$

Crystals of **$Et_2NapC_7Ph_5H$** suitable for X-ray diffraction were grown by slow evaporation of Hexane.

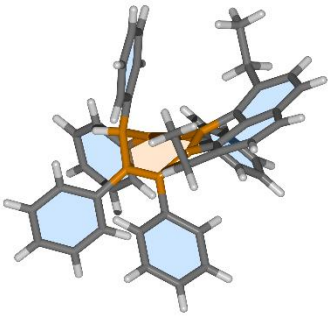

Figure 3.13. Solid-state structure of **$Et_2NapC_7Ph_5H$**.

Crystal System: Triclinic

Space group: P-1

Unit Cell Parameters a = 9.549(2) Å, b = 9.987(2) Å, c = 19.991(5) Å, α = 78.699(7) °, β = 88.107(6) °, γ = 79.154(7) °, V = 1836.1(7) $Å^3$, Z = 1.

$Ph_7C_7^+$

Crystals of $Ph_7C_7^+$ suitable for X-ray diffraction were grown by slow evaporation of CH_2Cl_2.

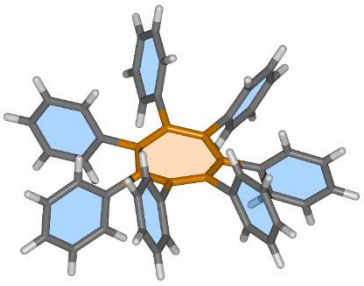

Figure 3.14. Sold-state structure of $Ph_7C_7^+$ viewed side-on the tropylium centre.

Crystal System: Monoclinic

Space Group: $P2_{1/c}$

Unit Cell Parameters: a = 26.864(2) Å, b = 27.059(2) Å, c = 22.8873(17) Å

3.6.5 UV-Vis Absorption Spectra

UV-Vis measurements were performed using anhydrous solvents CH_2Cl_2. Spectra were measured in 10 mm path-length cuvette at room temperature. 20 µM Sample concentrations of carbocycles **Ph_7C_7H**, **$Ph_7C_7^+$**, **$NapPh_5C_7OH$** and **$PhenPh_5C_7OH$** were all prepared from their corresponding solid materials. **$NapPh_5C_7^+$** and **$PhenPh_5C_7^+$** were recorded from 20 µM samples of their neutral species with 10 µL TfOH added. The samples were sparged briefly with N_2 to displace any $CF_3SO_3H{\cdot}H_2O$ fumes formed when TfOH is in contact with the air.

The intensities were plotted as molar absorptivity ε defined by the formula:

$$\varepsilon = \frac{I}{c \cdot l}$$

where I is the measured intensity, c is the concentration of sample, and l is path length of the cuvette.

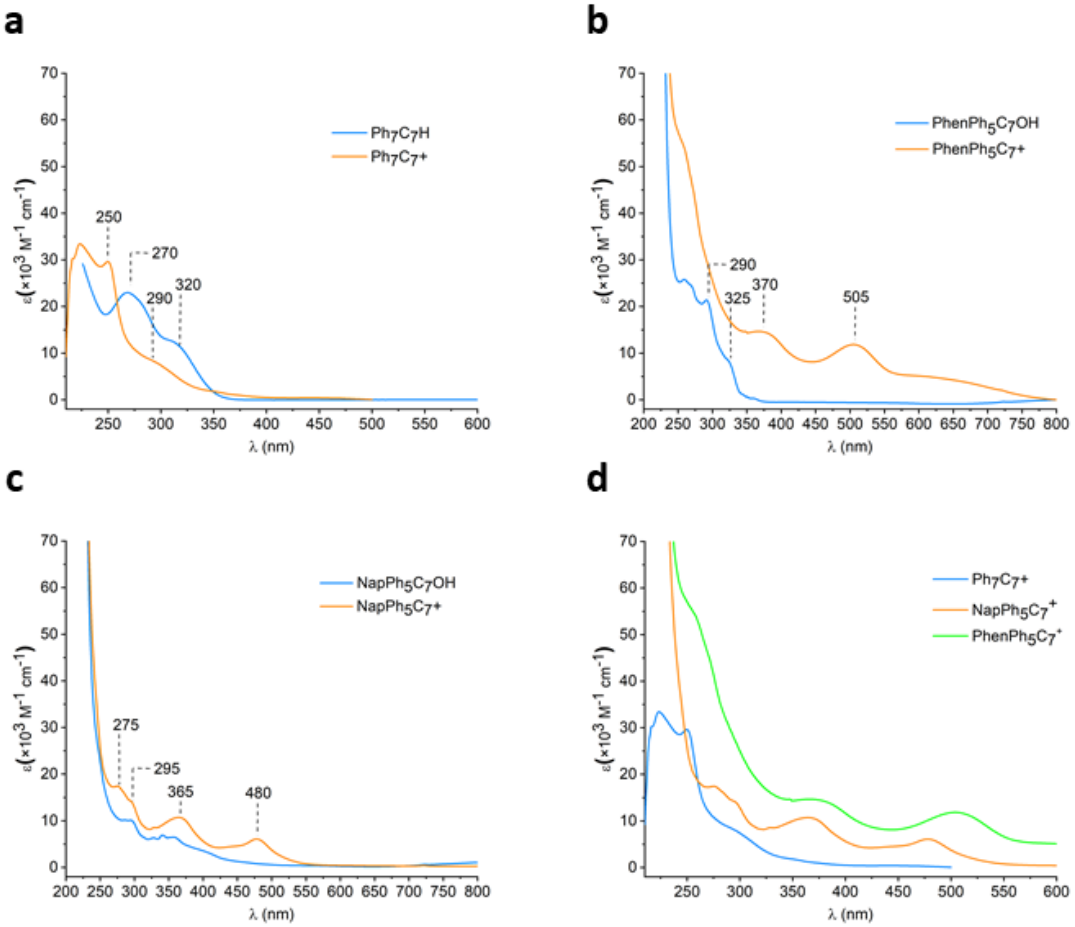

Figure 3.15. UV-Vis absorption spectra of CH_2Cl_2 solutions a) **Ph_7C_7H** and **$Ph_7C_7^+$** b) **$PhenPh_5C_7OH$** and **$PhenPh_5C_7^+$** c) **$NapPh_5C_7OH$** and **$NapPh_5C_7^+$**. d) Comparison of all three cations.

3.6.6 Room-Temperature Fluorescence

Samples for fluorescence were prepared using 1 mg/ml CH_2Cl_2 stock solutions. The desired quantity was diluted to achieve the desired 20 µM concentration. For cations **NapPh$_5$C$_7$$^+$** and **PhenPh$_5C_7$$^+$**, a 20 µM sample of the neutral species was prepared and a 10 µL of TfOH was added and stirred for 20 min. The samples were sparged briefly with N_2 to displace any $CF_3SO_3H{\cdot}H_2O$ fumes formed.

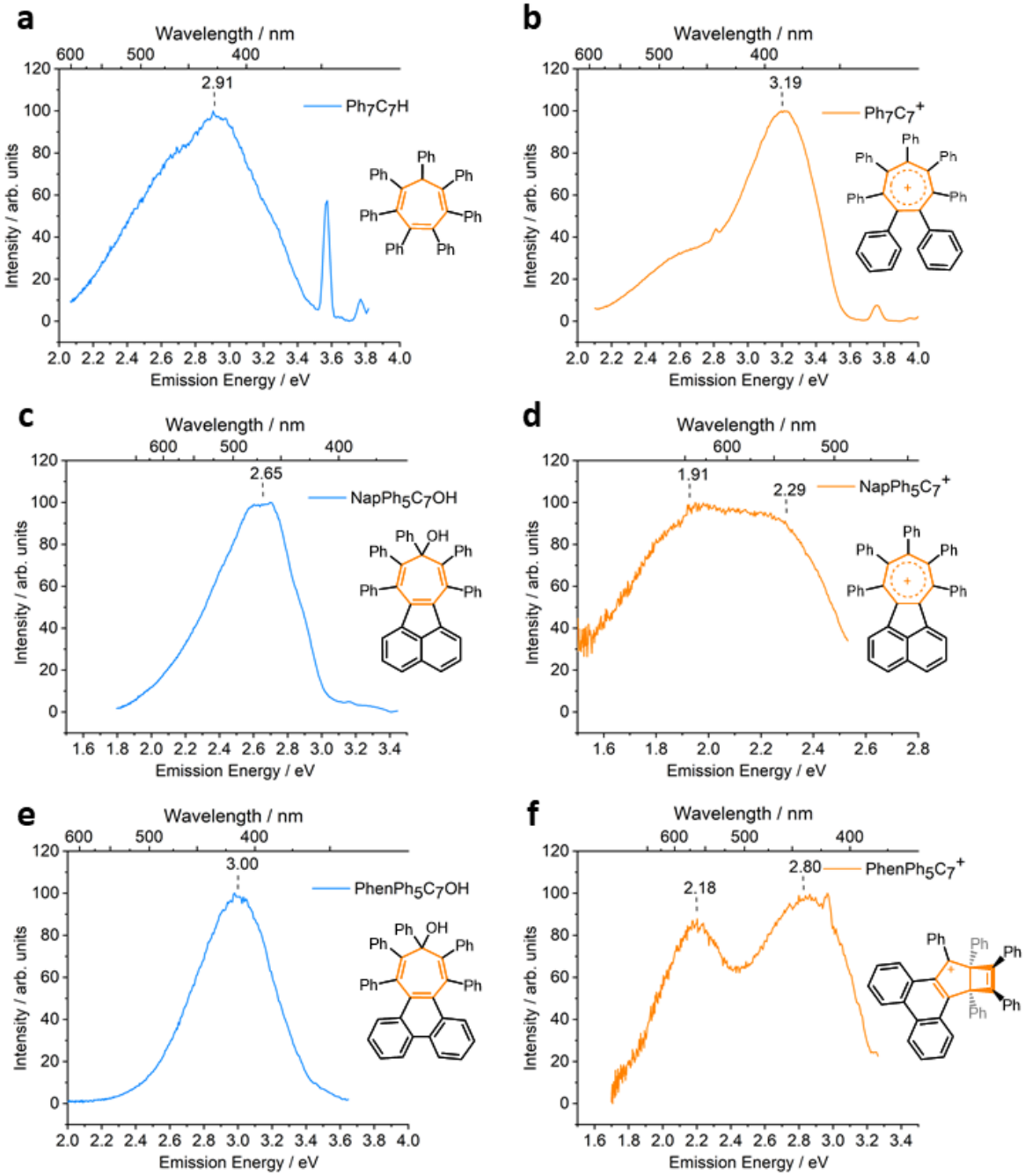

Figure 3.16. Room-temperature fluorescence spectra of a CH_2Cl_2 solutions (l = 10 mm, T = 298 K, c = 20 µM) of a) **Ph$_7$C$_7$H** b) **Ph$_7$C$_7$$^+$** c) **NapPh$_5C_7$OH** d) **NapPh$_5C_7$$^+$** e) **PhenPh$_5C_7$OH** f) **PhenPh$_5C_7$$^+$**.

3.6.7 Phosphorescence

The absorption of a photon from the ground state to the first excited singlet state (S_1) can be followed by decay back to the ground state and achieved through internal conversion or through the emission of a photon (Fluorescence). A third pathway back to the ground state is the relaxation of the system to a triplet state, T_1, via intersystem crossing. The triplet state is usually a long-lived state that decays over a longer time scale (phosphorescence). The presence of phosphorescence for the six molecular rotors discussed in this chapter were measured using an Intensified Charged Coupled Device (ICCD) (Figure 2.29). At room temperature no phosphorescence for any compound was observed therefore each recorded spectrum was at 80 K. The lower temperature reduces the rate of non-radiative decay promoting both fluorescence and phosphorescence.

To prevent unwanted energy transfer between the excited state and the solvent, each compound was measured as a 1% w/w ZEONEX film. The films were place inside a cryostat and the sample holder was held under active vacuum for 30 min to expel any oxygen that could quench phosphorescence. The sample was then cooled to 80 K and was held at temperature for 30 min before the measurement began.

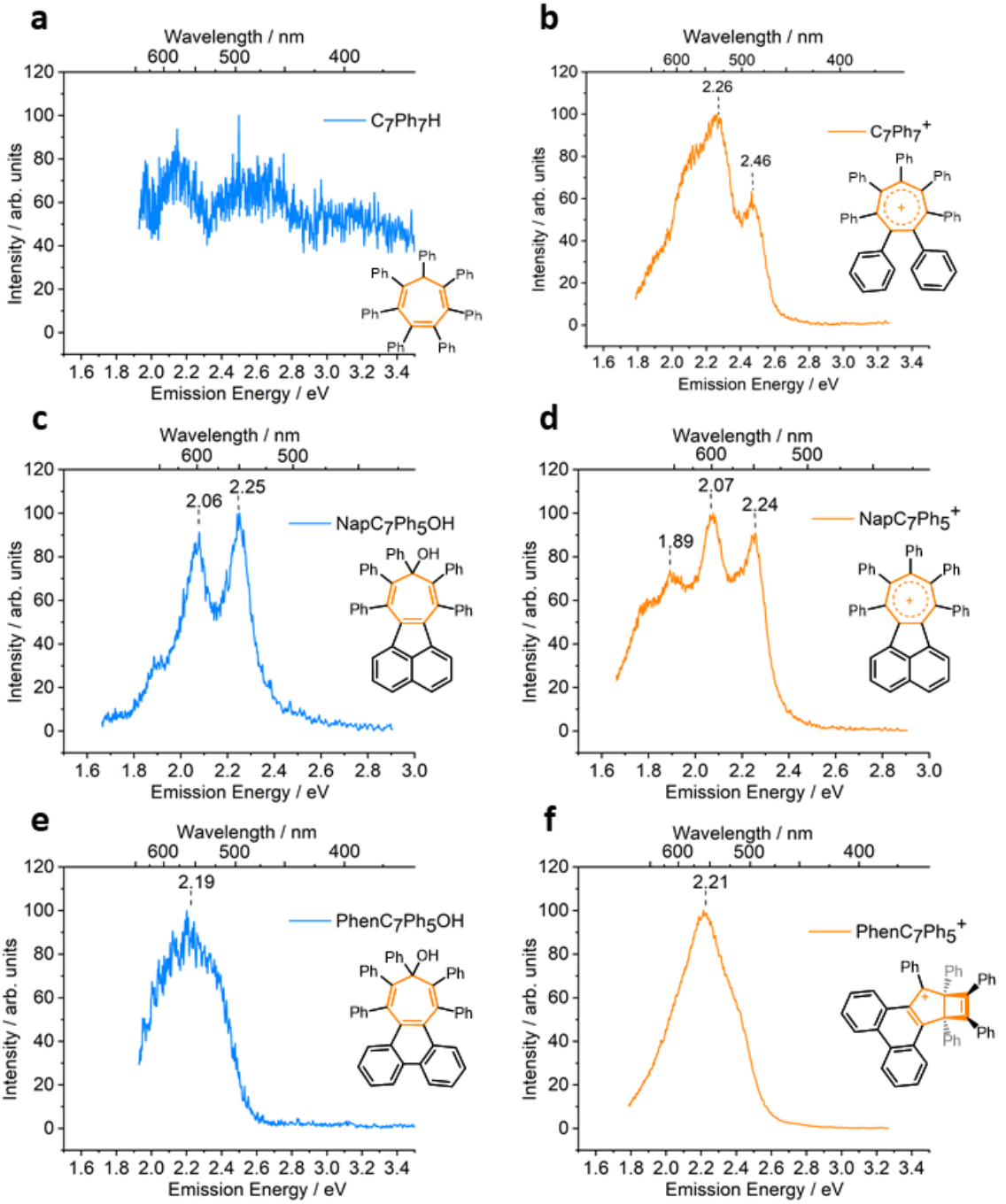

Figure 3.17. Phosphorescence spectra of 1% ZEONEX films (80 K) of a) **Ph_7C_7H** b) **$Ph_7C_7^+$** c) **$NapPh_5C_7OH$** d) **$NapPh_5C_7^+$** e) **$PhenPh_5C_7OH$** f) **$PhenPh_5C_7^+$**.

3.6.8 Time-Correlated Single Photon Counting (TCSPC)

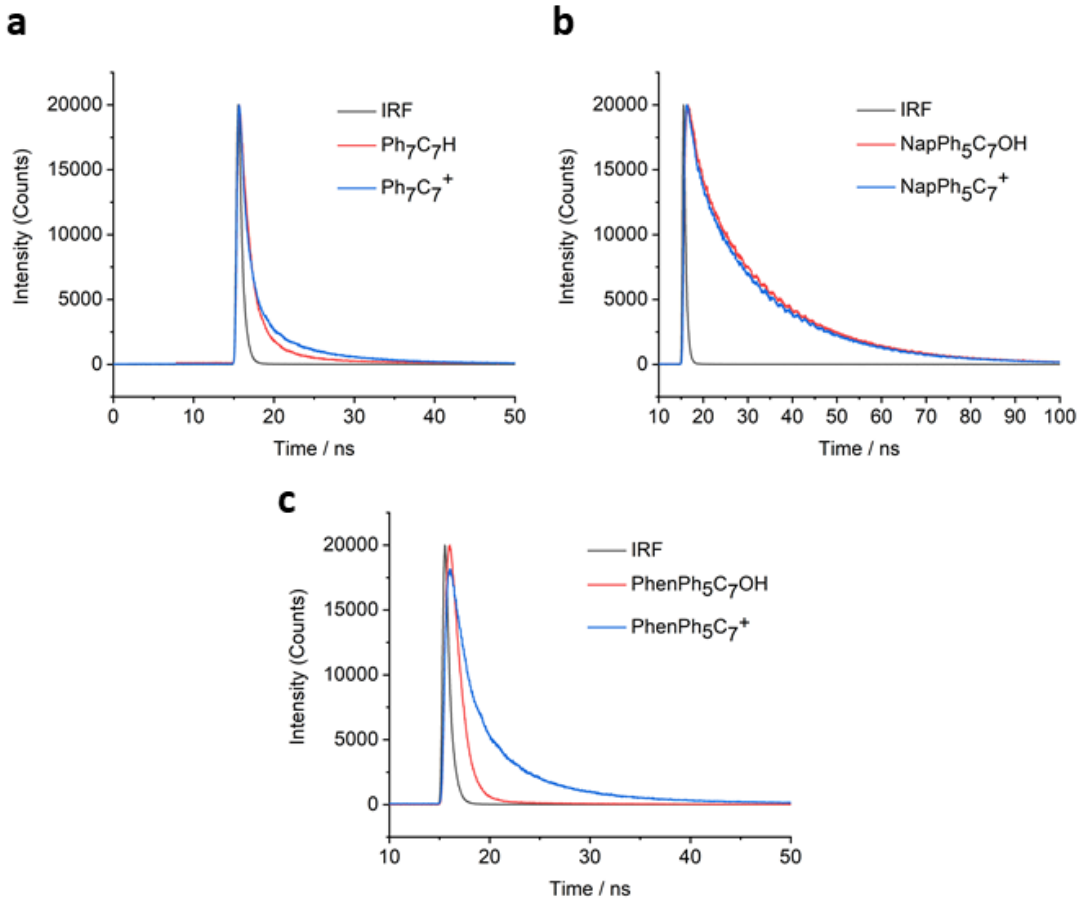

Figure 3.18. TCSPC decays of (a) **Ph_7C_7H** and **$Ph_7C_7^+$** (b) **$NapPh_5C_7OH$** and **$NapPh_5C_7^+$** (c) **Ph_7C_7H-O**, ***sym*-$phenPh_5C_7H$-O** and ***asym*-$phenPh_5C_7H$-O**. Measured as 2 µM solutions in 2-MeTHF.

Table 2. Lifetimes from the exponential fits for the decays of molecular rotors in 2-MeTHF.

Rotor	χ^2	I(t) = a1*exp(-τ/τ1) + a2*exp(-τ/τ2)) + a3*exp(-τ/τ3)					
		a1	τ1 /ns	a2	τ2 /ns	a3	τ3 /ns
C_7Ph_7H	6.02	0.9999	0.0034	0.0000	1.6341	0.0000	10.4311
$C_7Ph_7^+$	11.17	0.9533	0.1060	0.0035	19.8208	0.0432	3.5700
$NapPh_5C_7OH$	5.95	0.3352	1.5202	0.5127	14.1572	0.1521	25.0000
$NapPh_5C_7^+$	4.62	0.4213	1.1253	0.4585	14.2173	0.1202	25.0000
$PhenPh_5C_7OH$	1.630	0.0068	5.3186	0.0016	25.0000	0.9915	0.8356
$PhenPh_5C_7^+$	14.338	0.6760	0.6235	0.3080	4.5468	0.0160	25.0000

3.7 References

1. M. Rickhaus, M. Mayor and M. Juríček, *Chem. Soc. Rev.*, 2016, **45**, 1542–1556.
2. M. Rickhaus, M. Mayor and M. Juríček, *Chem. Soc. Rev.*, 2017, **46**, 1643–1660.
3. M. A. Majewski and M. Stępień, *Angew. Chemie - Int. Ed.*, 2019, **58**, 86–116.
4. R. Rieger and K. Mullen, *J. Phys. Org. Chem.*, 2010, **23**, 315–325.
5. Y. Segawa, A. Yagi, K. Matsui and K. Itami, *Angew. Chemie - Int. Ed.*, 2016, **55**, 5136–5158.
6. S. Ito, S. Hiroto, S. Lee, M. Son, I. Hisaki, T. Yoshida, D. Kim, N. Kobayashi and H. Shinokubo, *J. Am. Chem. Soc.*, 2015, **137**, 142–145.
7. M. A. Dobrowolski, M. K. Cyrański, B. L. Merner, G. J. Bodwell, J. I. Wu and P. V. R. Schleyer, *J. Org. Chem.*, 2008, **73**, 8001–8009.
8. M. Hermann, D. Wassy, D. Kratzert and B. Esser, *Chem. - A Eur. J.*, 2018, **24**, 7374–7387.
9. R. C. Haddon, *J. Am. Chem. Soc.*, 1990, **112**, 3385–3389.
10. M. Saito, H. Shinokubo and H. Sakurai, *Mater. Chem. Front.*, 2018, **2**, 635–661.
11. Y. Wu, M. Frasconi, D. M. Gardner, P. R. McGonigal, S. T. Schneebeli, M. R. Wasielewski and J. F. Stoddart, *Angew. Chemie - Int. Ed.*, 2014, **53**, 9476–9481.
12. J. A. Christensen, J. Zhang, J. Zhou, J. N. Nelson and M. R. Wasielewski, *J. Phys. Chem. C*, 2018, **122**, 23364–23370.
13. J. R. Brandt, F. Salerno and M. J. Fuchter, *Nat. Rev. Chem.*, 2017, **1**, 0045
14. P. Wang, I. Jeon, Z. Lin, M. D. Peeks, S. Savagatrup, S. E. Kooi, T. Van Voorhis and T. M. Swager, *J. Am. Chem. Soc.*, 2018, **140**, 6501–6508.
15. H. Tanaka, M. Ikenosako, Y. Kato, M. Fujiki, Y. Inoue and T. Mori, *Commun. Chem.*, 2018, **1**, 46.
16. S. Biswas, C. S. Qiu, L. N. Dawe, Y. Zhao and G. J. Bodwell, *Angew. Chemie Int. Ed.*, 2019, **58**, 9166–9170.
17. Y. Hu, P. Xie, M. De Corato, A. Ruini, S. Zhao, F. Meggendorfer, L. A. Straasø, L. Rondin, P. Simon, J. Li, J. J. Finley, M. R. Hansen, J. S. Lauret, E. Molinari, X. Feng, J. V. Barth, C. A. Palma, D. Prezzi, K. Müllen and A. Narita, *J. Am. Chem. Soc.*, 2018, **140**, 7803–7809.
18. Y. Zhong, B. Kumar, S. Oh, M. T. Trinh, Y. Wu, K. Elbert, P. Li, X. Zhu, S. Xiao, F. Ng, M. L. Steigerwald and C. Nuckolls, *J. Am. Chem. Soc.*, 2014, **136**, 8122–8130.
19. Y. Zhong, M. T. Trinh, R. Chen, G. E. Purdum, P. P. Khlyabich, M. Sezen, S. Oh, H. Zhu, B. Fowler, B. Zhang, W. Wang, C. Y. Nam, M. Y. Sfeir, C. T. Black, M. L. Steigerwald, Y. L. Loo, F. Ng, X. Y. Zhu and C. Nuckolls, *Nat. Commun.*, , DOI:10.1038/ncomms9242.
20. Y. Zhong, T. J. Sisto, B. Zhang, K. Miyata, X. Y. Zhu, M. L. Steigerwald, F. Ng and C. Nuckolls, *J. Am. Chem. Soc.*, 2017, **139**, 5644–5647.
21. J. Xiao, Y. Divayana, Q. Zhang, H. M. Doung, H. Zhang, F. Boey, X. W. Sun and F. Wudl, *J. Mater. Chem.*, 2010, **20**, 8167–8170.
22. K. S. Kharnaior, M. Devi and R. H. Duncan Lyngdoh, *Comput. Theor. Chem.*, 2016, **1091**, 150–164.
23. J. Sturala, M. K. Etherington, A. N. Bismillah, H. F. Higginbotham, W. Trewby, J. A. Aguilar, E. H. C. Bromley, A.-J. Avestro, A. P. Monkman and P. R. McGonigal, *J. Am. Chem. Soc.*, 2017, **139**, 17882–17889.

24. M. A. Battiste, *J. Am. Chem. Soc*., 1961, **83**, 4101.

25. S. Brydges, J. F. Britten, L. C. F. Chao, H. K. Gupta, M. J. McGlinchey and D. L. Pole, *Chem. Eur. J.*, 1998, **4**, 1201–1205.

26. M. Y. Berezin and S. Achilefu, *Chem. Rev.*, 2010, **110**, 2641–2684.

27. J. E. Norton and K. N. Houk, *J. Am. Chem. Soc.*, 2005, **127**, 4162–4163.

28. G. Yit Wooi and J. M. White, *Org, Biomol. Chem.*, 2005, **3**, 972-974

29. K. J. Schwarz, C. Yang, J. W. B. Fyfe and T. N. Snaddon, *Angew. Chemie Int. Ed.*, 2018, **57**, 12102–12105.

30. T. J. Seiders, E. L. Elliott, G. H. Grube and J. S. Siegel, *J. Am. Chem. Soc.*, 1999, **121**, 7804–7813.

CHAPTER 4

TOWARDS A REDOX-ACTIVE C_7-SYMMETRIC WARPED NANOGRAPHENE.

Synopsis

This chapter discusses our approach to devising aromatic-ion nanomaterials, focusing on the synthesis of a tropylium-centred nanographene, wherein the peripheral benzene rings are fused to produce a warped redox-active nanographene. In addition, this includes a counter ion that can be exchanged to allow for solution processing of the resulting material. The resulting structure will possess the unique and versatile characteristics of a charged aromatic system as well as a non-planar structural effect dictated by the odd-numbered central ring. Synthetic routes to many precursors have been successfully developed and promising steps have been made towards the targeted warped nanographene. The targeted redox-active warped nanographene is yet to be successfully isolated, however this chapter outlines the on-going investigation towards its synthesis.

Acknowledgments

The following people are gratefully acknowledged for their contribution to this chapter: Dr Aisha Bismillah performed the variable temperature NMR studies, Dr Paul McGonigal performed DFT studies and Dr Dimitry S. Yufit solved all X-ray crystal structures.

4.1 Introduction

The electronic properties and versatility of polyaromatic hydrocarbons (PAHs) make them promising materials for organic devices, such as light-emitting diodes (LEDs)[1], field effect transistors (FETs)[2], liquid crystal displays (LCDs) and solar cells.[3] Graphene[4–7] is the most notable PAH, containing, in theory, defect free one-dimensional hexagonal sheet. In reality, non-hexagonal defects are extremely common in the production of graphene, and through the Stone–Wales rearrangement embedded five-membered and seven-membered rings can form.[8,9] The optical absorption[10] and emission behaviour is of particular interest for those working with PAHs, because the absorption spectra is characteristic of their structure, like molecular fingerprints.[11] The chemical synthesis of PAHs was pioneered by Scholl[12–14] and Clar[15–17] and further developed throughout the 20th century by Mullen and Itami among others. Whilst most PAHs consist of a sp^2 carbon framework of fully conjugated benzene rings, even slight differences in their geometry and size can dramatically alter the optical, electronic and chemical properties of the resulting material. In order to model these defects, finite monomeric graphenes termed nanographenes were developed and extensively studied to deduce structure-property relationship.[18,19] Nanographenes, unlike conventional graphenes, show a non-zero band gap that is governed by their size and edge configurations.[20] A small number of reported nanographenes have structures distorted from planarity termed 'warped nanographenes'. These have shown an enhanced band-gap and unique physical properties which has attracted much recent interest.[21–23]

High impact neutral carbon materials such as graphene can be modified to possess the unique properties of charged aromatic systems *via* unsaturated odd numbered rings (aromatic ions).[24] Computational studies suggest that heptagon-embedded nanographenes with a negative Gaussian curvature possess a magnetic moment[25] and UV studies show increased fluorescence[26] compared to the planar counterparts. Alterations in electronic and optical properties of nanographenes are not only from non-planarity but also from simple changes in connectivity. Our approach to devising aromatic-ion nanomaterials focuses on synthesising a tropylium-centred nanographene to produce a warped redox active nanographene from C_7 molecular rotors.

4.2 Result and Discussion

Ph_7C_7H (Chapter 2) provides the basis of investigation towards a C_7 symmetric redox-active warped nanographene. Upon complete ring fusion of the peripheral rings in **Ph_7C_7H**, it is predicted to form a structure with a negative Gaussian curve (Figure 4.1a), as confirmed by DFT models (Figure 4.1b). Furthermore, the presence of the central cycloheptatriene also provides access to a stable aromatic cation through oxidation with a single-electron oxidant. Oxidation of the fully fused nanographene will produce redox-active nanographene (**1**).

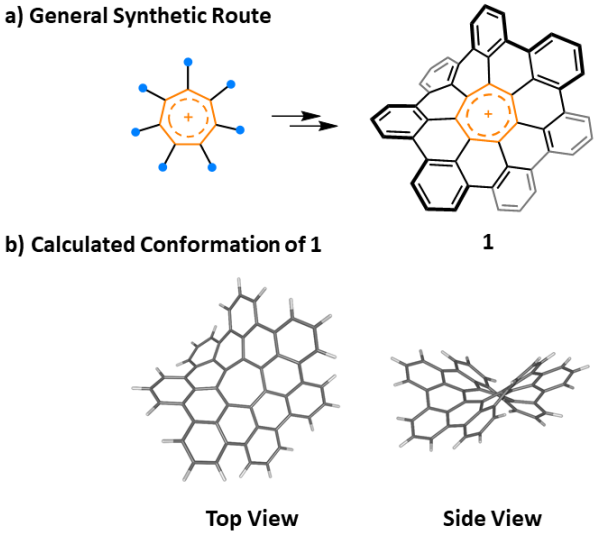

Figure 4.1. a) Proposed synthetic route to warped nanographene **1** from a heptaarylcycloheptatriene. b) Energy minimised conformation of nanographene **1**.

The aromaticity of the central ring in **$Ph_7C_7^+$** (Chapter 3) results in a planar conformation, as the p-orbitals align to allow for orbital overlap to produce a complete π-system (X-ray crystal analysis Figure 4.5). This planarization of the central ring pre-organises a conformation wherein the outer rings are orientated into the same plane, and thus coupling for **$Ph_7C_7^+$** would be expected to be easily facilitated. Initial reactions to link the peripheral phenyl rings in the ortho positions were first attempted with **Ph_7C_7H** and **$Ph_7C_7^+$** by exposing them to conventional intramolecular oxidative cyclodehydrogenation (IOCD) conditions[19] (Scholl conditions) of excess $FeCl_3$. Unfortunately, only the starting material was observed in the ^1H NMR and Mass spectrum (MS). As mentioned, a high-energy barrier is expected to exist to form **1**, as neighbouring rings must adopt a more sterically hindered co-planar orientation in order for IOCD to be successful. Since this is expected to be difficult, harsher conditions

were attempted. The use of DDQ/TfOH has gained popularity as a method for intramolecular arene coupling in recent years.[27] The presence of the strong acid prevents DDQ forming strong electron donor-acceptor complexes allowing DDQ to undergo a highly endothermic electron transfer reaction, forming the aromatic cation radical that is vital for arene coupling.[28]

The stronger oxidation conditions of DDQ/TfOH were successful in oxidising **Ph_7C_7H**, however, not *via* the expected IOCD mechanism. It was found that **$Ph_7C_7^+$** forms preferentially over any ring fusion products. Once central ring oxidation occurs, further oxidation of the cationic **$Ph_7C_7^+$** is not possible. The IOCD pathway (Scholl reaction) is thought to occur via a radical cation intermediate[29] (Scheme 4.1a). Due to the need to form a radical cation on an already conjugated cationic compound, IOCD is not possible from **$Ph_7C_7^+$**. The strong oxidant; DDQ/TfOH has an oxidation potential of 1.7 eV[30], therefore for successful oxidation the compound must have an oxidation potential less than this. As a result, all future efforts to synthesise nanographene **1** are from compounds that have neutral centres. Efforts in optimising the oxidation of **Ph_7C_7H** to **$Ph_7C_7^+$** have been reported in Chapter 3 using ICl as a one-electron oxidant and provides a much easier and higher yielding route than DDQ/TfOH.

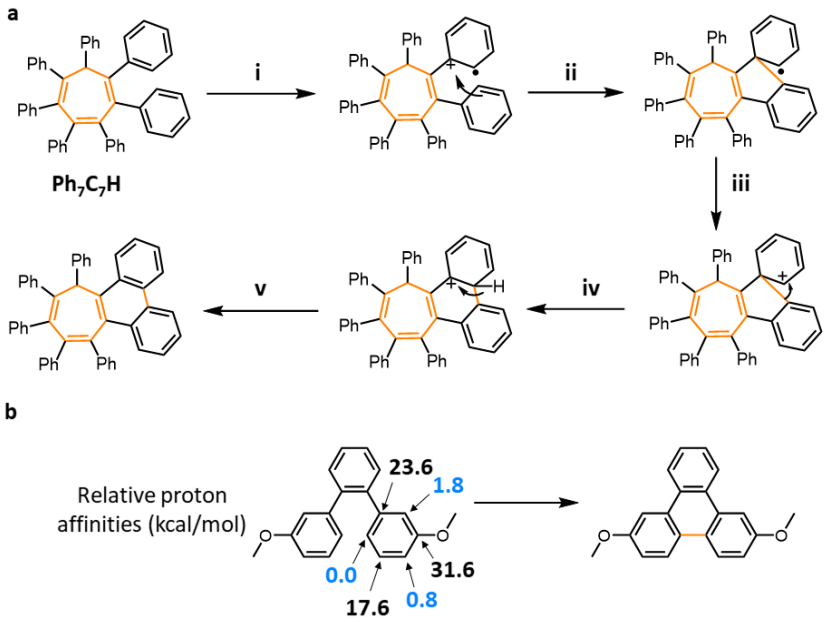

Scheme 4.1. a) The proposed mechanism of the intramolecular cyclodehydrogenation Scholl reaction of **Ph_7C_7H**; i) single-electron oxidation; ii) spirocyclisation iii) single-electron oxidation; iv) 1,2-aryl migration; v) deprotonation. b) Relative proton affinities of dimethoxy terphenyl as reported by King *et al.*[31] (B3LYP/6-31G*).

To favour peripheral ring fusion over central ring oxidation we modified the Diels-Alder precursors for **Ph_7C_7H** (Scheme 4.2a), replacing tetracyclone with phencyclone to give **phen-Ph_5C_7H**, (Scheme 4.2b). Whilst **phen-Ph_5C_7H** is categorised as an unfunctionalised CHT, it does contain an electron rich phenanthrene group and a pre-organised alignment of two adjacent rings. We propose that pre-organisation of two outer rings should give a thermodynamic advantage when it comes to fusion of the outer rings by orientating two rings in the desired co-planar orientation needed for successful IOCD. The IOCD of **phen-Ph_5C_7H** was partially successful using DDQ/TfOH, observing the formation of species with three, four, five and six fused peripheral rings in ESI-MS. The seven fused ring species (**1**) was the only homologue not observed *via* mass spectrometry. The most difficult ring to fuse is expected to be the phenyl ring sitting on the sp^3 carbon, above the central CHT ring. Fusion of this phenyl to the already six-fused phenyl rings would require overcoming a large energy barrier associated with increasing rigidity and conformational twisting. No isolation from this method was ever possible with the problems being accredited to the vast number of products and the very low yield of the resulting reaction. However, the evidence from mass spectrometry suggests that IOCD can occur in **phen-Ph_5C_7H** and provides evidence that the prefusion of two phenyl rings can favour further peripheral cyclodehydrogenation over central ring oxidation.

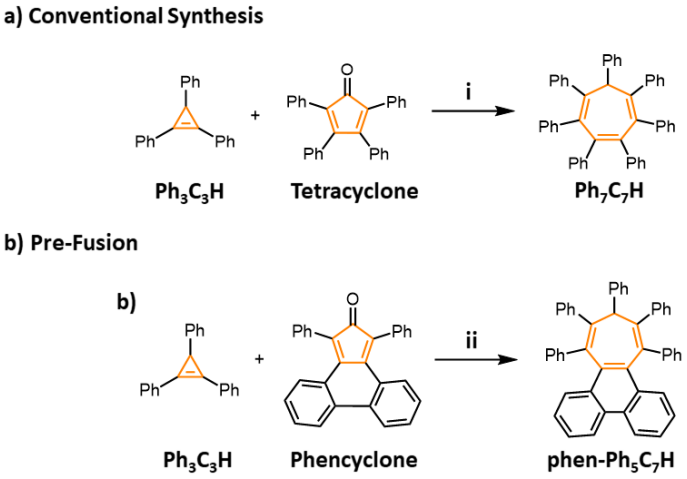

Scheme 4.2. a) The synthesis of **Ph_7C_7H** and **phen-Ph_5C_7H**. Reagents and conditions: i) *p*-xylene / 160 ˚C / 24 h / 74%; ii) *p*-xylene / 200 ˚C / 12 h / 70%.

Preliminary spectroscopic data for **phen-Ph_5C_7H** suggests that IOCD is possible in these molecular rotors however, further optimisation is required in order to isolate significant yields of targets compound. A reaction with high conversion to the final

product where all the peripheral rings are coupled together would greatly enhance the probability of isolating **1** by avoiding problems with complex, inseparable mixtures. In an attempt to overcome this problem, functionalisation of the peripheral phenyl rings of **Ph_7C_7H** were next assessed for their ability to undergo seven-fold cyclodehydrogenation to form a warped nanographene.

4.2.1 Peripheral Ring Functionalisation

In 2007, King et al.[31] calculated (B3LYP/6-31G*) the relative proton affinities (relative acidities) of dimethoxy terphenyl (Scheme 4.1b) and the susceptibility to IOCD. As expected, electron donating groups (e.g OMe groups), that are *ortho/para* directors, increase the stability of the cation radical intermediate in *ortho/para* positions. This occurs through electron donation into the *o/p* positions, stabilising the intermediate radical cation during IOCD. Hoping to exploit this, we synthesised a range of new functionalised **Ph_7C_7H** derivatives in an attempt to promote intramolecular oxidative cyclodehydrogenation over central ring oxidation. For this to be successful we had to redesign the precursors of **Ph_7C_7H** with the desired functionality embedded early in the synthesis to achieve this (Scheme 4.3 and 4.4). We decided initial efforts focus on introducing OMe groups to stabilise the radical cation intermediates. In addition, the methoxy groups should also increase the solubility of **Ph_7C_7H**, making samples easier to handle and purify.

Functionalisation of the peripheral rings of **Ph_7C_7H** provides a library of new heptaarylcycloheptatrienes (HACHTs). For ease of purification and characterisation only C_2 symmetric HACHTs were synthesised, where each peripheral ring bears the same functionality. Mixing the functionality of peripheral rings results in a large number of isomers through shifting of the sp^3 proton of the central cycloheptatriene. The following examples show two different pathways we developed to produce any desired functionalised HACHT. Flexible functionality is important when investigating future applications of HACHTs and nanographenes as potential donor–acceptor compounds and studying functionalisation effects on conformation and redox activity.

4.2.2 Synthesis of Substituted Cyclopropenes

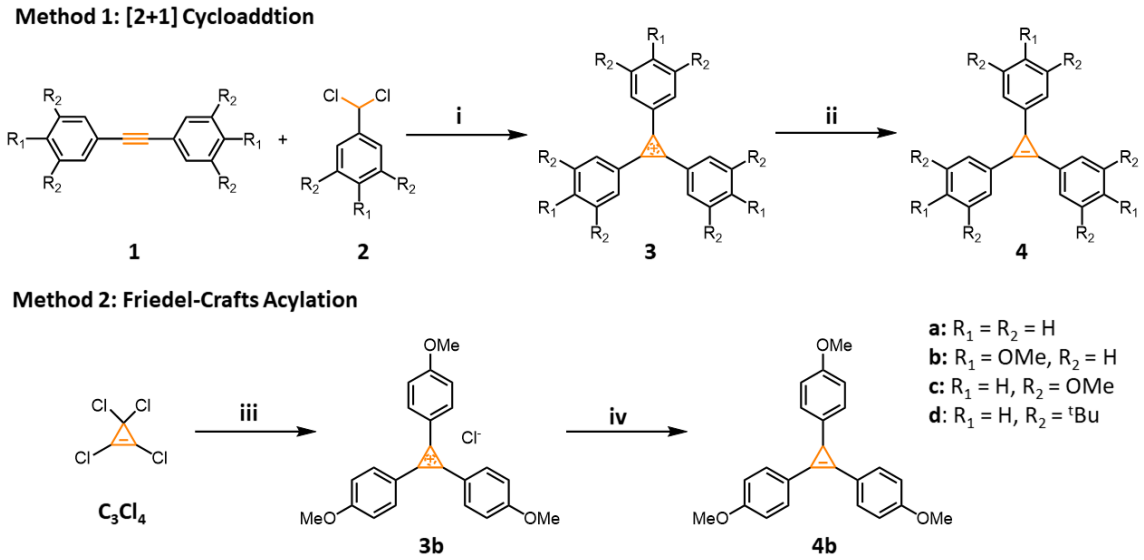

Scheme 4.3. Two synthetic methods towards triarylcyclopropene. Reagents and conditions; i) ^{t}BuOK / C_6H_6 / 100 ˚C / 3 h followed by HBr / Et_2O / rt / 30 min; ii) $NaBH_4$ / EtOH / 0 ˚C / 24 h; iii) Anisole / $AlCl_3$ / $CHCl_3$ / 80 ˚C / 30 min; iv) $NaBH_4$ / EtOH / 0 ˚C / 24 h / 94%.

The synthesis of cyclopropene precursors for the formation of functionalised CHTs is very dependent on the directing groups of the desired aryl groups and the regioisomers required (Figure 4.3) For example, if an *o/p* directing aryl group is desired with either *ortho* or *para* connection (relative to the functional group) to the central cyclopropene (i.e **4d**), then Method 2 is adequate. However, if *o/p* directors are used but require meta connection to the cyclopropene core (i.e **4c**), then method 1 would be required. Method 1 outlines a bottom-up synthetic approach adapted from M. Battises[32] procedure using diazo compounds to synthesise trisubstituted cyclopropenes. The [2+1] cycloaddition of alkynes with diazocompounds is a very reliable method for the formation of cyclopropenes, however its use is limited to compounds that have electron withdrawing groups required to stabilise the reactive diazocompounds. We report a modified method using *a,a*-dichlorotoluene as a carbene source, generated in-situ upon the addition of base. Upon formation the carbene can readily undergo a [2+1] cycloaddition with diphenylacetylene (**1a**) to form triphenylcyclopropenyl cation (**3a**) that can be subsequently reduced with $NaBH_4$ to give **Ph_3C_3H** (**4a**) in high yields. A benefit to this synthetic route towards trisubstituted cyclopropenes is the control over regiochemistry and functionality through modifying pre-cursors to synthesise **1** and **2**. This method was employed in achieving 3,5-dimethoxybenzenecyclopropene (**4c**) in a 52% yield. In most cases the diarylalkyne (**1**) and germinal dichloride (**2**) are not commercially

available, however both can be synthesised from the corresponding aryl bromide (precursor synthesis outlined in 4.5.2).

For molecules with the correct directing groups such as trianisolecyclopropene, **An_3C_3H** (**4b**), a much simpler two-step synthesis to functionalised cyclopropenes is possible (Method 2). With this in mind, **C_3Cl_4** is an ideal starting point for the synthesis of triarylcyclopropene. A threefold Lewis acid mediated substitution of chlorine atoms for anisole works in high yield of 94% over two steps to give **4d** with the correct configuration. The electron donating OMe groups of anisole are *o/p* directing however is shown to be regioselective to *para* substitution. This makes method 1 an ideal pathway to **An_3C_3H** (**4b**) ensuring retention of the correct stereochemistry. This route has now been used for the synthesis of multiple cyclopropenes, both symmetric and asymmetric, in the McGonigal group.

4.2.3 Synthesis of Substitued Cyclopentadieneones

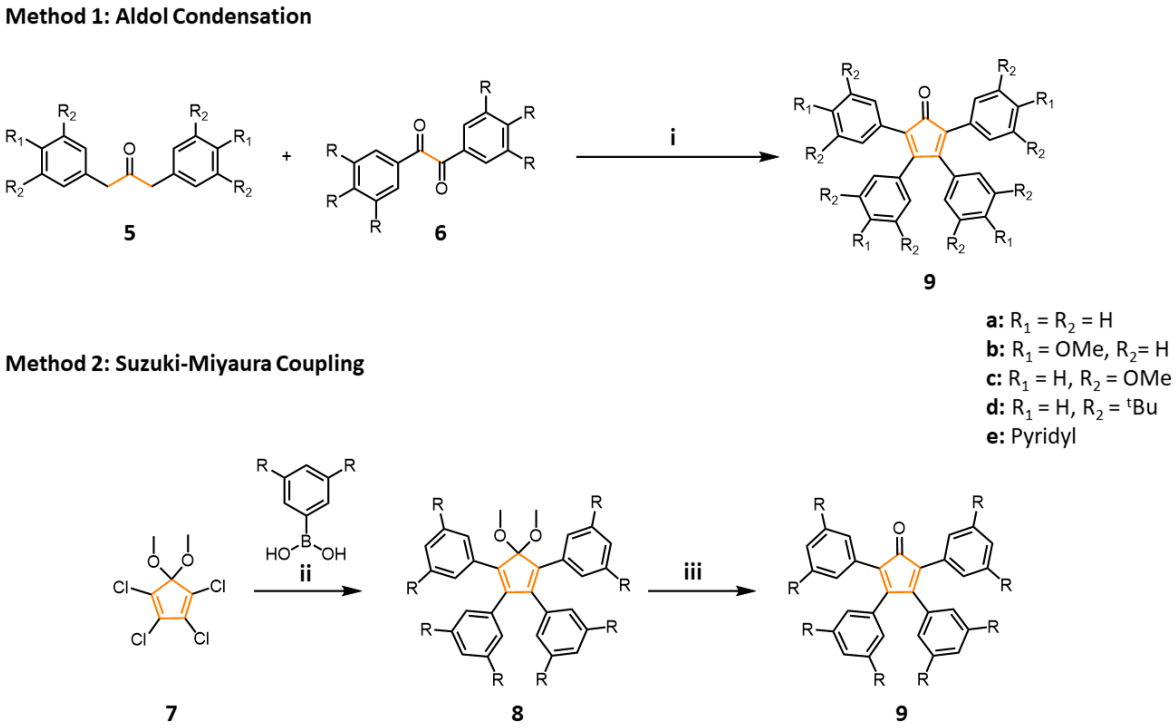

Scheme 4.4. Two synthetic methods towards triarylcyclopentadienone. Reagents and conditions; i) 2 M $NaOH_{(aq)}$ / EtOH / 90 ˚C / 2 h; ii) NaOH / SPhos / $Pd(OAc)_2$ / PhMe / 95 ˚C / 4 h; iii) 4% TFA / CH_2Cl_2 / 0 ˚C / 30 min.

Two synthetic routes for the formation of cyclopentadieneones are shown in Scheme 4.2. Method 1 is adapted from a 1943 report by Grummitt et al[33] for the synthesis of tetraphenylcyclopentadienone (**9a**). A base catalysed aldol condensation of

commercially available diphenylpropen-2-one (**5a**) and a benzil (**6a**) gives **9a** in high yields of 90%. When introducing functionality to **9**, commercially available precursors are unavailable and synthesis of **5** and **6** from the corresponding arylbromide are required (Precursor synthesis 4.5.2). One downside to this reaction is the long, usually low yielding synthesis of **5** and **6** greatly hindering the efficiency of HACHT synthesis. The low yields are likely a result of bulky R groups hindering the final aldol condensation. The syntheses of 3,5-tert-butyl derivatives **5d** and **6d** were successful, however after multiple attempts under various conditions, the synthesis of **9d** was never achieved as a result of the bulk tert-butyl groups.

To avoid the multiple, low yielding steps associated with Method 1, we developed a four-fold Suzuki–Miyaura coupling of 5,5-Dimethoxytetrachlorocyclopentadiene (**7**) with a corresponding aryl boronic acid as a method to produce tetraarylcyclopentaienones. To our knowledge, we successfully demonstrate the first four-fold Suzuki on vinyl chlorides. The Suzuki–Miyaura coupling was undertaken under microwave conditions to provide a convenient set up with inert conditions and reduce reaction time. Through a thorough screen we found NaOH was the ideal base with the combination of $Pd(OAc)_2$ and SPhos to give an easily accessible Pd(II) state for the reaction to proceed successfully to **8c** in moderate yields. Treatment of **8c** with a 4% CH_2Cl_2-TFA solution gives the desired tetraarylcyclopentadienone (**9**) in moderate yields. This method has been applied successfully to 3,5-dimethoxyphenylcyclopentadieneone (**9c**) and tetrapyridylcyclopentadieneone (**9e**). For the synthesis of **9e**, Suzuki–Miyaura coupling occurs from the corresponding tetrabromide derivative of **7** is required (Synthesis outlined in section 4.5.2).

The conventional Diels-Alder reaction followed by cheletropic cycloreversion with the loss of CO seen in (Figure 1.2) was successful to form *sym*-hepta-3,5-dimethoxyphenylcycloheptatriene (**DMB$_7$C$_7$H**) (**10b**) (Scheme 4.4) and heptaanisolecycloheptatriene (**An$_7$C$_7$H**) in moderate yields of 39% and 75% respectively. To date, a pyridyl derivative **Py$_7$C$_7$H** has not been successfully synthesised as a result of difficulties in the synthesis of dienophile **Py$_3$C$_3$H**.

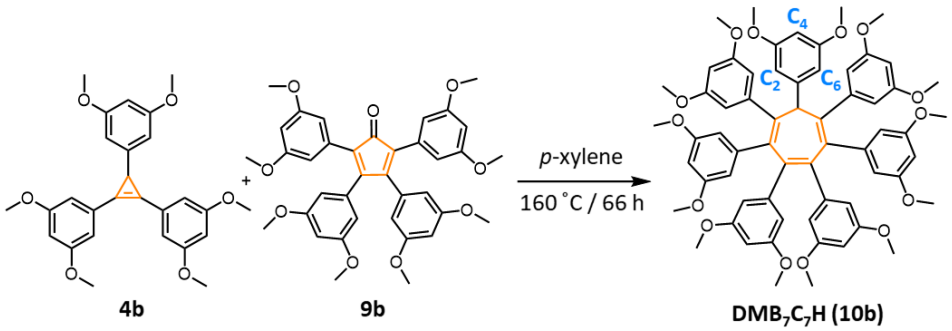

Scheme 4.5. Synthesis of **DMB_7C_7H** through a [4+2] cycloaddition of dienophile **5c** and diene **9c**. Reagents and conditions; i) *p*-xylene / 160 ˚C / 66 h / 30%. Resonance activated positions indicated in blue (C_2, C_4 and C_6).

X-ray crystal structure analysis of **An_7C_7H** (Figure 4.7) and **DMB_7C_7H** (Figure 4.8) reveals that the introduction of the methoxy groups does not drastically alter the characteristic boat like conformation of **Ph_7C_7H** (Figure 4.6), with the aryl groups at either end of the C_7 ring sitting above the central carbocycle. **DMB_7C_7H**, containing 3,5-dimethoxyphenyl peripheral rings provides an environment where the C_2 and C_6 positions, of each peripheral ring (Scheme 4.4), are activated through resonance donation, stabilising the radical cation intermediate of IOCD. It is possible that the C_4 position could also be activated through the same electronic effects, leading to potential intermolecular dimerization, however due to the size and non-planar arrangement of **DMB_7C_7H** this was not a concern and could be disfavoured by controlling reaction dilution if necessary. In theory, a single methyl ether could functionalise the C_3 position solely leading to the same stabilisation. However, if the fusion of the peripheral rings is successful, conformational lock would be expected to prevent single bond rotation of the outer rings, possibly resulting in the formation of an array of regioisomers, removing the C_7 symmetry element that is targeted.

4.2.4 Intramolecular Oxidative Cyclodehydrogenation

A range of Scholl oxidation conditions were applied (Table 4) to a series of HACHTs, to investigate the ability of each molecule to undergo IOCD. The classical Scholl conditions of $FeCl_3$ resulted in no product formation in any case. DDQ, a stronger oxidising agent was subsequently attempted with various acids with the results summarised in Table 1. In agreement with literature[34], DDQ/TfOH was the best combination.

Table 1. Results of DDQ/TfOH oxidation on HACHTs.

HACHT	Conditions	Temp (˚C) / Time (h)	SM %	Cation (%)	IOCD product (%)
Ph_7C_7H	DDQ / TfOH CH_2Cl_2	0˚C to rt	~90%	~10%	0
$phenPh_5C_7H$			Present	Present	Complex mixture
$Ph_7C_7^+$			100	0	0
An_7C_7H			100	0	0
DMB_7C_7H			0	0	Complex mixture

As previously discussed, **Ph_7C_7H** gives rise to **$Ph_7C_7^+$** under these strong oxidation condition, preventing any IOCD of the peripheral rings. A mixture of IOCD products were identified for **$phenPh_5C_7H$** by MS even though the cation was identified in ^{1}H NMR spectroscopy, however nothing could be isolated and the presence of the desired nanographene **1** was not observed. Interestingly, when using **An_7C_7H** or **DMB_7C_7H** the corresponding cation was not formed and in the case of **An_7C_7H**, only starting material was isolated after oxidation. Evidence of successful peripheral ring fusion of **DMB_7C_7H** was confirmed by high resolution mass spectroscopy (**HR-ESI MS** *m/z* = 1031.3308 $[M]^+$ (calculated for $C_{63}H_{51}O_{14}^+$ = 1031.3308). Unfortunately, all attempts to isolate the product were unsuccessful as a result of the vast number of products present from incomplete fusion. Increasing equivalents of the oxidant and reaction time lead to product decomposition and rather than an increase in yield of the desired nanographene.

In summary, the initial studies show that oxidation of the central cycloheptatriene is a more favoured process than peripheral ring fusion in non-functionalised CHTs. Upon formation of the tropylium cation further oxidation through cyclodehydrogenation is not possible. This is due to the unfavourable tropylium radical cation intermediate and an oxidation potential lower than 1.70 eV required for oxidation by DDQ/TfOH. Functionalisation and pre fusion of peripheral rings show positive signs towards the formation of warped nanographenes, however the conditions required provided difficulties in isolation of the product. We found that functionalisation of the peripheral rings with electron donating groups to stabilise the radical cation of the Scholl reaction, has shown evidence of partial success in a seven-fold Scholl reaction. Utilising strong electron donating groups would however reduce the redox activity of the central tropylium ring by essentially quenching the positive charge. As a result, further efforts avoided the use of highly electron rich systems such as **10b**.

4.2.5 Synthesis *via* Tropone Derivatives

To overcome central ring oxidation of phenyl CHTs we synthesised a series of tropone derivatives where the sp^3 position is replaced with a sp^2 hybridised ketone. Miao et al.[35] reported the synthesis of **12a** (Scheme 4.6) that was designed to produce a nanographene similar to **1**. In 2019 Miao et al.[36] synthesised heptabenzo[7]circulene, a [7]radialene centred warped nanographene with a saddle-shaped geometry of C_2 symmetry (Figure 4.2). The radialene structure of heptabenzo[7]circulene does not contain a true, cycloheptatriene core. Consequently, oxidation of the central heptagon ring would not be possible, as the resulting tropylium cation can not form. As a result, access to a redox active warped nanographene *via* this method would not be possible.

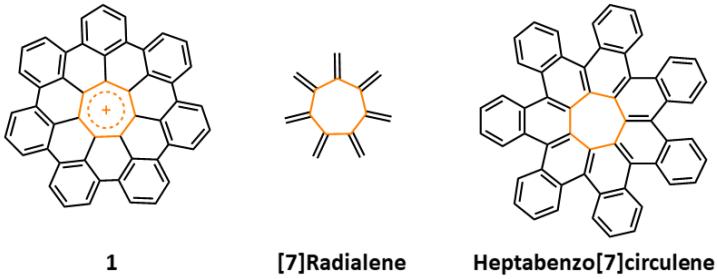

Figure 4.2. Comparison of target redox active warped nanographene **1** and Heptabenzo[7]circulene.

Miao's results however were consistent with our observations that pre-ring fusion and electron donating groups are both important factors that need to be taken into consideration for the successful synthesis of **1**. We targeted the synthesis of **12a/f** in pursuit of nanographene **1** and a part functionalised derivative **1f** respectively. The synthesis of **12a** was not possible and is thought to be a result of the relatively electron poor diene (phencyclone) not having sufficient HOMO energy to open the stable conjugated **Ph_2C_3O** dienophile. However, using to Miao's reported procedure, **11f** was successfully synthesised in a 55% yield. Pre-fusion and electron donating functionalisation meant a subsequent four-fold IOCD of **11f** with $FeCl_3$ was successful and **12f** was isolated in 69% yield. Knoevenagel condensation of the **12f** carbonyl using cyclohexa-1,3-dione was selected as the resulting compound would retain the desired sp^2 centre of **12f**, preventing the unwanted central ring oxidation occurring. Subsequently, it was planned to use Friedel-Crafts acylation reaction between carbonyl groups of the cyclohexa-1-3-dione neighbouring ring C-H to give **1f**. After multiple attempts of only isolating starting material, we moved to implementing the desired

cyclohexa-1,3-dione moiety in the cyclopropene Diels–Alder precursor (**13**). We successfully synthesised **13** from **Ph_2C_3O** with treatment with $[(CH_3CH_2)_3O]BF_4$ and cyclohexa-1,3-dione, however subsequent Diels–Alder reactions with diene **14a** or **14f** failed to proceed successfully. The failure of this reaction is likely a result of the now highly conjugated cyclopropene double bond, which reduces dienophile character. This results in the Diels-Alder transition state becoming more ridged and unfavourable to form new C-C bonds.

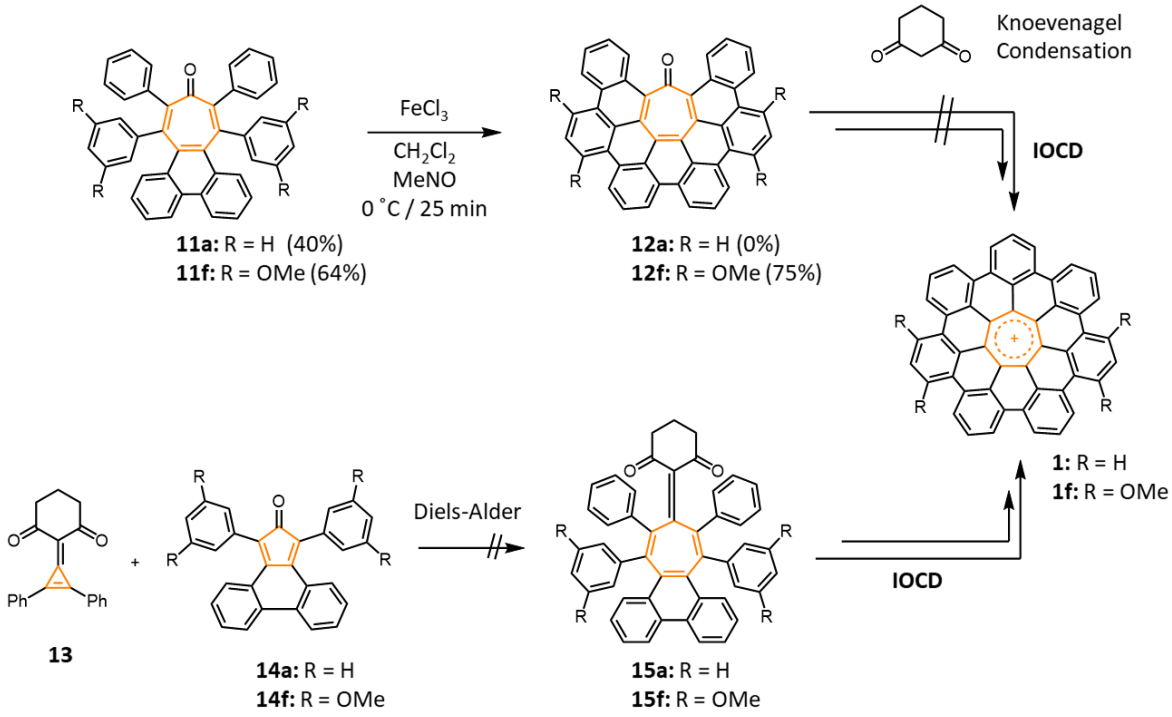

Scheme 4.6. Attempts to access redox-active warped nanographene through modification of Miaos report.[35]

To conclude, synthesis *via* tropone derivatives does provide enhanced peripheral ring fusion by masking the sp^3 and preventing central ring oxidation. Furthermore, a combination of electron-donating functionality and pre-fusion of two rings (**11f**) leads to more success than without (**11a**). This demonstrates the importance of both ring fusion and phenyl group functionalisation in the synthesis of **1**. However, it is important to note that a system like **1f** would not provide the desired C_7-symmetric structure as a result of two out of seven rings possessing 3,5-dimethoxy functionality. Most importantly however, the formation of **1f** would give an insight into conformational properties of tropylium warped nanographenes.

4.2.6 Photocyclisation

After unsuccessful attempts of making a redox-active warped nanographene through peripheral ring functionalisation, we returned to initial attempts of synthesising a non-functionalised **$Ph_7C_7^+$** warped nanographene through photocyclisation of **Ph_7C_7H**. As discussed in Chapter 2, **Ph_7C_7H-O** is more susceptible to photocyclisation compared to non-epoxide **Ph_7C_7H**, providing a convenient and quantitative method for partial ring fusion. The successful photocyclisation of **Ph_7C_7H-O** is a result of disruption of the central ring conjugation, resulting in a decrease in rigidity of the cycloheptatriene core. We have shown in Chapter 2 that photocyclization favours peripheral ring fusion in positions where new phenanthrene moieties can be formed. Irradiation with 254 nm light and I_2 as an oxidant, photooxidation of **Ph_7C_7H-O** to give **$phen_2Ph_3C_7H$-O** (Scheme 4.6) is possible in quantitative yields. Further photooxidation of **$phen_2C_7Ph_3H$-O** does not yield additional peripheral ring fusion and conventional cyclodehydrogenation techniques previously discussed are currently being attempted.
Additionally, epoxidation also provides favourable electronic effects to phenyl-CHTs by disrupting the central triene of **Ph_7C_7H** into a non-conjugated diene **Ph_7C_7H-O**. This disruption of the conjugated system prevents oxidation of the C_7 centre to form of the stable aromatic tropylium cation through IOCD conditions. This overcomes the major problem faced with IOCD of **Ph_7C_7H** where central ring oxidation out competed peripheral ring fusion. Access to the tropylium cation from **Ph_7C_7H-O** is not completely restricted and can be easily obtained through the addition of one equivalent of BBr_3 (Scheme 4.6). We demonstrate this by forming both **$Ph_7C_7^+$** and **$phen_2Ph_3C_7^+$** from **Ph_7C_7H-O** and **$phen_2Ph_3C_7H$-O** respectively in quantitative yields (Figure 4.4). A suggested mechanism for the oxidation is outlined in Scheme 4.7. We propose that the most promising method of accessing the desired redox-active warped nanographene **1** is through initial epoxidation of **Ph_7C_7H** to enable photocyclisation that results in an increase rigidity, favouring subsequent chemical oxidative cyclodehydrogenation. Work is on-going to find optimal conditions to synthesise **1** from **$phen_2Ph_3C_7H$-O** *via* this proposed method. A detailed account of future work for this project is outlined in section 4.4.

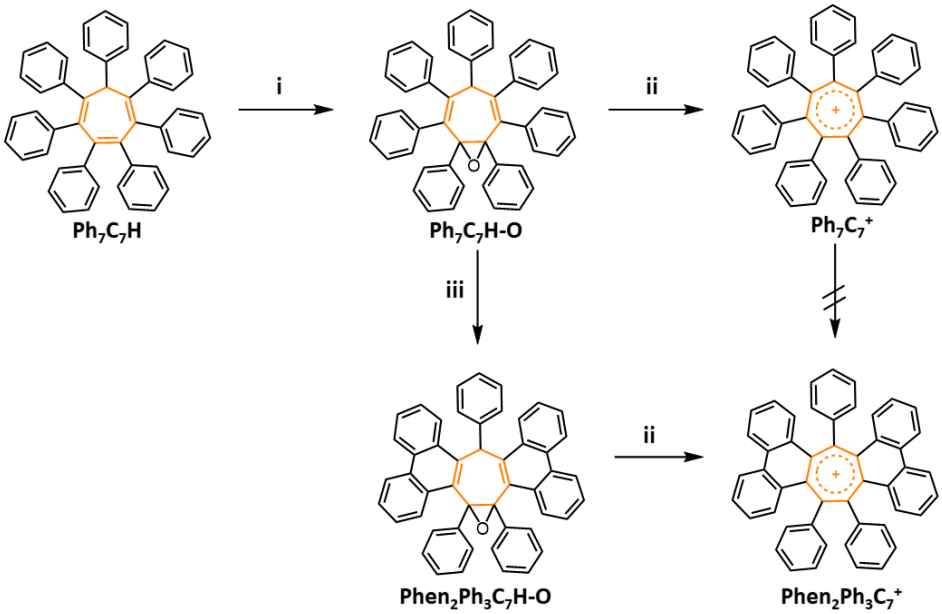

Scheme 4.7. Photocyclisation and oxidation of **Ph_7C_7H-O.** Reagents and conditions; i) *m*CPBA / $CHCl_3$ / 0 ˚C to 55 ˚C / 24 h / 70%; ii) BBr_3 / $CDCl_3$ / 10 min / quant. iii) I_2 / THF / PO / *hv* (254 nm) / 3 h / quant.

4.3 Conclusion

A series of CHTs have been synthesised to optimise the conditions required in order to produce a heptagon centred warped nanographene cation. The study so far reinforces the importance of sterics and the use of the correct directing groups while showing the benefits and drawbacks of certain features that will either aid or hinder fusion of the peripheral rings, a key challenge in the pursuit of **1**. We have found that pre-fusion of the peripheral rings of diene **9** provides an ideal method to introduce rigidity and induce further IOCD in HACHTs. Furthermore, we have shown that introducing electron donating functionality to the peripheral rings of **Ph_7C_7H** promotes IOCD, however leads to a large mixture of partially fused products. To overcome the challenges we have faced so far with complex product mixtures, we propose a more selective step-wise method of peripheral ring fusion, starting with photocyclisation of **Ph_7C_7H-O** to **$phen_2Ph_3C_7H$-O**. Synthesis of $phen_2Ph_3C_7H$-O from an epoxide form has shown to undergo IOCD much more readily whilst also avoiding central ring oxidation in favour of peripheral ring fusion.

4.4 Future work

Research will continue into stepwise ring fusion of **C_7Ph_7H**. A stepwise approach will aim to selectively fuse rings consecutively or concurrently to prevent a complex mixture of partially fused products forming, which has been the largest difficulty faced so far in the synthesis of **1**. Upon successful synthesis of **1**, variable temperature (VT) NMR will be employed upon successful synthesis of a warped nanographene to study the pseudorotation in the structure and study the energy barrier between its conformations. The study of the fundamental properties of these compounds will be important for understanding its function and as a reference for graphenes structural defects. Redox properties are characteristic of charged species and will be studied alongside their optical and photochemical properties for potential uses as organic active materials in, for example, lithium ion batteries and light-emitting electrochemical cells. The structure's positive charge also allows for potential uses in photovoltaics and forming charge carriers to create an electron–hole pair.

4.5 Experimental Details

4.5.1 Specific Experimental Methods

Materials: All reagents were purchased from commercial suppliers (Sigma-Aldrich, Acros Organics, or Alfa Aesar) and used without further purification. *meta*-Chloroperbenzoic acid (*m*CPBA) was purchased and used as a mixture of 77% purity, where the remainder is *m*-chlorobenzoic acid and water. Hydrogen bromide was purchased and used as a mixture of 33% w/w (45% w/v) soln. in acetic acid. Photocyclisation reactions were performed with a Rio 36W UV lamp fitted with 4 × 9W 254 nm bulbs.

4.5.2 Synthetic Procedures

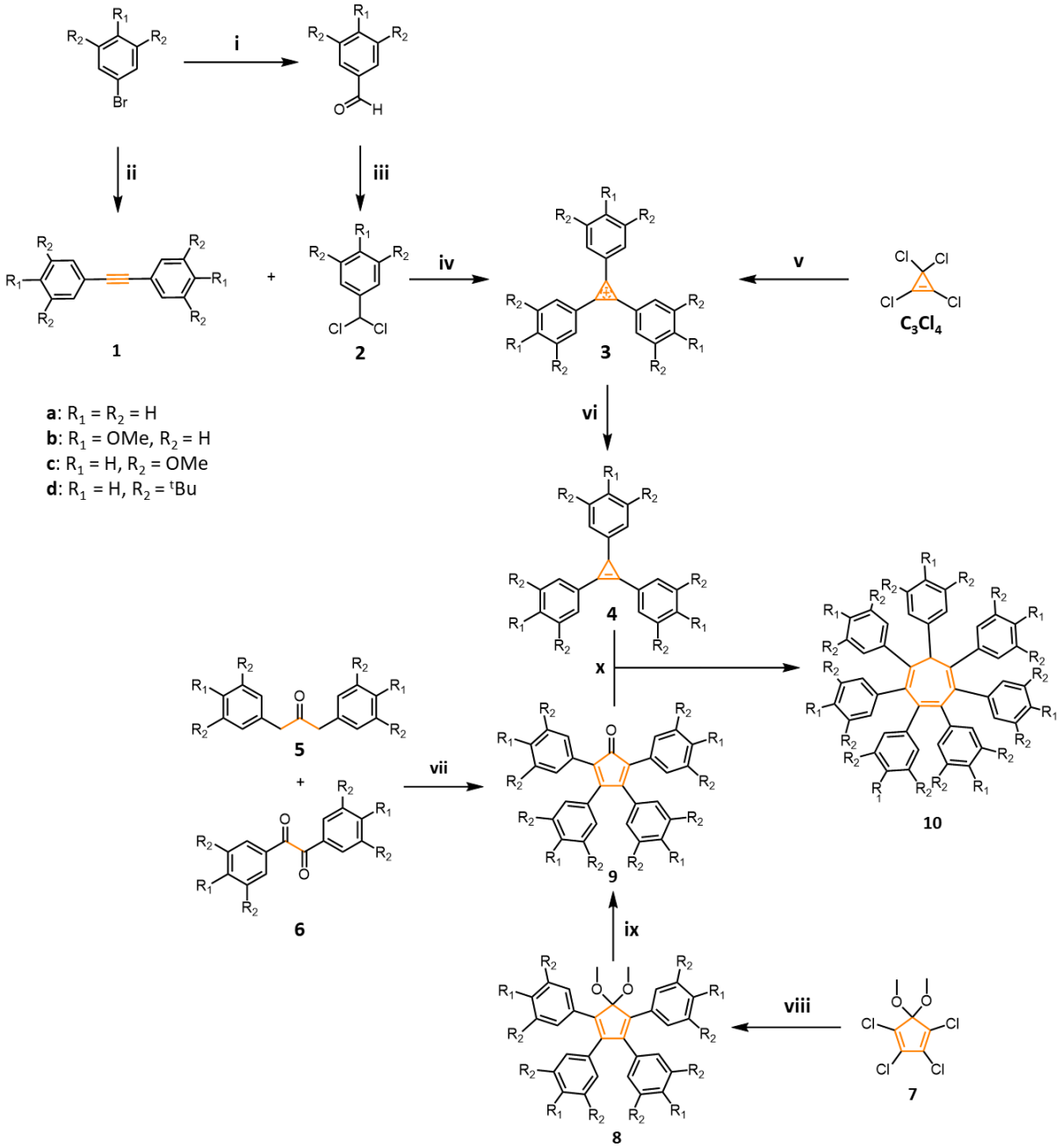

Scheme 4.6. Synthetic routes to functionalised HACHTs **10**. Reagents and conditions: i) n-BuLi / THF / DMF / 0 ˚C / 20 min; ii) $PdPPh_3$ / CuI / benzyltriethyl ammonium chloride / NaOH / 2-methyl-3-butyl-2-ol / PhMe / 70 ˚C / 5 d; iii) PPh_3-O / oxalyl chloride / $CHCl_3$ / 45˚C / 2h; iv) KO^{t}Bu / C_6H_6 then HBr or $HCl_{(g)}$ / 80 ˚C / 3 h /; v) anisole / 80 ˚C to rt / 1 h / 94%; vi) $NaBH_4$ / EtOH / 0 ˚C / 16 h; vii) EtOH / 90 ˚C / 2 h; viii) $Pd(OAc)_2$ / SPhos / NaOH / PhMe / 95 ˚C / 5 h / 55%; ix) TFA / CH_2Cl_2 / rt / 30 min.

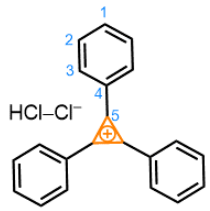

Triphenylcyclopropenylium hydrogen dichloride (Ph_3C_3·HCl_2) (3a): Diphenylacetylene (18.5 g, 104 mmol) and potassium *tert*-butoxide (35.0 g, 312 mmol) were placed in a two-necked oven-dried 500 mL round-bottomed flask fitted with a septum, under a N_2 atmosphere. Dry benzene (200 mL) was added and the mixture was stirred. α,α-Dichlorotoluene (25.0 g, 155 mmol) was added to the reaction mixture uniformly over a period of 30 min using a syringe pump. The reaction mixture was then heated to reflux for 3 h at 80 °C. After cooling, H_2O (200 mL) was added to dissolve the inorganic salts. The layers were separated, and the aqueous layer was extracted with Et_2O (2 × 200 mL). The ether extracts were combined with the benzene layer and dried over $MgSO_4$, before the solvent was removed under reduced pressure to give a solid, orange residue. This crude mixture was dissolved in a mixture of 2:1 Et_2O–CH_2Cl_2 (200 mL) and then sparged with gaseous HCl, leading to the formation of a colourless precipitate. Sparging was continued until no more precipitation was observed, then the mixture was filtered through a sintered glass funnel and the solid washed with Et_2O (3 × 50 mL). The solid was dried under vacuum to yield **Ph_3C_3·HCl_2** as cream powder (18.6 g, 61.4 mmol, 43%). **M.P.** 186 – 188 °C. **^{1}H NMR** (600 MHz, CD_3CN) δ 8.83 – 8.39 (m, 6H, H_3), 8.20 – 8.00 (m, 3H, H_1), 7.97 – 7.86 (m, 6H, H_2). **^{13}C NMR** (151 MHz, CD_3CN) δ 154.1 (C_5), 139.1 (C_1), 136.6 (C_2), 131.4 (C_3), 121.6 (C_4). **HR-ESI MS** *m/z* = 267.1169 $[M]^+$ (calculated for $C_{21}H_{15}^+$ = 267.1168).

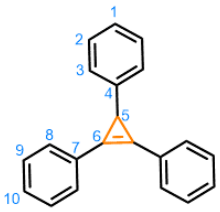

***sym*-Triphenylcyclopropene (Ph_3C_3H) (4a)**: Sodium borohydride (9.3 g, 246 mmol) was added to a solution of **Ph_3C_3·HCl_2** (18.6 g, 61.4 mmol) in EtOH (460 mL). The mixture was allowed to stir overnight at rt. The reaction was quenched with H_2O (500 mL) then extracted with Et_2O (3 × 200 mL). The organic layers were combined and washed with H_2O (500 mL) and brine (500 mL). The combined organic extracts were then dried over $MgSO_4$ and the solvent was removed under reduced pressure to give **Ph_3C_3H** as a colorless solid (14.2 g, 53.1 mmol, 97%). **M.P.** 113 – 115 °C (lit.[i] 114 – 115.5 °C). **^{1}H NMR** (400 MHz, $CDCl_3$) δ 7.71 – 7.66 (m, 4H, H_8), 7.47 – 7.40 (m, 4H, H_9), 7.38 – 7.32 (m, 2H, H_{10}), 7.24 (br s, 2H, H_2), 7.23 – 7.22 (m, 2H, H_3), 7.17 – 7.10 (m, 1H, H_1), 3.27 (s, 1H, H_5). **^{13}C NMR** (101 MHz, $CDCl_3$) δ 144.6 (C_4), 130.0 (C_8), 128.9 (C_9), 128.8 (C_{10}), 128.7 (C_7), 128.3 (C_3), 126.0

(C_2), 125.6 (C_1), 112.7 (C_6), 24.5 (C_5). **HR-ESI MS** *m/z* = 267.1172 $[M-H]^+$ (calculated for $C_{21}H_{15}^+$ = 267.1168).

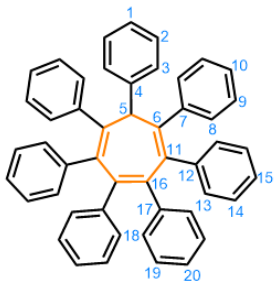

***sym*-Heptaphenylcycloheptatriene (10a)**: To a 20 mL microwave vial was added **Ph_3C_3H** (1.2 g, 4.47 mmol), tetraphenylcyclopentadienone (1.79 g, 4.47 mmol) and anhydrous *p*-xylene (13.5 mL). The reaction vessel was sealed and the mixture deoxygenated (3 × freeze–pump–thaw cycles under N_2) then stirred for 36 h at 140 °C in a microwave reactor. Upon cooling to rt, a crystalline solid formed, which was isolated by filtration through a sintered glass funnel, washing with Et_2O (3 × 10 mL). The solid was dried under vacuum to yield **Ph_7C_7H** as a pale pink solid (2.3 g, 3.68 mmol, 82%). A saturated solution of **Ph_7C_7H** in 1:1 $CHCl_3$–EtOH was allowed to slowly evaporate, yielding colorless crystals. **M.P.** 291 – 292 °C (lit.[2] 285 – 287.5 °C). **^{1}H NMR** (700 MHz, $(CD_3)_2CO$) δ 8.17 – 7.99 (m, 2H, H_3), 7.62 – 7.48 (m, 2H, H_2), 7.44 – 7.34 (m, 1H, H_1), 7.26 – 7.18 (m, 4H, H_8), 7.15 (br s, 4H, H_{13}), 7.05 – 7.02 (m, 4H, H_{14}), 7.02 – 6.98 (m, 4H, H_9), 6.98 – 6.96 (m, 2H, H_{15}), 6.96 – 6.93 (m, 2H, H_{10}), 6.63 – 6.59 (m, 2H, H_{20}), 6.60 – 6.55 (m, 4H, H_{19}), 6.36 – 6.32 (m, 4H, H_{18}), 5.35 (s, 1H, H_5). **^{13}C NMR** (176 MHz, $(CD_3)_2CO$) δ 144.8 (C_{16}), 144.4 (C_7), 144.1 (C_4), 141.9 (C_{12}), 141.6 (C_{17}), 140.2 (C_6), 138.0 (C_{11}), 132.7 (C_{13}), 132.3 (C_{18}), 130.7 (C_8), 129.4 (C_2), 128.5 (C_9), 128.1 (C_{14}), 127.9 (C_3), 127.7 (C_1), 127.3 (C_{10}), 126.93 (C_{15}), 126.87 (C_{19}), 126.0 (C_{20}), 59.0 (C_5). **HR-ESI MS** *m/z* = 625.2892 $[M+H]^+$ (calculated for $C_{47}H_{37}$ = 625.2890).

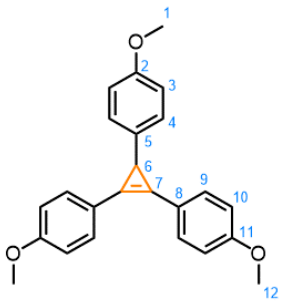

***sym*-Trianisolecyclopropene (4b)**: Perchlorocycloprop-1-ene (5.0 g, 28.1 mmol) and anisole (16.72 g, 155 mmol) were heated at 80 °C until the mixture became solid. The mixture was cooled to rt and put into water bath. Anisole (16.72 g, 155 mmol) was added dropwise (approx. 20 min). The mixture was then stirred for 1 h under nitrogen atmosphere at rt before being poured into H_2O (100 mL). The aqueous phase was separated, and the oily residue was washed with Et_2O (30 mL), forming an orange precipitate. The diethyl ether was decanted off and the orange solid

was extracted with hot MeCN (10 × 50 mL), combined and evaporated to dryness to isolate cation 1,2,3-tris(4-methoxyphenyl)cycloprop-2-en-1-ylium chloride. Sodium borohydride (193 mg, 5.09 mmol) was added to a solution of 1,2,3-tris(4-methoxyphenyl)cycloprop-2-en-1-ylium chloride (500 mg, 1.27 mmol) in EtOH (50 ml). The mixture was stirred overnight at rt before being evaporated to dryness. H_2O (50 mL) was added and the mixture was extracted with Et_2O (3 x 75 mL). The organic layers were combined and washed with H_2O (50 mL) and brine (50 mL). The organic layer was dried with $MgSO_4$, filter and evaporated to dryness, yielding the title compound as a yellow solid (0.43 g, 1.20 mmol, 94 %). **M.P.** 107 – 109 °C. **^{1}H NMR** (400 MHz, $CDCl_3$) δ 7.61 – 7.53 (m, 4H, H_9), 7.16 – 7.09 (m, 2H, H_4), 6.99 – 6.90 (m, 4H, H_{10}), 6.82 – 6.73 (m, 2H, H_3), 3.84 (s, 6H, H_{12}), 3.76 (s, 3H, H_1), 3.15 (s, 1H, H_2). **^{13}C NMR** (101 MHz, $CDCl_3$) δ 159.8 (C_{11}), 157.7 (C_2), 137.1 (C_9), 131.1 (C_5), 126.8 (C_4), 121.9 (C_8), 114.5 (C_{10}), 113.8 (C_3), 110.2 (C_7), 55.5 (C_1), 55.4 (C_{12}), 23.6 (C_6). **HRMS-ASAP** m/z = 359.1680 $[M+H]^+$ calculated for $C_{24}H_{24}O_3$ 359.1681

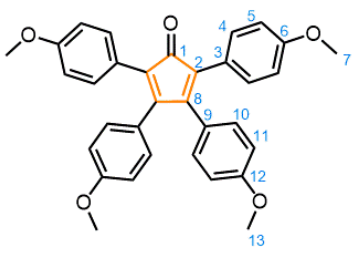

Tetraanisolecyclopentadienone (9b): 4,4'-Dimethoxybenzil (9.1 g, 33.7 mmol) and 1,3-bis(4-methoxyphenyl)acetone were added to a round bottom flask and suspended in EtOH (125 mL). The mixture was heated to 90 °C and stirred for 2 h. The mixture was cooled to 5 °C, and then filtered under vacuum. The dark purple solid was washed with EtOH (3 × 50 mL) then petroleum ether (3 × 50 mL). The isolated solid was dried under high vacuum to give the title compound as a dark purple solid (13.9 g, 27.5 mmol, 82%). **M.P.** 264 – 266 °C. **^{1}H NMR** (400 MHz, $CDCl_3$) δ 7.22 (d, *J* = 8.9 Hz, 4H, H_6), 6.88 (d, *J* = 8.8, 8.4 Hz, 4H, H_{11}), 6.82 (d, *J* = 8.9 Hz, 4H, H_4), 6.74 (d, *J* = 8.8 Hz, 4H, H_{10}), 3.81 (s, 12H, $H_{7,13}$). **^{13}C NMR** (101 MHz, $CDCl_3$) δ 201.2 (C_1), 159.6 (C_6), 158.8 (C_{12}), 152.7 (C_8), 132.4 (C_3), 131.4 (C_9), 125.7 (C_2), 123.9 (C_4), 123.7 (C_{10}), 113.6 (C_5), 113.4 (C_{11}), 55.2 (C_{7+13})**. HR-ESI MS** *m/z* = 504.1928 $[M+H]^+$ (calculated for $C_{33}H_{28}O_5$: 504.1931).

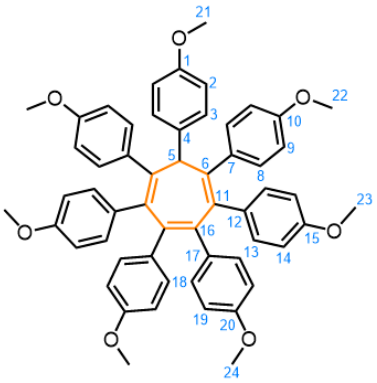

***sym*-Heptaanisylcycloheptatriene** (**An$_7$C$_7$H**, **10b**): To a 5 mL microwave vial was added 4',4''-(cycloprop-1-ene-1,2,3-triyl)tris(methoxybenzene) (**62**) (0.410 g, 1.144 mmol), 2, 3, 4, 5-tetrakis (4-anisyl cyclopentadien-1-one (**56**) (0.577 g, 1.144 mmol) and dry *p*-xylene (5 mL), then it was sealed with a magnetic stirring bar inside. The mixture was degassed (3 × freeze-pump-thaw cycles under argon) then stirred at 12 h at 140 °C. The reaction was allowed to cool to rt and the precipitated solid was collected by filtration, washed with PhMe (2 × 2 mL) and hexanes (3 mL). The mother liquor was concentrated under vacuum and washed with hexanes (2 x 10 mL). The resulting solid precipitate was combined with the original solid. The combined solids were then recrystallized from hot EtOH (7 mL) to give the title product as beige solid, (0.72 g, 0.89 mmol, 75%). **M.P.** 220 – 223 °C. **^{1}H NMR** (400 MHz, $CDCl_3$) δ 7.77 - 7.71 (m, 2H, H_2), 7.01 - 6.93 (m, 6H, $H_{3,8}$), 6.89 (d, J = 8.5 Hz, 4H, H_9), 6.58 (d, J = 8.8 Hz, 4H, H_{14}), 6.50 (d, J = 8.8 Hz, 4H, H_{13}), 6.18 (d, J = 8.9 Hz, 4H, H_{18}), 6.10 (d, J = 8.8 Hz, 4H, H_{19}), 5.20 (s, 1H, H_5), 3.84 (s, 3H, H_{21}), 3.70 (s, 6H, H_{24}), 3.65 (s, 6H, H_{22}), 3.53 (s, 6H, H_{23}) **^{13}C NMR** (176 MHz, $CDCl_3$) δ 158.6 (C_{16}), 157.6 (C_7), 157.6 (C_{12}), 156.7(C_{17}), 142.9(C_6), 139.1 (C_{11}), 136.7 (C_{13}), 135.9 (C_{18}), 135.8 (C_8), 133.9(C_2), 133.7 (C_9), 132.7 (C_{14}), 132.5(C_3), 131.1(C_1), 127.6 (C_{19}), 113.9 (C_{10}), 113.0 (C_{15}), 112.8 (C_4), 111.69(C_{20}), 57.6(C_5), 55.7(C_{21}), 55.2(C_{24}), 55.1(C_{22}), 54.9(C_{23}). **HR-ESI MS** *m/z* = 833.3521 $[M-H]^+$, calculated for $C_{56}H_{50}O_7$: 833.3517.

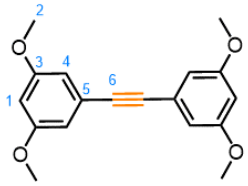

3,5-Dimethoxyphenylacetylene (**1c**): To an oven dried two-necked round bottom flask, $Pd(PPh_3)_4$ (0.06 g, 0.06 mmol), CuI (0.05 g, 0.26 mmol) and benzyltriethyl ammonium chloride (0.05 g, 0.231 mmol) were added. A condenser was fitted to one neck and the other sealed with a rubber septum before being evacuated through 3 × vacuum / argon cycles. Degassed NaOH solution 5.5M (4 mL) was added and stirred. 1-bromo-3,5-dimethoxybenzene (1.5 g, 6.95 mmol, 2 equiv) and 2-methyl-3-butyl-2-ol (0.32 mL, 3.3 mol) were dissolved in degassed PhMe (2.5 mL) and added to the reaction in one. The mixture was stirred at 70 °C for 5 days. The reaction mixture was allowed to cool to rt and neutralised with 1M HCl (1 mL) and extracted with CH_2Cl_2

(3 × 20 mL), washed with brine (40 mL) and dried over $MgSO_4$, before being filtered and evaporated under reduced pressure to afford a dark yellow oil. The crude mixture was purified by column chromatography (Teledyne Isco CombiFlash Rf+ system, 12 g, pet ether/ EtOAc, gradient) to give a white solid of the title compound (0.36g, 1.21 mmol, 37%). **M.P.** 127 – 129 °C. **^{1}H NMR** (700 MHz, $CDCl_3$) δ 6.71 (m, 4H, H_4), 6.49 (m, 2H, H_1), 3.83 (s, 12H, H_2). **^{13}C NMR** (176 MHz, $CDCl_3$) δ 161.02(C_3), 124.84(C_5), 109.88(C_4), 102.42(C_1), 89.39(C_6), 55.92(C_2). **HR-ESI MS** *m/z* 299.1293 $[M+H]^+$ (calculated for $C_{18}H_{19}O_4$: 299.1283).

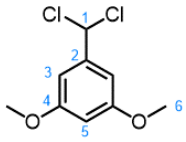

1-(Dichloromethyl)-3,5-dimethoxybenzene (**2c**): To an oven dried 2-necked round bottom flask, triphenylphosphine oxide (0.063 g, 2.4 mmol) in dry $CHCl_3$ (3 mL) was added to 3,5-dimethoxybenzaldehyde (0.50 g, 3 mmol) and heated to 45 °C. A solution of oxalyl chloride (0.33 mL, 3.9 mmol) in $CHCl_3$ (3 mL) was added over 2 h. Upon complete addition the mixture was allowed to stir for a further hour at 45 °C before being cooled to rt. The solvent was removed under reduced pressure before being purified by column chromatography (Teledyne Isco CombiFlash Rf+ system, 12 g, pet ether/ Et_2O, 0-10 %) to give a colourless oil of title compound (0.37 g, 1.68 mmol, 56%) **^{1}H NMR** (700 MHz, $CDCl_3$) δ 6.71 (s, 2H, H_3), 6.62 (s, 1H, H_1), 6.46 (s, 1H, H_5), 3.82 (s, 6H, H_6). **^{13}C NMR** (176 MHz, $CDCl_3$) δ 161.20 (C_4), 142.64 (C_2), 104.54 (C_3), 102.17 (C_5), 72.00 (C_1), 55.86 (C_6). **HRMS-ASAP** *m/z* = 221.0133 $[M+H]^+$ (calculated for $C_9H_{11}Cl_2O_2$: 221.0136).

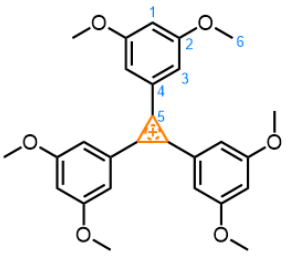

Tri-3,5-dimethoxyphenylcyclopropenylium (**3c**): To an oven dried 5 mL microwave vial, 1,2-bis(3,5-dimethoxyphenyl)ethyne (0.115 g, 0.39 mmol) and KO^{t}Bu (0.17 g, 1.54 mmol, 4 equiv) were added, sealed and evacuated through 3 × vacuum/argon cycles. Dry benzene (1.2 mL) was added and stirred for 10 mins before heating to reflux. 1-(dichloromethyl)-3, 5-dimethoxybenzene (0.17 g, 0.77 mmol, 2 equiv) was dissolved in dry benzene (1 mL) and added to the refluxing mixture over 2 h. Upon complete addition, the reaction was left to reflux for a further 1 h before being cooled to rt. H_2O (10 mL) was added and extracted with Et_2O (4 × 15 mL) before drying over

$MgSO_4$ and concentrated to half volume under reduced pressure. A 33% HBr solution in acetic acid (5 mL) was added dropwise forming a black precipitant. The solvent was decanted from the precipitant and washed with Et_2O (4 x 10 mL) to give a black solid of the title compound (0.13 g, 0.25 mmol, 63%). **M.P.** 195 – 197 °C. **^{1}H NMR** (600 MHz, CD_3CN) δ 7.53 (m, 6H, H_3), 7.14 (m, 3H, H_1), 3.98 (s, 18H, H_6). **^{13}C NMR** (151 MHz, CD_3CN) δ 162.8 (C_2), 157.4 (C_4), 122.1 (C_5), 113.6 (C_3), 111.4 (C_1), 56.9 (C_6) **HR-ESI MS** *m/z* = 447.1813 $[M]^+$ (calculated for $C_{27}H_{27}O_6$: 447.1808).

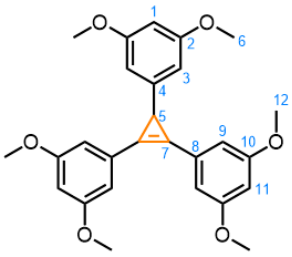

***sym*-Tri-3,5-dimethoxyphenylcyclopropene** (**4c**): To an oven dried round bottom flask, Tri-3,5-dimethoxyphenylcyclopropenylium bromide (0.11 g, 0.21 mmol) was dissolved in EtOH (3 mL) and cooled to 0 °C. $NaBH_4$ (0.032 g, 0.84 mmol, 4 equiv) was added to the cooled solution before being slowly warmed to rt and left to stir overnight. H_2O (10 mL) was added to quench the reaction and EtOH was removed under reduced pressure. The aqueous layer was extracted with Et_2O (4 x 20 mL) before being washed with brine (50 mL), dried over $MgSO_4$ and concentrated under reduced pressure to give a light brown solid (0.048 g, 0.11 mmol, 52%). **M.P.** 115 – 117 °C. **^{1}H NMR** (700 MHz, CD_3CN) δ 6.80 (m, 4H, H_9), 6.53 (m, 2H, H_{11}), 6.34 (m, 2H, H_3), 6.27 (s, 1H, H_1), 3.80 (s, 12H, H_{12}), 3.68 (s, 6H, H_6), 3.16 (s, 1H, H_5) **^{13}C NMR** (176 MHz, CD_3CN) δ 161.2 (C_{10}), 161.0 (C_2), 147.4 (C_4), 129.8 (C_6), 113.0 (C_8), 109.2 (C_1), 107.4 (C_9), 103.9 (C_3), 101.5 (C_{11}), 55.2(C_{12}), 54.8 (C_6), 24.5 (C_5). **HR-ESI MS** *m/z* = 447.1809 $[M-H]^+$ (calculated for $C_{27}H_{27}O_6$: 447.1808).

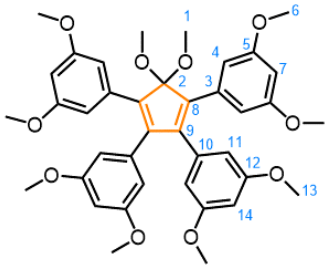

Tetra-3,5-dimethoxyphenylcyclopentadieneoacetate (**8c**): Dimethoxy-1,2,3,4-tetrachlorocyclopentadiene (0.05 g, 0.191 mmol) 3,5-dimethoxyophenylboronic acid (0.250 g, 1.37 mmol, 7 equiv), $Pd(OAc)_2$ (8.5 mg, 0.038 mmol, 20 %), SPhos (33.4 mg, 0.08 mmol) and NaOH (0.15 g, 3.82 mmol) were added to a 5 mL microwave vial and evacuated through 3 × vacuum – argon cycles. Dry toluene (2.5 mL) was deoxygenated through 3 × freeze-pump-thaw cycles before being added to the reaction mixture. The mixture was degassed once more

through a freeze-pump-thaw cycle before being heated to 95 °C for 5 h in the microwave reactor. The reaction was allowed to cool. Water (50 mL) was added to the reaction mixture and extracted with CH_2Cl_2 (3 × 30 mL) and washed with brine, dried over $MgSO_4$, filtered and the solvent was removed under reduced pressure to afford a dark brown solid. The crude mixture was purified by column chromatography (Teledyne Isco CombiFlash Rf+ system, 12 g SiO_2, CH_2Cl_2 - MeOH, 0-15 %). The resulting yellow oil was dried on the high vacuum overnight to give a yellow crystalline solid of title compound (0.14 g, 0.21 mmol, 55%). **M.P.** 260 – 262˚C. **^{1}H NMR** (400 MHz, $CDCl_3$) δ 6.78 (d, *J* = 2.3 Hz, 4H), 6.34 (m, *J* = 8.7, 2.3 Hz, 4H), 6.21 (d, *J* = 2.3 Hz, 4H), 3.62 (s, 12H), 3.61 (s, 12H), 3.33 (s, 6H). **^{13}C NMR** (151 MHz, $CDCl_3$) δ 161.6 (C_{12}) 160.3 (C_5) 154.2 (C_9) 132.5(C_3) 131.3 (C_{10}) 129.0 (C_8) 116.2 (C_4) 110.1 (C_{11}) 101.3 (C_7) 99.9 (C_{14}) 56.0 (C_6) 55.5 (C_{13}) 49.9 (C_1) **HR-ESI MS** *m/z* = 671.2834 $[M+H]^+$ (calculated for $C_{39}H_{43}O_{10}$: 671.2838).

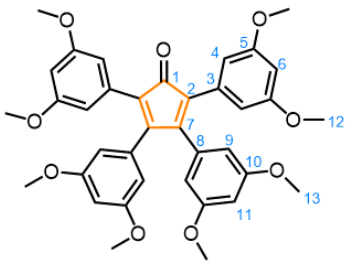

Tetra-3,5-dimethoxyphenylcyclopentadieneone (9c): **8c** (75 mg, 0.11 mmol) was dissolved in CH_2Cl_2 (3 mL) and cooled to 0° C in an ice bath under argon. A solution of CH_2Cl_2 (8.53 mL), TFA (0.36 mL, 4%) and water (0.11 mL, 1.25%) was added slowly to the reaction before being left to stir at rt for 30 min. The reaction was diluted with CH_2Cl_2 (30 mL) and washed with $NaHCO_3$ (2 × 30 mL), brine (2 × 30 mL), then dried over $MgSO_4$, filtered and evaporated to dryness to give a black solid. The crude mixture was purified by column chromatography (Teledyne Isco CombiFlash Rf+ system, 4 g SiO_2, pet ether-EtOAc, 0-100 %). The resulting black solid was dried overnight under high vacuum to yield the title compound (63 mg, 0.10 mmol, 95%). **M.P.** 253 – 255°C. **^{1}H NMR** (400 MHz, $CDCl_3$) δ 6.49 (d, *J* = 2.3 Hz, 4H, H_9), 6.38 (d, *J* = 2.3 Hz, 4H, H_4), 6.18 (d, *J* = 2.3 Hz, 4H, H_6), 3.66 (s, 12H, H_{12}), 3.56 (s, 12H, H_{13}). **^{13}C NMR** (151 MHz, $CDCl_3$) δ 200.2 (C_1), 162.0 (C_{10}), 161.3 (C_5), 153.2 (C_7), 132.5 (C_3), 131.4 (C_8), 125.2 (C_2), 116.2 (C_4), 115.7 (C_9), 102.1 (C_6), 101.2 (C_{11}), 55.8 (C_{12}), 55.5 (C_{13}). **HR-MS ESI** *m/z* = 624.2438 $[M+H]^+$ (calculated for $C_{37}H_{37}O_9$: 624.2440).

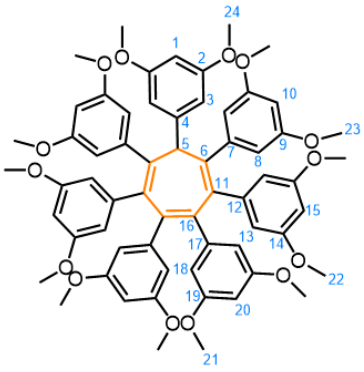

***sym*-Hepta-3,5-methoxyphenylcycloheptatriene (DMB$_7$C$_7$H) (10c)**: **4c** (0.12 g, 0.27 mmol) and **9c** (0.17 g, 0.27 mmol) were added to an oven dried microwave vial and evacuated through vacuum/argon cycles. Anhydrous *p*-xylene (4 mL) was degassed through 3 x freeze-pump-thaw cycles and added to the reaction flask. The mixture was heated to reflux for 3 days before being cooled to rt and the solvent removed under reduced pressure. The resulting crude solid was purified by column chromatography (Teledyne Isco CombiFlash Rf+ system, 12 g, pet ether - EtOAc , gradient) to give a dark solid that upon washing with minimal MeCN formed an off white crystalline solid of the title compound (0.11 g, 0.11 mmol, 39%) **M.P.** 195 – 197°C. **^{1}H NMR** (599 MHz, $CDCl_3$) δ 7.00 (m, 2H, H_3), 6.39 (m, 1H, H_1), 6.35 (m, 4H, H_8), 6.21 (m, 4H, H_{18}), 6.14 (m, 2H, H_{20}), 6.13 (m, 2H, H_{10}), 5.88 (m, 2H, H_{15}), 5.62 (m, 4H, H_{13}), 5.21 (s, 1H, H_5), 3.78 (s, 6H, H_{24}), 3.59 (s, 12H, H_{21}), 3.50 (s, 12H, H_{23}), 3.36 (s, 12H, H_{22}). **^{13}C NMR** (151 MHz, $CDCl_3$) δ 160.6 (C_2), 159.9 (C_9), 159.7 (C_{19}), 158.7 (C_{14}), 145.8 (C_4), 145.2 (C_7), 142.6 (C_{17}), 142.4(C_{12}), 141.9 (C_6), 139.7 (C_{11}), 136.6 (C_{16}), 110.1 (C_{18}), 109.1 (C_{15}), 107.6 (C_8), 105.7 (C_3), 99.7 (C_{13}), 99.4 (C_{10}), 98.2 (C_{20}), 97.8 (C_1), 57.3 (C_5), 55.3 (C_{24}), 55.1 (C_{21}), 55.0 (C_{23}), 54.9 (C_{22}). **HR-ESI MS** *m/z* = 1045.4370 $[M+H]^+$ (calculated for $C_{63}H_{65}O_{14}$: 1045.4370).

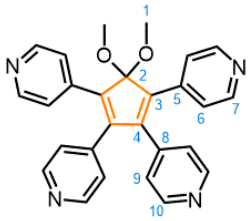

5,5-Dimethoxy-tetra(4-pyridyl)cyclopenta-1,3-diene (8e): To an oven dried 20 mL microwave vial 1,4-dioxane (13.7 mL) (degassed through 3 × freeze-pump-thaw cycles) and H_2O (4.53 mL) were added to a mixture of 1,2,3,4-tetrabromo-5,5-dimethoxycyclopenta-1,3-diene (0.250 g, 0.57 mmol), 4-pyridylboronic acid (0.417 g, 3.40 mmol), K_2CO_3 (1.25 g, 9.06 mmol) and $Pd(PPh_3)_4$ (90 mg, 97 μmol). The vial was sealed and heated to 100 ˚C for 40 h. The reaction mixture was then cooled to rt, washed with brine (20 mL) and extracted with CH_2Cl_2 (3 × 20 mL). The combined organic extracts were dried over $MgSO_4$, filtered and evaporated to dryness. The crude product was purified by column chromatography (Teledyne Isco CombiFlash Rf+ system, 24 g SiO_2, mixed: hexane−EtOAc, CH_2Cl_2−MeOH gradient elution) to yield a brown solid (0.211 g, 0.486 mmol, 86%).

M.P. 268 – 270 °C. **^{1}H NMR** (400 MHz, $CDCl_3$) δ 8.53 (dd, *J* = 1.6, 4.4 Hz, 4H, H_{10}), 8.50 (dd, *J* = 1.6, 4.8 Hz, 4H, H_7), 7.27 (dd, *J* = 1.6, 4.8 Hz, 4H, H_6), 6.87 (dd, *J* = 1.6, 4.4 Hz, 4H, H_9), 3.29 (s, 6H, H_1). **^{13}C NMR** (101 MHz, $CDCl_3$) δ 150.6 (C_{10}), 150.2 (C_7), 143.9 (C_4), 141.2 (C_8), 138.4 (C_5), 138.2 (C_3), 123.5 (C_9), 122.2 (C_6), 114.1 (C_2), 51.2 (C_1); **HR-MS ESI** *m/z* = 435.1832 $[M+H]^+$ (calculated for $C_{27}H_{23}N_4O_2$: 435.1821).

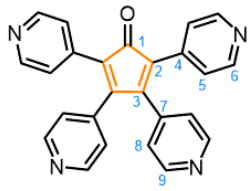

Tetra(4-pyridyl)cyclopenta-2,4-dien-1-one (9e): **8e** (17.0 mg, 0.039 mmol) was dissolved in a mixture of CH_3COOH (0.5 mL) and water (7 µL). HBr (33% wt., 189 mg, 0.780 mmol) was then added and the mixture was heated at reflux for 4 h. An aqueous saturated solution of $NaHCO_3$ (10 mL) was then added to make the solution alkaline. The solution was extracted with CH_2Cl_2 (3 × 20 mL). The combined organic extracts were washed with brine (20 mL) and dried over $MgSO_4$, filtered and evaporated to dryness, yielding a red solid of the title compound (14.1 mg, 93%). **M.P.** 259 – 261 °C. **^{1}H NMR** (400 MHz, $CDCl_3$) δ 8.57 (dd, *J* = 1.7, 4.4 Hz, 4H, H_9), 8.55 (dd, *J* = 1.7, 4.5 Hz, 4H, H_6), 7.09 (dd, *J* = 1.7, 4.5 Hz, 4H, H_5), 6.84 (dd, *J* = 1.7, 4.4 Hz, 4H, H_8). **^{13}C NMR** (101 MHz, $CDCl_3$) δ 196.2 (C_1), 153.4 (C_3), 150.5 (C_9), 150.0 (C_6), 139.2 (C_7), 136.6 (C_4), 125.4 (C_2), 123.9 (C_5), 122.7 (C_8). **HR-MS ESI** *m/z* = 389.1392 $[M+H]^+$ (calculated for $C_{25}H_{17}N_4O$: 389.1402).

Prefusion and Tropone Synthesis

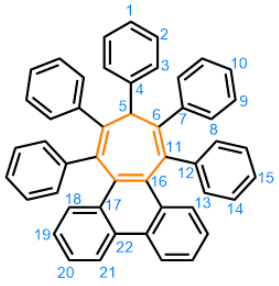

***sym*-phenPh_5C_7H**: Phencyclone (0.71 g, 1.86 mmol), *sym*-triphenylcyclopropene (**5a**) (0.50 g, 1.86 mmol) and anhydrous *p*-xylene (30 mL) were added to a 100 mL round bottom flask. The mixture was deoxygenated (3 × freeze-pump-thaw cycles under argon) before being heated to reflux at 165 °C for 66 h. The mixture was allowed to cool to rt where a white precipitate was produced. Me_2CO (20 mL) was added to induce further precipitation. The solid was isolated by filtration, washed with cold *p*-xylene (3 mL), then dried under vacuum to give **sym-phenPh_5C_7H** as a white solid (0.30 g, 0.48 mmol, 26%). Where possible, ^{1}H and ^{13}C NMR resonances have been assigned using bidimensional NMR techniques. However, some resonances could not be assigned on

account of overlap between peaks and the similarity of some nuclear environments. **M.P.** 318 – 321°C. **^{1}H NMR** (700 MHz, 1:7 CD_2Cl_2–CS_2) δ 8.31 (d, *J* = 8.3, 1.2 Hz, 2H, H_{21}), 7.82 (d, *J* = 8.4, 1.2 Hz, 2H, H_{18}), 7.46 (d, *J* = 8.1, 1.2 Hz, 2H, H_3), 7.35 – 7.29 (m, 2H, H_{20}), 7.15 – 7.11 (m, 4H, $H_{8\text{-}10}$ or $H_{13\text{-}15}$), 7.11 – 7.08 (m, 2H, H_{19}), 7.08 – 7.04 (m, 11H, $H_{8\text{-}10}$ or $H_{13\text{-}15}$), 7.04 – 7.02 (m, 5H, $H_{8\text{-}10}$ or $H_{13\text{-}15}$), 6.63 – 6.58 (m, 2H, H_2), 6.56 – 6.53 (m, 1H, H_1), 5.21 (s, 1H, H_5). **^{13}C NMR** (176 MHz, 1:7 CD_2Cl_2–CS_2) δ 146.4, 143.1, 143.1, 140.0 (C_4), 137.3 (C_{16}), 133.8, 131.2, 130.3 (C_{17}), 130.3 (C_{18}), 129.9, 129.4 (C_{22}), 128.0, 127.8 (C_2), 127.3, 126.7, 126.0, 125.8 (C_{20}), 125.5 (C_1), 125.4 (C_{19}), 124.8 (C_3), 122.0 (C_{21}), 60.5 (C_5). **HR-ASAP MS** *m/z* = 622.2685 $[M]^+$ (calculated for $C_{49}H_{34}^+$: 622.2655.)

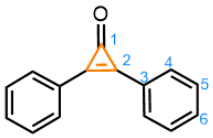

Ph_2C_3O

Diphenylcyclopropenone (Ph_2C_3O): Diphenylacetylene (6.02 g, 33.8 mmol) was dissolved in dry hexane (150 mL) and KO^{t}Bu (10.6 g, 95 mmol) was added then cooled to -20 °C under a N_2 atmosphere. $CHBr_3$ (2.68 mL, 30.6 mmol) was slowly added over 3 h at -20 °C and the reaction mixture was stirred and allowed to slowly warm to rt overnight. The reaction was quenched with H_2O (50 mL) and stirred for 30 min. The organic layer was then extracted with EtOAc (3 × 30 mL) and washed with a saturated aqueous solution of $Na_2S_2O_3$ (30 mL) and brine (30 mL), before being dried over $MgSO_4$, filtered and evaporated to dryness to give a dark red viscous oil. The crude solid was purified by column chromatography (Teledyne Isco CombiFlash Rf+ system, 80 g SiO_2, Hexane−EtOAc, gradient elution). The title compound was isolated as a pale yellow solid (4.54 g 21.9 mmol, 65%). **M.P.** 92 – 94 °C. **^{1}H NMR** (400 MHz, $CDCl_3$) δ 8.08 – 7.91 (m, 4H, H_4), 7.71 – 7.52 (m, 6H, $H_{5,6}$). **^{13}C NMR** (101 MHz, $CDCl_3$) δ 156.0 (C_1), 148.5 (C_3), 132.9 (C_4), 131.7 (C_5), 129.5 (C_6), 124.2 (C_2). **HR-ESI MS** *m/z* = 207.0787 $[M+H]^+$ (calculated for $C_{15}H_{11}O$ = 207.0810).

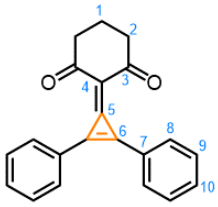

1-Cyclohexa-1,3-dione-2,3-diphenylcyclopropene: Diphenylcyclopropenone (260 mg, 1.26 mmol) and thionylchloride (1 mL) were heated to 40 ˚C for 2 hours under N_2. A solution of cyclohexan-1,3-dione (150 mg, 1.3 mmol) in anhydrous CH_2Cl_2 (5 mL) was added and heated to reflux for 16 hours. After cooling, H_2O (5 mL) was added to quench the reaction and was extracted

with CH_2Cl_2 (3 × 10 mL). The combined organic layers were washed with 1M HCl (5 mL), brine (10 mL) then dried over $MgSO_4$, filtered and evaporated to dryness. The crude mixture was purified by column chromatography (Teledyne Isco CombiFlash Rf+ system, 12 g SiO_2, pet ether-EtOAc, 0-100 %). The title compound was isolated as a yellow solid (90 mg, 0.38 mmol, 30%) **M.P.** 125 – 127 °C. **^{1}H NMR** (700 MHz, $CDCl_3$) δ 8.65 (m, 4H, H_8), 7.66 (m, 6H, H_{9+10}), 2.63 (t, *J* = 6.5 Hz, 4H, H_2), 2.08 (q, *J* = 13.3 Hz, 2H, H_1). **^{13}C NMR** (176 MHz, $CDCl_3$) δ 197.8 (C_3), 144.2 (C_5), 141.5 (C_6), 134.5 (C_8), 134.1 (C_9), 129.6 (C_{10}), 124.1 (C_7), 104.0 (C_4), 38.8 (C_2), 19.9 (C_1). **HR-ESI MS** *m/z* = 302.1299 $[M+H]^+$ (calculated for $C_{21}H_{18}O_2$ = 302.1307).

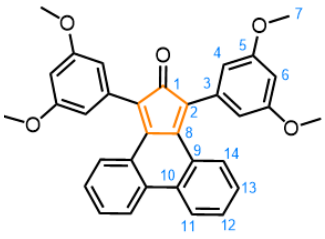

(14f): To a 5 mL microwave vial, bis-3,5-methoxydiphenylacetone (0.025 g, 0.076 mmol) and phenanthrene-9,10-quinone (16 mg, 0.076 mmol) were added in MeOH (1.3 mL) and heated to reflux. KOH (6 mg) in MeOH (50 µl) was added and refluxed for 15 min before being cooled to rt. The resulting solid was filtered and washed with a small amount of cold MeOH to give a dark green solid of the title compound (0.03g, 0.06 mmol, 79%). **M.P.** 183 – 185 ˚C. **^{1}H NMR** (599 MHz, $CDCl_3$) δ 7.80 (d, *J* = 8.0 Hz, 2H), 7.59 (d, *J* = 8.0, 2H), 7.28 (t, *J* = 15.6 Hz, 2H), 6.98 (d, *J* = 15.6 Hz, 2H), 6.53 (m 4H, H_4), 6.49 (m, 2H, H_6), 3.78 (s, 12H, H_7). **^{13}C NMR** (151 MHz, $CDCl_3$) δ 199.4 (C_1), 160.7 (C_5), 147.99, 133.78, 133.32, 131.22, 129.24, 128.10, 128.00, 124.14, 122.95 (C_3), 107.3 (C_4), 100.9 (C_6), 55.2 (C_7). **HR-ESI MS** *m/z* = 503.1840 $[M+H]^+$ (calculated for $C_{33}H_{27}O_5$ = 503.1859).

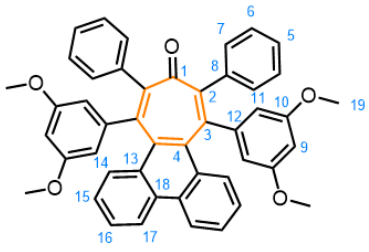

(11f): **14f** (30 mg, 0.06 mmol), **Ph_2C_3O** (21 mg, 0.1 mmol) and anhydrous PhMe (2 mL) were added to a 5 mL microwave vial, sealed and purged with N_2. The mixture was heated to 120 ˚C for 4 days. The reaction was allowed to cool to rt and the crude mixture was purified by column chromatography (Teledyne Isco CombiFlash Rf+ system, 4 g SiO_2, pet ether-EtOAc, 0-500 %). The title compound was isolated as a white solid (22 mg, 0.03 mmol, 55%). **M.P.** 268 – 270. **^{1}H NMR** (700 MHz, $CDCl_3$) δ 8.60 (m, 2H, H_{14}), 8.02 (m, 2H, H_{15}), 7.50 (m, 2H, H_{17}), 7.27 (m, 2H, H16), 7.18 (m, 4H, H_7), 7.05 – 7.02

(m, 6H, H_{6+5}), 6.24 (m, 4H, H_{11}), 6.22 (m, 2H, H_9), 3.46 (s, 12H, H_{19}). **^{13}C NMR** (176 MHz, $CDCl_3$) δ 199.4 (C_1), 160.5 (C_{10}), 146.5 (C_2), 142.3 (C_3), 135.3 (C_{12}), 135.3 (C_{13}), 133.9 (C_8), 130.92 (C_{15}), 130.2 (C_{18}), 129.9 (C_4), 129.6 (C_7), 128.1 (C_5), 127.8 (C_6), 126.9 (C_{16}), 126.2 (C_{17}), 122.5 (C_{14}), 108.7 (C_{11}), 99.9 (C_9), 55.2 (C_{19}). **HR-ASAP MS** *m/z* = 681.2653 $[M+H]^+$ (calculated for $C_{47}H_{37}O_5$: 681.2641).

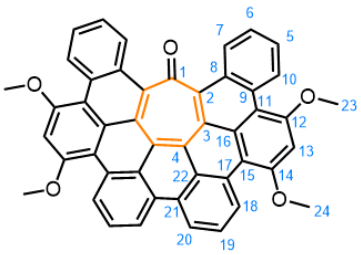

(**12f**): **11f** (20 mg, 0.029 mmol) in anhydrous CH_2Cl_2 (30 mL) was sparged with N_2 for 10 min and cooled to 0 ˚C. A solution of $FeCl_3$ (143 mg, 0.87 mmol, 30 equiv) in 1 mL CH_3NO_2 was sparged with N_2 for 10 mins and added to the 11b solution over 15 mins while being continually sparged with N_2. The reaction was quenched by the addition of MeOH (1 mL) and H_2O (5 mL). The aqueous phase was extracted with CH_2Cl_2 (3 × 5 mL). The combined organic fractions were with a saturated aqueous solution of $NaHCO_3$ (10 mL), brine (10 mL) and dried over $MgSO_4$, filtered and evaporated to dryness. The crude solid was purified by column chromatography (Teledyne Isco CombiFlash Rf+ system, 4 g SiO_2, Hexanes: CH_2Cl_2, 0 – 60%). The title compound was isolated as a red solid (13 mg, 0.02, 69%). Spectroscopic data is consistent with literature.[35]

Epoxides Ph_7C_7H-O and sym-$phen_2Ph_3C_7H$-O

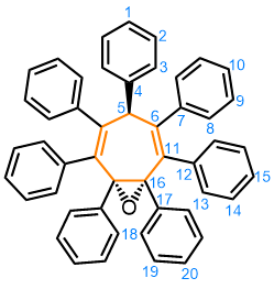

Ph_7C_7H-O: *sym*-Heptaphenylcycloheptatriene (1.0 g, 1.6 mmol) was dissolved in $CHCl_3$ (50 mL) and cooled to 0 °C. The mixture was stirred for 5 min. A cooled solution of *m*CPBA (1.6 g, 6.5 mmol) in $CHCl_3$ (20 mL) was added and stirred for a further 5 min before being allowed to warm to rt. The solution was slowly heated to 55 °C and left to stir for 16 h before being allowed to cool to rt and a further equivalent of *m*CPBA (0.28 g, 1.6 mmol) was added. The mixture was heated to 55 °C for 3 h before allowing to cool to rt. A saturated aqueous solution of $NaHCO_3$ (20 mL) was added and the resulting biphasic mixture was stirred for 15 min. The organic layer was separated and then washed with a saturated aqueous solution of $NaHCO_3$ (2 × 20 mL) and brine (30 mL), before being dried over $MgSO_4$, filtered and evaporated to dryness to give a crude orange solid. The crude mixture was recrystallized by slow evaporation of a saturated

EtOAc solution to yield the title compound as a crystalline colorless solid (0.72 g, 1.12 mmol, 70%). **M.P.** > 350 °C. **^{1}H NMR** (700 MHz, $CDCl_3$) δ 8.11 – 8.05 (m, 2H, H_3), 7.60 (t, *J* = 7.7 Hz, 2H, H_2), 7.49 – 7.43 (m, 1H, H_1), 7.14 – 7.12 (m, 4H, H_8), 7.11 – 7.08 (m, 4H, H_{13}), 7.06 – 6.98 (m, 12H, H_9, H_{10}, H_{14} and H_{15}), 6.81 – 6.75 (m, 2H, H_{20}), 6.72 – 6.66 (m, 4H, H_{19}), 6.63 – 6.52 (m, 4H, H_{18}), 5.14 (s, 1H, H_5). **^{13}C NMR** (176 MHz, $CDCl_3$) δ 146.7 (C_6), 144.6 (C_4), 144.5 (C_7), 140.4 (C_{12}), 138.8 (C_{11}), 137.4 (C_{17}), 131.0 (C_{13}), 129.0 (C_8), 128.9 (C_2 or C_3), 128.8 (C_2 or C_3), 128.8 (C_{18}), 128.0 (C_9 or C_{14}), 127.4 (C_9 or C_{14}), 127.2 (C_1), 126.6 (C_{10} or C_{15} or C_{20}), 126.5 (2C, C_{10} and/or C_{15} and/or C_{20}), 126.4 (C_{19}), 74.7 (C_{16}), 58.4 (C_5). **HRMS-ASAP** *m/z* = 641.2834 $[M+H]^+$ (calculated for $C_{49}H_{37}O$: 641.2839).

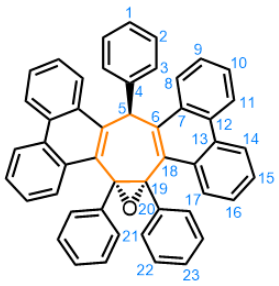

***sym*-phen$_2$Ph$_3$C$_7$H-O:** A pure sample of **Ph$_7$C$_7$H-O** (0.055 g, 0.09 mmol) and iodine (0.051 g, 0.2 mmol, 2.1 equiv) was added to a small quartz tube and fitted with a septa and purged with $N_{2(g)}$. THF (6 mL) was degassed through 3 × freeze-pump-thaw cycles and added. The mixture was bubbled through with N_2 for 10 min followed by the addition of propylene oxide (0.5 mL) and sparged with N_2 for a further 5 min. The reaction mixture was then irradiated by 4 × 9W 254nm bulbs for 3 h, while being bubbled through with $N_{2(g)}$. A saturated aqueous solution of $Na_2S_2O_3$ (2 mL) was added and the resulting biphasic mixture was stirred for 2 min. The reaction mixture was diluted with $CHCl_3$ (5 mL) and the organic layer was separated and then washed with a saturated aqueous solution of $Na_2S_2O_3$ (2 × 5 mL) and brine (5 mL), before being dried over $MgSO_4$, filtered and evaporated to dryness to give a dark solid. The crude solid was purified by column chromatography (Teledyne Isco CombiFlash Rf+ system, 12 g SiO_2, Hexanes: CH_2Cl_2, 0 – 30%). The title compound was isolated as a white crystalline solid (54 mg, 0.09 mmol, quant.) **M.P.** > 350 °C. **^{1}H NMR** (600 MHz, $CDCl_3$) δ 8.80 (m, 2H, H_8), 8.72 (m, 2H, H_{14}), 8.61 (m, 2H, H_{11}), 8.52 (m, 2H, H_{17}), 7.91 (s, 1H, H_5), 7.72 (m, 2H, H_{16}), 7.67 (m, 2H, H_{17}), 7.54 (m, 6H,H_{2+9+10}), 7.32 (m, 2H, H_3), 7.29 (m, 1H, H_1), 7.18 (m, 4H, H_{22}), 6.85 (m, 2H, H_{24}), 6.80 (m, 4H, H_{23}), .**^{13}C NMR** (151 MHz, $CDCl_3$) δ 141.8 (C_6), 138.2 (C_4), 137.4 (C_{21}), 133.4 (C_{18}), 133.2 (C_{13}), 131.4 (C_{12}), 130.9 (C_{19}), 130.9 (C_7), 129.9 (C_9), 129.4 (C_{22}), 128.5 (C_3), 127.9 (C_{16}), 127.9 (C_8), 127.9 (C_2), 126.9 (C_{24}), 126.9 (C_{10}), 126.8 (C_{23}), 126.7 (C_{15}), 126.7 (C1), 124.7 (C_{17}), 123.4 (C_{14}),

122.6 (C_{11}), 71.3 (C_{20}), 44.0 (C_5). **HRMS-ASAP** *m/z* = 637.2505 $[M+H]^+$, calculated for $C_{49}H_{33}O^+$: 637.2531.

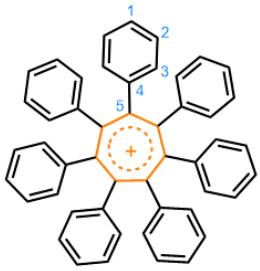

***sym*-Heptaphenyltropylium:** **Ph_7C_7H-O** (10 mg, 0.016 mmol) was added to an over dried round NMR tube and dissolved in $CDCl_3$ (0.7 mL). BBr_3 (10 uL, 0.11 mmol) was added. An immediate colour change from colourless to orange was observed. ^1H NMR confirmed immediate conversion to **$Ph_7C_7^+$**. The mixture was triturated with Et_2O (1 mL) and the resulting orange precipitate was isolated as the title compound (0.097 g, 0.096 mmol, 60%) **M.P.** 275 – 277 °C **^1H NMR** (400 MHz, CD_3CN) δ 6.92 – 6.88 (m, 14 H, H_3), 6.87 – 6.78 (m, 21H, H_{1+2}) **^{13}C NMR** (101 MHz, CD_3CN) δ 167.31(C_5), 141.6(C_4), 130.5 (C_3), 127.8 (C_2), 127.6 (C_1) **HRMS-ASAP** *m/z*= 623.2720 $[M]^+$ (calculated for $C_{49}H_{35}^+$: 623.2739).

4.5.3 Smaller precursor synthesis

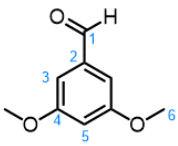

3,5-Dimethoxybenzaldehdye: To an oven dried round bottom flask, 3,5-dimethoxybromobenzene (1.5 g, 6.95 mmol) was added and purged under a positive pressure of argon. Dry THF (45 mL) was added and cooled to -78 °C. The mixture was allowed to cool whilst stirring for 10 min. n-BuLi 2.5M (3.4 mL, 8.34 mmol, 1.2 equiv) was added slowly and stirred for 20 min before adding DMF (1.65 mL, 20.9 mmol, 3 equiv) in one and stirred for another 20 min before slowly warming to rt. 1M HCl (30 mL) was added and stirred for 5 min. The aqueous layer was extracted with CH_2Cl_2 (3 × 30 mL) and washed with brine, dried over $MgSO_4$, filtered and the solvent was removed under reduced pressure to afford colourless oil. The crude mixture was purified by column chromatography (Teledyne Isco CombiFlash Rf+ system, 24 g SiO2, pet ether/ EtOAc, 0-30 %) to give a colourless oil that crystallised upon drying to give title compound (0.82g, 4.94 mmol, 71%). **M.P.** 40 – 41˚C. **^1H NMR** (700 MHz, $CDCl_3$) δ 9.91 (s, 1H, H_1), 7.01 (m, 2H, H_3), 6.70 (m, 1H, H_5), 3.84 (s, 6H, H_6). **^{13}C NMR** (176 MHz, $CDCl_3$) δ 191.87(C_1), 161.22(C_4), 138.38(C_2), 107.15(C_5), 107.10(C_3), 55.61(C_6). **HR-ESI MS** *m/z* = 205.0495 found for $[M+Na]^+$ (calculated for $C_9H_{10}O_4Na$: 205.0477).

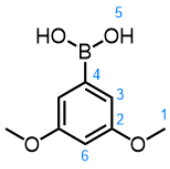

1,3-Dimethoxyphenyl boronic acid: 3,5 dimethoxybenzene (4.61 g, 21 mmol) was added to a dry 2-necked RBF and evacuated through 3 × vacuum – argon cycles. THF (100 mL) was added and cooled to -78 °C. n-BuLi 2.5 M in THF (10 mL, 25 mmol, 1.2 equiv) was added dropwise and stirred at -78 °C for 1 h. Trimethoxyborate (3.6 mL, 32 mmol, 1.5 equiv) was added and stirred for 30 mins at -78 °C then rt for 1.5 h. Saturated aqueous ammonium chloride (65 mL) was added followed by 3M HCl (15 mL) and stirred for 10 min. The mixture was extracted with CH_2Cl_2 (3 × 50 mL) and washed with brine, dried over $MgSO_4$, filtered and the solvent was removed under reduced pressure to afford a white solid. The resulting white solid was washed with n-pentane (3 × 30 mL) to give a white solid of the boronic acid product (2.5 g, 13.7 mmol, 65%) **M.P.** 202 – 204 °C. **^{1}H NMR** (400 MHz, DMSO-d_6) δ 8.04 (s, H_5, 4H), 6.95 (s, H_3, 2H), 6.51 (m, H_6, 1H), 3.73 (s, H_1, 6H). **^{11}B NMR** (128 MHz, DMSO-d_6) δ 27.02. **^{13}C NMR** (176 MHz, DMSO-d_6) δ 55.3 (C_1), 99.9 (C_6), 102.5 (C_3), 111.7 (C_4), 160.2 (C_2). **HR-ESI MS** *m/z* = 181.0658 found for $[M-H]^-$ (calculated for $C_8H_{10}BO_4$: 181.0672).

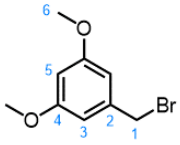

3,5-Dimethoxybenzylbromide: 3,5-dimethoxybenzyl alcohol (1.00 g, 5.98 mmol) in dry benzene (10 mL) was added PBr_3 (0.62 mL, 6.58 mmol) and stirred at 40 ˚C for 1 hour. After cooling, the reaction was quenched with a saturated aqueous solution of $NaHCO_3$ (20 mL) and the aqueous phase was extracted with EtOAc (3 × 20 mL). The combined organic layer was washed with brine (20 mL), dried over $MgSO_4$, filtered and evaporated to dryness to give the title compound as yellow solid (1.37 g, 5.98 mmol , quant.) **M.P.** 74 – 76 ˚C. **^{1}H NMR** (400 MHz, $CDCl_3$) δ 6.54 (m, H_3, 2H), 6.39 (s, H_5. 1H), 4.42 (s, H_1, 2H, 3.80 (s, H_6, 6H). **^{13}C NMR** (176 MHz, $CDCl_3$) δ 160.9 (C_4), 139.7 (C_2), 106.9 (C_3), 100.6 (C_5), 55.4 (C_6), 33.6 (C_1). **HR-ESI MS** *m/z* = 231.0043 found for $[M+H]^+$ (calculated for $C_9H_{12}BrO_4$: 231.0021).

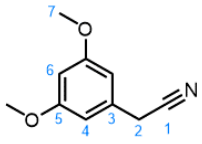

3,5-Dimethoxyphenylacetonitrile: 3,5-dimethoxybenzylbromide (1.5 g, 6.5 mmol), KCN (0.46 g, 7.0 mmol) and 18-crown-6 (1.8 g, 7.0 mmol) were dissolved in anhydrous MeCN (30 mL) and stirred at RT for 16 h. The reaction was quenched with H_2O (30 mL) and MeCN was removed under vacuum. The aqueous layer was extracted with

EtOAc (3 × 30 mL) and washed with brine (30 mL), dried over $MgSO_4$, filtered and evaporated to dryness to give the product as a white solid (0.9 g, 5.1 mmol, 78%). **M.P.** 50 – 52 ˚C. **^{1}H NMR** (400 MHz, $CDCl_3$) δ 6.45 (m, 2H), 6.39 (m, 1H), 3.78 (s, 6H), 3.67 (s, 2H). **^{13}C NMR** (176 MHz, $CDCl_3$) δ 161.6 (C_5) 125.3 (C_3) 118.9 (C_1) 110.2 (C_4) 103.4 (C_6), 55.8 (C_7), 23.5 (C_2). **HR-ESI-MS** *m/z* = 178.0867 found for $[M+H]^+$ (calculated for $C_{10}H_{12}NO_2$: 178.0868).

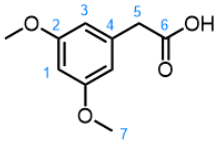

3,5-Dimethoxybenzylacetic acid: Dimethoxybenzylcyanide (1.8 g, 10.16 mmol) and NaOH (1.0 g, 25 mmol) were refluxed in a 2:1 mixture of n-butanol: H_2O (3 mL) overnight. The reaction was cooled to rt, before being diluted with H_2O (15 mL) and acidified with a 1M HCl (20 mL), causing a white precipitate to form. The result precipitate was filtered and washed with CH_2Cl_2 (100 mL). The filtrate was evaporated to dryness to give an off white solid of the title compound (1.2 g, 6.2 mmol, 62%). **M.P.** 100 – 102 ˚C. **^{1}H NMR** (700 MHz, $CDCl_3$) δ 6.44 (d, *J* = 2.5 Hz, 2H, H_3), 6.39 (d, *J* = 2.3 Hz, 1H, H_1), 3.78 (s, 6H, H_7), 3.58 (s, 2H, H_5). **^{13}C NMR** (176 MHz, $CDCl_3$) δ 177.6 (C_6), 161.0 (C_2), 135.4 (C_4), 107.6 (C_3), 99.6 (C_1), 55.5 (C_7), 41.4 (C_5). **HR-ESI-MS** *m/z* = 197.0801 found for $[M+H]^+$ (calculated for $C_{10}H_{13}O_4$: 197.0814).

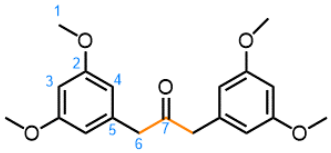

3,5-Dimethoxyphenylpropan-2-one: 3,5-dimethoxybenzylacetic acid (0.5 g, 2.55 mmol) in anhydrous CH_2Cl_2 (5 mL) was added dropwise to a stirring solution of dicyclohexyl-carbodiimide (0.26, 1.28 mmol, 0.5 equiv) and DMAP (0.63 mmol) in anhydrous CH_2Cl_2 (10 mL) and stirred at rt for 24 h. The resulting precipitate was removed by filtration and the supernatant was concentrated and purified by column chromotography (Teledyne Isco CombiFlash Rf+ system, 24 g SiO_2, pet ether/ EtOAc, 0-100 %) to give a colourless oil that crystallised upon drying to give title compound as a white solid (0.19, 0.58 mmol, 45%). **M.P.** 119 – 120 ˚C. **^{1}H NMR** (599 MHz, $CDCl_3$) δ 6.36 (t, *J* = 3.5 Hz, 2H, H_3), 6.30 (d, *J* = 4.0, 1.0 Hz, 4H, H_4), 3.76 (s, 12H, H_1), 3.64 (s, 4H, H_6). **^{13}C NMR** (151 MHz, $CDCl_3$) δ 205.6 (C_7), 161.1 (C_2), 136.2 (C_5), 107.7 (C_4), 99.3 (C_3), 55.5 (C_1), 49.4 (C_6). **HR-ESI-MS** *m/z* = 331.1551 found for $[M+H]^+$ (calculated for $C_{19}H_{23}O_5$: 331.1545).

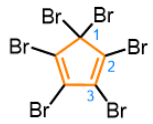

Hexabromocyclopenta-1,3-diene: Br_2 (6.5 mL, 127 mmol) was added dropwise to an aqueous saturated of solution of KOH (159 mL, 2.9 mol) at -5 °C and stirred vigorously. Freshly distilled cyclopentadiene (1.40 g, 21.2 mmol) was added dropwise and allowed to stir for 15 min at -5 °C. The mixture was extracted with CH_2Cl_2 (3 × 25 mL) and the combined organic extracts were dried over $MgSO_4$, filtered and evaporated to dryness. The crude product was purified by column chromatography (Teledyne Isco CombiFlash Rf+ system, 12 g SiO_2, hexane−EtOAc, gradient elution) and subsequently recrystallised from a hot saturated hexane solution over 72 h to yield yellow crystals (3.06 g, 5.67 mmol, 27%). **M.P.** 81 – 84 °C. **^{13}C NMR** (101 MHz, $CDCl_3$) δ 130.1 (C_2), 122.8 (C_3), 56.8 (C_1). **HR-MS ESI** *m/z* = 454.5902 found for $[M\text{-}Br]^-$ (calculated for C_5Br_5: 454.5917).

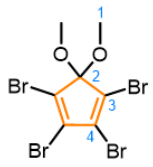

Tetrabromo-5,5-dimethoxycyclopenta-1,3-diene: Freshly prepared NaOMe (1.55 mL, 30% in MeOH, 14.46 mmol) was slowly added to a solution of hexabromocyclopentadiene (1.3 g, 2.41 mmol) in diethylene glycol dimethyl ether (6.7 mL) at -78 °C. The mixture was slowly warmed to rt and left to stir for 3 h and then poured over ice (70 g). After the ice had melted, the mixture was extracted with CH_2Cl_2 (3 × 25 mL) and the combined organic extracts were dried over $MgSO_4$, filtered and evaporated to dryness to yield an orange solid of the title compound (0.57 g, 1.29 mmol, 53 %). **M.P.** 95 – 96 °C. **^{1}H NMR** (400 MHz, $CDCl_3$) δ 3.28 (s, 6H, H_1). **^{13}C NMR** (101 MHz, $CDCl_3$) δ 126.2 (C3), 124.0 (C4), 52.4 (C2). **HR-MS ESI** *m/z* = 358.7891, found for $[M\text{-}Br]^-$ (calculated for $C_7H_6O_2Br_3$: 358.7918).

4.5.4 Intramolecular Oxidative Cyclodehydrogenation Conditions

General Conditions of Scholl Oxidation with $FeCl_3$

HACHT (1 equiv) was added to an oven dried 2-neck round bottom flask with one neck fitted with a dropping funnel. The reaction flask was evacuated through 3 × vacuum-argon cycles. Anhydrous CH_2Cl_2 was added to make a 0.01 mmol solution of HACHT. The mixture was purged with $N_{2(g)}$ for 10 min and was continually purged throughout the reaction. A solution of $FeCl_3$ (20 equiv) in $MeNO_2$ (100 mg $FeCl_3$ per mL) was

added to the dropping funnel and purged with $N_{2(g)}$ for 10 min. The $FeCl_3$ solution was then added dropwise and left to stir at rt for 1.5 h upon complete addition. The crude mixture was quenched with H_2O and extracted with CH_2Cl_2. The combined organic fractions were washed with brine, dried over $MgSO_4$, filtered and evaporated to dryness. The crude product was purified by column chromatography (Teledyne Isco CombiFlash Rf+ system, SiO_2).

General Conditions of Scholl Oxidation with DDQ/TfOH

HACHT (1 equiv) and DDQ (10 equiv) were added to an oven dried microwave vial and sealed. The reaction flask was evacuated through 3 × vacuum-argon cycles. Anhydrous CH_2Cl_2 was added to make a 1 mmol solution of HACHT and cooled to 0 ˚C. TfOH (100 equiv) was added dropwise and allowed to stir at 0 ˚C for 24 h or until all starting material had be consumed, as confirmed by TLC. The reaction mixture was neutralized with a saturated aqueous solution of $NaHCO_3$ and extracted with CH_2Cl_2. The combined organic fractions were washed with brine, dried over $MgSO_4$, filtered and evaporated to dryness. The crude product was purified by column chromatography (Teledyne Isco CombiFlash Rf+ system, SiO_2).

General Conditions of Scholl Oxidation with $AlCl_3$/NaCl

NaCl (10 equiv) and $AlCl_3$ (20 equiv) were added to a dry flask, sealed and purged with $N_{2(g)}$. The mixture was heated to 200 ˚C form a melt. HACHT (1 equiv) was added to the melt and stirred for 5 h at 200 ˚C. Upon cooling, the solid was dissolved in CH_2Cl_2 and washed with H_2O to yield the crude material.

General Conditions of Scholl Oxidation with $Cu(CF_3SO_3)_2$ / $AlCl_3$

$Cu(CF_3SO_3)_2$ (40 equiv) was dried overnight in a vacuum oven at 70 ˚C. Once dry, $Cu(CF_3SO_3)_2$ and $AlCl_3$ (40 equiv) were added and CS_2 (1 mL per 1 mg HACHT) was added and heated to 30 ˚C and stirred for 15 min. HACHT (1 equiv) was dissolved in the minimum amount of CS_2 and added dropwise to the reaction mixture dropwise and stirred at 30 ˚C for 24 h.

4.6 Appendix of Supplementary Data and Discussion

4.6.1 Variable-Temperature (VT) NMR Spectroscopy

Detailed analysis of variable temperature (VT) NMR spectroscopy for **sym-phenPh$_5$C$_7$H** and **Ph$_7$C$_7$H-O** was outlined in **Chapter 2.5.1.** The variable temperature NMR for **Ph$_7$C$_7$H** was published by McGonigal et al in 2017.[37] Table 1 below summaries the activation energies ($\Delta G^{\ddagger}$), entropy of activation ($\Delta S^{\ddagger}$) and enthalpy of activation ($\Delta H^{\ddagger}$).

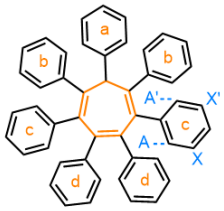

Table 1. Calculated activation energies ($\Delta G^{\ddagger}$) for the rotation of ring c.

Compound	Ring	Temp / K	$\Delta G^{\ddagger}$ / kJ mol^{-1}	$\Delta S^{\ddagger}$ / J mol^{-1}K^{-1}	$\Delta H^{\ddagger}$ / kJ mol^{-1}
Ph$_7$C$_7$H	C	196.8	38.7	-94.3	20.1
sym-phenPh$_5$C$_7$H	C	196.6	41.8	-27.9	36.2
Ph$_7$C$_7$H-O	D	196.2	43.6	+27.0	48.5

Activation energy barriers for the 180° rotation of the ring with the lowest energy barrier (as concluded by the broadening of their relative peaks into the baseline that reappear at much lower temperature as two distinctive peaks in ^{13}C NMR as free bond rotation shows to make A/A′ and X/X′ different environments) were calculated for each of the eight temperatures using equation **1**:

$$\Delta G^{\ddagger} = -RT \ln \frac{k_r h}{k_B T}$$

Equation 1. A variation of the Eyring equation. k_r is the measured rate constant, k_B is the Boltzmann constant, T is temperature, h is Planck's constant, and R is the ideal gas constant.

Pre-fusion of two peripheral phenyl rings of **Ph$_7$C$_7$H** increases the activation energy of peripheral ring 'C' by ~ 3 kJ mol^{-1} in the resulting structure ***sym*-phenPh$_5$C$_7$H**. As discussed in Chapter 4.2, pre-fusion increases the likelihood of IOCD occurring in the rest of the system. This can be quantified by VT NMR spectroscopy whereby an increase in the activation energy of rotation of ring C in ***sym*-phenPh$_5$C$_7$H** may result in the phenyl ring being more likely to undergo IOCD, as a result being in a more

strained environment and an increase in energy release upon C-C formation between peripheral rings.

Only symmetrical structures were studied by VT NMR spectroscopy. Asymmetric structures such as ***asym*-phenPh$_5$C$_7$H** contains 39 unique carbon environments and the significant broadening associated with low temperature NMR resulted in tracking the disappearance and reappearing of selected peaks not possible.

4.6.2 Thermally Induced Isomerism

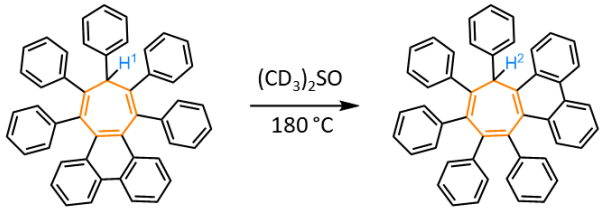

Scheme 4.7. Thermal isomerisation of ***sym*-phenPh$_5$C$_7$H** to **a*sym*-phenPh$_5$C$_7$H**.

At high reaction temperatures (≥180 °C), the synthesis of pre-fused CHT ***phen*Ph$_5$C$_7$H** forms as two isomers ***sym*-phenPh$_5$C$_7$H** to **a*sym*-phenPh$_5$C$_7$H** in a 1:2 ratio. At lower reaction temperatures (~160 °C) the minor product, ***sym*-phenPh$_5$C$_7$H**, can be isolated as the stand-alone isomer. Therefore, we can assume that ***sym*-phenPh$_5$C$_7$H** exists as the kinetic product and **a*sym*-phenPh$_5$C$_7$H** as the thermodynamic product.

Using ^{1}H NMR spectroscopy we can monitor the thermal isomerisation between ***sym*-phenPh$_5$C$_7$H** and **a*sym*-phenPh$_5$C$_7$H** and calculate a rate of isomerisation (k). To calculate k a ^{1}H NMR spectrum of ***sym*-phenPh$_5$C$_7$H** in $(CD_3)_2SO$ was collected. Between each spectrum the sample was heated to 180 °C in an oil bath and the formation of **a*sym*-phenPh$_5$C$_7$H** was monitored. (Figure 4.3). Relative ratios of the two isomers were collected through integration of the sp^3 proton on each compound, H^1 and H^2 respectively. (Table 2).

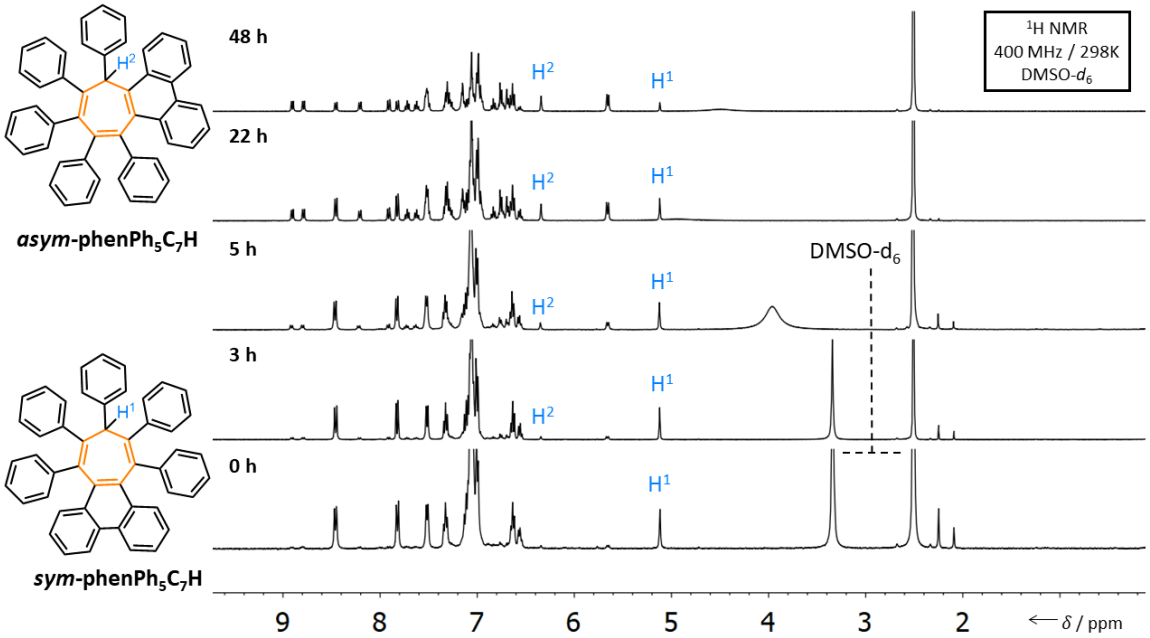

Figure 4.3. ^{1}H NMR stack of the thermal isomerisation of ***sym*-phenPh$_5$C$_7$H** to **a*sym*-phenPh$_5$C$_7$H** over time.

Table 3. The ratio of ***sym*-phenPh$_5$C$_7$H** and **a*sym*-phenPh$_5$C$_7$H** over time at heating to 180 °C.

Time / h	*sym*-phenPh$_5$C$_7$H :	a*sym*-phenPh$_5$C$_7$H
0	1	0
1	0.806	0.194
2	0.787	0.213
3	0.741	0.259
4	0.649	0.351
5	0.634	0.366
22	0.239	0.761
25	0.225	0.775

4.6.3 Tropylium Cation Synthesis *via* Epoxidation

We found that treating **Ph_7C_7H-O** with 1 equivalent of BBr_3 can form the corresponding **$Ph_7C_7^+$** cation immediately. (Figure 4.4) We suggest the mechanism as follows (Scheme 4.7): σ-Complexation of Lewis acid BBr_3 with the oxygen of **Ph_7C_7O** epoxide forms a thermodynamically favoured σ-bond with the oxygen lone pair. This reaction is also favoured by the formation of benzylic and allylic stabilised cation in **Ph_7C_7H-O**. From here, the cation can be quenched through the deprotonation of **Ph_7C_7H-O′** with nucleophilic Br^- formed in the previous step. The cycloheptatriene core is reformed and is now functionalised with good leaving group BBr_2O compared to the original sp^3 H on **Ph7C7H-O**. Elimination of BBr_2O^- is now thermodynamically favoured to form **$Ph_7C_7^+$** by the energy gained through aromatic stabilisation.

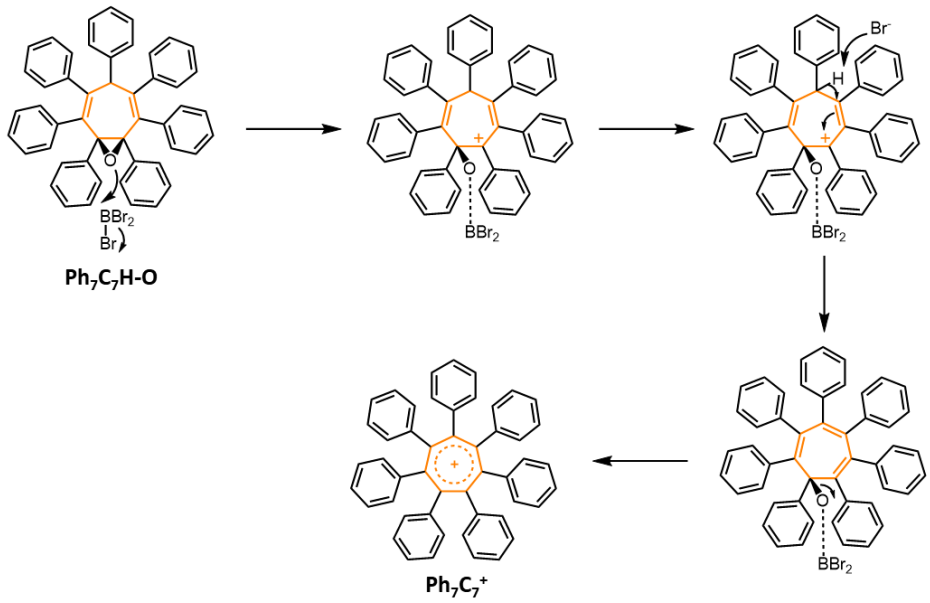

Scheme 4.7. The proposed mechanism for the formation of **$Ph_7C_7^+$** from **Ph_7C_7H-O** with BBr_3.

This is an extremely useful pathway to access the cation when direct oxidation methods fail. In chapter 3 we demonstrate that direct oxidation of **Ph_7C_7H** to **$Ph_7C_7^+$** is significantly easier compared to formation of **$phenPh_5C_7^+$** from **$phenPh_5C_7H$**. As a result, we pass *via* tropone intermediates to replace the sp^3 proton of **$phenPh_5C_7H$** with an OH group that is more readily oxidised. We propose that this trend continues and as more fused rings form between the stages of **Ph_7C_7H** and nanographene **1**, the ease of oxidation of the central ring decreases.

Miao *et al.*[35] has shown that synthesis of **1** *via* tropone intermediates may be possible by subjecting 14b to a phenyl Grignard to form a structure similar to **1** but with the final ring not fused. The main concern with this method is that IOCD conditions would need to be employed to fuse the final ring and would most likely be strong enough to oxidise the resulting OH group on the central ring preferentially.

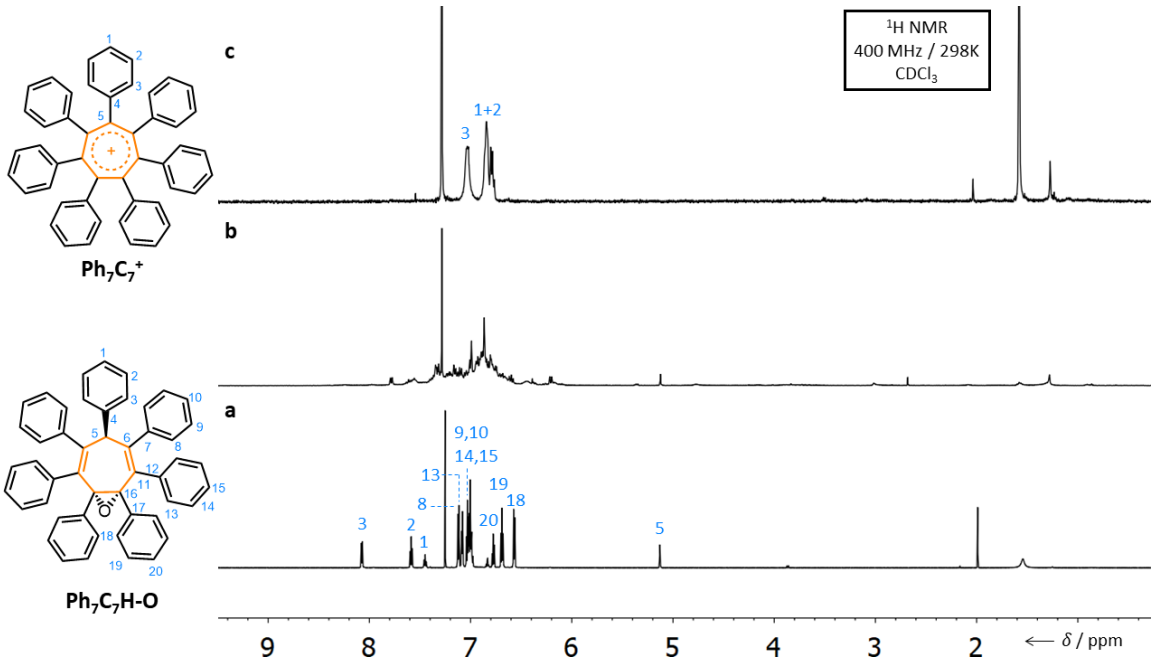

Figure 4.4. ^{1}H NMR spectrums indicating the formation of **$Ph_7C_7^+$** from **Ph_7C_7H-O**. a) A pure sample of **Ph_7C_7H-O** in $CDCl_3$. b) A crude mixture formed upon addition of BBr_3 c) The resulting **$Ph_7C_7^+$** isolated after purification.

4.6.4 Scholl Reactions

General procedures for Scholl oxidation conditions were outlined in 4.5.2. Table 4 outlines the attempts of IOCD using Scholl oxidation conditions with the HACHTs reported in this chapter.

Table 4. Selected results of attempted Scholl oxidation for a range of HACHTs. Yield % are calculated from ^{1}H NMR. Observation of NG and IOCD products confirmed by HR-ESI MS.

HACHT	Oxidant	Temp (˚C)	SM (%)	Cation (%)	NG (%)	Other
Ph_7C_7H	$FeCl_3$	rt	100	0	0	-
	DDQ/TfOH	0	90	10	0	-
	$AlCl_3$ / NaCl	200	0	0	0	Decomposed
	$Cu(CF_3SO_3)_2$ / $AlCl_3$	30	100	0	0	-
$Ph_7C_7^+$	$FeCl_3$	rt	>99	-	0	-
	DDQ / TfOH	0	100	-	0	-
	$AlCl_3$ / NaCl	200	-	-	0	Decomposed
	$Cu(CF_3SO_3)_2$ / $AlCl_3$	30	100	-	0	-
***sym*-phenPh_5C_7H**	$FeCl_3$	Rt	Present	0	0	Chlorination of rings
	DDQ / TfOH	0	Present	Trace	0	IOCD mixture
	$AlCl_3$ / NaCl	200	0	0	0	Decomposed
An_7C_7H	$FeCl_3$	Rt	>99	0	0	Trace single fused
	DDQ / TfOH	0	0	0	0	IOCD mixture
DMB_7C_7H	$FeCl_3$	rt	0	0	0	IOCD mixture
	DDQ / TfOH	0	0	0	Trace	IOCD mixture
Ph_7C_7H-O	$FeCl_3$	rt	Trace	0	0	IOCD mixture
	DDQ / TfOH	0	0	0	0	IOCD mixture

When a large mixture of IOCD products formed it was difficult to integrate relative amounts of starting material. In this case, SM is indicated as present but cannot be quantified. IOCD mixtures were confirmed by HR-ESI MS.

4.6.5. X-Ray Crystallographic Analysis

Analysis of all final novel crystal structures and their packing are shown (Figure 4.5-4.7) with the crystal system, space group, and unit cell parameters reported below. In depth X-ray crystals analysis including bond lengths, bond angles and dihedral angles X-ray for ***sym*-phenPh$_5$C$_7$H**, **asym-phenPh$_5$C$_7$H**, **Ph$_7$C$_7$H-O** and **phen$_2$Ph$_3$C$_7$H** are outlined in Chapter 2 (Section 2.5.2).

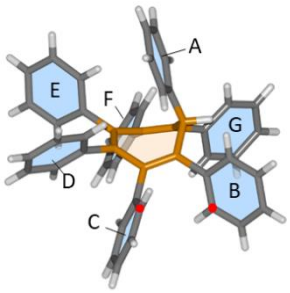

Table 5. Intramolecular distances (Å) between neighbouring aryl rings. Distances are measured as C-C distance from their ortho-position, where IOCD is desired (red). Dashes in table indicate fused C-C bond.

Compound	A-B	B-C	C-D	D-E	E-F	F-G	G-A
Ph$_7$C$_7$H	3.83	3.69	4.28	3.34	4.24	3.43	3.84
Ph$_7$C$_7^+$	3.53	3.54	3.78	3.54	3.40	3.13	3.31
***sym*-phenPh$_5$C$_7$H**	4.28	3.07	3.55	-	3.65	3.29	4.27
An$_7$C$_7$H	4.02	3.34	3.90	3.25	3.35	3.58	4.24
DMB$_7$C$_7$H	3.49	3.56	3.36	3.57	3.83	3.18	3.87
Ph$_7$C$_7$H-O	4.61	3.43	3.64	3.83	3.41	3.29	3.72
phen$_2$Ph$_3$C$_7$H-O	3.64	-	3.65	3.42	3.34	-	3.49

The boat-like conformation of **Ph$_7$C$_7$H** and its derivatives make peripheral ring fusion challenging, as rings A, D and E sit significantly out of plane. Comparing the distances between peripheral rings may give insight to the effects of prefusion, functionalisation and epoxidation for potential ring fusion. Table 1 outlines the distance between neighbouring carbons in the desired position of IOCD to occur. It is important to note that the crystal structure only represents one conformation of the compound in the solid state and may not fully represent true conformation during a reaction. However, we can assume it represents a low energy conformation of each compound that gives a good indication of the influence of functionality on peripheral ring orientation and distance.

Comparing the X-ray crystal data of **Ph_7C_7H** and ***sym*-phenPh_5C_7H** demonstrates that pre-fusion of rings D-E can reduce distance between rings B-C by >0.5 Å indicating IOCD in this position may be more likely. This is consistent with the experimental data where products of successful IOCD for **sym-phenPh_5C_7H** were observed in HR-MS ESI. Furthermore we see an increase in the bond distance between A-B and G-A for **sym-phenPh_5C_7H** as a result of ring A forming close face-face local dimers with rings phenanthrene rings D and E (as reported in chapter 2) that may explain why we observe six fused-rings in the HR-MS ESI but do not observe the complete fused nanographene **1**.

Functionalising the peripheral rings with electron-donating groups, 4-OMe (**An_7C_7H**) and 3,5-OMe (**DMB_7C_7H**), has significant effect on the electronic properties but also on the conformation and C-C distance between neighbouring aryl rings. The increased steric hindrance of aryl groups in **DMB_7C_7H** is expected to limit free bond rotation and result in conformations that minimise interactions of the 3,5-OMe groups of peripheral rings. The bond angle of the $O{-}CH_3$ groups are ~117˚, forcing the rings to adopt a more perpendicular structure similar to **$Ph_7C_7^+$**. The presence of the methoxy groups also reduces face-face interaction between ring A and D/E and hence reduces the C-C distance between rings A-B and G-A, that we have previously found difficult to fuse due to large distances between the neighbouring rings. The slight conformational change coupled with electronic contributions of the EDGs may explain why a complete fused nanographene was observed in HR-MS ESI for **DMB_7C_7H**.

Finally, as discussed in chapter 2 epoxidation breaks central ring conjugation and as a result ring fusion of B-C and F-G occurs selectively in the presence of high energy light to form **$phen_2Ph_3C_7H$-O**. X-ray crystal analysis of **$phen_2Ph_3C_7H$-O** shows a ~0.5-1 Å reduction in the C-C distance of ring A with its neighbouring ring which we have previously shown as the most difficult position to fused, showing a promising route towards the desired nanographene **1** without the need for peripheral ring functionalisation.

$Ph_7C_7^+$

Crystals of **$Ph_7C_7^+$** suitable for X-ray diffraction were grown by slow evaporation of CH_2Cl_2.

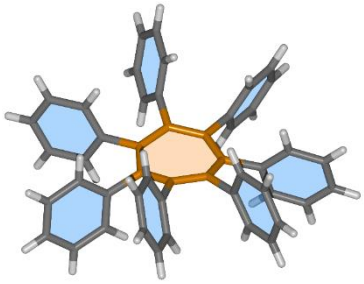

Figure 4.5. Sold-state structure of **$Ph_7C_7^+$** viewed side-on the tropylium centre.

Crystal System: Monoclinic

Space Group: $P2_{1/c}$

Unit Cell Parameters: a = 26.864(2) Å, b = 27.059(2) Å, c = 22.8873(17) Å

An_7C_7H

Crystals of **An_7C_7H** suitable for X-ray diffraction were grown by slow cooling of a saturated MeCN solution.

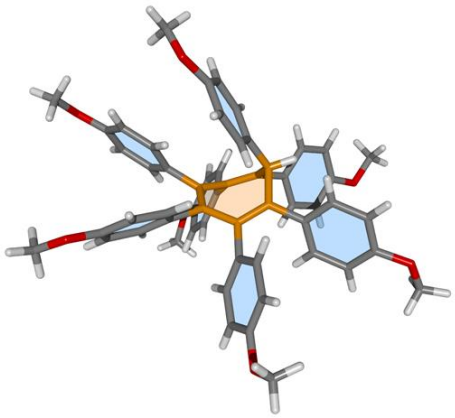

Figure 4.6. Sold-state structure of **An_7C_7H** viewed side on the cycloheptatriene centre.

Crystal System: Triclinic

Space Group: P-1

Unit Cell Parameters: a = 13.2207(7) Å, b = 14.0284(7) Å, c = 14.8093(7) Å

DMB_7C_7H

Crystals of **DMB_7C_7H** suitable for X-ray diffraction were grown by slow evaporation of $CDCl_3$.

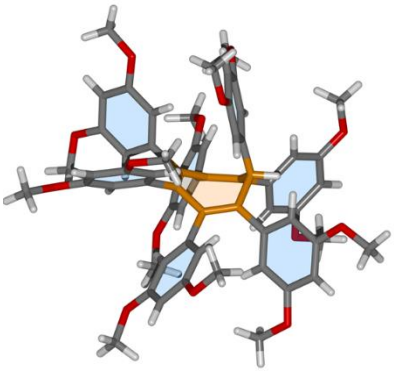

Figure 4.7. Sold-state structure of **DMB_7C_7H** viewed side on the cycloheptatriene centre.

Crystal System: Monoclinic

Space Group: $P2_{1/c}$

Unit Cell Parameters: a = 18.0826(7) Å, b = 18.3587(7) Å, c = 17.1166(7) Å

4.7 References

1. H. Uoyama, K. Goushi, K. Shizu, H. Nomura and C. Adachi, *Nature*, 2012, **492**, 234–238.
2. F. Schwierz, *Nat. Nanotechnol.*, 2010, **5**, 487–496.
3. L. Kurti and B. Czako, *Strategic Applications of Named Reactions in Organic Synthesis : Background and Detailed Mechanisms.*, Elsevier Science, 2005.
4. A. K. Geim and K. S. Novoselov, *Nat. Mater.*, 2007, **6**, 183–191.
5. A. K. Geim, *Science*, 2009, **324**, 1530–1534.
6. A. Hirsch, *Nat. Mater.*, 2010, **9**, 868–871.
7. K. S. Novoselov, A. K. Geim, S. V Morozov, D. Jiang, Y. Zhang, S. V Dubonos, I. V Grigorieva and A. A. Firsov, *Science*, 2004, **306**, 666–9.
8. F. Banhart, J. Kotakoski and A. V. Krasheninnikov, *ACS Nano*, 2011, **5**, 26–41.
9. S. Letardi, M. Celino, F. Cleri and V. Rosato, *Surf. Sci.*, 2002, **496**, 33–38.
10. J. Costa, R. Taveira, C. Lima, A. Mendes and L. Santos, *Opt. Mater. (Amst).*, 2016, **58**, 51–60.
11. A. Ladenburg, *Berichte der Dtsch. Chem. Gesellschaft*, 1881, **14**, 2126–2131.
12. R. Scholl, C. Seer and R. Weitzenböck, *Berichte der Dtsch. Chem. Gesellschaft*, 1910, **43**, 2202–2209.
13. R. Scholl and C. Seer, *Justus Liebigs Ann. Chem.*, 1912, **394**, 111–177.
14. R. Scholl and C. Seer, *Berichte der Dtsch. Chem. Gesellschaft (A B Ser.*, 1922, **55**, 330–341.
15. E. Clar and D. G. Stewart, *J. Am. Chem. Soc.*, 1953, **75**, 2667–2672.
16. E. Clar and J. F. Stephen, *Tetrahedron*, 1965, **21**, 467–470.
17. E. Clar and W. schmidt, *Tetrahedron*, 1979, **35**, 2673–2680.
18. A. Narita, X.-Y. Wang, X. Feng and K. Müllen, *Chem. Soc. Rev.*, 2015, **44**, 6616–6643.
19. C. Ashworth, *Nat. Rev. Mater.*, 2019, **4**, 81.
20. P. Sharma, V. Mangla and R. Dhyani, *J. Innov. Res. Technol.*, 1011, **1**, 2349–6002.
21. K. Kawasumi, Q. Zhang, Y. Segawa, L. T. Scott and K. Itami, *Nat. Chem.*, 2013, **5**, 739–744.
22. J. J. Urgel, M. Di Giovannantonio, Y. Segawa, P. Ruffieux, L. T. Scott, C. A. Pignedoli, K. Itami, R. Fasel, *J. Am. Chem. Soc.*, 2019, **33**, 13158-13164.
23. P. J. Evans, E. R. Darzi and R. Jasti, *Nat. Chem.*, 2014, **6**, 404–408.
24. W. Von E.Doering and L. H. Knox, *J. Am. Chem. Soc.*, 1954, **76**, 3203–3206.
25. R. Willstätter, *Justus Liebig's Ann. der Chemie*, 1901, **317**, 204–265.

26. J. F. Liebman and A. Greenberg, *Chem. Rev.*, 1989, **89**, 1225–1246.

27. L. Zhai, R. Shukla and R. Rathore, *Org. Lett.*, 2009, **11**, 3474–3477.

28. K. Y. Cheung, C. K. Chan, Z. Liu and Q. Miao, *Angew. Chemie Int. Ed.*, 2017, **56**, 9003–9007.

29. P. Rempala, J. Kroulík and B. T. King, *J. Am. Chem. Soc.*, 2004, **126**, 15002–15003.

30. M. S. Subhan ˙ I, N. K. Bhatt ˙ I, M. Mohammad and A. Y. Khan, *Spectroscopic Studies of Charge-Transfer Complexes of 2,3-Dichloro-5,6-Dicyano-P-Benzo-Quinone*, 2000, vol. 24.

31. B. T. King, J. Kroulík, C. R. Robertson, P. Rempala, C. L. Hilton, J. D. Korinek and L. M. Gortari, *J. Org. Chem.*, 2007, **72**, 2279-2288.

32. M. A. Battiste and T. J. Barton, Teterahedron. Lett., 1968, **25**, 2951–2954.

33. J. Johnson and O. Grummitt, *Org. Synth.*, 1943, **23**, 92.

34. L. Zhai, R. Shukla and R. Rathore, *Org. Lett*. 2009, **11**, 3474-3477.

35. X. Yang and Q. Miao, *Synlett.*, 2016, **27**, 2091–2094.

36. S. H. Pun, Y. Wang, M. Chu, C. K. Chan, Y. Li, Z. Liu and Q. Miao, *J. Am. Chem. Soc.*, 2019, **141**, 9680–9686.

37. J. Sturala, M. K. Etherington, A. N. Bismillah, H. F. Higginbotham, W. Trewby, J. A. Aguilar, E. H. C. Bromley, A.-J. Avestro, A. P. Monkman and P. R. McGonigal, *J. Am. Chem. Soc.*, 2017, **139**, 17882–17889.

CHAPTER 5

MODULATION OF CHARGE TRANSFER BY *N*-ALKYLATION TO CONTROL FLUORESCENCE ENERGY AND QUANTUM YIELD.

Synopsis

This project discusses how *N*-alklylation of tertiary amines can provide a simple synthetic tool to tune charge transfer, fluorescence energy and quantum yields. Herein we use quinine as a model system due to being widely used as a fluorescent standard. Through systematic *N*-methylation of the two tertiary amines of quinine, we are able to deconvolute the changes in emission spectra observed traditionally as a function of pH. Photoluminescent measurements and DFT analysis have provided fundamental insight into the through-space charge-transfer (CT) state of quinine and how it provides a loss pathway that can be turned on or off with simple methylation of the quinuclidine nitrogen. Additionally, with this information we have successfully synthesised a superior blue-emitting fluorescent standard that is independent of solvent pH or polarity.

Acknowledgements

The following people are gratefully acknowledged for their contribution to this chapter: Dr Marc Etherington for developing the project and for inviting me to work with him towards this exciting research. Furthermore, I would like to thank Dr Etherington for his role in overseeing the data collection and analysis of photophysical measurements. Dr Basile Curchod for DFT modeling and Dr Dimitry S. Yufit for solving all the X-ray crystal structures.

5.1 Introduction

Fluorecence spectroscopy is an incredibly powerful tool to characterise a wide range of compounds and uncover new and functional phenomena such as thermally activated delayed fluorescence (TADF),[1–3] aggregation-induced emission (AIE)[4] and room temperature phosphorescence (RTP).[5] TADF is one phenomenon that is of particular interest to industrial stakeholders to enhance organic light-emitting diode (OLED) technology for use in a variety of displays and devices. The TADF process is contingent on the presence of charge-transfer (CT) states that form when there is electron and hole localisation on the different component moieties of the molecule. This localisation of the electron and hole reduces overlap between the highest occupied molecular orbital (HOMO) and lowest unoccupied molecular orbital (LUMO). CT states have a significant impact on the photochemistry of the molecule and are commonplace in nature; their presence has been observed in mechanisms involving photosynthesis[6,7] and DNA[8,9]. TADF is one way in which CT states can contribute to enhancing light emission in organic compounds, but their presence is not always positive.

In this work, we utilize quinine (**Qn**) as a model system to unpack the general role of CT states on the photoluminescence efficiency of organic compounds. Recent literature has shown that some of the cinchona alkaloids display CT and proton transfer that have a significant effect on their photophysical properties.[10,11] These studies have previously been performed using protonation and deprotonation *via* acidic and basic solvents. Here we use *N*-alkylation to permanently modify quinine, allowing investigation into the structure-property relationship of fluorescence energy and quantum yield in quinine. We propose alkylation as a superior method for studying the effects of protonation in organic solvents and the solid state, as they do not require acidic conditions and therefore are not subject to equilibrium in the solution. The new compounds produced by this modification display superior photoluminescence quantum yields (PLQYs) to acidified quinine sulfate, which is the leading fluorescence standard for characterising blue emitters. This means these new emitters have the potential to disrupt the *status quo* of the past 50 years and open the pathway for tuning of quinine, cinchona alkaloids and any tertiary amine[12–14] to imbue further functional properties, such as TADF.

5.2 Results and Discussion

Molecular quinine (**Qn**) typically exhibits low photoluminecence emission efficiency, rendering it useless as a quantum yield standard. However, enhanced emission is observed in acidified aqueous solutions, most commonly 0.1 M H_2SO_4, which protonates both tertiary amines, giving acidified quinine sulfate (**QS**). **QS** exhibits characteristically high PLQY (60%) and blue emission, providing an industry-wide quantum efficiency standard.[15] To systematically study the origins of the photophysical properties of **Qn** we synthesised (Scheme 1) a series of three new methylated salts: **MeQn**·BF_4, **Me$_2$Qn**·2BF_4 and **iMeQn**·BF_4. After methylation with MeI at room temperature, the resulting **MeQn**·I salt was exchanged with BF_4^- to avoid fluorescent quenching arising from the heavy atom effect of iodine. Methylation was chosen as a method to permanently 'protonate' the tertiary amines of **Qn** and, unlike with acidified solutions, can be achieved selectively to investigate the role of N_1 and N_2 in CT independently. Also, one-pot exhaustive *N*-methylation of **Qn** gives access to **Me$_2$Qn**·2BF_4 (Scheme 5.1), a highly blue PLQY standard that is soluble in most common organic solvents and not limited to aqueous acidified solutions. **iMeQn** was succesfully synthesised through protection of highly nucleophilic N_1 followed by N_2 methylation. Subsequent deprotection of N_1 with barbituaric acid allowed for the systematic study of the effect of alkylation of N_2 independant of N_1 methylation.

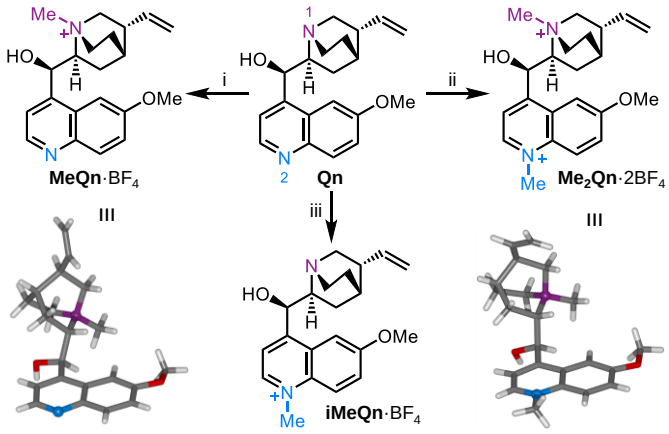

Scheme 5.1. *N*-alkylation of **Qn** to *N*-methylquinium tetrafluoroborate, **MeQn**·BF_4, *N*,*N*'-dimethylquinium bis(tetrafluoroborate), **Me$_2$Qn**·2BF_4 and iso-*N*-methyl-quinium tetrafluoroborate, **iMeQn**·BF_4. Solid-state structures of **MeQn**·BF_4 and **Me$_2$Qn**·2BF_4 are depicted in stick representation with the nitrogen atoms shown as balls. Reagents and conditions: i) a. MeI, rt, 3 d, b. $AgBF_4$, MeCN, 60 °C, 10 min, 74% over two steps; ii) a. MeI, MeCN, 100 °C, 4 h, b. $AgBF_4$, MeOH, rt, 10 min, 79% over two steps; iii) a. allyl bromide, CH_2Cl_2, rt, 16 h, b. MeI, MeCN, 100 °C, 3 h, c. barbituric acid, $Pd(PPh_3)_4$ (5 mol%), Me_2SO, 40 °C, 16 h, d. diisopropylaminomethyl polystyrene, MeOH, rt, 1h, e. $AgBF_4$, MeOH, rt, 10 min, 79% over 5 steps.

The cinchona alkaloid series all share the same core quinoline and quinuclidine moieties that are linked (see Figure 5.1 for numbering) through a single carbon atom C_{11}. The overall conformation of these alkaloids are determined by the torsional angle of the two bonds connecting C_{11} to either cyclic moiety. To ensure methylation was not having drastic effects on the conformation of **Qn**, which might be responsible for modifying its photoluminescence, we measured the torsion angle of N_1-C_{12}-C_{11}-C_8 observed in the solid state by X-ray crystallography. In each case (Table 2, appendix) we found a similar increase of ~6.0˚ in the torsion angle of **Me$_2$Qn**·2BF_4 and **QS** compared to free base **Qn**. The conformation of the quinine cation adopts an 'open conformation', consistent with Svendsen *et al.*[16] nomenclature, whereby H_{12} and H_{11} approach a staggered conformation that requires the quinuclidine ring to move away upon protonation/methylation of N_1, resulting in an increase in torsion angle. We also monitored the chemical shift of H_{11} (Figure 5.1) in each case to show the effect of methylating each nitrogen. We observe a downfield shift of H_{11} compared to free base **Qn**, consistent with reports of N_1 protonation of cinchona bases.[17]

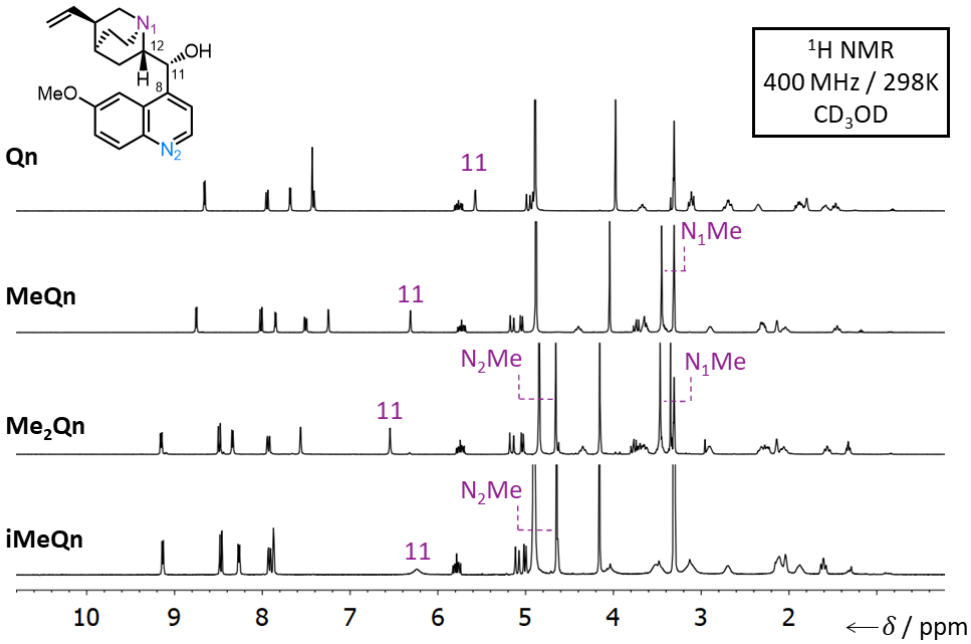

Figure 5.1. ^{1}H NMR stack of **Qn**, **MeQn**·BF_4, **Me$_2$Qn**·2BF_4 and **iMeQn**·BF_4 indicating characteristic shift in H_{11} upon methylating N_1.

In our calculations, we used protonation of N_1 and N_2 instead of a methylation, with Table 5 (appendix) summarising our findings that the effect of such substitution is minimal for emission energies. Recent work by Qin *et al.*[10] shows that protonation of

N_1 in quinidine, a stereoisomer of **Qn**, prevents the formation of a CT state and therefore results in its increased PLQY. Theoretical studies (Section 5.6) show that such CT excited states correspond to the transition from a lone-pair located on N_1 to an unoccupied π-orbital on the quinoline ring (n-π* transition). We can also observe this experimentally by measuring the photoluminescence solvatochromism of **Qn** (Figure 5.2a) in a range of protic and aprotic solvents, whereby protonation of N_1 modulates the CT state. (The nature of the CT state is described in detail in Section 5.6). This allows us to draw the conclusion that the low PLQY of **Qn** is a consequence of a low-lying CT state that results in non-radiative decay, giving rise to barely detectable fluorescence. This CT state can be controlled by protonation or alkylation of N_1, coordinating to the lone-pair and preventing the CT state n-π* transition from the lone pair to the quinoline ring. This results in the observed increase in PLQY in **MeQn**·BF_4 and **Me$_2$Qn**·2BF_4.

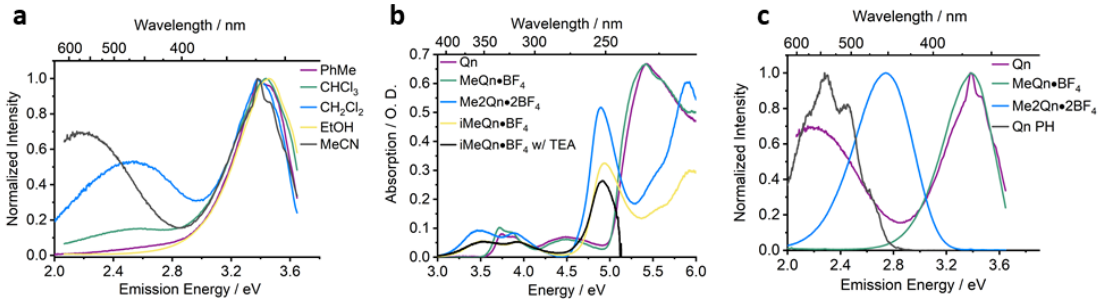

Figure 5.2. a) Emission spectra of molecular quinine (**Qn**) (20 µM) as a function of solvent polarity. For aprotic polar solvents there is a lower energy emissive CT state. In a protic, polar solvent such as ethanol the CT state does not form due to the protonation of the nitrogen. b) UV-Vis absorption spectra c) emission spectra of **Qn**, **MeQn**·BF_4 and **Me$_2$Qn**·2BF_4 in MeCN at 20 µM concentration. The **iMeQn**·BF_4 was measured in pure MeCN and MeCN with 10 mM of triethylamine (Et_3N) to ensure N_1 reamins deprotonated. The significant shift in the absorption spectra are associated to the methylation of the second nitrogen atom site. The emission of **iMeQn**·BF_4 is included in Fig 5.10c due to the low signal to noise ratio. The phosphorescence spectra of **Qn**, (Qn PH), obtained from a 1 wt% doped zeonex film at 80 K and at a 40 ms time delay is included to show where the energy of the CT state would be required to be for efficient TADF in **Qn**.

For **iMeQn**·BF_4, where only N_2 is methylated, a significant bathochromic shift in the absorption is observed compared to **Qn** (Figure 5.2b). Due to the high nucleophilicity of N_1, **iMeQn**·BF_4 is extremely sensitive to protonation in both organic and aqueous solvents, and gives absorption and emission data similar to **Me$_2$Qn**·2BF_4 in the presence of trace moisture. To overcome this, the photoluminescence is measured in a 10 mM Et_3N / MeCN solution to ensure deprotonation of N_1. As a result, a significant decrease in the PLQY is observed (0%) when N_1 is deprotonated, compared to a 60%

PLQY in H_2O where N_1 is protonated (Figure 5.10e appendix). Calculations for **iMeQn**·BF_4 show a large red-shift in the local emission (π-π*), which is consistent with the bathochromic shift observed in Figure 5.2c, and also indicates the presence of CT (n-π*) vertical transition. The calculated vertical emission energies (Table 5) show that the lowest energy emission of **iHQn** is expected to be quenched due to the presence of the CT state, reinforcing the undetectable fluorescence in the analogous methylated derivative **iMeQn**·BF_4 (Figure 5.10c). Protonation of both N_1 and N_2 (**Me$_2$Qn**·$2BF_4$) causes a significant bathochromic shift in the absorption (Figure 5.2b), similar to **iMeQn**·BF_4, however this compound shows an emission band at 450 nm which is bathochromic shifted compared to **Qn** (Figure 5.2c). The bathochromic shift in both absorption and emission of **Me$_2$Qn**·$2BF_4$ is further confirmed using linear-response time-dependent density functional theory (LR-TDDFT) (Tables 4-5). The calculations show that **H$_2$Qn** exhibits both a change in the colour of its fluorescence and a decrease in non-radiative decay as the possible CT state is blocked. This is observed experimentally with an increase in PLQY from 0% in **iMeQn**·BF_4 to 63% in **Me$_2$Qn**·$2BF_4$. We therefore demonstrate that alkylation provides a tool to systematically control the PLQY and fluorescence energy of **Qn** compounds and, in theory, other cinchona alkaloids.

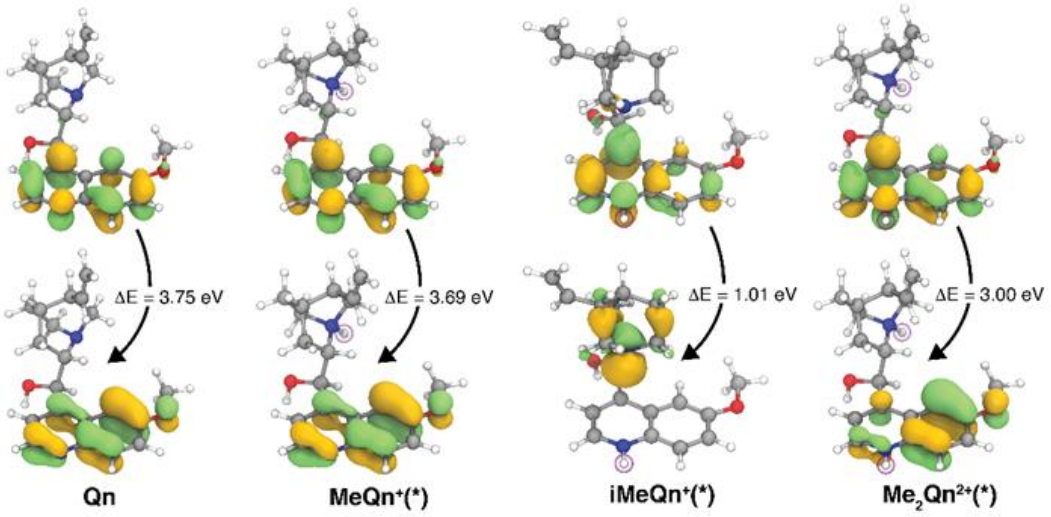

Figure 5.3. (a-d) Natural transition orbitals and energies characterizing the emission of the different molecules, calculated at the LR-TDDFT/wB97X-D/6-31G* level of theory with state-specific implicit solvation. (*) indicates that protonation is considered instead of methylation (see section 5.5.2 for validation)

To account for the sensitivity of N_1 to protonation and to ensure all compounds were compared equally, the PLQY of each compound was measured in H_2O, MeCN and 10 mM Et_3N / MeCN (Figure 5.7 – 5.12). Measuring **Qn** in MeCN and 10mM Et_3N / MeCN show no effect on the emission profile and gives negligible PLQY. This is as a result of the low-lying CT state that is only modulated when H_2O is added, increasing the PLQY to 22% upon N_1 protonation and inhibiting the CT state (Table 1). It is worth noting that the reduced acidity of H_2O compared to 0.1% H_2SO_4 results in less N_1 protonation and hence drastically different PLQY versus **QS** (~54%). The absence of a low-lying CT state in **MeQn**·BF_4 and **Me$_2$Qn**·$2BF_4$ means the emission profiles are unaffected in MeCN upon addition of Et_3N as N_1 is permanently methylated. This prevents access of the CT state independent of acidity, unlike **Qn**. On the other hand, **iMeQn**·BF_4 shows a dramatic difference in the emission profile between solutions of MeCN and 10 mM Et_3N / MeCN, resulting from the deprotonation of N_1 under basic conditions. This allows the lone pair to donate into the π^* giving the 'quenching' (n-π^*) CT state. The deprotonation of N_1 in the presence of Et_3N is demonstrated using ^{1}H NMR (Figure 5.4, appendix), where the N_1 proton is removed and an upfield-shift of H_{11} is observed, consistent with our reported shifts in Figure 5.1.

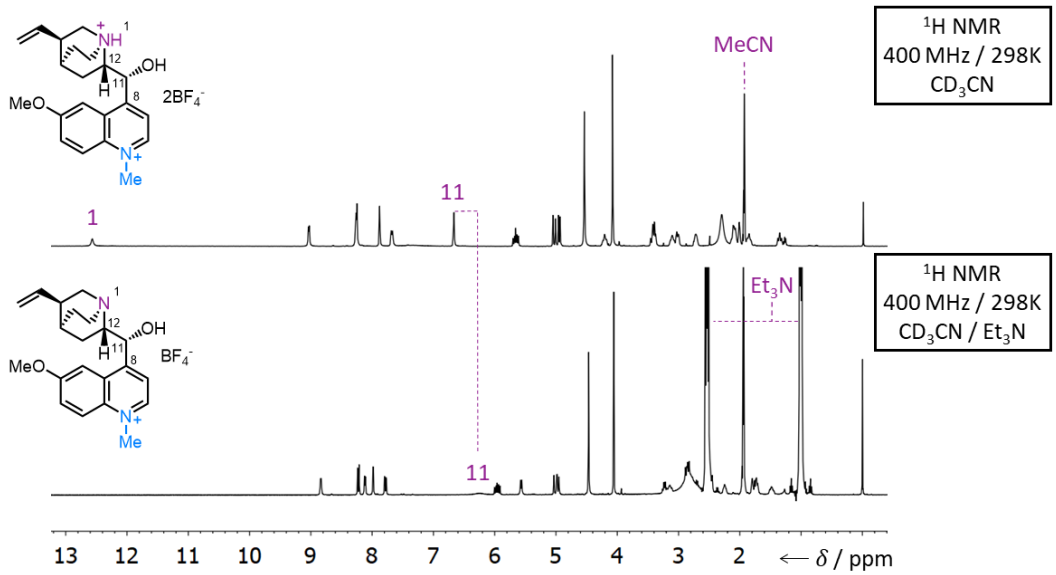

Figure 5.4. ^{1}H NMR stack of **H-iMeQn**·$2BF_4$ and **iMeQn**·BF_4. H_{11} shift labelled and is consistent with the literature when deprotonating N_1.[17]

The permanent methylation of N_1 eliminates the equilibrium present between the free base and N_1 protonation of **Qn** in H_2O. As a result, an increase in PLQY for both

MeQn·BF_4 and **Me$_2$Qn**·$2BF_4$ in H_2O compared to **Qn** is observed. The decrease in PLQY of each compound in MeCN is a result of enhanced ion quenching which occurs when solvent polarity decreases. In both MeCN and H_2O, a significant increase in the PLQY occurs upon N_2 methylation (when N_1 is also methylated), further increasing the PLQY to 63% and 70% respectively (Table 1). The PLQY of **Me$_2$Qn**·$2BF_4$ significantly decreases in the 10 mM Et_3N in MeCN, as a result of a non-linear relationship between emission and optical density (Figure 5.10d). As expected, the emission profile and PLQY of **iMeQn**·BF_4 in H_2O is comparable to **Me$_2$Qn**·$2BF_4$, as the CT state is blocked, and emission at 450 nm is observed. The CT state is reformed in 10 mM Et_3N / MeCN and calculations show that, upon relaxation in the excited state, the CT state always appears at a lower energy than the locally excited (LE) state of the quinoline π-system, which is attributed as the main emissive state in each compound (Table 5 appendix). This indicates a possible nonradiative decay from the emissive LE state to the non-emissive CT, resulting in fluorescent quenching. This is demonstrated by the undetectable emission of **iMeQn**·BF_4 in 10 mM Et_3N/MeCN.

Table 1. A table summarising the key characteristics of the compounds as a function of methylation of the nitrogen atom sites. The presence (or lack) of CT state is shown either by experimental observation or theoretical calculation reported in electron volts (eV). The PLQYs for **Qn** and **MeQn**·BF_4 are measured compared to 2-aminopyridine in 0.1 M H_2SO_4 and those of **Me$_2$Qn**·$2BF_4$ and **iMeQn**·BF_4 are measured with respect to quinine sulphate in 0.1 M H_2SO_4.

Compound	Φ_{MeCN}[a]	Φ_{H_2O}	E_{em}	Calculated E_{LE}[b]	Calculated E_{CT}[b]	Presence of CT
Qn	0% (0%)	22%	3.4 (2.2)	3.75	0.87	Yes
MeQn•BF_4	5% (8%)	32%	3.4	3.69	-	No
Me$_2$Qn•$2BF_4$	63% (12%)	70%	2.8	3.0	-	No
iMeQn•BF_4	N/A (0%)	60%	-	-	1.01	Yes

[a]Value in brackets gives quantum yield in MeCN with 10 mM of Et_3N. [b]Values for protonated rather than methylated compounds calculated at the LR-TDDFT/ωB97X-D/6-31G level of theory with state-specific implicit solvation (MeCN).*

The modulation of the CT state with alkylation provides another interesting parameter. In these particular compounds the CT state acts as a loss pathway. This is due to the triplet energy of **Qn** being significantly lower than the CT state, as shown in Figure 5.2. The CT state that forms in **iMeQn**·BF_4 is unfortunately too low in energy to benefit from reverse intersystem crossing (rISC) from the triplet state, however if the energies of the CT state and triplet state could be matched, TADF can be turned on, giving

promising future research with this material, beyond a control study for methylation as reported in this chapter.

Acidified quinine sulfate (**QS**) is a popular and commonly used PLQY standard for new blue emitters, with a PLQY of around 54%. This value arises specifically in an aqueous 0.1% H_2SO_4 solution and fluctuates at higher acid concentrations. The PLQY is limited by the equilibrium between the free base and protonated N_1, therefore the formation of the unfavorable CT state is never completely blocked. Herein, we have presented **Me$_2$Qn**·2BF_4 a superior blue PLQY standard (70%). Methylation of both N_1 and N_2 means **Me$_2$Qn**·2BF_4 can be measured in common organic solvents and non-acidified water, negating any errors associated with solvent acidity. The enhanced performance in both organic and aqueous solvents positions **Me$_2$Qn·2BF$_4$** as a promising new fluorophore for biological tagging.

5.3 Conclusion

Through experimental and computational methods we have uncovered the nature of the CT state in molecular quinine and its role in quenching its PLQY. We show that methylation provides a permanent and solvent independent method to block the formation of the CT state and hence resulting in enhanced PLQYs. Through the systematic methylation of N_1 and N_2 we confirm that N_2 is responsible for the colour of the emission, shifting the emission from UV to visible upon methylation. Methylation of only N_2 strengthens the CT state and all visible emission is quenched. Understanding the component effect of each nitrogen gives us a detailed insight into why **Me$_2$Qn**·BF_4^- provides superior PLQY compared to acidified **QS** in organic and aqueous solvents. Furthermore, the understanding of the component effects in **Qn** will allow us to further manipulate the photoluminescent properties through the tuning of the CT state to possibly give rise to new derivatives with TADF properties.

5.4 Experimental Details

5.4.1 Specific Experimental Methods

Materials: All reagents were purchased from commercial suppliers (Sigma-Aldrich, Acros Organics, or Alfa Aesar) and used without further purification.

Measurements: UV-Vis-NIR absorbance spectra of solution samples were recorded using an Agilent Technologies Cary Series UV-vis-NIR spectrophotometer at room temperature. Steady-state photoluminescence of films and solutions were measured using a Jobin Yvon Fluoromax or Fluorolog with machine-specific calibration curves. The photoluminescence quantum yields (PLQYs) of the compounds were measured using the relative method[18] and comparing to known standards of quinine sulfate[19] and 2-aminopyridine[20] in 0.1 M H_2SO_4. The absorption spectra and photoluminescence spectra for the PLQYs were measured on a Shimadzu UV-3600 UV-VIS-NIR spectrophotometer and a Jobin Yvon Fluoromax or Fluorolog.

5.4.2 Synthetic Procedures

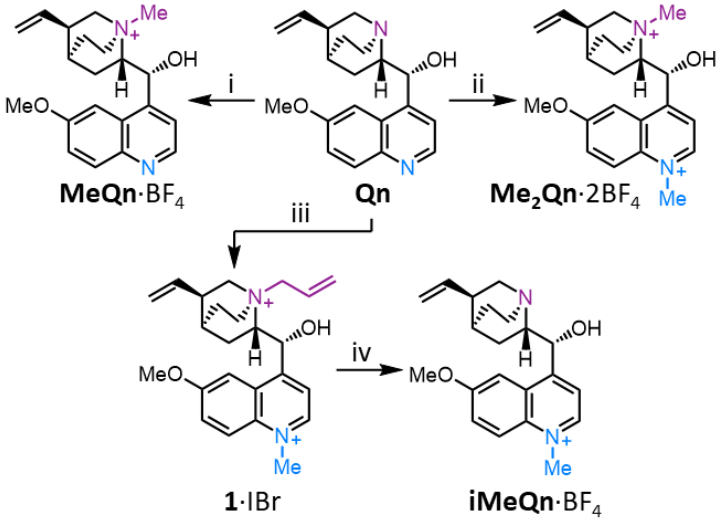

Scheme 2. Synthetic routes to **MeQn**·BF_4, **Me_2Qn**·BF_4 and **iMeQn**·BF_4. Reagents and conditions: i) a. MeI / rt / 3 d, b. $AgBF_4$ / MeCN / 60 °C / 10 min / 93%; ii) a. MeI / MeCN / 100 °C / 4 h, b. $AgBF_4$ / MeOH / rt / 10 min / quant.; iii) a. Allyl bromide / CH_2Cl_2 / rt / 16 h, b. MeI / MeCN / 100 °C / 3 h / 81%; iv) a. Barbituric acid / $Pd(PPh_3)_4$ (5 mol%) / Me_2SO / 40 °C / 16 h, b. Diisopropylaminomethyl polystyrene / MeOH / rt / 1h, c. $AgBF_4$ / MeOH / rt / 10 min / quant..

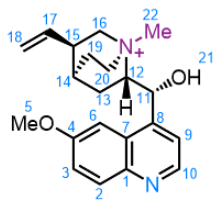

MeQn·BF_4: Quinine (500 mg, 1.54 mmol) was added to an oven-dried microwave vial and sealed. MeI (5 mL) was added and the mixture was sonicated at rt for 20 min. The reaction mixture was stirred for 3 days at rt. The mixture was filtered to isolate the precipitate, washing with CH_2Cl_2 (2 × 5 mL) and drying the precipitate under high vacuum. The resulting solid was recrystallized from MeCN to yield the iodide salt of title compound as a crystalline solid (618 mg, 1.23 mmol, 80 %). **MeQn**·I (106 mg, 0.227 mmol) was dissolved in MeCN (8 mL) and heated to 60 °C. A solution of $AgBF_4$ (44.0 mg, 0.227 mmol) in MeCN (1 mL) was added dropwise and allowed to stir at 60 °C for 10 min. The resulting mixture was filtered, and the filtrate was evaporated to dryness to give the title compound as a colourless solid (87 mg, 0.20 mmol, 93%). **M.P.** 185 – 187 °C. **^{1}H NMR** (700 MHz, DMSO-d_6) δ 8.79 (d, J = 4.5 Hz, 1H, H_{10}), 8.00 (d, J = 9.2 Hz, 1H, H_2), 7.70 (d, J = 4.9 Hz, 1H, H_9), 7.48 (dd, J = 9.2, 2.7 Hz, 1H, H_3), 7.21 (d, J = 2.7 Hz, 1H, H_6), 6.54 (d, J = 2.7 Hz, 1H, H_{21}), 6.21 (d, J = 3.2 Hz, 1H, H_{11}), 5.75 (ddd, J = 17.3, 10.5, 6.8 Hz, 1H, H_{17}), 5.13 – 5.01 (m, 2H, H_{18}), 4.07 (m, 1H, H_{20}), 4.00 (s, 3H, H_5), 3.74 – 3.60 (m, 3H, H_{16+12}), 3.45 – 3.35 (m, 4H, H_{20+22}), 2.85 – 2.76 (m, 1H, H_{15}), 2.20 – 2.10 (m, 2H, H_{13+19}), 2.06 – 2.01 (m, 1H, H_{14}), 1.97 – 1.87 (m, 1H, H_{19}), 1.38 – 1.31 (m, 1H, H_{13}). **^{13}C NMR** (176 MHz, DMSO-d_6) δ 157.4 (C_4), 147.4 (C_{10}), 143.8 (C_8), 143.6 (C_1), 137.9 (C_{17}), 131.5 (C_2), 125.1 (C_7), 121.5 (C_3), 119.9 (C_9), 116.5 (C_{18}), 101.6 (C_6), 66.78 (C_{12}), 63.9 (C_{11} + C_{16}), 55.48 (C_5), 54.2 (C_{20}), 48.7 (C_{22}), 37.6 (C_{15}), 25.9 (C_{14}), 24.6 (C_{19}), 19.3 (C_{13}). **^{19}F NMR** (376 MHz, CD_3OD) δ -150.48 (m), -150.54 (m). **HR-ESI-MS** m/z = 339.2088 $[M\text{-}BF_4]^+$ (calculated for $C_{21}H_{27}N_2O_2$ = 339.2073).

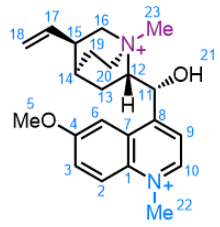

Me$_2$Qn·2BF_4: Quinine (2.00 g, 6.17 mmol) was added to an oven-dried microwave vial and sealed. MeCN (18 mL) was added and stirred at rt before adding MeI (1.92 mL, 30.8 mmol). The resulting mixture was heated at 100 °C for 4 h then allowed to cool to rt and further cooled to 5 °C in a fridge to allow the product to crystallise. The supernatant was decanted and the resulting crystals were isolated and dried under high vacuum to give the diiodide salt of the title compound (2.98 g, 4.9 mmol, 79%).

Me_2Qn·2I (200 mg, 0.329 mmol) was dissolved in MeOH (5 mL) and a solution of $AgBF_4$ (128 mg, 0.658 mmol) in MeOH (5 mL) was added dropwise and stirred at rt for 10 min. The reaction mixture was filtered, and the filtrate was evaporated to dryness to yield the title compound as a colourless solid (135 mg, 0.329 mmol, quantitative). **M.P.** 195 – 197 °C. **^{1}H NMR** (600 MHz, DMSO-d_6) δ 9.32 (d, J = 6.1 Hz, 1H, H_{10}), 8.51 (d, J = 9.7 Hz, 1H, H_2), 8.28 (d, J = 6.0 Hz, 1H, H_9), 7.99 (dd, J = 9.7, 2.6 Hz, 1H, H_3), 7.54 (d, J = 2.7 Hz, 1H, H_6), 7.16 – 7.05 (m, 1H, H_{21}), 6.53 – 6.46 (m, 1H, H_{11}), 5.70 (ddd, J = 17.3, 10.5, 6.9 Hz, 1H, H_{17}), 5.13 – 5.03 (m, 2H, H_{18}), 4.62 (s, 3H, H_{22}), 4.14 (m, 4H, H_{5+20}), 3.77 – 3.61 (m, 3H, H_{12+16}), 3.48 – 3.38 (m, 4H, H_{20+23}), 2.87 – 2.79 (m, 1H, H_{15}), 2.10 (m, 3H, H_{13+19}), 2.00 – 1.92 (m, 1H, H_{14}), 1.36 (m, 1H, H_{13}). **^{13}C NMR** (151 MHz, DMSO-d_6) δ 159.3 (C_4), 154.9 (C_1), 146.3 (C_{10}), 137.9 (C_{17}), 133.6 (C_8), 127.1 (C_7), 126.6 (C_3), 121.8 (C_2), 121.1 (C_9), 116.6 (C_{18}), 103.9 (C_6), 66.2 (C_{12}), 64.5 (C_{11}), 64.2 (C_{16}), 56.3 (C_5), 54.4 (C_{20}), 48.8 (C_{23}), 45.6 (C_{22}), 37.4 (C_{15}), 25.8 (C_{14}), 24.6 (C_{19}), 19.4 (C_{13}). **^{19}F NMR** (376 MHz, CD_3OD) δ -150.49 (m), -150.54 (m). **HR-ESI MS** *m/z* = 440.2379 $[M\text{-}BF_4]^+$ (calculated for $C_{22}H_{30}N_2O_2{}^{10}BF_4$ = 440.2373).

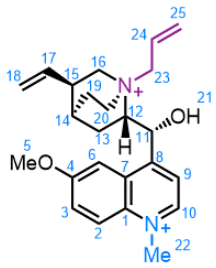

1·IBr: Quinine (500 mg, 1.54 mmol) was placed into an oven-dried round-bottomed flask. CH_2Cl_2 (2.5 mL) was added and stirred at rt before adding allyl bromide (0.13 mL, 1.54 mmol). The resulting solution was stirred at rt for 16 h. The volatiles were then removed under vacuum. The resulting solid was dissolved in MeCN (2.5 mL) and MeI (0.13 mL, 2.09 mmol) was added dropwise and the mixture was heated to 100 °C for 3 h. The mixture was allowed to cool to rt and further cooled to 5 °C in a fridge to allow the product to precipitate. The orange precipitate was isolated by filtration and washed with CH_2Cl_2 (2 × 5 mL), then dried under high vacuum to give the title compound as an orange solid (710 mg, 1.25 mmol, 81%). **M.P**. 203 – 205 °C. **^{1}H NMR** (400 MHz, DMSO-d_6) δ 9.32 (d, J = 6.1 Hz, 1H, H_{10}), 8.50 (d, J = 9.7 Hz, 1H, H_2), 8.25 (d, J = 6.0 Hz, 1H, H_9), 8.00 (dd, J = 9.7, 2.7 Hz, 1H, H_3), 7.54 (d, J = 2.7 Hz, 1H, H_6), 7.10 (d, J = 4.1 Hz, 1H, H_{21}), 6.55 (m, 1H, H_{11}), 6.26 (m, 1H, H_{24}), 5.81 – 5.59 (m, 3H, H_{17+23}), 5.09 – 4.97 (m, 2H, H_{18}), 4.58 (s, 3H, H_{22}), 4.54 (m, 1H,

H_{25}) 4.29 (m, 1H, H_{25}), 4.12 (s, 3H, H_5), 4.05 – 3.96 (m, 1H, H_{20}), 3.76 – 3.65 (m, 2H, H_{12+16}), 3.57 – 3.39 (m, 2H, H_{16+20}), 2.79 (m, 1H, H_{15}), 2.13 – 1.96 (m, 4H, $H_{13+14+19}$), 1.32 (m, 1H, H_{13}). **^{13}C NMR** (101 MHz, DMSO-*d*$_6$) δ 159.4 (C_4), 154.9 (C_1), 146.4 (C_{10}), 138.1 (C_{17}), 133.7 (C_8), 127.5 (C_{23}), 127.3 (C_7), 126.6 (C_3), 126.2 (C_{24}), 121.9 (C_2), 121.5 (C_9), 116.7 (C_{18}), 104.4 (C_6), 65.9 (C_{12}), 64.6 (C_{11}), 62.5 (C_{25}), 60.3 (C_{16}), 56.5 (C_5), 52.2 (C_{20}), 45.7 (C_{22}), 37.3 (C_{15}), 26.1 (C_{14}), 24.5 (C_{19}), 20.4 (C_{13}). **HR-ESI-MS** *m/z* = 507.1505 $[M\text{-}Br]^+$ (calculated for $C_{24}H_{32}N_2O_2I$ = 507.1508).

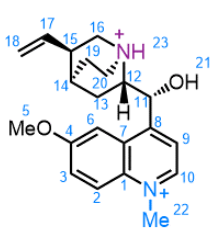

H-iMeQn·2Cl**:** **1**·IBr (80 mg, 0.14 mmol) was dissolved in Me_2SO (1 mL) then $Pd(PPh_3)_4$ (8 mg, 6.92 µM, 5 mol%) and barbituric acid (52 mg, 0.4 mmol) were added to the reaction mixture and stirred overnight at 40 °C. A 1 M aqueous solution of HCl (1 mL) was added and stirred for 5 min. The mixture was then purified by reverse phase column chromatography (Teledyne Isco CombiFlash Rf+ system, 40 g C18, 0.05 M $HCl_{(aq)}$ / MeOH, 0 – 100% elution). The product was isolated as a yellow film (57 mg, 0.14 mmol, quantitative). **^{1}H NMR** (400 MHz, DMSO-*d*$_6$) δ 9.14 (d, *J* = 6.1 Hz, 1H, H_{10}), 8.45 (d, *J* = 9.8 Hz, 1H, H_2), 8.28 (d, *J* = 6.1 Hz, 1H, H_9), 7.88 (m, 2H, H_{3+6}), 6.51 (s, 1H, H_{11}), 5.75 (ddd, *J* = 17.4, 10.4, 7.2 Hz, 1H, H_{17}), 5.10 – 5.00 (m, 2H, H_{18}), 4.63 (s, 3H, H_{22}), 4.27 – 4.19 (m, 1H, H_{20}), 4.16 (s, 3H, H_5), 3.67 (m, 1H, H_{12}), 3.60 (m, 1H, H_{16}), 3.31 (m, 1H, H_{16}), 3.24 (m, 1H, H_{20}) 2.81 (m, 1H, H_{15}), 2.19 (m, 2H, H_{13+19}), 2.09 (m, 1H, H_{14}), 1.98 (m, 1H, H_{19}), 1.57 (m, 1H, H_{13}). **^{13}C NMR** (101 MHz, DMSO-*d*$_6$) δ 162.4 (C_4), 158.0 (C_1), 147.1 (C_{10}), 139.2 (C_{17}), 135.9 (C_8), 129.8 (C_7), 129.4 (C_3), 122.4 (C_2), 121.6 (C_9), 117.3 (C_{18}), 104.5 (C_6), 68.1 (C_{11}), 60.9 (C_{12}), 58.6 (C_5), 55.5 (C_{16}), 46.5 (C_{23}), 45.3 (C_{20}), 38.5 (C_{15}), 28.4 (C_{14}), 25.1 (C_{19}), 19.2 (C_{13}). **HR-ESI-MS** *m/z* = 409.1472 $[M\text{-}H]^+$ (calculated for $C_{21}H_{27}N_2O_2Cl_2$ = 409.1449).

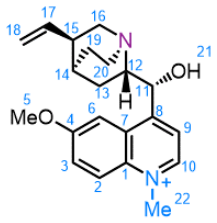

iMeQn·BF_4: **H-iMeQn**·2Cl (64 mg, 0.16 mmol) was dissolved in MeOH (10 mL) and then added diisopropylaminomethyl polystyrene, polymer-bound 100-200 mesh, 2.0-3.5 mmol/g (467 mg, 1.4 mmol) was added. The reaction mixture was stirred for 1 h at rt before being filtered. The filtrate was evaporated to dryness and the film was washed with hexanes (5 × 10 mL) to remove residual polymeric reagent then dried under high vacuum to yield **iMeQn**·Cl (45 mg, 0.12 mmol, 86%). The chloride salt was dissolved in anhydrous MeOH (3 mL) and a solution of $AgBF_4$ (23 mg, 0.12 mmol) in anhydrous MeOH (2 mL) was added dropwise then stirred for 10 min at rt. The reaction mixture was filtered, and the filtrate was evaporated to dryness to yield the title compound as an off white solid (51 mg, 0.12 mmol, quantitative). **M.P.** 204 – 206 °C. **^{1}H NMR** (400 MHz, CD_3OD) δ 9.14 (d, *J* = 6.1 Hz, 1H, H_{10}), 8.48 (d, *J* = 9.7 Hz, 1H, H_2), 8.27 (d, *J* = 6.1 Hz, 1H, H_9), 7.92 (d, *J* = 9.7, 2.4 Hz, 1H, H_3), 7.87 (m, 1H, H_6), 6.24 (s, 1H, H_{11}), 5.79 (ddd, *J* = 17.4, 10.4, 7.2 Hz, 1H, H_{17}), 5.10 – 5.01 (m, 2H, H_{18}), 4.65 (s, 3H, H_{22}), 4.16 (s, 3H, H_5), 4.06 (m, 1H, H_{20}), 3.52 (m, 1H, H_{12}), 3.48 (m, 1H, H_{16}), 3.13 (m, 2H, H_{16+20}), 2.70 (m, 1H, H_{15}), 2.14 (m, 3H, H_{13+19}), 2.04 (m, 1H, H_{14}) 1.87 (m, 1H, H_{19}), 1.61 (m, 1H, H_{13}). **^{13}C NMR** (101 MHz, CD_3OD) δ 162.1 (C_4), 147.2 (C_{10}), 140.1 (C_{17}), 135.9 (C_8), 129.9 (C_7), 129.0 (C_3), 122.4 (C_2), 121.5 (C_9), 116.7 (C_{18}), 104.5 (C_6), 69.4 (C_{11}), 61.2 (C_{12}), 57.7 (C_5), 56.2 (C_{16}), 46.4 (C_{22}), 45.2 (C_{20}), 39.2 (C_{15}), 28.5 (C_{14}), 25.9 (C_{19}), 20.2 (C_{13}). **^{19}F NMR** (376 MHz, CD_3OD) δ -153.71 (m), -153.76 (m). **HR-ESI-MS** *m/z* = 339.2087 $[M\text{-}BF_4]^+$ (calculated for $C_{21}H_{27}N_2O_2$ = 339.2037).

5.5 Appendix of Supplementary Data and Discussion

5.5.1 X-Ray Crystallographic Analysis

Analysis of all crystal structures and their packing are shown (Figure 5.5 – 5.6) with the crystal system, space group and unit cell parameters reported below.

To ensure methylation of N_1 and N_2 did not give vastly different conformations that could in turn modify their photoluminscent properties, the torsion angles of N_1-C_{12}-C_{11}-C_8 were measured. (Table 2). We observe minimal changes in the torsion angles between protonation and methylation, therefore we can assume changes in the PLQY, absorption and emission profile are independent of conformation and are indeed electronic effects.

Table 2. Comparisons of the torsion angle N_1-C_{12}-C_{11}-C_8 upon protonation/methylation of N_1 and N_1/N_2.

Compound	N_1-C_{12}-C_{11}-C_8 Torsion Angle
Qn	156.08
QS	161.20
MeQn·BF_4	162.02
Me_2Qn·$2BF_4$	168.47

A difference in intermolecular hydrogen bonding arises when N_2 is methylated or is in its free base form. Surprisingly hydrogen bonding from N_1 is not present even when in free base form. Therefore as expected **Qn** and **MeQn**·BF_4 show intermolecular hydrogen bonding between N_2 and OH_{21}**.** When this position is methylated, hydrogen bonding from the nitrogen lone pair is not possible, therefore is not observed in the crystals of **Me_2Qn**·$2BF_4$. Knowing this, we can predict that in the solid state, **iMeQn**·BF_4 would have comparable torsion angles and does not partake in intermolecular hydrogen bonding.

MeQn·BF_4

Crystals of **MeQn**·BF_4 suitable for X-ray diffraction were grown by slow cooling of a saturated MeCN solution.

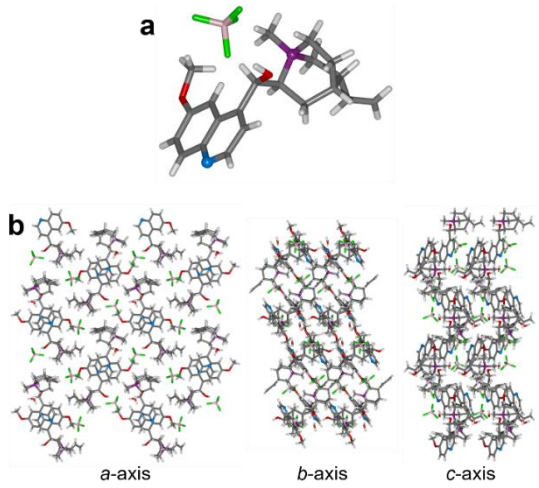

Figure 5.5. a) Solid-state structure and b) crystal packing of **MeQn**·BF_4.

Crystal System: Monoclinic

Space group: $P12_11$

Unit Cell Parameters: a = 8.0721(2) Å, b = 15.6353(5) Å, c = 16.4422(5) Å, α = β = 98.2832(14) °, γ = 90 °, V = 2053.52(10) $Å^3$, Z = 4

Me_2Qn·$2BF_4$

Crystals of **Me_2Qn**·$2BF_4$ suitable for X-ray diffraction were grown by slow cooling of a saturated MeCN solution.

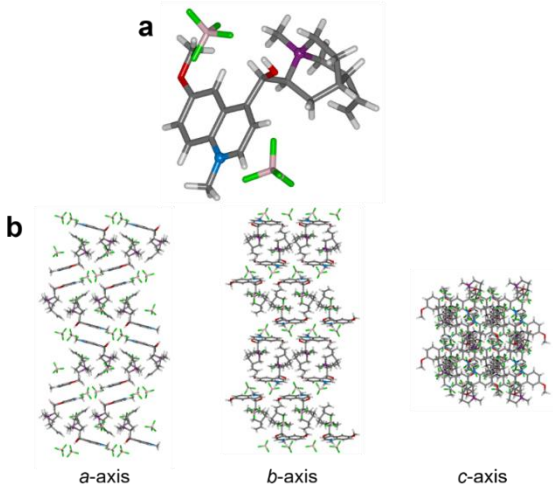

Figure 5.6. a) Solid-state structure and b) crystal packing of **Me_2Qn**·$2BF_4$.

Crystal System: Orthorhombic
Space group: $P2_12_12_1$
Unit Cell Parameters: a = 9.6961(3) Å, b = 10.2407(3) Å, c = 23.6533(8) Å, α = β = γ = 90 °, V = 2348.65(13) $Å^3$, Z = 4

5.5.2 Photoluminescence Quantum Yield measurements

Photoluminescence Quantum Yields (PLQYs) were measured for each compound in MeCN, H_2O and 10 mM Et_3N / MeCN. The first data point for each sample was collected with an absorption optical density (OD) of 0.1 and successively diluted with the desired solvent to around ~0.01 OD over 10 measurments. At each OD an emission spectra was recorded and the emission maxima (E_{em}) was plotted against the recorded OD to give a straight line. The gradient of the slope is the measured PLQY.

We used acidified quinine sulphate in 0.1 M H_2SO_4 (**QS**) and 2-aminopyridine in 0.1 M H_2SO_4 as two standards to ensure our PLQY measurments are accurate. Acidifed QS was selected as we are studying derivatives of this compound, and the excitation (350 nm) used for the standard matches the excitation of the new alkylated quinine compounds. A second standard was selected to ensure minimal error. 2-aminopyridine in 0.1 M H_2SO_4 was selected due to its high PLQY (60%) and requires the same solvent system as **QS** to allow direct comparison. Each figure (Figure 5.7-5.12) shows measurment of the desired compound in the desired compound, and is also supported by measurment with a PLQY standard measured on the same day on the same instrument to ensure reliable, reproducable results.

H_2O was selected as a protic source to measure effects of N_1/N_2 protonation. MeCN shows the alkylated quinine derivatives can be measured in organic solvents, proving a new range of PLQY standards that can be possible in organic solvents. To ensure N_1 remains as the free base in **iMeQn·BF_4** Et_3N/MeCN was used, allowing the expected CT state to be present. To ensure the measurments were consistent every compound was also measured in a 10 mM Et_3N/MeCN solution even if both N_1 and N_2 were alkylated such as **Me_2Qn·2BF_4**.

Aqeuous PLQY studies.

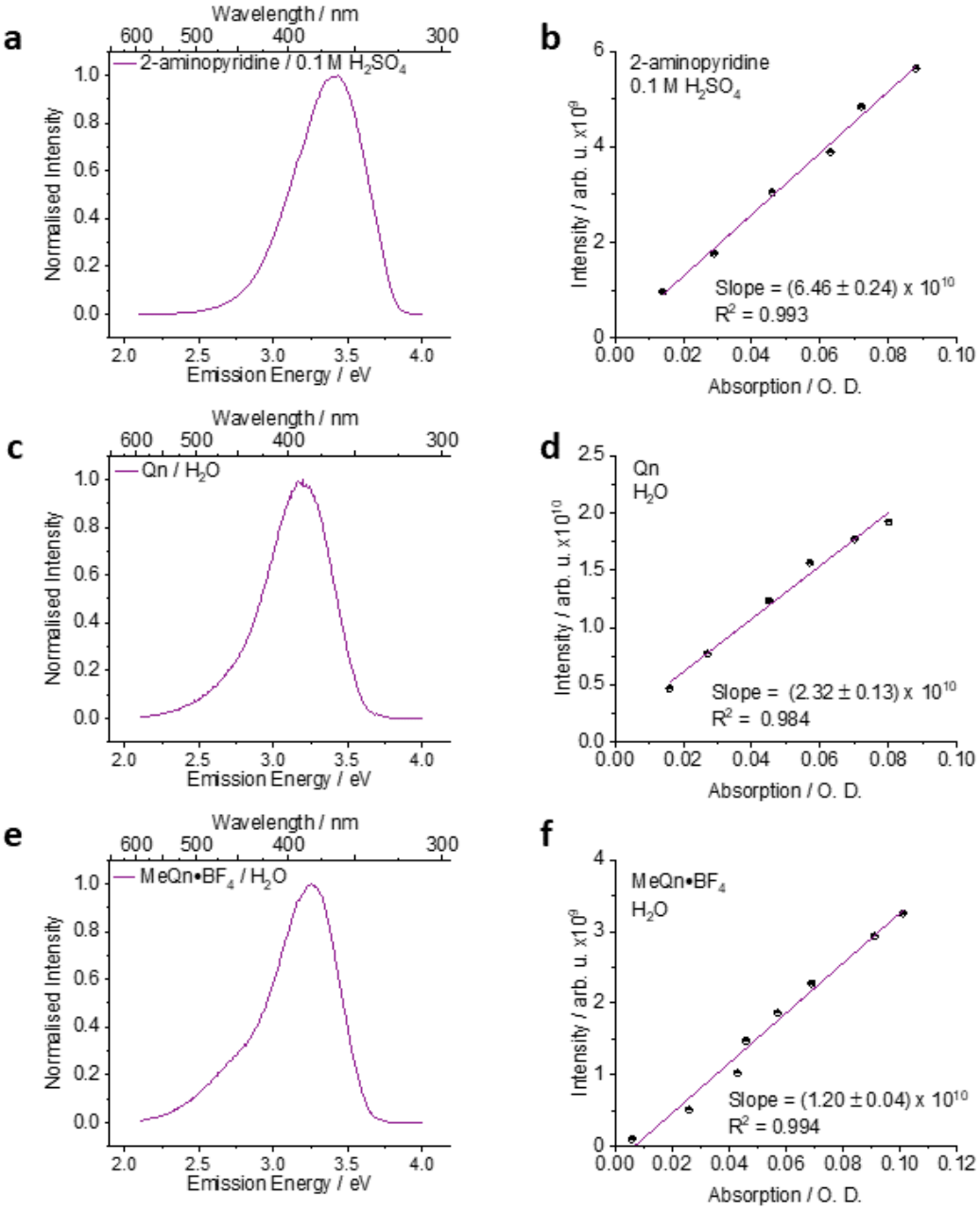

Figure 5.7. The emission spectra and emission/absorption slope of (a-b) 2-aminopyridine in 0.1 M H_2SO_4, (c-d) **Qn** in H_2O and (e-f) **MeQn·BF$_4$** in H_2O.

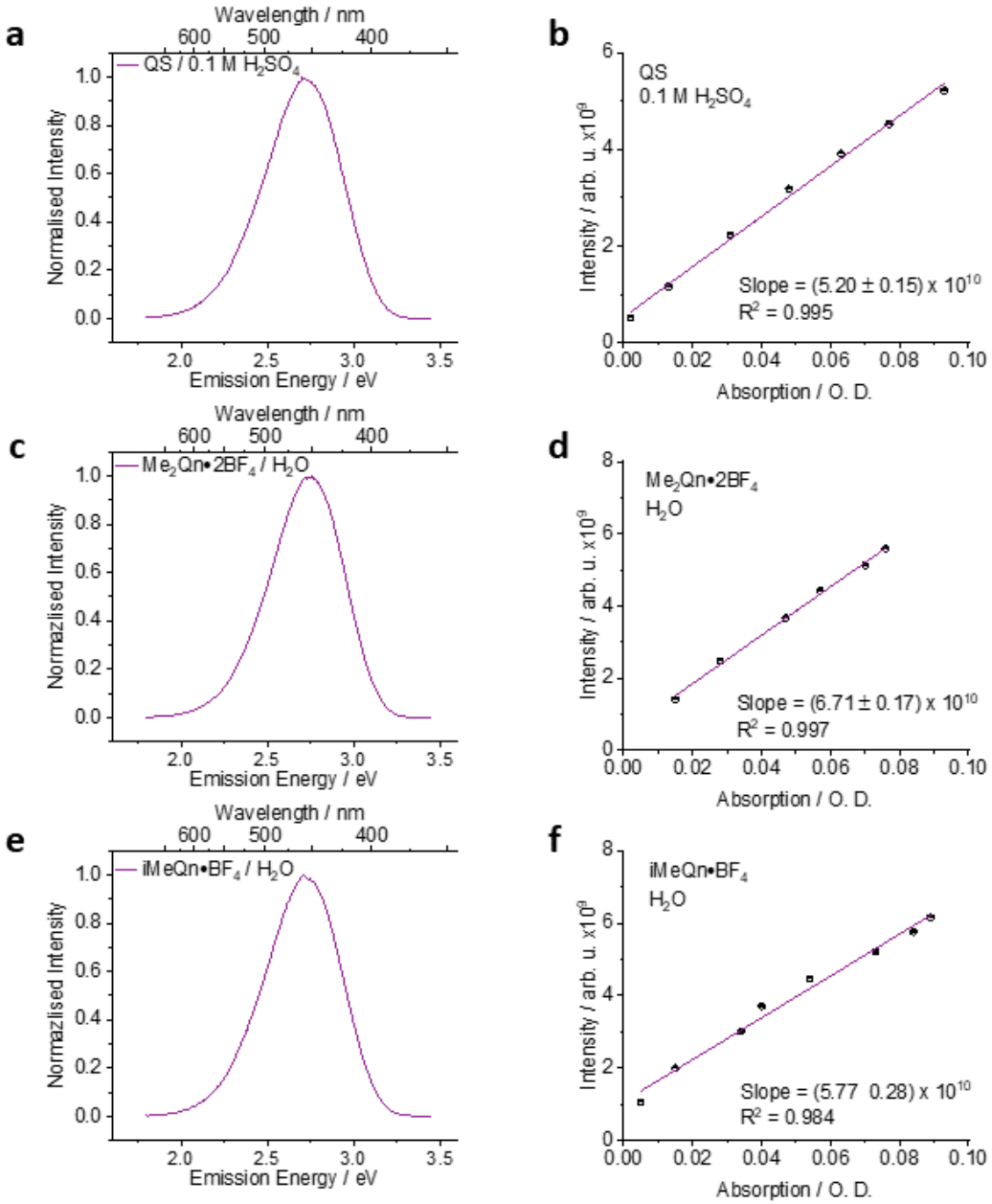

Figure 5.8. The emission spectra and emission/absorption slope of (a-b) **QS** in 0.1 M H_2SO_4, (c-d) **$Me_2Qn \cdot 2BF_4$** in H_2O and (e-f) **iMeQn·BF_4** in H_2O.

MeCN/Et₃N PLQY Studies.

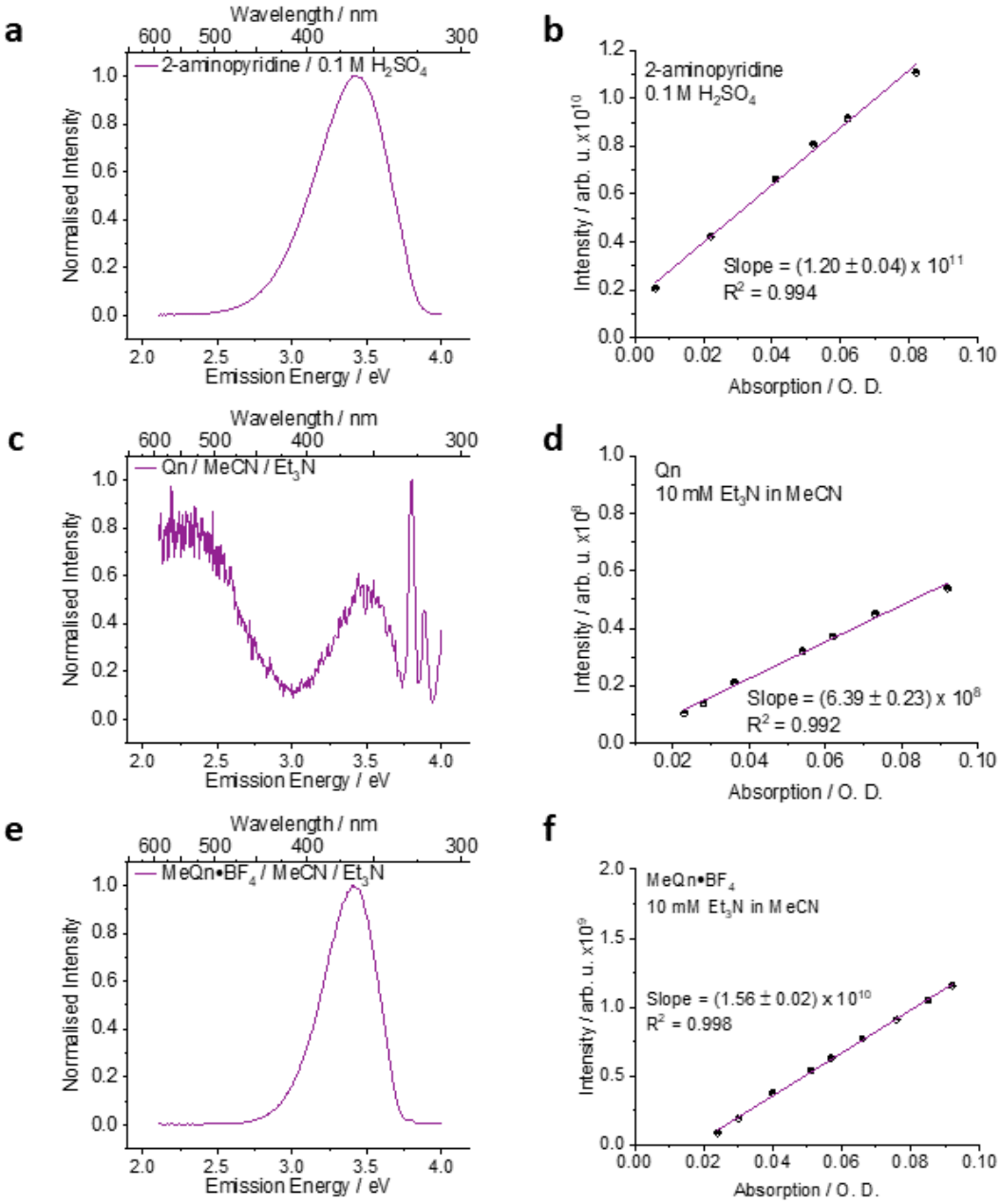

Figure 5.9. The emission spectra and emission/absorption slope of (a-b) 2-aminopyridine in 0.1 M H_2SO_4, (c-d) **Qn** in 10 mM Et_3N in MeCN and (e-f) **MeQn·BF₄** in 10 mM Et_3N in MeCN.

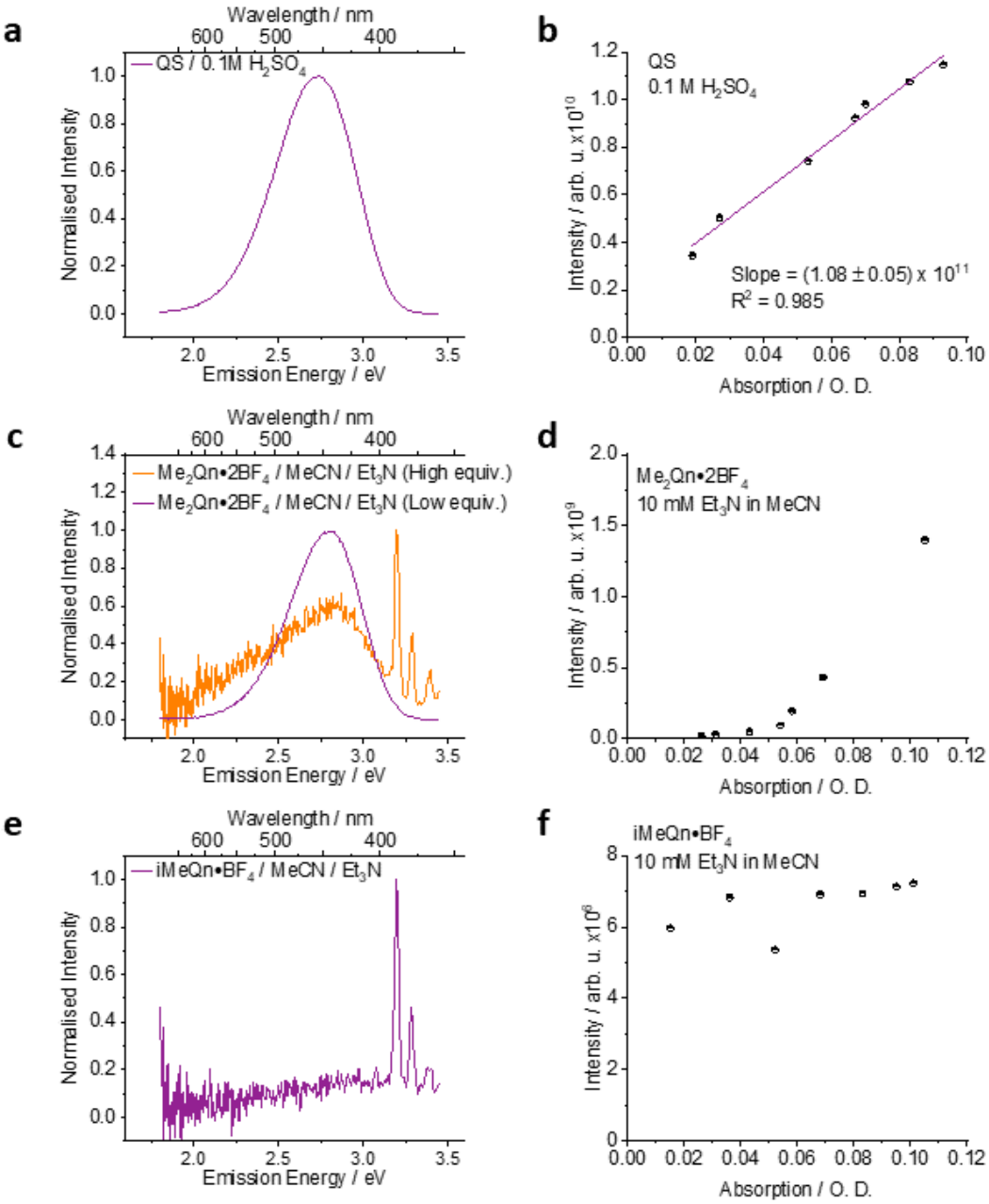

Figure 5.10. The emission spectra and emission/absorption slope of (a-b) **QS** in 0.1 M H_2SO_4, (c-d) **Me_2QN·2BF_4** in 10 mM Et_3N in MeCN and (e-f) **iMeQn·BF_4** in 10 mM Et_3N in MeCN.

MeCN without Et_3N PLQY Studies.

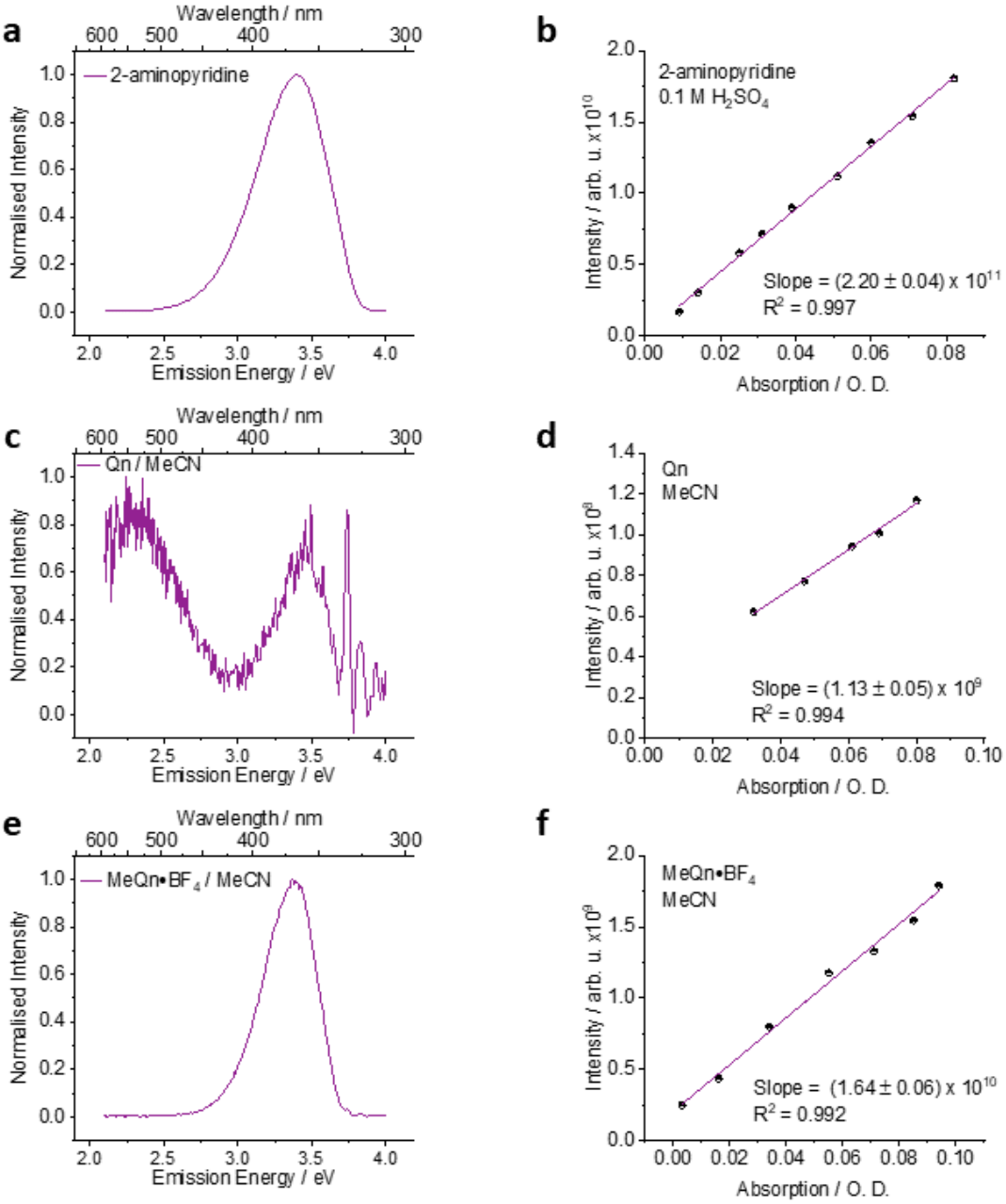

Figure 5.11. The emission spectra and emission/absorption slope of (a-b) 2-aminopyridine in 0.1 M H_2SO_4, (c-d) **Qn** in MeCN and (e-f) **MeQn·BF4** in MeCN.

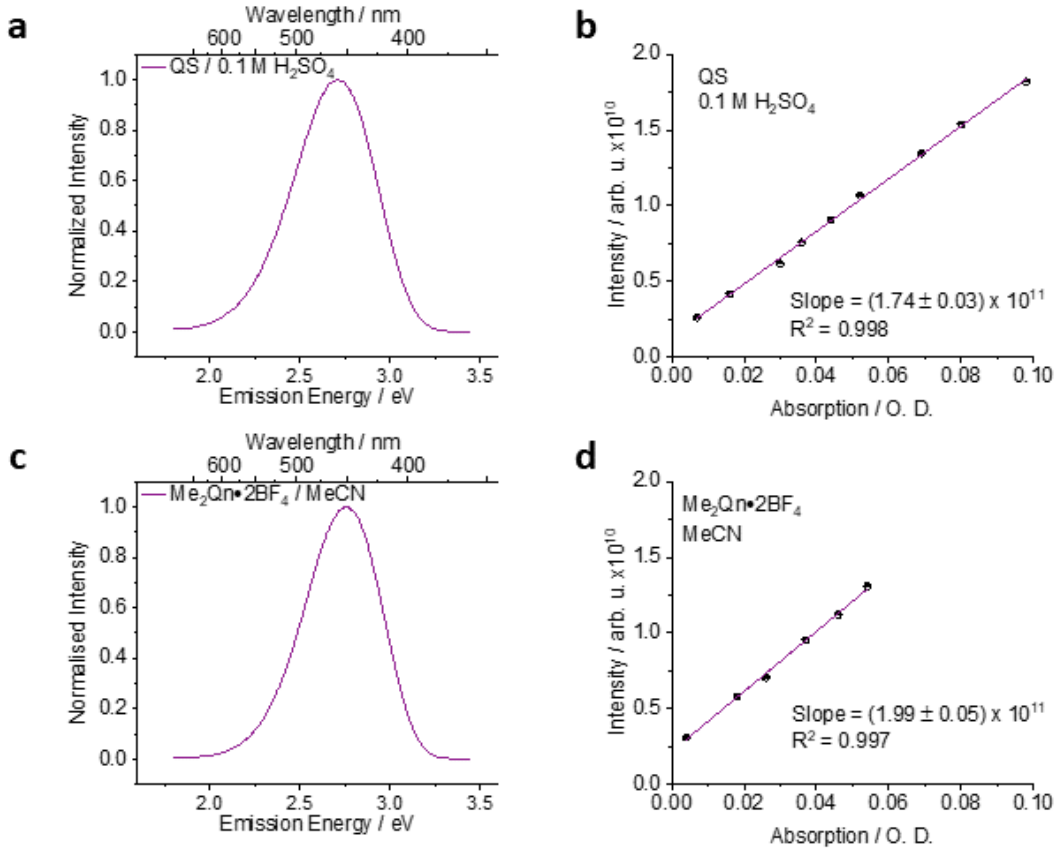

Figure 5.12. The emission spectra and emission/absorption slope of (a-b) **QS** in 0.1 M H_2SO_4 and (c-d) **$Me_2Qn \cdot 2BF_4$** in MeCN

5.6 Theoretical Study

Computational details

Ground state geometry optimizations of quinine and its derivatives were performed both *in vacuo* and using an implicit MeCN solvent. We used a protonation of N_1 and N_2 instead of a methylation, but Table 7 below shows that the effect of such substitution is minimal for emission energies. We employed density functional theory (DFT) with the ωB97X-D exchange-correlation functional[21] and a 6-31G* basis set.[22] The latter functional contains both long-range and dispersion interaction corrections. Solvent effects were taken into account using self-consistent reaction field (SCRF) model, where the solvent is represented by a dielectric continuum. More specifically, we employed the integral equation formalism of the polarisable continuum model (IEFPCM).[23] Harmonic vibrational frequencies were computed to confirm the nature of all stationary points.

Excited electronic states were computed using linear-response time-dependent density functional theory (LR-TDDFT) at the ωB97X-D/6-31G* level of theory and systematically compared to results obtained with the wavefunction-based second-order algebraic diagrammatic construction method (ADC(2)),[24] used along with a cc-pVDZ basis set.[25] ADC(2) calculations were performed with frozen core and resolution of identity approximations. To justify the use of a small basis set, tests were conducted for comparison with the larger aug-cc-pVDZ basis set.[26]

Vertical transitions were calculated based on the optimized ground state geometries using LR-TDDFT, with nonequilibrium linear-response IEFPCM solvation (MeCN). As our main focus is to determine the emission properties of the studied compounds, we also located minimum energy structures on the potential energy surface of the first excited state (and also the second one for some specific cases). For these excited-state geometry optimizations, we used LR-TDDFT combined with equilibrium linear-response IEFPCM solvation (MeCN). Harmonic vibrational frequencies were computed for excited state minima, and the corresponding zero point energies were used to estimate $E_{0\text{-}0}$ transitions. The linear-response approach for implicit solvation models is known to provide reliable excited-state geometries, but less accurate emission energies.[27] Therefore, the emission energies were also computed with the state-specific approach as implemented in Gaussian09. ADC(2) excited-state optimizations were performed only *in vacuo*, and harmonic frequencies were not computed due to the high computational cost. To estimate the emission energy for the solvated systems, single-point ADC(2) computations with the conductor-like screening model (COSMO)[28] for solvation were performed *a posteriori* on the optimized gas phase geometries. This protocol relies on the assumption that the calculated excited-state structures are similar in gas phase and solvent. We also assume the equilibrium solvation limit, in which the electronic and nuclear degrees of freedom of the solvent adapt to the excited-state (rather than the ground-state) charge distribution of the solute.[29] It is important to note, however, that we do not attempt here to closely reproduce the experimental values with our calculations, but rather to detect the main qualitative changes in absorption and emission upon protonation of quinine.

Excited-state characteristics were analysed by computing natural transition orbitals (NTO),[30] both with TD-DFT and ADC(2). All DFT/LR-TDDFT calculations were performed with the Gaussian09 software,[31] while ADC(2) calculations were conducted with Turbomole 7.3.1 program package.[32] Molecular representations were produced with VMD 1.9.2.[33]

Supporting calculations

Qn can have different conformations, and its stable conformers were analyzed in detail in earlier theoretical and experimental work.[34,35] Here, we have mainly focused our attention on the so called cis-γ-open(3) conformer, which was identified as the most stable conformer based on jet-cooled spectroscopy, vibrational circular dichroism and theoretical calculations.[35] The same conformer is found for the crystal structure of **Qn**.[36]

The absorption spectrum of **Qn** contains both locally excited (LE) bright π-π* transition localized on the quinoline moiety, and a higher-lying CT state in which the electron is transferred from a *n*(N) orbital of quinuclidine to a π* orbital of quinoline (*n*-π*). As shown in Table 3, the LE(π-π*) state is the lowest excited singlet state both with ωB97X-D and ADC(2). At the ground-state (i.e. Franck–Condon) geometry, the CT(*n*-π*) state lies higher in energy, and is likely to be overestimated by ωB97X-D. Using a larger basis set does not alter these trends – the relevant transitions are only slightly down shifted.

Table 3. Excited states of quinine (*in vacuo*) at the ground-state geometry optimized at ωB97X-D/6-31G* level. Excitation energies are given in eV, along with corresponding oscillator strengths (f).

	ωB97x-D/6-31G*	ωB97x-D/aug-cc-pVDZ	ADC(2)/cc-pVDZ	ADC(2)/aug-cc-pVDZ
S_1	4.47 (LE), f=0.0993	4.35 (LE), f=0.0992	4.27 (LE), f=0.0949	4.15 (LE), f=0.0979
S_2	4.72, f=0.0029	4.67, f=0.0019	4.63, f=0.0024	5.53, f=0.0018
S_3	4.92, f=0.0336	4.81, f=0.0296	4.89 (CT), f=0.0013	4.63 (CT), f=0.0010
S_4	5.44 (CT), f=0.0029	5.34 (CT), f=0.0020	4.97, f=0.0529	4.71, f=0.0061
S_5	5.79, f=0.0002	5.71, f=0.0029	5.51, f=0.0002	4.82, f=0.0400

Upon protonation of the N atoms having an available lone pair, the excited states are either shifted in energy or removed from the spectrum (as they cannot be formed anymore). Table 4 compares the absorption energies of the LE(π-π*) and CT(*n*-π*) states of **Qn** and its protonated derivatives, **HQn** (proton on N_1), **iHQn** (proton on N_2)

and **H_2Qn** (protons on N_1 and N_2) in MeCN. Protonation of N1 prevents the formation of the CT(*n*-π*) states, while protonation of N_2 causes a large red-shift of the LE(π-π*) and CT(*n*-π*) vertical transition (when the latter exists). **H_2Qn** exhibits both effects.

Table 4. LE(π-π*) and CT(*n*-π*) excited states of quinine and its protonated derivatives with ωB97X-D/6-31G* in MeCN. Vertical transitions were evaluated at the ground-state geometries optimized at the same level of theory with DFT. Excitation energies are given in eV, along with corresponding oscillator strengths (f).

	Qn	HQn	iHQn	H_2Qn
LE	4.43, f=0.1312	4.38, f=0.1402	3.93, f=0.1289	3.88, f=0.1263
CT	5.32, f=0.0025	-	4.06, f=0.0064	-

The calculated vertical emission energies (Table 5) indicate that protonation of N_2 causes a significant red-shift of the emission as compared to the pristine **Qn**. However, the LE emission of **iHQn** is expected to be quenched due to the presence of the CT state, i.e., the molecule is likely to undergo nonradiative decay. This is consistent with experimental findings on analogous methylated derivatives, which found barely detectable fluorescence. Interestingly, even in **Qn** the CT state falls down in energy upon geometry relaxation, and the nonradiative population exchange between LE and CT states becomes more likely (keeping in mind that CT energies are overestimated by ωB97X-D). Therefore, LE emission in **Qn** has very low intensity, while CT emission becomes almost equally pronounced (as see in Figure 5.2). Protonation of N_1 causes only slight red-shift in emission. Again, **H_2Qn** benefits from two effects, the colour of its fluorescence is altered, while deleterious nonradiative effects are less likely due to the lack of CT state.

Table 5. Vertical emission energies computed with ωB97X-D/6-31G* and ADC(2)/cc-pVDZ. Note that with ωB97X-D equilibrium linear-response solvation (MeCN) is used, while ADC(2) optimizations were performed in gas phase. Nevertheless, qualitative conclusions are similar. Emission energies are given in eV, along with corresponding oscillator strengths (f).

		Qn	HQn	iHQn	H_2Qn
ωB97X-D	LE	3.8 (S_1), f=0.2641	3.76 (S_1), f=0.2635	converge to CT	3.21 (S_1), f=0.1741
	CT	4.10 (S_2; above LE), f=0.0095	-	2.20 (S_1), f=0.0074	-
ADC(2)	LE	3.75 (S_1), f=0.1078	3.59 (S_1), f=0.1262	2.69 (S_2; above CT), f=0.0777	2.58 (S_1), f=0.0924
	CT	3.01 (S_1), f=0.0000	-	0.73 eV (S_1), f=0.0005	-

We have also evaluated emission energies based on a state-specific solvation schemes (Table 6), in which solvent is supposed to fully equilibrate with the excited state from the solute, while the ground state of the solute is treated in a non-equilibrium limit. The underlying assumption is that the excited-state lifetime is sufficiently long such that the slow and fast degrees of freedom of the solvent have sufficient time to adapt.[29] One possible explanation for the too low emission energies of the CT states could be related to a breakdown of this assumption, the CT states being too short lived to allow for a full relaxation of the solvent (leading to an overestimation of relaxation effects in the calculations). This effect is particularly striking for **Qn**, which exhibits experimentally an emission band centred at around 2.2 eV, see Figure 5.2). We note here that such underestimation of CT bands with state-specific implicit solvent models were reported in the literature.[37,38] explicit solvent effects might be required to improve the description of this band. The LE states of **Qn** and **iHQn** may also not have sufficiently long lifetime due to the nonradiative effects mentioned above, but the variations in LE emission energy with and without state-specific solvation are generally not very large.

Table 6. Emission energies from state-specific equilibrium solvation (MeCN). The optimized geometries are the same as those in Table 5, but additional single-point computations were conducted. Emission energies are given in eV.

		Qn	HQn	iHQn	H_2Qn
ADC(2) ωB97x-D	LE	3.75	3.69	-	3.00
	CT	0.87	-	1.01	-
	LE	3.61	3.47	2.56	2.43
	CT	1.14	-	0.09	-

Finally, Table 7 shows that methylation has almost the same impact on fluorescence as protonation.

Table 7. Comparison of vertical emission energies for the protonated and methylated quinine derivatives. Excited states were optimized with ωB97X-D/6-31G* and equilibrium linear-response solvation (MeCN). Emission energies are given in eV, along with corresponding oscillator strengths (f).

	HQn	iHQn	H_2Qn
LE	3.76 (S_1), f=0.2635	converge to CT	3.21 (S_1), f=0.1741
CT	-	2.20 (S_1), f=0.0074	-

	MeQn	iMeQn	Me_2Qn
LE	3.75 (S_1), f=0.2574	converge to CT	3.23 (S_1), f=0.1840
CT	-	2.23 (S_1), f=0.0088	-

5.7 References

1. H. Uoyama, K. Goushi, K. Shizu, H. Nomura and C. Adachi, *Nature*, 2012, **492**, 234–238.
2. M. K. Etherington, J. Gibson, H. F. Higginbotham, T. J. Penfold and A. P. Monkman, *Nat. Commun.*, 2016, **7**, 13680.
3. F. B. Dias, K. N. Bourdakos, V. Jankus, K. C. Moss, K. T. Kamtekar, V. Bhalla, J. Santos, M. R. Bryce and A. P. Monkman, *Adv. Mater.*, 2013, **25**, 3707–3714.
4. J. Mei, N. L. C. Leung, R. T. K. Kwok, J. W. Y. Lam and B. Z. Tang, *Chem. Rev.*, 2015, **115**, 11718–11940.
5. Kenry, C. Chen and B. Liu, *Nat. Commun.*, 2019, **10**. 2111
6. V. I. Novoderezhkin, J. P. Dekker and R. van Grondelle, *Biophys. J.*, 2007, **93**, 1293–1311.
7. T. K. Ahn, T. J. Avenson, M. Ballottari, Y.-C. Cheng, K. K. Niyogi, R. Bassi and G. R. Fleming, *Science.*, 2008, **320**, 794–797.
8. D. B. Bucher, C. L. Kufner, A. Schlueter, T. Carell and W. Zinth, *J. Am. Chem. Soc.*, 2016, **138**, 186–190.
9. L. Martinez-Fernandez, Y. Zhang, K. de La Harpe, A. A. Beckstead, B. Kohler and R. Improta, *Phys. Chem. Chem. Phys.*, 2016, **18**, 21241–21245.
10. W. Qin, A. Vozza and A. M. Brouwer, *J. Phys. Chem. C*, 2009, **113**, 11790–11795.
11. J. Qian and A. M. Brouwer, *Phys. Chem. Chem. Phys.*, 2010, **12**, 12562–12569.
12. K.-L. L. Wang, W.-T. T. Liou, D.-J. J. Liaw and S.-T. T. Huang, *Polymer (Guildf).*, 2008, **49**, 1538–1546.
13. J. Zhang, J. Chen, B. Xu, L. Wang, S. Ma, Y. Dong, B. Li, L. Ye and W. Tian, *Chem. Commun.*, 2013, **49**, 3878–3880.
14. S. Achelle, J. Rodríguez-Lopez, C. Katan and F. Robin-Le Guen, *J. Phys. Chem. C*, 2016, **120**, 26986–26995.
15. A. N. FLETCHER, *Photochem. Photobiol.*, 1969, **9**, 439–444.
16. J. S. Svendsen, I. Markó, E. N. Jacobsen, C. P. Rao, S. Bott and K. B. Sharpless, *J. Org. Chem.*, 1989, **54**, 2263–2264.
17. M. Kubicki, T. Borowiak, K. G. Aw Rońska and J. Gawroński, *Formation and Structure of Cinchona Alkaloid (Bis-2,3-naphthalenediyl)orthoborate Salts*, 2000, vol. 55.
18. A. T. R. Williams, S. A. Winfield and J. N. Miller, *Analyst*, 1983, **108**, 1067.
19. W. H. Melhuish, *J. Phys. Chem.*, 1961, **65**, 229–235.
20. R. Rusakowicz and A. C. Testa, *J. Phys. Chem.*, 1968, **72**, 2680–2681.
21. J.-D. Chai and M. Head-Gordon, *Phys. Chem. Chem. Phys.*, 2008, **10**, 6615.
22. R. Krishnan, J. S. Binkley, R. Seeger and J. A. Pople, *J. Chem. Phys.*, 1980, **72**, 650–654.
23. J. Tomasi, B. Mennucci and R. Cammi, *Chem. Rev.*, 2005, **105**, 2999–3093.
24. A. Dreuw and M. Wormit, *Wiley Interdiscip. Rev. Comput. Mol. Sci.*, 2015, **5**, 82–95.
25. T. H. Dunning, *J. Chem. Phys.*, 1989, **90**, 1007–1023.
26. R. A. Kendall, T. H. Dunning and R. J. Harrison, *J. Chem. Phys.*, 1992, **96**, 6796–6806.
27. R. Improta, G. Scalmani, M. J. Frisch and V. Barone, *J. Chem. Phys.*, 2007, **127**, 07405.

28. A. Klamt and G. Schüürmann, *J. Chem. Soc. Perkin Trans. 2*, 1993, 799–805.

29. B. Lunkenheimer and A. Köhn, *J. Chem. Theory Comput.*, 2013, **9**, 977–994.

30. R. L. Martin, *J. Chem. Phys.*, 2003, **118**, 4775–4777.

31. M. J. Frisch, G. W. Trucks, H. B. Schlegel, G. E. Scuseria, M. A. Robb, J. R. Cheeseman, G. Scalmani, V. Barone, G. A. Petersson, H. Nakatsuji, X. Li, M. Caricato, A. Marenich, J. Bloino, B. G. Janesko, R. Gomperts, B. Mennucci, H. P. Hratchian, J. V. Ortiz, A. F. Izmaylov, J. L. Sonnenberg, D. Williams-Young, F. Ding, F. Lipparini, F. Egidi, J. Goings, B. Peng, A. Petrone, T. Henderson, D. Ranasinghe, V. G. Zakrzewski, J. Gao, N. Rega, G. Zheng, W. Liang, M. Hada, M. Ehara, K. Toyota, R. Fukuda, J. Hasegawa, M. Ishida, T. Nakajima, Y. Honda, O. Kitao, H. Nakai, T. Vreven, K. Throssell, J. A. Montgomery Jr, J. E. Peralta, F. Ogliaro, M. Bearpark, J. J. Heyd, E. Brothers, K. N. Kudin, V. N. Staroverov, T. Keith, R. Kobayashi, J. Normand, K. Raghavachari, A. Rendell, J. C. Burant, S. S. Iyengar, J. Tomasi, M. Cossi, J. M. Millam, M. Klene, C. Adamo, R. Cammi, J. W. Ochterski, R. L. Martin, K. Morokuma, O. Farkas, J. B. Foresman and D. J. Fox, *Gaussian, Inc., Wallingford CT*, 2016.

32. F. Furche, R. Ahlrichs, C. Hättig, W. Klopper, M. Sierka and F. Weigend, *Wiley Interdiscip. Rev. Comput. Mol. Sci.*, 2014, **4**, 91–100.

33. W. Humphrey, A. Dalke and K. Schulten, *J. Mol. Graph.*, 1996, **14**, 33–38.

34. M. K. Bilonda, L. Mammino and S. Scheiner, *Molecules*, 2017, **22**, 1–13.

35. A. Sen, A. Bouchet, V. Lepère, K. Le Barbu-Debus, D. Scuderi, F. Piuzzi and A. Zehnacker-Rentien, *J. Phys. Chem. A*, 2012, **116**, 8334–8344.

36. B. Pniewska and A. Suszko-Purzycka, *Acta Crystallogr. Sect. C Cryst. Struct. Commun.*, 1989, **45**, 638–642.

37. P. Kautny, F. Glöcklhofer, T. Kader, J. M. Mewes, B. Stöger, J. Fröhlich, D. Lumpi and F. Plasser, *Phys. Chem. Chem. Phys.*, 2017, **19**, 18055–18067.

38. J. M. Mewes, J. M. Herbert and A. Dreuw, *Phys. Chem. Chem. Phys.*, 2017, **19**, 1644–1654.